CRANFIELD UNIVERSITY

YAO LIU

APPLICATION OF MECHANICAL SURFACE TREATMENTS TO IMPROVE FATIGUE CRACK GROWTH LIFE OF AIRCRAFT FUSELAGE MATERIALS

SCHOOL OF AEROSPACE, TRANSPORT AND MANUFACTURING
PhD THESIS

PhD
Academic Year: 2014 – 2018

Supervisor: Prof. P.E. Irving, Dr. S. Ganguly

June 2018

CRANFIELD UNIVERSITY

SCHOOL OF AEROSPACE, TRANSPORT AND MANUFACTURING
PhD THESIS

APPLICATION OF MECHANICAL SURFACE TREATMENTS TO
IMPROVE FATIGUE CRACK GROWTH LIFE OF AIRCRAFT
FUSELAGE MATERIALS

Academic Year 2014 - 2018

YAO LIU

APPLICATION OF MECHANICAL SURFACE TREATMENTS TO
IMPROVE FATIGUE CRACK GROWTH LIFE OF AIRCRAFT
FUSELAGE MATERIALS

Supervisor: Prof. P.E. Irving, Dr. S. Ganguly

June 2018

This thesis is submitted in partial fulfilment of the requirements for the
degree of PhD

Abstract

Mechanical treatment for surface processing is a cost-effective tool and has the potential to improve the dynamic strength of a component or structure significantly through creation of a residual compressive stress state. This research is aimed to investigate mechanical surface processing treatments, e.g. deep surface rolling, machine hammer peening, in aircraft fuselage structural alloys to reduce fatigue crack growth rate and improve damage tolerance. The study also revealed that such processing could be used effectively to improve damage tolerance properties of such safety critical structures. However, optimisation of such processes is important as distortion from the processing would need to be minimised, to maximise the benefit from the residual compressive stress field.

This thesis focuses on the application of deep surface rolling to understand the underpinning interaction between stress states and a long fatigue crack under a variably distributed residual stress field. Centre notch of 8 mm length were machined in Middle-tension M(T) specimens of 1.6 mm thickness 2024-T351 and 2524-T351 clad aluminium alloys. The M(T) specimens were locally rolled by a deep surface rolling process to create a spatially resolved compressive residual stress fields on both sides of the notch and under different loads. Prior to application of deep surface rolling on the M(T) specimens, the process was trialled on similar thickness specimens to ensure minimum distortion so that it can be applied on both the surfaces. The spatial position of the DSR patches with respect to the crack tip were varied to understand the interaction of the stress field on crack propagation and how the benefit of the process can be maximised. Following rolling of M(T) specimens, fatigue testing were performed at a stress ratio R = 0.1 and maximum stress of 100 MPa.

A three-dimensional finite-element (FE) model of the DSR process was developed to predict the residual stress field and distortion. This model was validated with experimentally measured residual stress data and distortion. An

analytical method based on experimental residual stress data, was developed to determine the residual stress intensity factor (K_{res}). The crack closure behaviour was taken account for the prediction of the fatigue crack growth rate (FCGR).

Despite formation of a compressive residual stress (CRS) field through the thickness below the DSR patch it was found that improvement of fatigue performance depends on the location of the patch with respect to the crack tip. It was observed that the rolling load parameters and distance from the crack tip are vital in the reduction of crack propagation behaviour. The former balances the stress field and distortion while the later determines the crack driving force, when the crack enters the compressive residual stress field, and a large distance between the crack tip and stress field will cause acceleration of the crack before it enters the compressive stress field. The analytical method of computing K_{res} was successfully contributed to the prediction of FCGR and showed good agreements with experiments. In a further study, the analytical method was used to calculate K_{res} by using the predicted residual stress field from FEA (finite element analysis). Based on the predicted K_{res}, the predicted FCGR showed a good agreement with experiments as well.

The application of DSR to the metal fatigue enhancement is significantly effective and cost-effective. By optimising DSR process to intentionally treat the high possibility of fatigue damage region, the fatigue life can be significantly enhanced, resulting in improvement in damage tolerant design of aerospace structures or components.

Keywords:

Residual stress, deep surface rolling, stress intensity factor, finite element modelling, aluminium alloys, crack closure

Acknowledgements

TABLE OF CONTENTS

LIST OF FIGURES

LIST OF TABLES

LIST OF ABBREVIATIONS

N_{tot}	Total Fatigue Life
N_i	Number of Cycles Until Crack Initiation
N_p	Number of Cycles to Propagate the Crack to Fracture
K_c/K_{Ic}	Fracture Toughness
σ_{max}	Maximum Applied Stress
σ_{min}	Minimum Applied Stress
$\Delta\sigma$	the Applied Stress Range
σ_{op}	Crack Opening Stress Level
R	Stress Ratio
R_{eff}	Effective Stress Ratio
K_{max}	Maximum Stress Intensity Factor
K_{min}	Minimum Stress Intensity Factor
ΔK	Stress Intensity Factor Range
K_{res}	Residual Stress Intensity Factor
ΔK_{eff}	Effective Stress Intensity Factor Range
K_{op}	Crack Opening Stress Intensity Factor
E	Young's Modulus
v	Poisson's Ratio
P	External Force
RS	Residual Stress
CRS	Compressive Residual Stress
TRS	Tensile Residual Stress
FE	Finite Element
C(T)	Compact Tension
M(T)	Middle Tension
PICC	Plastically Induced Crack Closure
EDM	Electrical Discharge Machining
DSR	Deep Surface Rolling
FCGR	Fatigue Crack Growth Rate
WFM	Weight Function Method
CTOD	Crack Tip Open Displacement
ICHD	Incremental Centre Hole Drilling
ND	Neutron Diffraction
HP	Hammer Peening
LSP	Laser Shock Peening

1 Introduction

The effects of metal fatigue plays a vital role in optimising the design of aerospace structures [1-3], since the constraints of reduced costs and an increased design life of parts have changed the design cycle of new products by introducing new materials [4]. The fatigue phenomenon is often referred to as a process of damage accumulation in a component undergoing repeating load. Parameters such as cyclic load, stress intensity and fatigue crack growth rate are used to describe the mechanical fatigue process resulting from a repeated cyclic load being applied to a structure containing a pre-existing defect.

Aircraft design has turned to an approach which incorporates improved performance, extended operating life and reduced environmental impact of an aircraft structure [5]. Modern aircraft are pre-designed using the damage tolerance methodology [6,7]. This research approach ensures that the duration between aircraft service intervals allows for repair of a fatigue crack before it can propagate to a critical length.

Since the first half of the 20th Century, the surface engineering process of shot peening has been widely used for industrial applications in mass production [8]. In the U.S.A., deep rolling was applied as a surface treatment to strengthen axles of the Ford Model T and the axles of trains were also deep rolled for mechanical improvement. In the 1970s, the basic effects of deep rolling on fatigue behaviour were thoroughly investigated, and the influence of notches and material hardness on fatigue strength enhancement of deep rolled components became clear [9,10,11].

A variety of parameters, of which the contact force or pressure is undoubtedly the most important, used during mechanical processes like shot peening or deep rolling severely influence the near-surface residual stress state [12,13]. It is known that only optimised rolling forces increase the fatigue strength. Rolling forces that are too low have no pronounced effect on the fatigue behaviour, whilst forces that are too high may result in the generation of microcracks [12]. The

possibility of controlled residual stress field to influence fatigue crack propagation has been investigated by many researchers as mechanical surface treatments are increasingly applied nowadays [13,14,15]. A significant decrease in the fatigue crack growth rates was observed by Hatamleh [16] in specimens treated by laser shock peening (LSP) versus untreated samples.

As a repair method, DSR and other mechanical surface treatments such as SP, LSP are commonly used to reduce the propagation of fatigue cracks, by inducing highly compressive residual stresses into the material [16-19].

The linear elastic fracture mechanics (LEFM) method is the most commonly employed approach used to study the effect of an existing residual stress field on the long fatigue crack growth behaviour [20]. It is assumed that the principle of superposition is valid and that residual stress redistribution is not affected by the presence of the small-scale plasticity associated with long fatigue crack propagation [21]. Knowledge of crack closure helps to understand the effects on crack behaviours and hence fatigue performance by induced residual stress fields.

Extensive work has been reported in the literature to fill the gap between residual stress fields and fatigue crack growth rates. In most research of the DSR, a more attractive advantage of the DSR treatment is to reduce the tensile residual stress generated during welding and additive manufacturing. In aerospace, most surface treatments are still considered as a repair process only.

1.1 Project Objectives

The commonly applied process of laser peening a material's surface is a novel, yet expensive. Deep surface rolling and alter methods such as hammer peening (HP) are used to improve fatigue resistance, more precisely, to reduce fatigue crack growth.

This research aims to investigate the application of deep surface treatments in aircraft fuselage structural alloys to increase fatigue life. Another underpinning work is to optimise DSR process by the study of stress interaction mechanisms with FE.

The objectives of the research were:
- Investigate DSR parameters to provide compressive residual stress through the entire thickness of thin (1.6mm) aluminium alloy sheets (AA2024-T351 and AA2524-T351 mainly used)
- To investigate the effects and behaviours of the DSR treated sheets on distortion and induced residual stresses by using finite element analysis (FEA), FE results are validated by experimental measurements of deep rolled specimens
- To investigate the predicted effect on the crack closure of residual stress by using superposition and Newman theory
- The application of the hammer peening treatment and its effect on hardness and residual stress fields
- Understand the formation of the RS field by the hammer peening treatment
- Influence of the hammer peening in reduction of fatigue crack growth
- To obtain the residual stress field from FE models and to predict FCGR of DSR treated samples by the obtained RS, and validate by fatigue tests

1.2 Methodology

The research process to build a relationship between residual stress and FCGR is briefly demonstrated in figure 1.1. The methods used to achieve the objectives are described.
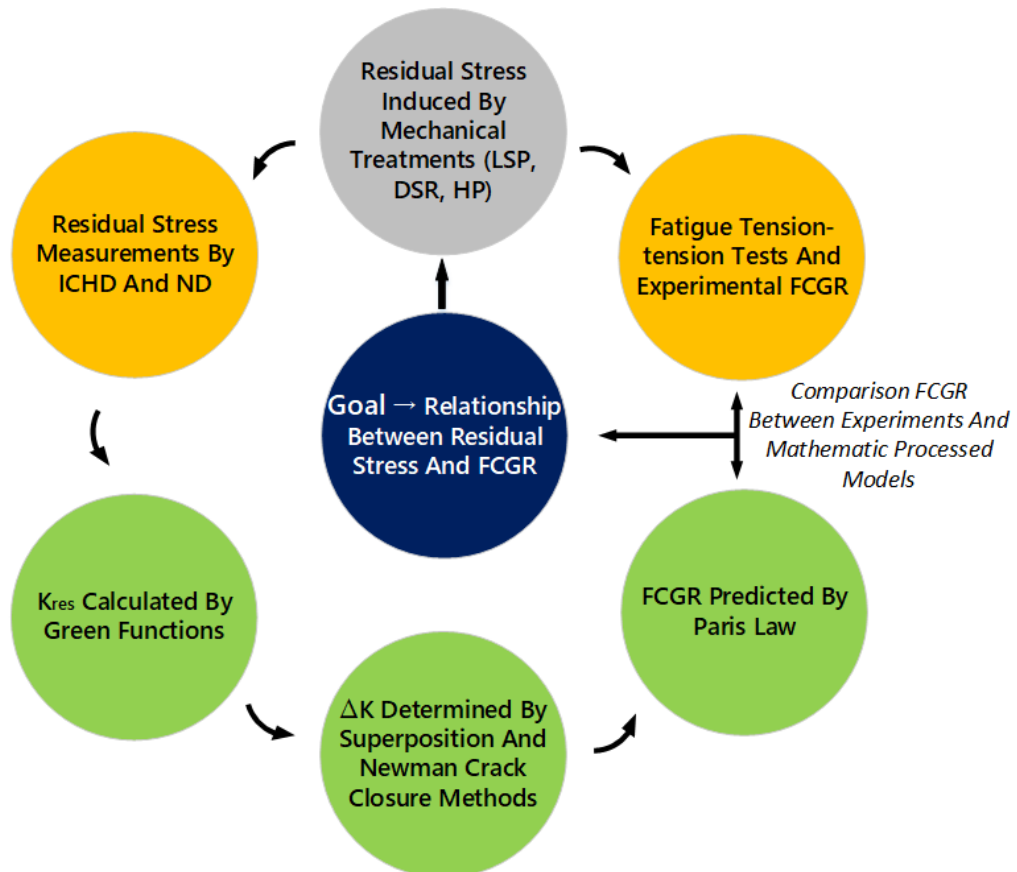
Figure 1.1 The research process for building the relationship between residual stress and fatigue crack growth rates (FCGR)

By the qualitative and quantitative analysis of residual stress and distortion generated after DSR treatments, the DSR process was optimised to improve fatigue performance, in order to accomplish the aim of this research, application of DSR in aircraft fuselage structural alloys.

The effect on FCGR by various DSR treatments and fatigue loading conditions was studied using centre-slit specimens of 1.6 mm thickness AA2024-T351 and AA2524-T351. The centre-slit of test specimens were made to 8 mm length by EDM (Electrical Discharge Machining) and then tested in constant amplitude fatigue loading until sample fracture. The effect on fatigue performance of various DSR treatments was considered. All testing specimens were deep rolled after the samples were centre-slited. Specimens treated by DSR were characterised by measuring the effect on distortion and by the measurement of the induced residual stress fields using the incremental hole drilling method and the neutron diffraction method.

Analyses of crack propagation in residual stress fields are of practical importance in welded structures and for aircraft maintenance. The determination of stress intensity factor for the crack absent stress distribution is based on superposition principle and most conveniently used as the Green's function.

When additional external loads were also present during fatigue tests, the effect of stress intensity factor range and stress ratio was determined by superposition and Newman approaches. The effect of the induced residual stress fields on plasticity induced crack closure was studied and further developed by the Newman equations.

Finally, Paris and Walker equations were developed and compared to predict the fatigue crack propagation rates by the effect of induced residual stress fields.

1.3 Thesis Structure

In chapter 2 a literature review is presented. The theoretical background of fatigue crack propagation mechanisms and overviews of crack closure phenomenon are presented. The sources of residual stress in components and measurements of residual stresses are reviewed. Effects of residual stress on distortion and fatigue performance are emphatically reviewed. A description of the DSR treatment and

developments of DSR are reviewed. Other mechanical surface techniques are described as well. Finally, FEA of deep surface rolling techniques in welding processes is reviewed. In addition, FEA of deep rolling on inducing compressive residual stress is presented.

Material properties and experimental methods are given in chapter 3. The test material is characterised and the geometries of test samples are presented. As the main mechanical surface treatments, DSR and HP are described. Experimental measurements of distortion and microhardness are demonstrated. The particular description of residual stress measurements is detailed. The fatigue test procedures and test parameters applied are described. The procedures used for fractographic inspection are detailed.

The experimental results are demonstrated in chapter 4. The physical effect on the fatigue specimens of DSR treatment is presented. Tension-tension fatigue test results are demonstrated. Calculated fatigue crack growth rates from measured scratch lines are presented and fatigue crack trajectories are reported.

In chapter 5, FE modelling techniques used to study the effect of distortion and residual stress distribution on thin aluminium alloy sheets (1.6 mm thickness) treated by the DSR process. A finite element model of the deep surface rolling process was developed and various parameters of different loads and roller mobility is investigated. The effect of DSR on distortion reduction and 3D distribution of residual stress are reported.

In Chapter 6, methods of residual stress intensity factor calculation are provided. Under different residual stress fields, effective stress intensity factors are determined by superposition and crack closure methods. The effect of fatigue crack growth rates influenced by DSR is further investigated. Residual stress fields obtained by FE models are applied to the prediction of FCGR of deep rolled samples. Results are validated by experimental FCGR from the fatigue tests.

The research results are discussed in chapter 7. Chapter 8 presents the conclusions from the research and recommendations for future work are made in chapter 9.

2 Literature Review

In section 2.1 is a brief overview of the fundamentals of fatigue crack propagation mechanisms in aircraft fuselages. For a detailed review of fracture mechanics see references books by Anderson [22] and Hertzberg [23]. Section 2.2 mainly introduces the fundamentals of residual stresses, as well as the measurements of the RS fields and their effects on fatigue performance. Compressive residual stress is widely known to have beneficial effects on reducing fatigue crack propagation rates. Unintentional tensile residual stresses are known to contribute to the shortening of component lifetime. In the majority of reviewed cases in this thesis, residual stresses were induced by deep surface rolling or other surface treatments. A brief description of surface treatment processes is shown in section 2.3.

2.1 Fatigue Crack Propagation Mechanisms

Maintenance services in aeronautics, transport, machines and installations often encounter the existence of cracks in metal components that have been subjected to a cyclic loading of varying amplitude [24]. It is of significant importance to divide the fatigue life of a structural component into different periods and to treat them separately.

The fatigue life of a metallic material contains different stages; crack nucleation, micro-crack growth, macro-crack growth, and final failure. Crack nucleation is associated with cyclic slip and is controlled by the local stress or strain concentrations. Micro-crack growth, a term now referred to as the "small-crack growth" regime, is the growth of cracks from inclusions, voids, or slip bands in the

range of 1 to 20 µm in length [25]. Schijve [26] has reported that for polished surfaces of pure metals and commercial alloys, the formation of a small crack to about 100 µm in length can consume 60% to 80% of the fatigue life. The AGARD [27,28] and NASA/CAE [29,30] studies on small-crack behaviour showed that about 90% of the fatigue life was consumed for crack growth from about 10 µm to failure on a variety of materials. This is the reason that there is significant interest in the growth behaviour of small cracks. Macro-crack growth and failure are research area where fracture mechanics parameters have been successful in correlating and in predicting fatigue-crack growth and fracture.

Events in the naval, nuclear and aircraft industries have fostered the development of fracture mechanics and the application of stress intensity factor (SIF) analyses to fatigue crack growth, since the 1950's [31]. The failure of the Comet transport jet aircraft, as a result of fatigue cracks, gave rise to treatments to reduce crack propagation using notch-root parameters and the stress intensity factor (SIF) concept of Irwin [33] and Paris et al. [34]. The simplicity of the SIF concept rapidly developed into the durability and damage-tolerance models used to design fatigue/fracture critical components. The vital connection between fatigue and fracture mechanics was the discovery of fatigue crack closure by Elber [35]. This crack-closure concept began to explain many crack-growth characteristics. These developments have greatly improved our understanding of the complex interactions that occur during fatigue crack growth in materials under variable-amplitude cyclic loading [32].

Cyclic fatigue involves the microstructural damage and failure of materials under cyclically varying loads. Structural materials, however, are rarely designed with compositions and microstructures optimised for fatigue resistance. A component or structure throughout its service is usually subjected to cyclic stress with varying upper and lower stress bounds. The type of loading is generally referred to as a variable amplitude load, usually in the form of a sinusoidal waveform as illustrated in figure 2.1.
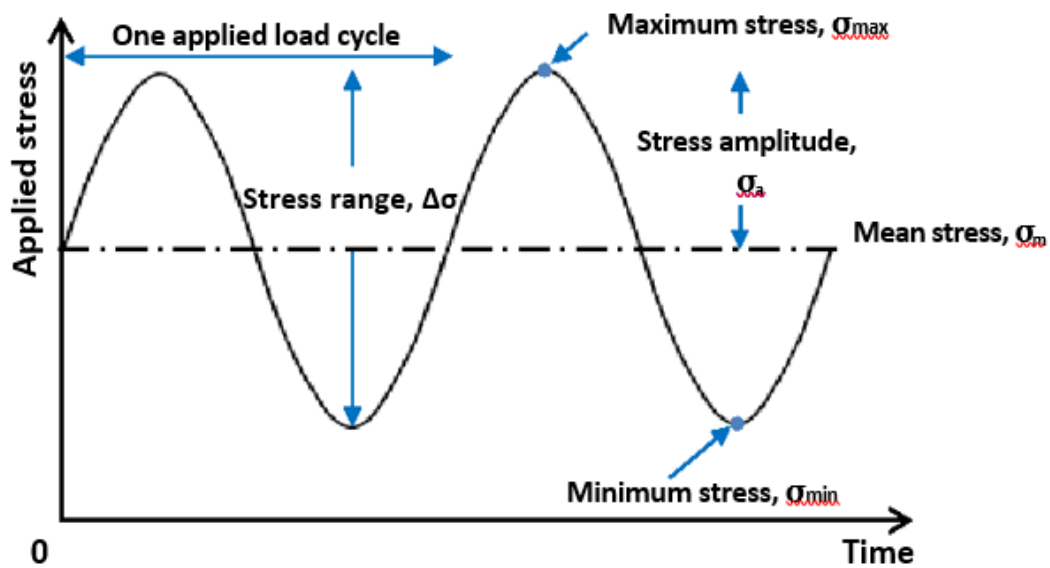
Figure 2.1 The parameters of the waveform involved in fatigue testing

The total fatigue life can be characterised by four stages, and briefly described below.

1. Crack nucleation

Macroscopically, fatigue cracks in flaw-free materials and structures mostly nucleate at the free surface. In materials containing defects, the cracks will preferentially initiate at these defects. Stress concentrations, leading to higher local cyclic plastic strains, result from this behaviour. By microscopically observing the surfaces, it is shown that there are three basic types of nucleation sites; fatigue slip bands, grain and twin boundaries, and inclusions. Fatigue crack nucleation is preceded by cyclic slip localisation. With continued cyclic loading, the slip bands broaden and intensify until the separation of microstructural material grains occurs, and a crack is formed. The number of cycles required to initiate a crack, frequently accounts for the majority of the total fatigue life.

2. Stage I crack-growth (short cracks)

Once initiated, a fatigue crack propagates along high shear stress planes. The stage is characterised by the crack being orientated at an angle to the surface but not normal to the applied load. Grain refinement is capable of improving fatigue strength, and works by inserting a large number of microstructural barriers, which have to be overcome in stage I of crack propagation. Surface mechanical treatments such as shot peening and surface rolling, contribute the number of microstructural barriers per unit of length due to the flattening of the grains [36].

3. Stage II crack-growth (long cracks)

When the stress intensity factor K increases as a consequence of crack propagation or higher applied loads, slips start to develop in different planes close to the crack tips, thus activating stage II [37]. In this stage, the crack propagates across other grains that are normal to the loading direction. This crack growth occurs, not as a consequence of any structural damage, but as a result of the stress concentration effect at the crack tip, since it becomes sharp during unloading. An important characteristic of this stage is the presence of surface ripples known as "striations", which are visible under a scanning electron microscope. Not all engineering materials exhibit striations. They are clearly observed in pure metals and many ductile alloys such as aluminium alloys. The most acceptable mechanism that justifies the formation of striations on the fatigue fracture surface of ductile metals, is the successive blunting and re-sharpening of the crack tip.

Stage I and stage II crack growth are often grouped together and the total fatigue life N_{tot} is characterised using equation 2.1 below.

$$N_{tot} = N_i + N_p \qquad 2.1$$

Where N_i is the number of cycles until crack initiation and N_p is the number of cycles to propagate the crack to fracture.

4. Final failure

Failure of the material occurs when the crack extends in a rapid and unstable manner. The fracture toughness (K_c or K_{lc}) of a material indicates the strength of the material in the presence of a defect or crack. The fracture toughness is also affected by the thickness of the material. As a material thickness increases, the shear lips occupy a decreasing proportion of the cross-section. So the material acts more and more like a brittle material, with reducing toughness. Eventually, the effect of the lips becomes insignificant, and the toughness assumes a constant minimum value, known as the plane-strain fracture toughness [38]. Plane-strain fracture is characterised by having a flat surface perpendicular to the applied load. The fracture surface of thin sections is generally characterised by shear lips as a result of 45° shear fractures known as plane stress fractures.

Crack propagation rate depends primarily on crack length, the applied stress range ($\sigma_{max} - \sigma_{min}$) and the stress ratio ($R = \sigma_{min}/\sigma_{max}$). The relationship accounts for these parameters as demonstrated in equation (2.2) and (2.3).

$$\Delta K = K_{max} - K_{min} \qquad 2.2$$

$$R = \frac{K_{min}}{K_{max}} \qquad 2.3$$

The value of K_{max} is always dependent on σ_{max}, which is subjected to remote tensile stress. However, the value of K_{min} can be influenced by other effects such as crack closure which will be discussed in more detail in section 2.2.

2.1.1 Models of the Fatigue Crack Growth Behaviour

Paris [34] was the first to report a relationship between the fatigue crack growth rate and the stress intensity factor range, as shown in equation 2.4 below, where C and m are material constants determined experimentally.

$$\frac{da}{dN} = C(\Delta K)^m \qquad 2.4$$

The formula describes the linear portion of the log-log plot of *da/dN vs ΔK* as shown in Figure 2.2. This figure illustrates the analytical model of calculated fatigue crack growth curves for a crack starting from a very sharp notch *(Δa = 0 mm)* and for a crack after substantial growth *(Δa = 10 mm)*.
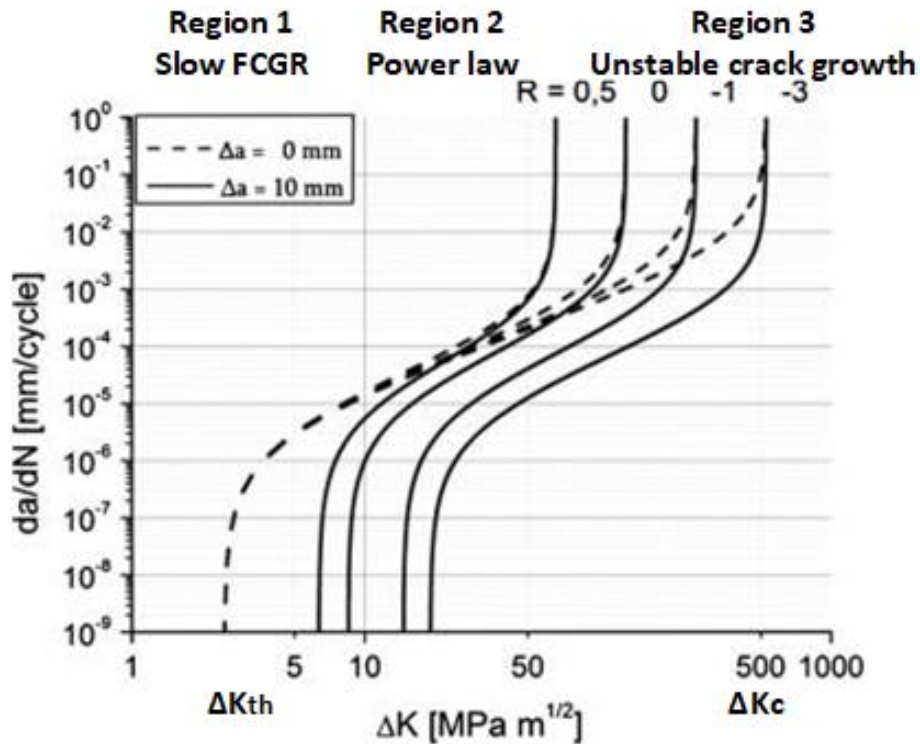
Figure 2.2 Calculated fatigue crack growth curves at a crack extension Δa of 0 and 10 mm and different load ratios R – the analytical model, 25CrMo4 [39]

For constant amplitude loading and small-scale yielding condition that no crack can grow faster than a physically short crack (dashed line), and that no crack can grow slower than a long crack (full line) at a given load ratio R. It should be noted that the crack growth rate of a very short crack is in the threshold region (branch I) and in the Paris region (branch II) independent from the load ratio *R* [39].

The major limitation of the Paris law is that the material constants must be determined for different load conditions. Under constant amplitude loading, fatigue crack growth rates (FCGR) will only be influenced by the stress ratio R which cannot be taken into account by this law. Other researchers have developed equations which describe all or part of the *da/dN vs ΔK* relationship. The Walker equation [40] was an enhancement of the Paris equation that accounted for the effect of stress ratio on FCGR. The Walker equation is shown below where *m* is an exponent that controls the shift in the crack growth data.

$$\frac{da}{dN} = C\big(\Delta K (1-R)^{(m-1)}\big)^n \quad 2.5$$

The Forman equation [41] is a further improvement on the Walker equation that accounts for the upper portion of the *da/dN vs ΔK* curve. The Forman equation is shown below where K_c is the fracture toughness of the material as shown in Figure 2.3.

$$\frac{da}{dN} = \frac{C(\Delta K)^n}{\big((1-R)K_c - \Delta K\big)} \quad 2.6$$

Klesnil & Lukas [42] modified the Paris equation to account for material threshold as shown in the equation below.

$$\frac{da}{dN} = C(\Delta K^n - \Delta K_{th}^n) \quad 2.7$$

The NASGRO equation [43] accounts for the complete fatigue crack growth curve and is shown below where *C* and *n* are material constants, and *p* and *q* control the slope of the threshold and failure regions respectively.

$$\frac{da}{dN} = C\left[\left(\frac{1-f}{1-R}\right)\Delta K\right]^n \frac{\left(1 - \frac{\Delta K_{th}}{\Delta K}\right)^p}{\left(1 - \frac{K_{max}}{K_c}\right)^q} \quad 2.8$$

where *da/dN* is the crack growth rate, *ΔK* is the applied stress-intensity factor range, and *R* is the stress ratio; ΔK_{th} is the fatigue threshold, K_{max} is the stress-

intensity factor corresponding to peak applied load, and K_c is the critical stress intensity; f is Newman's crack opening function.

2.1.2 Analytical Methods of Cracks in Residual Stress Fields

Analyses of cracks that develop in a residual stress field are of practical importance in welded structures, as well as in many other applications. The residual stress field is, in the absence of external loads, a self-balanced, built-in field. Determination of the intensity of the crack-tip elastic field for cracks introduced into the residual stress field requires no special treatment. The method is based on the superposition principle [44].

This so-called residual stress intensity factor (K_{res}) is required in the prediction of fatigue crack growth rates as well as in the residual strength calculation [45]. Currently, analytical methods are based on the superposition rule of linear elastic fracture mechanics. One popular engineering method is to account for the residual stress effect (within structures) by determining the effective stress intensity factor ratio R_{eff} [46]. An alternative method is based on the crack closure concept originally proposed by Elber [47] by calculating the effective stress intensity factor range (ΔK_{eff}) in a combined stress field of the applied and residual stresses. The crack closure process will be detailed in section 2.2. The validity of both methods has generally been accepted. Both R_{eff} and ΔK_{eff} are determined by calculating the K_{res} and using the superposition method [48]. Therefore, the key is to evaluate the K_{res}.

The weight function method (WFM) has been widely employed for calculating SIFs and has been successfully used by many researchers for welded test samples [49,50]. Closed-form or approximate analytical solutions are available for calculating the K_{res} and, in general, the solutions are exact. The K_{res} solution is most conveniently obtained as the Green's function K_{IG}. For the case of a two-dimensional plane stress or plane strain problems, a cracked sheet contains crack length $2a$ in an infinite body subjected to a localised force P acting at points

of the crack surface and normal to the crack faces, the SIF is calculated by using equation 2.9:

$$K_{IG}(a,b;P) = \frac{2P}{\sqrt{\pi a}} \cdot \frac{1}{\sqrt{1 - \left(b/a\right)^2}} \qquad 2.9$$

The stress intensity factor for the crack-free stress distribution $\sigma_y(x)$ is readily determined by integration and presented by equation 2.10 and 2.11.

$$K_{res} = \int_0^a K_{IG}(a,x;\sigma_y(x)dx) \qquad 2.10$$

$$K_{res} = \frac{2}{\sqrt{\pi a}} \int_0^a \frac{\sigma_y(x)dx}{\sqrt{1 - (x/a)^2}} \qquad 2.11$$

To calculate the SIF resulting from induced residual stresses using WFM, it is necessary to know $\sigma_y(x)$ and crack geometries. The residual stress distributions, $\sigma_y(x)$, can be obtained by other experimental measurements [51-56], e.g. diffraction methods [51-53], hole drilling techniques [54], or the contour method [55,56]. The WFM should give an accurate solution providing that the proper crack geometries are used. The following graphs in figure 2.3 offer solutions for various "crack-free" residual stress distributions, as well as when crack geometries are used. An actual, practical situation may be approximately represented by one of these solutions. When additional external loads are also present, the total solution is obtained by superposition.

In figure 2.3, the SIF solution was obtained by the Green's function for centre crack in a plate of infinite width. Where the residual stress distribution is expressed by equation 2.12, figure 2.3, Kres is given by equation 2.13.

$$\sigma_y(x) = \sigma_0 \cdot e^{-\frac{1}{2}\left(\frac{x}{c}\right)^2} \left[1 - \left(\frac{x}{c}\right)^2\right] \qquad 2.12$$

$$K_{res} = \sigma_0 \sqrt{\pi a} e^{-0.42\left(\frac{a}{c}\right)^2} \left[1 - \frac{1}{\pi}\left(\frac{a}{c}\right)^2\right] \qquad 2.13$$

For a finite width rectangular plate, Wu and Carlsson [57] presented the SIF solution according to this residual stress distribution using their weight function. Tada's and Wu's solutions are compared in figure 2.3, which firstly shows that the SIF results given by Tada and Wu agree with each other very well when the width of the plate is adequate when compared with the distribution of the residual stress. Secondly, for an inadequate width of the plate, e.g. *W/c=4*, although the stress at the edge is almost zero, the width effect could not be ignored; weight functions with width correction gives a more accurate result in this case.

However, residual stresses of welded samples as measured are not always in the single peak form as figure 2.3 and equation 2.12, 2.13 described. Most cases need numerical integration of equation 2.10. This will be demonstrated in chapter 6.

(a)   (b)
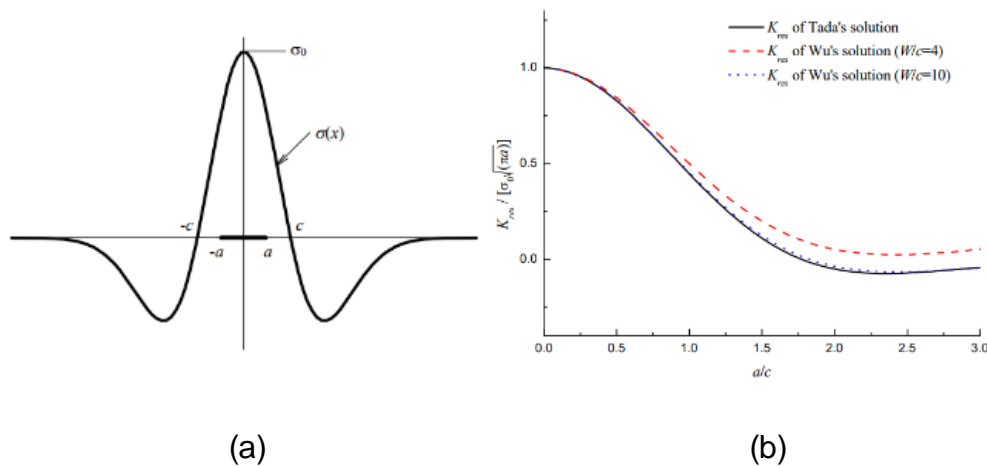
Figure 2.3 WFM solution of SIF provided for a given residual stress field; (a) residual stress distribution; (b) comparison of Tada's and Wu's solutions

In figure 2.4, another two different stress fields are presented and corresponding K_{res} are integrated as well.
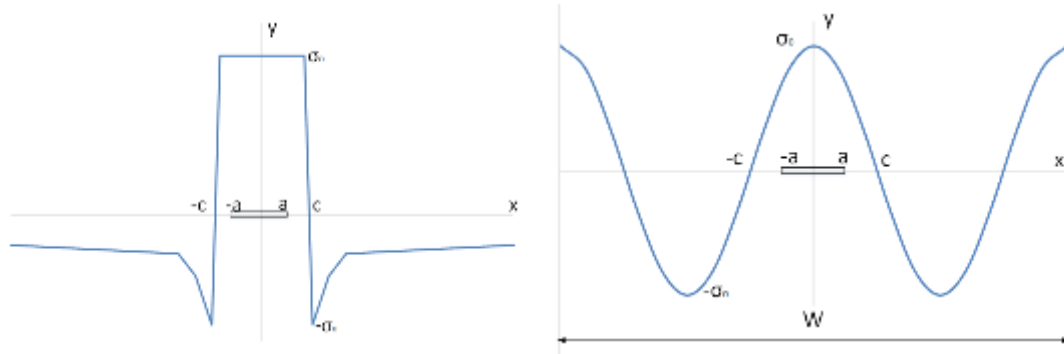
(a) $\sigma_y(x) = \begin{cases} \sigma_0 & \left|\frac{x}{c}\right| \leq 1 \\ \sigma_0\left[-\frac{1}{(x/c)^2}\right] & \left|\frac{x}{c}\right| \geq 1 \end{cases}$

(b) $\sigma_y(x) = \sigma_0 \cos\frac{4\pi x}{W}$

Figure 2.4 Examples of residual stress fields in the absence of external loads

K_{res} solution can be integrated by using equation (2.10) and by having a given residual stress state. The calculated K_{res} of figure 2.4 is presented in equation 2.14 and equation 2.15, respectively [58].

$$K_{res} = \sigma_0\sqrt{\pi a} \begin{cases} 1 & \alpha \leq 1 \\ \frac{2}{\pi}\left(\sin^{-1}\frac{1}{\alpha} - \frac{\sqrt{\alpha^2-1}}{\alpha^2}\right) & \alpha \geq 1 \end{cases}, where\ \alpha = \frac{a}{c} \qquad 2.14$$

$$K_{res} = \sigma_0\sqrt{\pi a}\sqrt{\frac{W}{\pi a}\tan\frac{\pi a}{W}}\left(\cos\frac{\pi a}{W}\right)^2\left[3\left(\cos\frac{\pi a}{W}\right)^2 - 2\right] \qquad 2.15$$

2.2 Crack Closure

A variety of different mechanisms can be involved in the development of crack closure such as: plasticity-induced crack closure, roughness-induced crack closure, oxide-induced crack closure, viscous fluid-induced crack closure, transformation-induced crack closure and grain boundary closure [59]. Crack closure plays an important role in the effect of the stress ratio on FCGR and on the near-threshold crack growth behaviour. The focus of this section is plasticity-induced crack closure as firstly observed by Elber [60]. During cyclic loading residual plastic deformation is built up in the wake of an advancing fatigue crack. This plastic deformation induces compressive stresses that cause the crack faces to close prior to the minimum load being reached. Upon reapplication of the applied external load the crack faces do not separate at the minimum load but at a higher load termed the opening stress level (σ_{op}). The crack is no longer open at K_{min} but instead opens at K_{op} hence a new SIF range must be defined. This is termed the effective SIF range (ΔK_{eff}) and is calculated using equation 2.16.

$$\Delta K_{eff} = (\sigma_{max} - \sigma_{op})\beta\sqrt{\pi a} \quad 2.16$$

The crack closure concept is illustrated in Figure 2.5. The portion of the fatigue cycle below K_{op} does not contribute to crack growth since the crack is closed. Crack closure shields the crack tip from the full effects of the stress intensity factor range so that it only experiences the effective stress intensity factor range and therefore has a reduced driving force for crack growth.
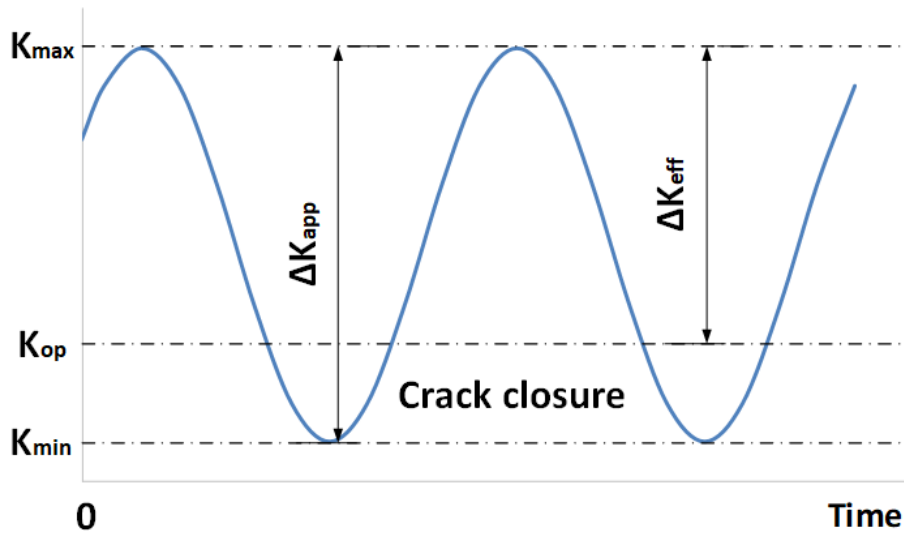
Figure 2.5 Illustration of the effective stress intensity factor range ΔK_{eff}

Experimental methods to measure the crack opening stress level have a high associated cost and effort [61]. It is difficult to locate the exact crack displacement if deformation of the crack face is not uniform [61]. Elber [60] proposed an empirical rule for 2024-T3 alloys to correlate the opening stress ratio with *R* ratio as presented in equation 2.17.

$$\frac{\sigma_{op}}{\sigma_{max}} = 0.5 + 0.1R + 0.4R^2 \qquad 2.17$$

Equation 2.17 is plotted in figure 2.5 and results in unrealistic opening stress ratios at negative stress ratios. Schije [62] proposed a new equation based on experimental observations:

$$\frac{\sigma_{op}}{\sigma_{max}} = 0.45 + (0.1 + \alpha)R + (0.45 - 2\alpha)R^2 + \alpha R^3 \qquad 2.18$$

Where α is a constraint parameter. Equation 2.18 is plotted in figure 2.6 for *α=0.1* to *0.15*. De Koning [63] developed the following equations based on experiments of *AA7075-T6* alloys:

$$For \; R > 0 \quad \frac{\sigma_{op}}{\sigma_{max}} = 0.45 + 0.2R - 0.15R^2 + 0.9R^3 - 0.4R^4 \quad 2.19$$

$$For \; R \leq 0 \quad \frac{\sigma_{op}}{\sigma_{max}} = 0.45 + 0.2R \quad\quad 2.20$$

This is also plotted in figure 2.6. Even though there are some differences between predicted crack opening stress ratios when using these equations, it is important to observe that the significant results are at low and negative stress ratios. The stress opening level can be determined using the Newman crack closure method and by implementing finite element methods.
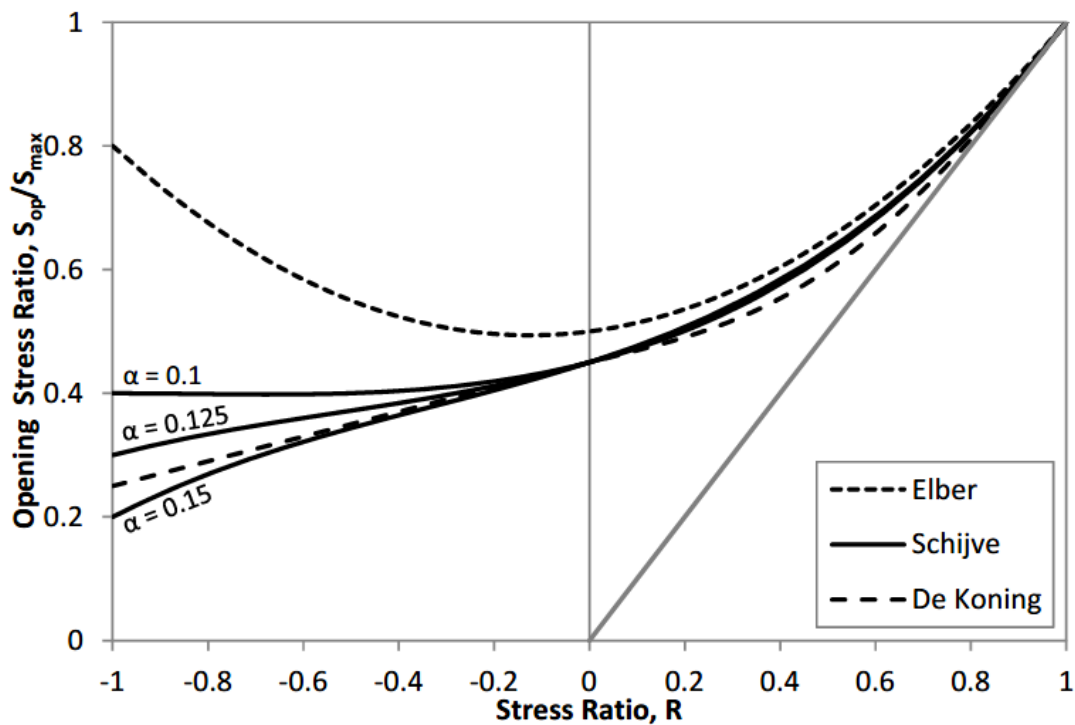
Figure 2.6 Crack opening stress ratio according to different empirical formulas [60,62,63]

Kukawki [64,65] has argued that crack closure may not be the sole mechanism responsible for correlating the effect of load ratio, overloads and type of loading with the FCGR. He considered the case of partial crack closure when the crack

face contacts first behind the crack tip. This phenomenon can occur particularly in the near-threshold region of crack growth when the fracture surfaces are often faceted and mismatched. In his perspective, the result of changing the crack shape from a blunt parabolic to a sharper wedge shape can induce damaging strain ahead of the crack.

Based on a crack closure approach, Newman equations [66] were used to calculate an effective stress intensity factor range (ΔK_{eff}). A crack opening stress ratio was calculated using equation 2.21- 2.23. These questions were achieved and based on finite element simulations of plasticity-induced crack closure for long cracks.

$$\frac{\sigma_{op}}{\sigma_{max}} = \max(\text{R}; A_0 + A_1 R + A_2 R^2 + A_3 R^3), for\ R \geq 0 \quad 2.21$$

$$\frac{\sigma_{op}}{\sigma_{max}} = A_0 + A_1 R, for\ -2 \leq R < 0 \quad 2.22$$

$$\frac{\sigma_{op}}{\sigma_{max}} = A_0 - 2A_1, for\ R < -2 \quad 2.23$$

where

$$A_0 = \left(0.825 - 0.34\alpha + 0.05\alpha^2\right)[\cos(\pi\sigma_{max}/2\sigma_0)]^{1/\alpha} \quad 2.24$$

$$A_1 = (0.415 - 0.071\alpha)\sigma_{max}/\sigma_0 \quad 2.25$$

$$A_2 = 1 - A_0 - A_1 - A_3 \quad 2.26$$

$$A_3 = 2A_0 + A_1 - 1 \quad 2.27$$

For plane stress conditions α = 1 while for plane strain conditions α = 3. The flow stress (σ_0) is defined as the average of yield stress and the ultimate tensile strength of the material. It applies for approximate plane strain condition and largely elastic crack behaviour; for a more detailed discussion of these parameters see [66].

2.2.1 Crack Closure in Plane Stress Conditions

For the explanation of the plasticity-induced crack closure, one has to distinguish between cases of plane strain and plane stress. Under the plane stress conditions, the explanation can be simple and is widely accepted in the fatigue world.

Under plane stress conditions, the volume elements in the plastic zone are elongated. This elongation is mainly balanced by an out of the plane flow of the material; as a result, the thickness within the plastic zone is reduced. The plastic zone size under plane stress conditions is generally regarded as being three times larger than when under plane strain conditions [67]. The plasticity-induced crack closure under plane stress conditions can be expressed as a consequence of an extra material layer behind the crack tip. This can be considered as a "wedge" that is inserted in the crack. Hence, both the cyclic plastic deformation at the crack tip and FCGR are reduced [68]. The formation of this plastic wedge is properly described by the Dugdale model [69], calculated by Budiansky and Hutchinson [70], and by the mostly used modified versions of Newman [71]. The effects of the stress ratio, load interaction or short cracks are described by strip yield models [72-74]. However, the disadvantage is that these models can only describe physically correct closure for the plane stress case. Newman [75] attempted to reflect the plane strain case with some adaptions.

A series of experiments of AA2024-T3 MCT specimens are reported [76]. By measuring fatigue crack growth and crack closure, results indicated that the crack tip was open during 72% of the applied load cycle, under stress ratio $R = 0.1$. The thickness was reduced from 10.2 mm to 7.2 mm through layer removal on both sides. It was concluded that crack closure was greater at the sample surface where plane stress conditions existed than in the centre of the plate where plane strain conditions occurred.

The situation for the plasticity-induced crack closure under plane strain conditions is significantly different. The key point is that there seems to be no source for the

plastic wedge because it is impossible to define the out-of-plane flow. Under plane strain conditions and a constant ΔK or constant load amplitudes, there is no plastic wedge at large distances behind the crack tip. However, the material in the plastic wake is plastically deformed. It is plastically sheared; this shearing induces a rotation of the volume elements, and as a consequence, a local wedge is formed in the vicinity of the crack tip [77,78,79].

2.2.2 Crack Closure of Initial Residual Stress Fields

Although there have been many studies on fatigue crack closure using experimental, numerical and FE approaches, few have considered the effects of an initial residual stress field. A distinction is made here between an initial residual stress field defined as a pre-existing stress field in the component prior to crack propagation and residual stress as a result of plasticity during crack propagation such as in the plastic wake or forward plastic zone. This section reviews the effects on crack closure of a fatigue crack propagating through an initial residual stress field.

A 2-D elastic-plastic finite element analysis (FEA) of crack closure in a middle-tension (MT) specimen was studied [80]. The model used 4 node plane stress elements and isotropic hardening. A compressive residual stress field was induced through application and removal of an overload. A fatigue crack was advanced from the notch at the maximum applied load. Crack closure was simulated by monitoring the position of the nodes behind the crack tip. During unloading if the nodal position became negative relative to the crack tip a node fix condition was applied. This induced compressive residual stress field increased the crack opening stress level by up to three times compared to a residual stress-free analysis. The crack was advanced through the residual stress field, and ΔK_{eff} was calculated. The results correlated well with experimental data. It was noted that prediction of the closure level was highly dependent on the $da/dN = f(\Delta K_{eff})$ relationship used.

Beghini and Bertini [81] considered a residual stress field due to welding in 12 mm thick steel. Three distinct situations were recognised: (1) the crack is completely open at the minimum load, (2) the crack tip is open while crack surfaces are partially closed at minimum load and (3) the crack is completely closed at minimum load. Crack closure prediction using FE and weight function methods were compared to experimental results. Predicted K_{op} values compared well with estimations using FE and weight functions however it was noted that caution is required when dealing with partially open cracks.

Kang et al. [82] studied the behaviour of fatigue crack growth (FCG) and closure through a compressive residual stress field evolving from electron beam welding in 6 mm thick steel. They found that depending on the type of residual stress field in the region of crack growth, the growth and closure of the crack showed different patterns, particularly in the transition region from a compressive to tensile residual stress field. This was attributed to partial crack opening when the load was released i.e. it didn't close at the crack tip first. These findings are similar to those reported by Choi and Song [83]. Kang et al. [84] also studied the effect on FCG and closure level through a tensile residual stress field under compressive applied loading. Comparisons were made between experimental FCGR and predictions were generated. They concluded that prediction based on the R_{eff} method and the ΔK_{eff} method correlated well with FCGR measurements. However they also concluded that a version of the Reff method where $\Delta K_{eff} = K_{max} + K_{res}$ and $R_{eff} = 0$ when $K_{min} < 0$ may lead to non-conservative estimates.

Schnubel and Huber [85] considered closure in a welded 5 mm thick compact tension C(T) specimen. An elastic FE model was used with and without hard contact of the crack faces to compare the superposition approach with a contact approach. A significant difference between calculated SIF with and without contact was found particularly in the transition region from compressive to tensile residual stress. This attributed to the effect of the contact condition on the local opening behaviour of the crack face near the crack tip.

Moshier and Hilberry [86] considered a 2.54 mm thick AA2024-T3 SENT (single edge notched tension) specimen. A tensile overload was applied to induce a compressive residual stress field. They noted that when a crack grows in a component without compressive residual stress, it leaves plasticity in the wake of the crack. However when compressive residual stress is present, the residual stress acts as an external closing mechanism, opposing the applied tensile load, which forces the crack closed and reduces the amount of plastically deformed material. This results in an opening stress due to plasticity that is less than the original opening stress when residual stress was not present.

The effect of compressive residual stress on FCG resulting from hole drilling was modelled using elastic-plastic FE analysis [87]. Both isotropic hardening and plastically induced crack closure (PICC) were considered. Predicted FCGR compared well with experimental results, to within a factor of 5%.

Liljedahl et al. [88] considered a residual stress field resulting from welding in 7mm thick AA2024-T351 alloys. They compared the ΔK_{eff} approach with superposition approach. Superposition compared well with experimental results at lower load levels. In contrast, the ΔK_{eff} approach was better at greater load levels. However, it was noted that the reason for this may have been due to the experimental measurement technique used.

Wang et al. [89] considered a compressive residual stress field generated after shot peening on etched 7075-T7451 dogbone samples (t = 6.35 mm). They extended the Newman PICC method by using crack tip open displacement (CTOD). The predicted fatigue lives based on the closure model were within a factor of 2-3 of experimental lives.

Good agreement, between predicted results and experimentally measured FCGR, was found by Ma et al when they investigated a weld-induced residual stress field [90]. A crack closure-based approach was used where crack opening levels were predicted using Newman's equations [66].

The effect of residual stress induced by shot peening on crack closure was measured by Zhu et al. [91]. Crack closure levels were found to increase with shot peening intensity and were on average 2x greater than for the unpeened condition. They noted that the opening level initially increased prior to decreasing with crack extension, but no residual stress measurements were made. A closure based model [FASTRAN] was used to predict FCGR from a machine made scratch in 4340 steel [91]. Crack growth was through a residual stress field induced by shot peening. Very good agreement between predictions and experimental measurements were reported. Variances in FCGR behaviour were accounted for by working within the closure corrected effective stress intensity factor range on LSP treated titanium [92,93].

Hill and Kim [94] considered crack closure in a residual stress field induced by LSP. An elastic analysis was performed in places where crack closure had occurred due to the strain fields locked in the material (i.e. the residual stress field). These strain fields were found to have altered the shape of the crack faces and caused contact. The contact pressure arising from a closed crack was calculated using the weight function method (WFM) and finite element method (FEM), in order to show a comparison and the results compared well. A number of FCGR prediction methodologies were compared to experimental measurements in 3.8 mm thick 7075-T6 aluminium C(T) specimens. It was found that prediction methodologies that included crack closure improved the accuracy of the results.

2.3 Residual Stress

The mechanism of residual stress formation by deep rolling and laser shock peening and the effect on fatigue performance is reviewed in sections 2.1.1 and 2.1.3. Residual stress measurements are reviewed in section 2.1.2.

Residual stresses can be defined as those stresses that remain in a material or body after manufacture and processing in the absence of external forces or thermal gradients [95,102]. Compressive residual stress acts by pushing the material together, while tensile residual stress pulls the material apart. From a mathematics perspective, compressive stress is negative and tensile stress is positive. Normal stress is characterised by the fact that it acts perpendicular to the face of a material and shear stress acts parallel to the face of a material.

Residual stresses are generated, affecting the equilibrium of material, after plastic deformation that has been caused by applied mechanical treatments, thermal loads or phase changes [95,96]. Mechanical and thermal processes applied to a component during service may also alter its residual stress state [95].

Residual stresses can be induced into the material unintentionally for example during welding or other manufacturing processes [97-99]. On the other hand, they can be deliberately introduced into the material by mechanical procedures such as deep surface rolling [13,15,18] and laser shock peening [15,18,101]. Residual stresses can be initiated by a variety of mechanisms including plastic deformations, temperature gradients or structural changes [15,95].

To summarise, residual stresses can be classified into three types [103]:

Type I: Refers to macro residual stresses that develop in the body of a component, and are on a scale larger than the grain size of the material.

Type II: Are micro residual stresses that vary within the scale of an individual grain. Such stresses are expected to exist in single-phase materials and may also develop in multi-phase materials, due to the different properties of the different phases.

Type III: Are micro residual stresses that exist within a grain, but at a much smaller scale that type II. Essentially, they are formed as a result of the presence of dislocations and other crystalline defects. Type II and III are often grouped together as microstresses.

Knowledge of the residual stress state is important in order to be able to determine the actual loads experienced by a component. In general, compressive residual stress in the surface of a component is beneficial. It tends to increase fatigue strength and fatigue life, slow crack propagation, whilst helping to increase resistance to environmentally assisted cracking such as corrosion cracking and hydrogen induced cracking [104]. Tensile residual stress in the surface of the component is generally undesirable as it decreases fatigue strength and fatigue life, increases crack propagation and lowers resistance to environmentally assisted cracking [105].

2.3.1 Residual Stress Formation by Deep Surface Rolling

Numerous manufacturing processes are able to induce, as an inherent by-product, residual stress in components such as welding, machining, forming, hardening, casting and forging [98-101]. These stresses are generally undesired and sometimes additional steps are added to the manufacturing process to induce beneficial compressive residual stress at safety-critical locations such as shot peening [101,106], laser shock peening [101,107], low plasticity burnishing [108], deep surface rolling [13,15,18], hammer peening [109-111]. The benefits of compressive residual stresses to enhance fatigue strength in metallic components have long been recognised [112]. Residual stress can also be induced from pre-service loading (such as proof testing) and in-service loading (such as maximum service load causing yielding at stress concentrations) [113]. For the majority of cases reviewed on residual stresses in this thesis have focused on those induced from deep surface rolling or laser shock peening processes.

The beneficial effect of compressive residual stresses on the fatigue behaviour of metallic components cannot be taken as a general rule, owing to the fact that substantial relaxation may occur during the initial cycles depending on the material properties, residual stress depth distribution and loading (mode and intensity frequency) [114]. Within this scenario, relaxation seems to be closely

related to the method used to induce the scale of residual stress and applied subsequent stress states. In the particular case of deep rolling (schematically represented in Fig. 2.7), cold working due to plastic deformation takes place as the tool travels along the path determined by rolling speed and feed while a predetermined load, higher than yield strength of the work material, is applied. As a result, axial and tangential compressive residual stresses are induced together with an increase in hardness and, occasionally, in strength [115]. However, the maxima for residual stress and hardness are found beneath the surface due to the Hertzian contact pressure [116]. Finally, flattening of the roughness peaks owing to plastic flow leads to the improvement of the surface finish, thus hindering the nucleation of surface cracks, compared to the shot peening treatment.
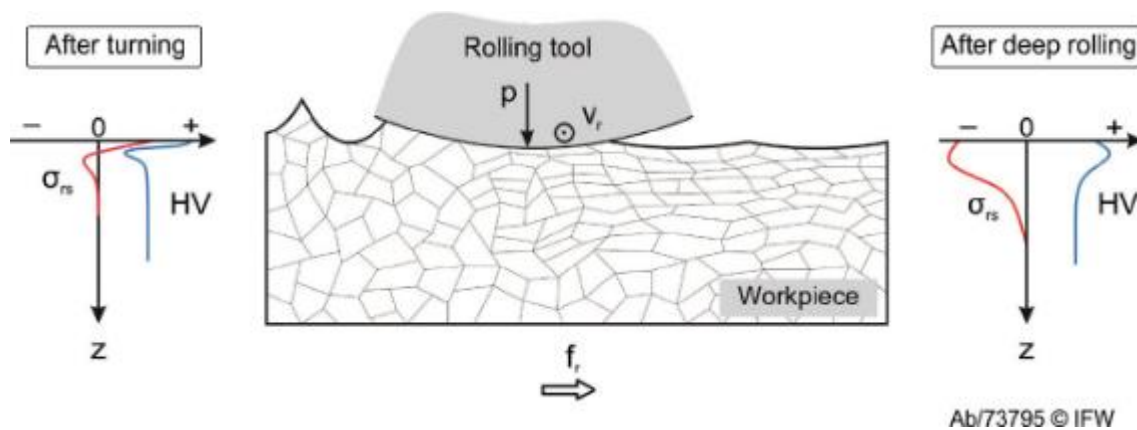
Figure 2.7 Effect of deep rolling on residual stress and hardness distribution in steels [115]

Residual stress relaxation occurs when a critical value for the applied stress amplitude is exceeded, and cyclic direct dislocation movement converts the elastic strain associated with the macro residual stress into microplastic strain [117].

2.3.2 Measurements of Residual Stress Fields

Residual stress measurement techniques invariably measure strains rather than stresses, and the residual stresses are then deduced using the appropriate material parameters such as Young's modulus and Poisson's ratio. Often only a single stress value is quoted and the stresses are implicitly assumed to be constant within the measurement volume, both in the surface plane and through the depth.

When comparing results from different techniques, consideration should be given to the sampling volume and resolution of each measurement method in relation to the type of residual stress being measured, particularly when the Type II and Type III micro residual stresses are of interest. It is also important to consider the concept of the characteristic volume, which can be used to describe the volume over which a given type of residual stress averages to zero. Most material removal techniques (e.g. hole-drilling, layer removal) remove large volumes of material over which Type II and III stresses average to zero so that only the macro residual stresses can be measured.

Different residual stress measurement techniques exist for different applications. Each of the methods has unique advantages and disadvantages which need to be considered when selecting the appropriate measurement technique. Some information on the workpiece to be measured is therefore required, including its material properties, geometry as well as measurement location and direction. The more information is known in advance, the easier it is to select the most useful method.

Residual stress measurement can be categorized into three different groups: destructive, semi-destructive, and non-destructive techniques. Techniques belonging to the destructive group are mechanical relaxation and crack techniques, which can result in somehow damaging the material. In the semi-destructive group, the workpiece can be partially sectioned, however, to some extent it could be still used. Hole drilling and incremental centre hole-drilling are

included into this group. Non-destructive techniques contain the diffraction methods and the use of the stress-sensitive properties.

In most cases, numerous measurements are taken to define the residual stress distribution. As a result, the accuracy of each measurement is less relevant [118].

    a. Hole Drilling [115,119]

Hole drilling is one of the most widely used techniques for measuring residual stresses. It is relatively simple, cheap, quick and universal. Equipment can be laboratory-based or portable, and the technique can be used to a wide range of materials and components.

Hole drilling or Mathar-Soete drilling technique consists in drilling a hole in a material which has residual stress and measure the stress released after it. The hole is made between at least three strain gauges in a rosette distribution [122,123].

Kelsey [124] proposed to drill the hole by steps and measure the strain at each step giving a profile of the residual stresses through the thickness. The problem with this method lies in determining the correlation coefficients needed to establish the stress. The main advantage of this method is its low cost and flexibility. Moreover, in some cases the workpiece can be still used by filling the hole (for this reason this method is frequently called semi destructive).

This method is valid when the residual stress profile is uniform and does not vary significantly with the depth of samples. Non-uniform residual stresses from incremental strain data via the Integral Method can be calculated. And it was shown to be a preferred technique for accurate determination of residual stresses irrespective of the original stress distribution.

Despite some shortcomings the hole drilling technique remains a popular means of measuring residual stresses.

    b. X-Ray Diffraction [125]

X-Ray diffraction relies on the elastic strains within a polycrystalline material to measure internal stresses in a material. The deformations cause changes in the spacing of the lattice planes from their stress free value to a new value that corresponds to the magnitude of the applied stress. This new spacing will be the same in any similarly oriented planes, with respect to the applied stress and crystal lattice, therefore effectively acts as a very small strain gauge. The measurement itself is relatively straight forward and equipment readily available. During a measurement the specimen is irradiated with high energy X-rays that penetrate the surface, the crystal planes diffract some of these X-rays, according to Bragg's law and a detector, which moves around the specimen to detect the angular positions where diffracted X-rays are located, records the intensity of these rays at that angular position. The location of the peaks enable the user to evaluate the stress within the component.

XRD is a non-destructive technique for measuring surface stresses. It can be combined with some form of layer removal technique so that a stress profile can be generated, but then the method become destructive.

One of the main disadvantages with XRD is the limitation imposed on the test piece size and geometry. The geometry has to be such that X-ray can both hit the measurement area and still be diffracted to the detector without hitting any obstructions. Problems may also occur if the surface is too rough, so surface condition is a consideration. Size may also be a problem, because the entire artefact or component must fit into the diffractometer. X-ray diffraction has a spatial resolution of 1-2 mm down to tens of µms and a penetration depth of around 10-30 µm, depending on the material and source.

c. *Synchrotron generated X-Rays [126]*

Synchrotron, or hard X-rays, provide very intense beams of high energy X-rays. These X-rays have a much higher depth penetration than conventional X-rays, typically around 50 mm in aluminium. The increased penetration depth means that synchrotron diffraction is capable of providing high spatial resolution, three-

dimensional maps of the strain distribution to millimetre depths in engineered components.

This increased penetration depth is one of the major advantages of synchrotron diffraction over the more conventional X-ray diffraction. Another great advantage that synchrotrons have is that intense narrow beams of 1 mm-10 μm in size are possible. This leads to spatial resolutions that are limited not by the instrument but by the crystallite size within the sample. The measurement is also very much quicker than with conventional X-ray diffraction. With measurements times of a fraction of a second, detailed strain maps of components can be constructed using a few hours of beam time.

Presently, synchrotron diffraction is only available at central facilities, in much the same way as with neutron diffraction. Two such facilities are the European Synchrotron Research Facility in Grenoble, France, and the SRS in Daresbury, UK.

d. Neutron Diffraction [115,121]

Neutron diffraction (ND) as is classical X-ray diffraction (XRD) and strong X-ray synchrotron diffraction (SD) are based on the same principle and are complementary. Due to their very nature, XRD is suitable for surface measurements, SD for shallow depths and thin specimens, and ND for bulk measurements within thick specimens. The greatest advantage that neutrons have over X-rays is the very large penetration depths that neutrons can obtain, which makes them capable of measuring at near surface depths of around 0.2 mm down to bulk measurements of up to 100 mm depth in aluminium or 25 mm in steel. With high spatial resolution, neutron diffraction can provide complete three-dimensional strain maps of engineered components. This is achieved through translational and rotational movements of the component.

This method of stress measurement, with the capacity for collecting large quantities of data (via position sensitive detectors) over the whole surface and depth (depending on the thickness of the sample) has made neutron diffraction a

particularly useful technique for the validation of theoretical and numerical models of mechanical treated components or welded parts [127].

Figure 2.8 schematically shows a typical continuous source based diffractometer for measuring strain. And the gauge volume over which the strain measurement is made, is given by the intersection of the incident and diffracted beams.
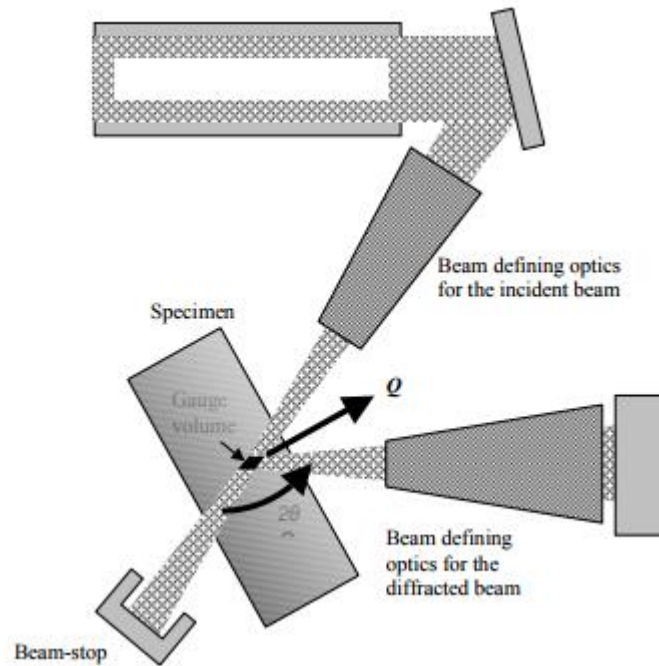
Figure 2.8 Schematic illustration of a typical continuous source based diffractometer for strain measurement [121]

Neutron diffraction has been applied to measure residual stresses in various types of materials and industrial components [128]. This method has been extensively used for measurement of residual stresses in welds as the stresses are usually high, the gauge volume typically used is small compared to the weld and the penetration depth of the neutron beam into the material is large. The method is non-destructive at the point of application and is therefore ideal for the monitoring of residual stress field in fatigue samples, although some components require the machining of access channels and welds require the determination of

a point-to-point stress-free lattice reference which requires extraction of material from the weld being measured or an identical component [121].

Withers and Bhadeshia [103] suggest that, generally, continuous sources provide the best results, when single peaks of the diffractogram is studied (as for mild steel residual stress measurements), while time-of-flight based instruments are particularly good when the complete diffractogram or a certain number of peaks are necessary, as for a multiphase material. In addition, Webster et al [126] recommend neutron diffraction as the best technique available currently to map two and three-dimensional internal strain.

Furthermore, the method is non-destructive at the point of application and is therefore applicable for monitoring of residual stress fields in fatigue samples.

2.3.3 Effects of Residual Stress on Distortion and Fatigue Performance

The load history plays a vital role in fatigue performance. A primary variable that influences fatigue performance is the amplitude of the applied cyclic load. Also of significant influence is the mean (or maximum) value of the applied load during each cycle. Significant in fatigue are residual stress fields established in the component before service. Although residual stress fields do not directly influence the amplitude of cyclic loading, they do alter the mean (or maximum) value of the load in each cycle and therefore can have a significant influence on the fatigue performance. Residual stresses are self-equilibrating, and so any region of compressive residual stress must be counterbalanced by tensile residual stress elsewhere in the component.

This is most evident of residual stress fields induced through welding processes. Tensile residual stress parallel with the weld line normally forms in the centre the weld with balancing compressive residual stress at the edges.

Residual stress and distortion are two phenomena closely related and largely opposed [129]. The uneven heating cycle during welding causes localised plastic

strains in the weld metal and surrounding material. This misfit of the plastic strain causes the residual stress. To minimise the strain energy of the weldment, it distorts.

In-plane distortions include shrinkage in the transverse and longitudinal directions, and rotational distortion of the workpiece with respect to the weld line due to material shrinkage as the weld progresses. Out-of-plane distortion types include longitudinal bending, bucking, and angular distortion. Dong et al, [130] distinguishes the distortions which are linearly dependent on the residual stress as stable, while the nonlinear modes are described as unstable (buckling). On the other hand, residual stress after welding has a wider influence than only causing distortion. It could reduce the fatigue life and corrosion resistance, and accelerate the fatigue crack growth rate [131]. Beghini *et al*. [132] studied the effect on FCGR of welding induced residual stress fields in C(T) specimens. It was found that fatigue cracks grew faster through the tensile residual stress and slower through the compressive residual stress field compared to in the baseline material. Crack propagation can also be influenced by changes to micro-hardness and microstructure in the weld heat affected zone however it has been found that residual stresses are the most important parameter influencing FCGR [133,134].

As a conventional treatment, shot peening has been applied to components to improve fatigue performance for years by inducing a compressive residual stress field near the surface region. There has been extensive research on the effect on fatigue of shot peening [106,115]. Early research by Reed & Viens [135] found a 25% improvement of the endurance limit after shot peening of Ti-6Al-4V. The effect of shot peening induced residual stress on the fatigue performance of AA7010 and AA8090 was studied by Mutoh et al. [136]. They found that the crack initiation time after peening was shorter due to the rough peened surface. However, the FCGR was significantly reduced by the compressive residual stress field and total fatigue life was greater after peening.

Residual stresses develop during most manufacturing processes involving material deformation, heat treatment, machining or processing operations that transform the shape or change the properties of a material. They arise from a number of sources and can be present in the unprocessed raw material, introduced in manufacturing or can arise from in-service loading [137]. The residual stresses may be sufficiently large to cause local yielding and plastic deformation, both on a microscopic and macroscopic level, and can severely affect component performance. For this reason it is important that some knowledge of the internal stress state can be deduced either from measurements or modelling predictions.

2.3.4 Effects of Residual Stress on Fatigue crack growth

Two methods have been widely used to predict the fatigue crack growth rate through residual stress fields. The first uses the superposition method and the other is based on the crack closure. The superposition method requires calculation of the stress intensity factor associated with the initial stress state (K_{res}) [45]. The stress intensity factor account for the residual stress is then superimposed on the stress intensity factor due to the externally applied loading (K_{app}) to give a total resultant stress intensity factor as shown in equation 2.28 and 2.29 below.

$$K_{tot,max} = K_{app,max} + K_{res} \quad 2.28$$

$$K_{tot,min} = K_{app,min} + K_{res} \quad 2.29$$

The stress intensity factor range and stress ratio are then calculated using equations 2.30 and 2.31 below. It is interesting to note that for the superposition method ΔK is independent of the residual stress field and it is only the mean stress and stress ratio that are affected.

$$\Delta K_{tot} = K_{tot,max} - K_{tot,min} = K_{app,min} - K_{app,min} = \Delta K \quad 2.30$$

$$R_{tot} = \frac{K_{tot,min}}{K_{tot,max}} \quad 2.31$$

Fatigue crack growth rate can then be calculated using a correlation of the form shown in equation 2.32 below.

$$\frac{da}{dN} = f(\Delta K, R_{tot}) \qquad 2.32$$

The weight function method and elastic-plastic FE analysis can be used to calculate K_{res} and both have been found to produce similar results when applied to the same problem [195]. The advantage of the weight function method is that it provides fast reliable predictions however it does require a specific weight function for the specimen geometry being analysed.

Predicted and measured FCGRs through a residual stress field in a welded M(T) sample were compared by Servetti [196]. Three prediction methodologies were assessed namely superposition, crack closure based on Newman's equations [66], and crack closure based on an FE contact model. He found that the closure method based on an FE contact model was in best agreement (within 20%) with experimental measurements. From his work, it was noted that accurate measurement of the residual stress field, in particular the compressive region, was critical for accurate predictions.

2.4 Introduction of Deep Surface Rolling And Other Surface Treatments

In this section, several mechanical surface treatment methods for surface optimization are described and compared. After a brief development of the deep rolling process, the current developments are addressed in detail.

2.4.1 Past and Present Development of Deep Surface Rolling

In all further elaborations, the terminology "deep rolling" refers to a surface rolling treatment using rolls or ball-point tools with the purpose of inducing deep plastic deformations and residual stresses in near-surface layers in contrast to "roller

burnishing" which is usually applied with much lower forces or pressures and mostly aims to obtain a certain surface quality especially in terms of roughness.

It is well-known that mechanical surface treatments, such as deep rolling, shot peening and laser shock peening, can significantly improve the fatigue behaviour of highly-stressed metallic components. Deep rolling belongs to a group of manufacturing technologies, which are used to induce the mechanical strain hardening of the surface layer.

Deep surface rolling is particularly attractive since it is possible to generate compressive residual stresses near the surface and work hardened layers while retaining a relatively smooth surface finish. With regards to the component requirement, deep surface rolling distinguishes itself by two substantial advantages from all the other mechanical strain hardening methods. The first advantage is that the highest and deepest compressive residual stress can be induced into the component surface layer. Secondly, the surface quality can be maintained, especially in comparison to the shot peening and laser shock peening.

It can be assumed that mechanical surface treatments of metallic materials have been used for thousands of years (e.g. hammering of swords after forging), but it was not until the first half of the last century that treatments like deep rolling or shot peening have experienced widespread industrial applications in mass production. In the U.S.A., deep rolling was applied in the twenties of the last century as a surface treatment to strengthen axles of the Ford T and in the thirties, axles of trains were also deep rolled [12]. Significant pioneer work in the U.S. in that field was carried out by Horger [138], in Germany, Foppl [139] and Thum [140] have debated about the causes of fatigue enhancement by deep rolling, probably inspired by materials failures in the oil industry. In the seventies, the basic effects of deep rolling on fatigue behaviour were thoroughly investigated and the influence of notches and material hardness on fatigue strength enhancement of deep rolled components became clear [141-143]. In the eighties,

deep rolling was already used in combination with thermal surface treatments such as induction hardening, especially in the automotive industry [144]. Certainly today, the most well-known example for the application of deep rolling are deep rolled crankshafts, but this outstanding surface treatment has also found its way into other technical fields and applications, for example for surgical implants as well as for turbine blades in the power plant and aircraft industry among numerous others.

A variety of parameters during the deep rolling process severely influences the near-surface residual stress state among which the rolling force or pressure is certainly the most important. It is known that only optimised rolling forces increase the fatigue strength, where overly low rolling forces have no pronounced effect on the fatigue behaviour and where overly high ones may even aggravate it, for instance by inducing microcracks. Typically, especially for hard materials, deep rolling leads to a subsurface maximum of residual stresses as expected by Hertzian theory [145] predicting maximum equivalent stresses below the surface. It should be noted that the position of the residual stress maximum not only depends on the rolling force, but also on the exact contact geometry of the involved workpiece and rolling tool. With increasing rolling force the compressive residual stresses also increase until a "saturated" level of compressive residual stress is reached (usually determined by the yield strength or work hardened state of the material) [12]. However, a further increase of rolling force shifts the area of compression into greater depths and finally higher rolling forces can lead to subsurface compressive residual stresses but tensile residual stresses at the surface. Simultaneously, usually near surface hardness is also increased by work hardening effects.

Experimental results [146] have demonstrated that deep surface rolling (DSR) can improve the fatigue life in metallic materials and components significantly, compared to untreated baselines and shot peened conditions. It was suggested in reference [113] that deep rolling could offer even higher fatigue lives, if the component or coupon were heated to an optimised temperature range during the

deep rolling treatment, similar to warm peening. This process is known as "thermomechanical deep rolling". DSR and similar mechanical surface enhancement technologies such as low plasticity burnishing [108] have many attractive features, including deep beneficial compressive residual stresses at the surface to a depth of 1 mm or further, great tolerance to residual stress relaxation at elevated temperature and under fatigue loading, due to less cold work induced by the controlled DSR process (in comparison with SP), and good surface finish [108,147,148].

2.4.2 Other Surface Mechanical Treatments

The resistance of a material against fatigue can be increased by surface treatment techniques such as cold deep rolling [12,149], water peening [151], shot peening [12,150], low plasticity burnishing [108], laser shock peening [14,16,113], ultrasonic shot peening [148].

The shot peening process is widely used in aerospace and other industries to improve the fatigue performance of components as a conventional and inexpensive mechanical surface treatment. The shot peening technique was invented in the 1920's in Germany and the USA independently and has been widely used in industry since the 1950's [152]. It is often used for the specific purpose of improving the fatigue strength and fatigue life. During the process ceramic or metallic balls, called shot, are fired with force onto the surface to be treated. Each shot acts as a hammer and creates a dimple on the components surface plastically deforming the near-surface layer by stretching as illustrated in Figure 2.9 (A). The neighbouring elastic material reacts against the stretching and a compressive residual stress field is formed, illustrated in Figure 2.9 (B). However other changes to the material can occur such as microhardness, dislocation density, surface roughness, surface defects and changes in phase composition [153].
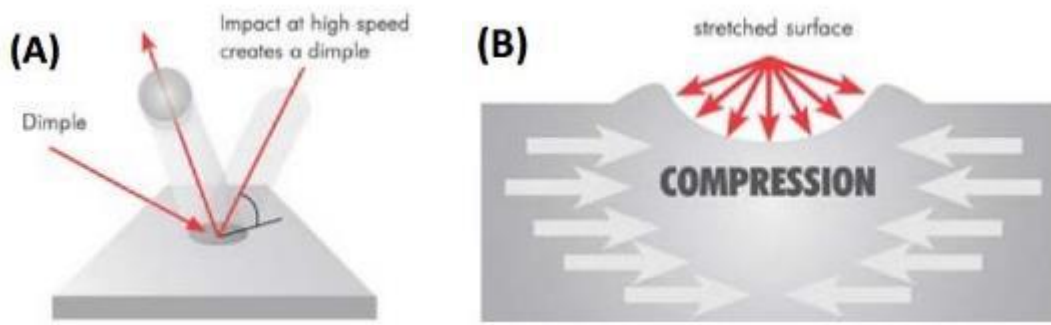
Figure 2.9 (A) Dimple creation on material surface during shot peening and (B) formation of compressive residual stress around dimple [106]

The residual stress field created by shot peening is generally referred to as cold worked residual stresses whereas from welding they are termed thermal residual stresses. It is interesting to note at this point that the residual stress field induced during laser shock peening is actually the result of cold working.

Due to the lack of precise control, other mechanical treatments by piezo peening (figure 2.10) and laser peening will be applied.
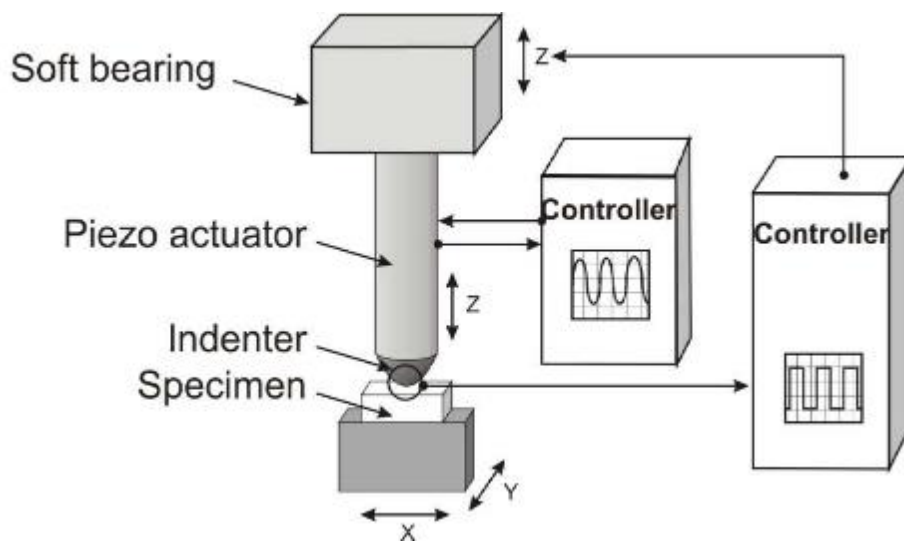
Figure 2.10 Schematic illustration of piezo peening plant [110]

The piezo actuator is oscillating with a given frequency f and an amplitude a. A spherical indenter is attached to the actuator. The indenter impacts on the specimen which is moved by a linear guide unit in a meandering pattern. An important factor is that the indenter lifts off after each impact. Using the soft bearing, the z-position can be adjusted so that the contact can be regulated as desired. During the peening process, there are several values measured, the average load at different time steps, the time, the excitation voltage between indenter and specimen, the strain of the piezo actuator, respectively.

Laser shock peening is a technique for the surface treatment of metallic materials. LSP is applied to improve the fatigue performance of the treated component by creating a layer of compressive residual stress at the surface. The first reported investigation on the effect of stress waves created by lasers and their effect on metals was by White in 1963 [154]. The first patent for an application of LSP was in 1974 [155]. Initially applications of LSP were limited due to the size and expense of the required laser systems. However over the last two decades its application has increased significantly as more suitable laser systems were developed. It has been used extensively in the aerospace industry for the treatment of gas turbine blades and discs, and more recently wing attachment lugs. Other applications of laser peening include treatment of steam turbine blades [156], forming of metals [157,158] with applications to aircraft wing panels, enhance service life of automotive springs [159], and as a preventative measure against SCC in nuclear power reactors [160]. The effect of LSP process variations on the induced residual stress fields has been assessed for a range of materials such as steel [161-163], titanium [164-166], and aluminium [167-169].

2.5 Computation Simulation and Finite Element Analysis of DSR

For welding engineering, deep rolling, to reduce residual stress and distortion, is a stress engineering technique that exploits the action of a normal loaded roller

to induce strain in the in-plane directions. This technique is proposed in some books [112,170] as a method to reduce distortion. However, there only a few publications about deep surface rolling [171–175]. In addition, some of the literature is focused on preventing hot cracking, and improving mechanical properties rather than reducing residual stresses or distortion.

In the literature different rolling approaches have been found. They can be divided according to the location where the rolling process is applied: rolling both sides of the weld seam simultaneously (upper and lower surfaces) [172]; rolling over the weld seam with either one [173,174] or two consecutive rollers [175]; or rolling beside the weld seam [173,174]. Additionally, the roller can be applied after welding, or in situ at a certain distance from the welding torch (or welding tool in FSW). Rolling the upper surface of the weldment has operational advantages. It can be easily adapted to different weldment geometries, and can be applied in situ during welding.

The mechanical elementary process of deep surface rolling is the surface pressure created between the workpiece and the roller in the contact area. During this process, triaxial stress states are generated, which change with the distance to the surface. They are dependent on contact geometry, such as the elastic contact between a sphere and a flat plate. The beneficial effects from deep surface rolling are the smoothing and low friction at the immediate surface. When the yield strength is exceeded by the resulting equivalent stress, local plastic deformations occur, generating residual stress and the corresponding microstructural work-hardening or work-softening effects.

Backer *et al*. [176] analysed the deep rolling process on turbine blades using the FEM/BEM-Coupling. Moreover, this enabled the computing of large-scale models at low computational cost and with high result accuracy, allowing investigation of the effect of the deep rolling on damages caused by the unavoidable impact of foreign objects.

Earlier models focused more on the use of two-dimensional models due to their reduced cost and ability to capture the effects of the key parameters of the deep cold rolling (DCR) process. These two-dimensional models used the plane strain assumption, which leads to these models being unable to accurately predict residual stresses in the axial (perpendicular to rolling) direction and the near-surface regions [178]. Another method utilised microscale FE models, through the use of mathematical algorithms and assumptions, to map macroscale FE models [179].

A comprehensive 3D finite element dynamic analysis with considering spring back effect was conducted to simulate the deep rolling process. The model was validated by comparison of the residual stress profiles obtained by simulation and result of X-Ray diffraction technique [177].

A three-dimensional finite-element (FE) model, validated with experimental residual stress data, was used to study the effect of the process [149]. The result showed that previous assumptions of residual stress distributions based on a single residual stress profile measurement could be over simplistic at best and at worst neglect to consider the impact of the burnished–unburnished boundary. Especially problematic since the largest impact of the DCR process can be observed at the boundary of the treated zone. A deeper understanding of the residual stress distributions and the location of the balancing tensile residual stresses were critical for ensuring that there was overall fatigue life enhancement.

2.6 Conclusions

There is a large amount of study on the aspect of introducing compressive residual stresses by the variety of surface treatments. Deep surface rolling method is considered as a cost-effective tool, to improve the dynamic strength of a component by the generation of compressive residual stress state. However, distortion is a major cause of a structural failure and material waste. There are

not many studies mentioning how to balance distortion and compressive residual stresses. It was reported that balancing tensile stress field can increase the FCGR enough to effectively wipe out the beneficial effect of the induced compressive residual stress field [197].

Finite element models provide an approach to optimise the mechanical surface processes, to meet manufacturing requirements. There are many advantages of FE modelling the distortion behaviour and the residual stress during the deep surface rolling process. Firstly, it allows a deep understanding of the phenomena involved, and allows exploring different conditions, such as loads, roller movement, friction and multiple overlaps. Secondly, it permits (in some cases) time and material savings in the development and optimisation of this technique.

Superposition method, crack closure based on Newman's equations and FE models were commonly used to predict FCGRs. However, the predicted FCGR through a residual stress field is quite sensitive to the accurate measurement of the residual stress field, particularly in the compressive region. The weight function method can be used to calculate K_{res}. The reliable prediction requires a specific weight function for the specimen geometry being analysed.

Therefore, this thesis will optimise deep surface rolling process by finite element simulation, then to improve the fatigue performance of aerospace materials. Furthermore, an analytical method will be developed to predict the fatigue crack growth rate in an initial residual stress field.

Besides, this research will provide a better understanding of the distortion and the residual stress distribution after deep surface rolling process. The effect of deep surface rolling using finite element analysis will be validated with experimental results. Two predictive models of FCGRs will be compared and validated by experimental measured FCGRs. The limitations and drawbacks will be discussed in chapter 7.

3 Materials and Experimental Methods

In this chapter, all experimental methods and measurements are presented and detailed. The material used is characterised in section 3.1 and in section 3.2 the applied surface treatments are described. To fully understand and optimize mechanical treatments, three case studies are defined, and related geometries are designed in section 3.3. Distortion is also assessed in consideration of thin parts. Section 3.4 introduces the distortion measurement technique and investigates the effects of distortion by DSR. In section 3.5 matrix measurements of hardness are detailed. Section 3.6 concludes the induced residual stresses by different DSR parameters, which was measured by ICHD and Neutron diffraction. The tension-tension fatigue test procedures are given in section 3.7. Measurement of crack length is briefly introduced in section 3.8. Finally, measurement of striation spacing on the fracture surface was performed after fatigue tests and the methodology followed is given in section 3.9.

3.1 Materials and Mechanical Properties

The material was supplied by Airbus and sourced from Alcoa. The materials were 2024-T351 and 2524-T351 wrought aluminium sheet 1.6 mm thick and clad on both sides with soft unalloyed aluminium that constitutes nominally 2.5% of thickness (i.e. 50 µm thick on each side). Following the requirements of test specimen geometries, 120 mm × 240 mm rectangular sheets were machined. AA2024-T351 is commonly used in the aerospace industry for aircraft fuselage panels and wing skins. AA2524-T351 is newly applied to replace the AA2024-T351 for relevant components. 2000 series alloy uses copper as its major alloying element. Table 3.1 shows the composition of 2024 aluminium as specified by Alcoa. Table 3.2 shows the main alloying elements and specific properties of 2524-T351.

Table 3-1 Chemical composition limit (WT.%) of alloy 2024-T351 [180]

Si…	0.06	Zn…	0.15
Fe…	0.12	Ti…	0.10
Cu…	4.0-4.5	Others, each.	0.05
Mn…	0.45-0.70	Others, total.	0.15
Mg…	1.2-1.6	Balance, Aluminum	
Cr…	0.05		

Note: Value maximum if range not shown

Table 3-2 Chemical composition limit (WT.%) of alloy 2524-T351 [181]

Si…	0.5	Zn…	0.25
Fe…	0.5	Ti…	0.15
Cu…	3.8-4.9	Others, each.	0.05
Mn…	0.3-0.9	Others, total.	0.15
Mg…	1.2-1.8	Balance, Aluminum	
Cr…	0.1		

Note: Value maximum if range not shown

Regarding the heat treatment of both alloys, the T351 solution heat treatment requires heating the material to a temperature of 500°C followed by quenching to less than 40°C. After heat treatment, the material is stress relieved by controlled stretching (1-3%) and then aged naturally. There is no further straightening after stretching.

The mechanical properties of the material using in this study were obtained by a tensile test according to ASTM standard E8M [182]. Three samples of each alloy were tensile tested parallel to the rolling direction and perpendicular to the rolling direction as well. The dimension of the tension test specimens is shown in figure 3.1, and the average is reported in table 3.3.
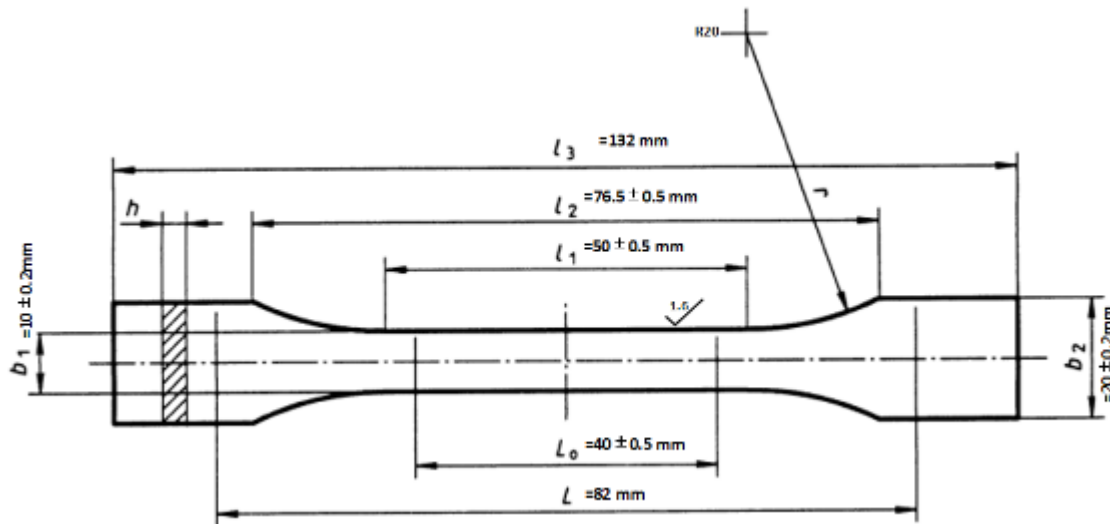
Dimensions in millimetres

l_3 Overall length	≥ 132
l_1 Length of naroow parallel-sided portion	50 ± 0.5
r Radius	20
l_2 Distance between broad parallel-sided portions	76.5 ± 0.5
b_2 Width at ends	20 ± 0.2
b_1 Width of narrow portion	10 ± 0.2
h Thickness	1.6
L_0 Gauge Length	40 ± 0.5
L Initial distance between grips	82 ± 1

Figure 3.1 Standard dimensions of rectangular tension test specimen (ASTM-E8, 182)

Tension tests were conducted on the 100kN servo hydraulic Instron system. Small strips of silver reflective tape were applied to the template at the top and bottom of the section with the tabs of each specimen [183]. The displacement was 1mm/min for all tension testing specimens. Changes in gauge length were measured by using a laser extensometer. Figure 3.2 gives stress-strain results of 2524-T351 (*LT*) samples tested by tensile tests, as an example.
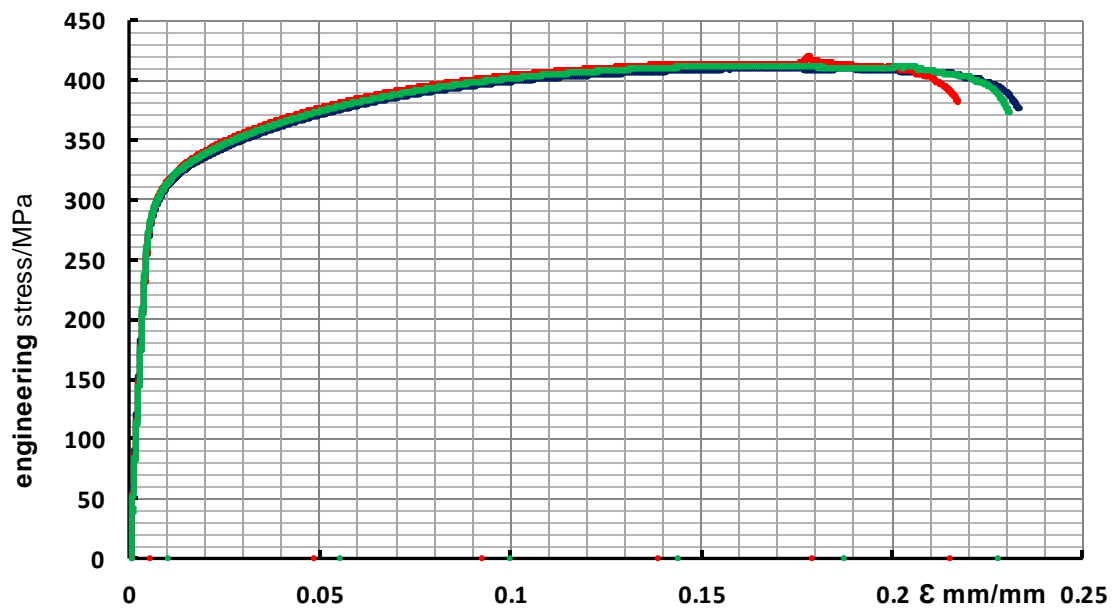
Figure 3.2 Stress-strain result of 2524-T351 (LT) samples measured by tensile tests

The proof stress, ultimate tensile stress and elongation at fracture are measured and averaged from the results of BL tensile tests. The mechanical properties of AA2024-T351 and AA3524-T351 are summarised in table 3.3.

Table 3-3 Mechanical properties of AA2024-T351 and AA2524-T351

Material	0.2% Proof Stress (MPa)	Ultimate Tensile stress (MPa)	Elongation at Fracture (%)
2024/L	330 ± 6.2	443.3 ± 4.2	16.5 ± 1.1
2024/TL	294 ± 1.4	425.6 ± 3.2	20.9 ± 2.3
2524/L	351 ± 2.6	436.7 ± 2.8	15.6 ± 1.2
2524/TL	299 ± 3.6	412.7 ± 2.5	22.5 ± 0.9

The Values for Young's modulus (E) and Poisson's ratio (v) are referred from Alcoa database and are shown in table 3.4.

Table 3-4 Young's Modulus and the ratio of AA2024-T351 and AA2524-T351

Material	Young's Modulus E (MPa)	Poisson's Ratio v
2024-T351	73000	0.33
2524-T351	71000	0.33

Mechanical properties shown in table 3.3 and table 3.4 were used as material properties when carrying out FE analysis and residual stress calculation via the integral method. Figure 3.2 shows the stress-strain curve of AA2524-T351 (*LT*) as measured by tensile testing. Results of stress-strain data are used to determine isotropic material properties using FEM.

3.2 Mechanical Surface Treatments

Metal fatigue and corrosion damage to aircraft components, are a major threat to safety, and to the flight availability, of civil and military aircraft. This has led to novel surface enhancement methods, alongside advanced aircraft repair technologies being extensively investigated in the last decade.

3.2.1 Deep Surface Rolling

A schematic drawing of a typical rolling rig is given in figure 3.3. The sample sheets are fixed during the rolling process by a vacuum clamping system. This machine provides a constant force. The oscillating mass is fixed to the crossbeam and the rolling load is provided by a lowering of the roller assembly, activated by hydraulic piston pressure between the workpiece and the crossbeam. Deep surface rolling generates a highly compressive residual stress region along the rolling direction of the workpiece material. The rolling load can provide up to 200kN force.

The roller assembly can be dissembled so that the roller can be changed for a more appropriate roller profile, if necessary. The roller diameter can vary between 100 to 200 mm and a maximum thickness of 30 mm. The linear crossbeam translation is performed by the feed motor. The travel speed of the roller has a maximum value of 25 mm/s.
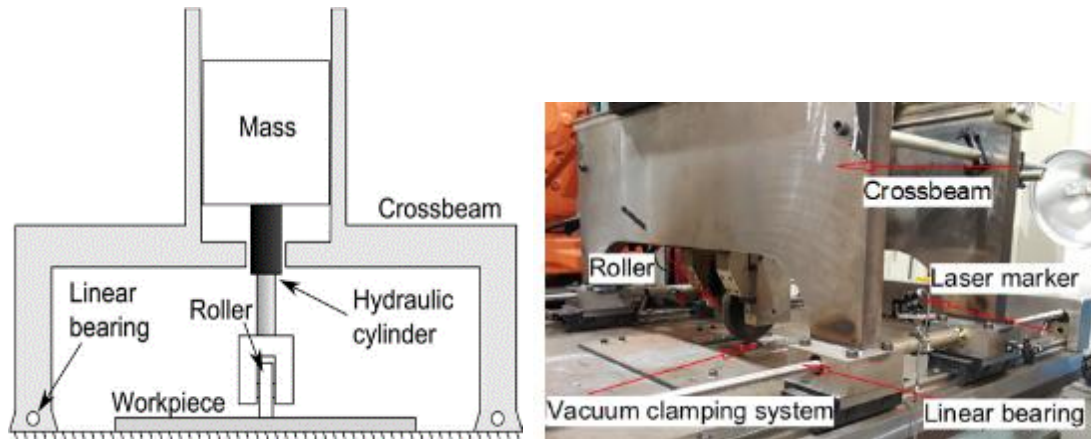
Figure 3.3 Schematic diagram of a rolling rig [184]. Includes oscillating mass, crossbeam, linear bearing, main hydraulic system, roller assembly, vacuum clamping system and laser marker

In order to monitor roller positions during the process of movement, a battery-powered laser marker is attached to the linear bearing. A vertical beam perpendicular to the rolling direction is opened during the rolling process. By adjusting the position, the roller centre can be located in the line of the laser beam. As a result, the symmetric rolled area of another surface can be accurately controlled by recording the laser marks.

As a well-developed surface treatment, that is widely used in welding studies, DSR has rarely been applied to stress-free components or structures.

To investigate and optimise the deep surface rolling technique, figure 3.4 illustrates the research process.
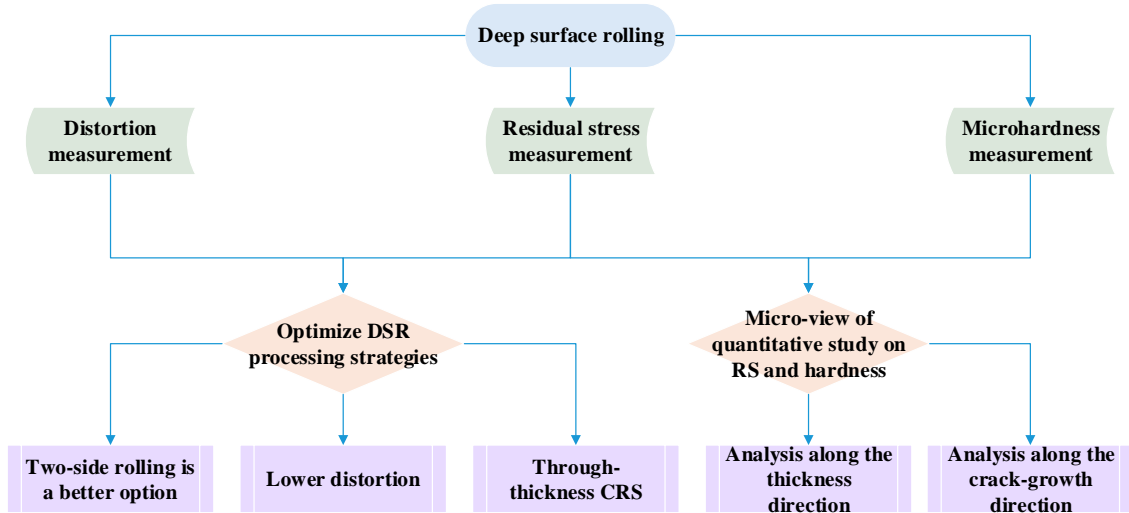
Figure 3.4 A flow diagram of the research process used to establish *vital parameters* of deep surface rolling on fatigue crack growth rates in terms of effects on distortion, hardness, and residual stress distribution

Three major mechanical properties were evaluated after samples had been DSR treated, distortion, residual stress and microhardness, respectively. Optimum treatment parameters can be configured by assessing the accurate results of measured distortion and induced residual stress profiles. By improving DSR processing strategies and optimising the DSR parameters, it is concluded that the two-side rolling method is a better option compared with the one-side rolling method. Moreover, optimised DSR parameters can serve the purpose of lowering the maximum distortion and through-thickness distribution of induced compressive residual stress.

An interesting study would be to establish a micro-view relationship between induced residual stress and microhardness. During the DSR process, the contact pressure is quite high and can exceed the yield strength of the material. Compressive residual stress near the surface is generated by work hardening. Additional research into the microhardness distribution within the induced residual stress field may also be beneficial to this field of study.

3.2.2 Hammer Peening

Due to the way that the clamping arrangement within the DSR apparatus restricts the flexibility and movement of the surface being rolled, it is not a suitable process to use on complex structures. Hammer peening is a novel mechanical surface treatment which could replace DSR in some respects. Specimens were hammer peened by using a prototype in KUKA, Germany. Figure 3.5 demonstrates the equipment components of the hammer peening system.
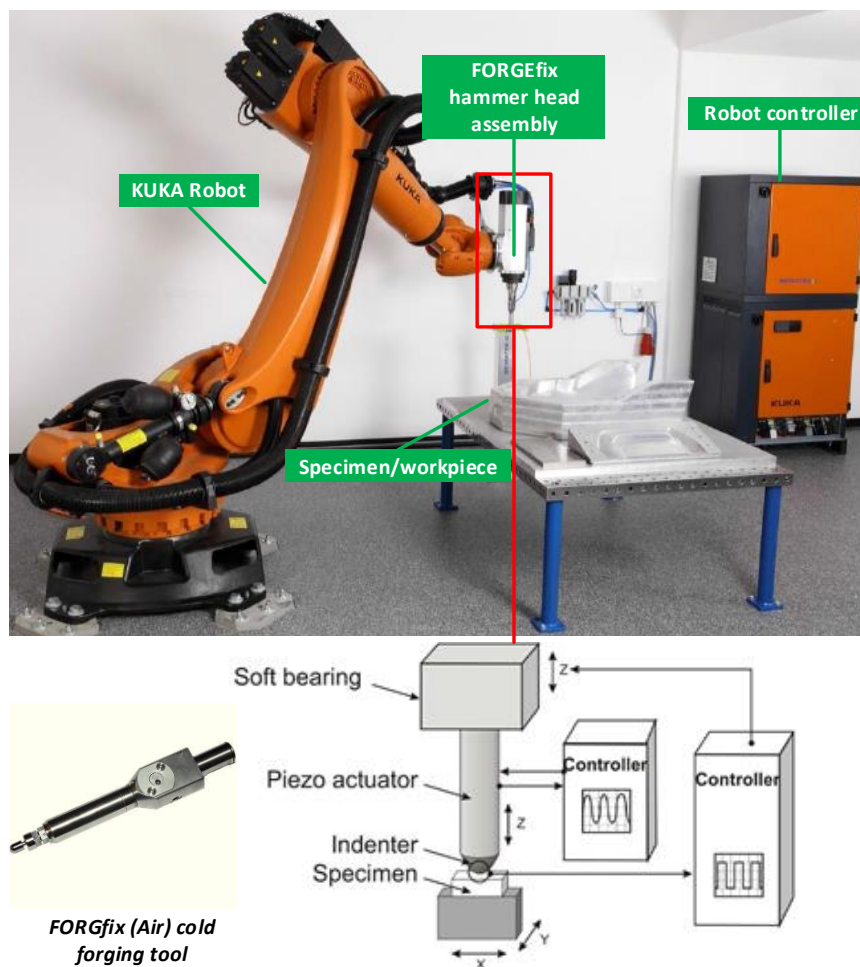
Figure 3.5 Hammer peening equipment components and schematic illustration of the hammer peening plant [111]. Surface processing with a KR QUANTEC and KUKA.CNC; main components include robot, controller, hammer head and specimen/workpiece

The Kuka robot is a pneumatically operated tool with a linearly oscillating hammer head (FORGfix from 3s-engineering GmbH) employed for mechanical surface treatments. Prior to the peening process, the robot measures the workpiece and then, controlled by software, guides the hammer head over the surface along the hammer peening path. The piezo actuator oscillates within a given frequency f and an amplitude a. The sphere diameter, feed rate, path distance, free motion angle, as well as the load fraction (see below) must be selected, and set, to suit the requirements. An important characteristic of the process is that the hammer head indenter-lifts off after contact with the surface of the specimen. The ratio of time between the hammer head making contact with the specimen surface, is defined as the load fraction. The load fraction can be adjusted by movement of the z-position of the soft bearing.

As an optional surface treatment, hammer peening, with limited parameters was carried out, and evaluation of microhardness is demonstrated later in this chapter. More experimental results of residual stress assessments are detailed in chapter 4. Fatigue performance is also presented in chapter 6.

3.3 Test Specimen Geometry of DSR

To complete this research, three case studies were performed and are as shown in figure 3.6.
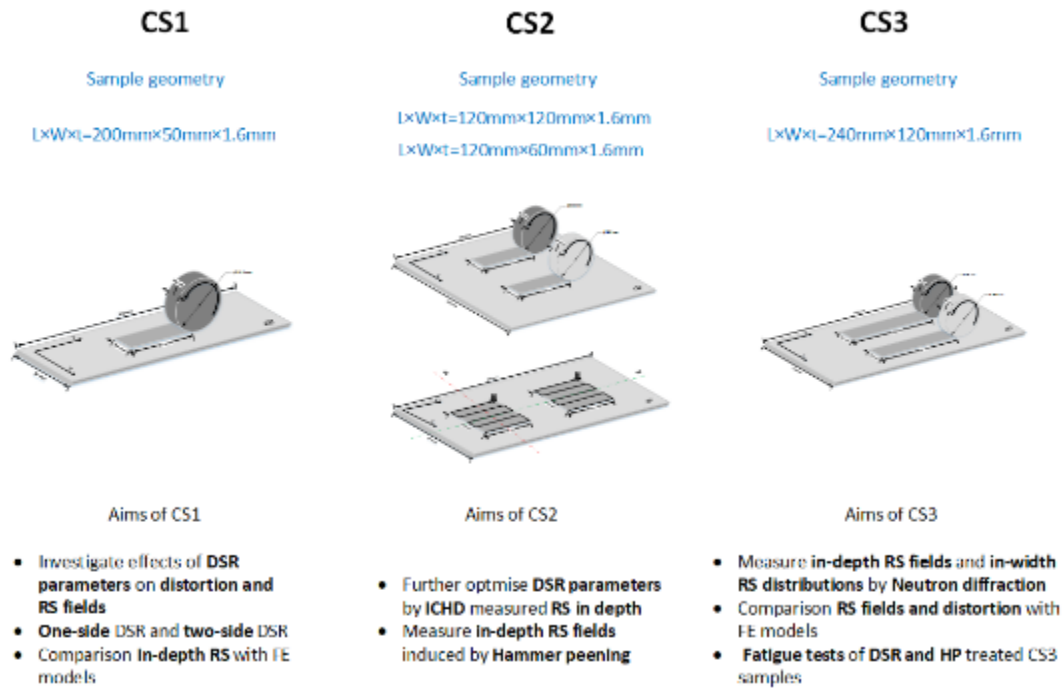
Figure 3.6 Illustration of three case studies and main aims of each case study

CS1 aimed to investigate the effects that systematic modifications to the DSR parameters can have on distortion and residual stress profiles. Modified parameters are not only used for the rolling loads but also to investigate the effects of two-side rolling methods. Finally, measured distortion and in-depth residual stress are compared with FEM.

Dependent on the results of CS1, CS2 mainly aimed to obtain more specific DSR parameters by ICHD (incremental centre hole drilling) measured depth of residual stress fields. Another investigation of CS2 sought to measure the in-depth residual stress fields that were induced by hammer peening (HP). A primary

comparison between experimental results from DSR and HP is summarised in section 4.3.

The samples of CS3 were treated by DSR and HP, by using the parameters concluded for the study of CS2. Residual stress fields (in-depth and in-width) of two specimens treated by DSR were measured by Neutron Diffraction. The measured RS fields were then compared with FEM, as shown in chapter 5. Fatigue tests were performed on CS3 samples and the results are revealed in chapter 4.

DSR case study 1 (CS1)

Aluminium alloy was machined to rectangular sheets of dimensions 200mm×50mm×1.6mm, depicted in figure 3.6. Samples were deep rolled on (1) one side and on (2) two sides, separately (the rolling process are detailed in chapter 5). The distortion was measured and defined giving the maximum value at the very centre point, shown in section 3.3 (distortion methods). The residual stresses at the measured point of maximum distortion were determined by incremental centre hole drilling (ICHD) and then, the comparative relationship between residual stresses and the maximum distortion value is presented in chapter 4. Methods of averaging residual stress are described in section 3.6. Figure 3.7 shows the single surface rolling process performed on a 50mm × 200mm rectangular sheet, and the rolled area was generated by a 20 mm width flat roller with a diameter of 100 mm.
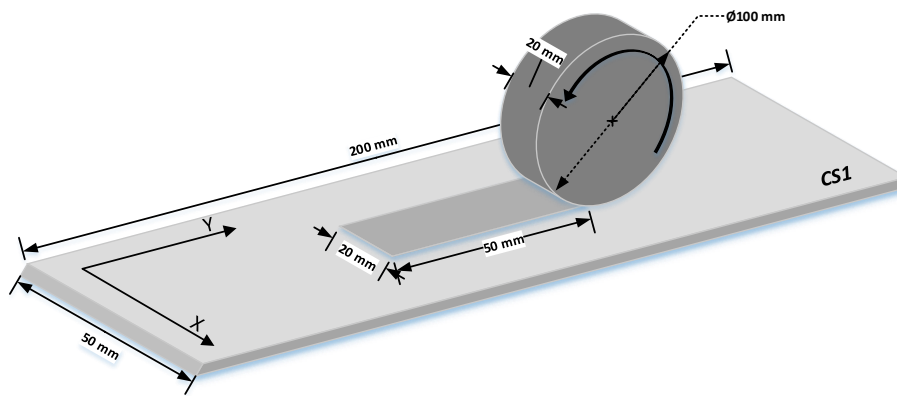
Figure 3.7 Single surface rolling process schematic with dimensions of sample and roller

For the two-sided DSR process, the sample was simply turned over and fixed again by the clamping system.

DSR case study 2 (CS2)

Aluminium alloy was machined to square sheets of dimensions 120mm×120mm×1.6mm, as depicted in figure 3.7. Samples were deep rolled on two sides (the rolling process is detailed in chapter 5). Two DSR strips on each surface were applied to CS2 samples. CS2 mainly aimed to optimise residual stress profiles to minimise distortion and to contribute reasonable DSR parameters for fatigue tests on CS3. The specific rolling loads of measured samples were 60/15kN, 30/30kN and 30/15kN, respectively. Figure 3.8 shows the process of DSR on one surface by inducing two rolled strips.
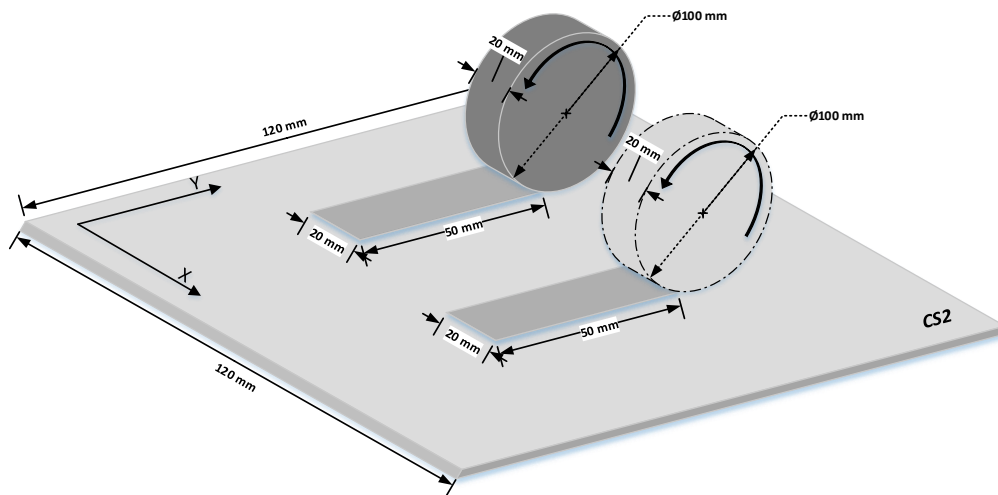
Figure 3.8 Two rolled strips on one side induced by DSR process

As for CS1, two-sided rolling processes can be performed by rotating samples by 180 degrees along the centreline.

Aluminium alloy was machined into rectangular sheets of dimensions 120mm×60mm×1.6mm as shown in figure 3.9. Samples were treated by hammer peening and the parameters can be found in table 3.5. The geometry of the peened patch is 20 mm × 20 mm square. Hammer peening is known to induce compressive residual stresses equally balanced in all directions. However, mostly the CRS values along the x-axis (σ_1) were higher than values along the y-axis (σ_3). In an attempt to illustrate a better comparison between deep surface rolling processes and the hammer peening method, the peening tool travelled along the y-axis perpendicular to the deep rolling operation direction.
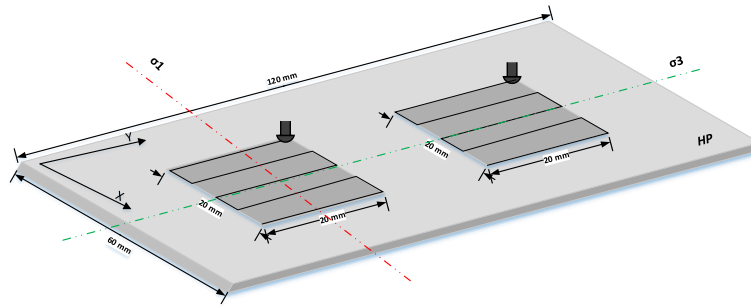
Figure 3.9 Mechanical process of hammer peening

Samples were hammer peened by a prototype in Hamburg, Germany. The peened geometry is shown in figure 3.9. Samples were firstly measured by ICHD to acquire the residual stress profiles. Two different parameters of hammer peening were experimented with, by performing fatigue tests. These are analysed in section 6.

Table 3-5 Hammer peening parameters

	ball diameter (mm)	Travel speed (mm/s)	Step (mm)	Impact force (kN)
Lower peening	8	50	0.2	~4
Higher peening	8	100	0.4	~4

DSR case study 3 (CS3)

Aluminium alloy was machined to the square sheets of dimensions 240mm×120mm×1.6mm as shown in figure 3.10. Samples were deep rolled on two sides. Two rolled strips on each surface were applied to CS3 samples. In CS3, residual stresses of three load parameters (table 3.6) were evaluated by using incremental centre hole drilling (ICHD) and neutron diffraction (ND).

Table 3-6 Experimental exploration on residual stress distribution in-width (crack growth direction)

Load parameters	30/18kN	20/10kN	60/15kN
Measurements	ICHD	ND	ND
Objectives	Limited exploration of RS distribution across rolling strips	Detailed investigation of RS distribution across rolling strips	Detailed investigation of RS distribution across rolling strips
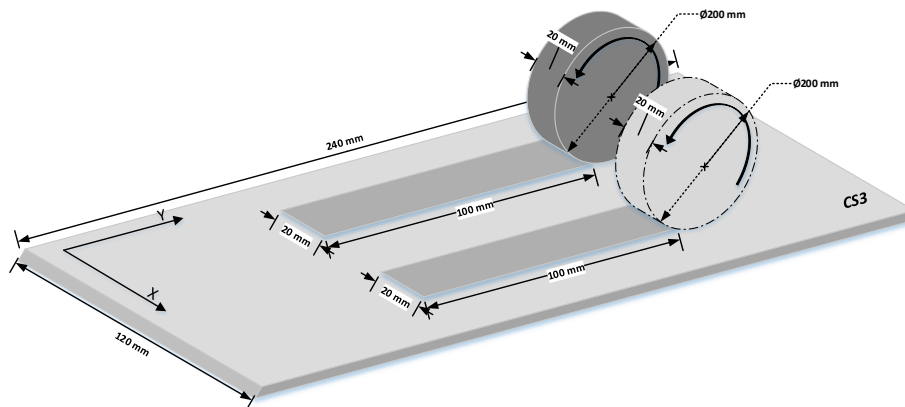
Figure 3.10 Optimised parameters of roller diameter and load parameters in CS3

On completion of the above investigation, DSR samples of CS3 were used for fatigue tests, where specific DSR loads were obtained from the results of CS2. In CS3, the effects of various DSR parameters on fatigue performance were investigated, and the conclusion ware revealed in chapter 5 and chapter 6.

3.4 Distortion Measurements

As a mechanical surface treatment, DSR can induce the highly compressive residual stresses, and at the same time, more distortion may be generated. By measuring distortion and residual stress within samples, the relationship between these two factors can be clarified and systematically analysed.

Distortion measurement was conducted by a Cyclone laser scanner, and a contact scanning probe was used to identify the scanned surfaces. Scanning is the process of gathering data from an undefined 3-dimensional surface, where there is a need to reproduce a complex, freeform shape. Figure 3.11 shows the equipment for distortion measurement and the clamped sample (right image).

Figure 3.11 Surface mapping scanner and the clamping system of a DSR sample

To obtain the undefined surface in a 3D point cloud, firstly, an analogue contact probe moves across the unknown surface, after the area and orientation in which to scan has been defined. As the probe follows the surface, the system records information in the form of numerical position data. Finally, the data can be exported in various formats to a CAD/CAM system for further processing.

For most applications, the highest accuracy and quality of surface finish are obtained using contact sensors, which have several fundamental advantages over the majority of available non-contact systems.
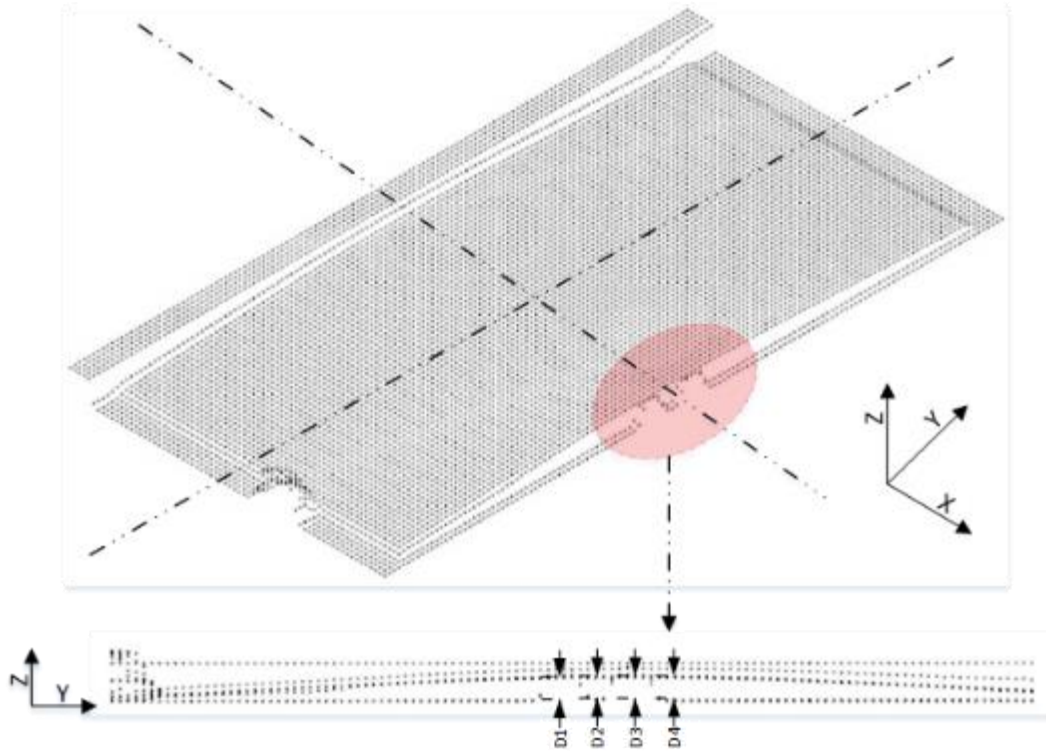
Figure 3.12 Determination of maximum distortion by the scanned point cloud

By viewing the Y-Z plane, a distorted side-surface is mapped by dash-dot lines. The maximum distortion can be found near the centre line. Near the centre, several points are selected and measured; then the largest distortion value was obtained by comparison (see figure 3.12). The final results were concluded in section 3.6.

3.5 Microhardness Matrix Measurements

As a characteristic of a material, hardness is not a fundamental physical property. It is defined as a material's resistance to indentation, and the value of hardness is calculated by measuring the geometry measuring the permanent of the imprint left in the material surface by the indenter. The Vickers hardness test method, also referred to as a microhardness test method, is commonly used for small parts, thin sections, or case depth work. Microhardness testing [185] gives a

suitable range of loads for testing with a diamond indenter; the resulting indentation is measured and converted to a hardness value. The equipment of hardness testing is shown in figure 3.13 where the principles of Vickers hardness are also included.
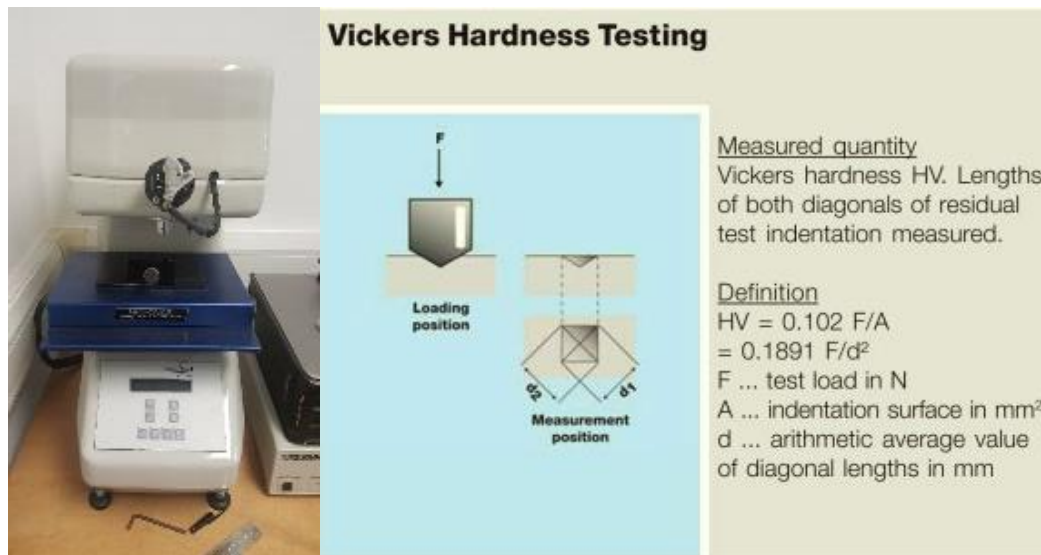
Figure 3.13 Zwick/Roell micro Vickers hardness tester and the schematic diagram of Vickers hardness [185]

For aluminium alloys, an indenter made of diamond was pressed into specimens supported on a firm base. The test load (100 grams-force) was applied perpendicularly to the surface of the specimen, with a defined initial application time and duration (10 seconds). The indentation was measured after removal of the load. The length measurement values (indentation depth, diagonals, diameter) were used to calculate the hardness value.

Figure 3.14 demonstrates the microhardness measurements of DSR samples, used to evaluate the effects using DSR and HP.
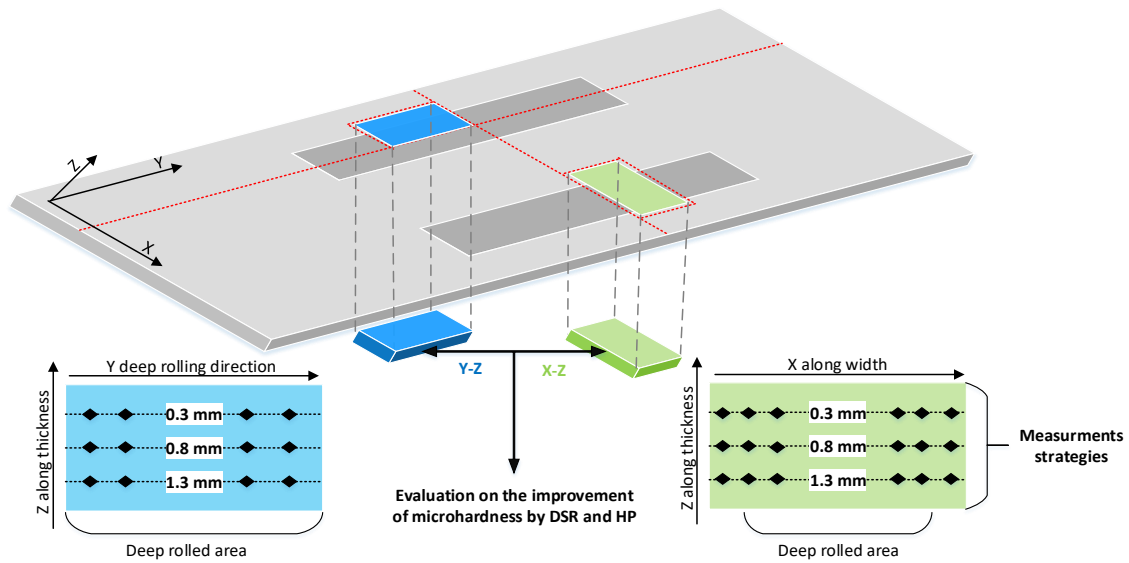
Figure 3.14 The demonstration of microhardness measurement planes obtained by cutting from deep rolled samples

As shown in figure 3.14, measurements of Y-Z cross-section were entirely located within the deep rolled area. Due to the 50µm thickness of clad layers close to both surfaces, measurements were selected from depth 0.3mm to 1.3mm away from the very top surface, and ar a data interval of 0.5mm. Measurements of X-Z cross-section consisted of the un-rolled area and the deep rolled area. Results were compared with the baseline, the effects on microhardness when using DSR are presented in section 4.2.

The relationship between microhardness and residual stresses distribution is further built upon and concluded in Chapter 4.

3.6 Residual Stresses Measurements

Various techniques used to quantify residual stress have already been illustrated in chapter 2. In this research, incremental centre hole drilling (ICHD) and neutron diffraction (ND) methods were applied to quantitatively map the residual stress distribution either in depth or width.

3.6.1 Residual Stress Measurement by ICHD

The residual stress fields induced by deep surface rolling and hammer peening were measured using the incremental centre hole drilling method as implemented in ASTM-E837 [186]. A brief description of the results is provided in this section to aid understanding of the fatigue results that follow in subsequent sections. The platform of ICHD is demonstrated in figure 3.15 along with the setting panel (right) of residual stress measurements on aluminium alloys.
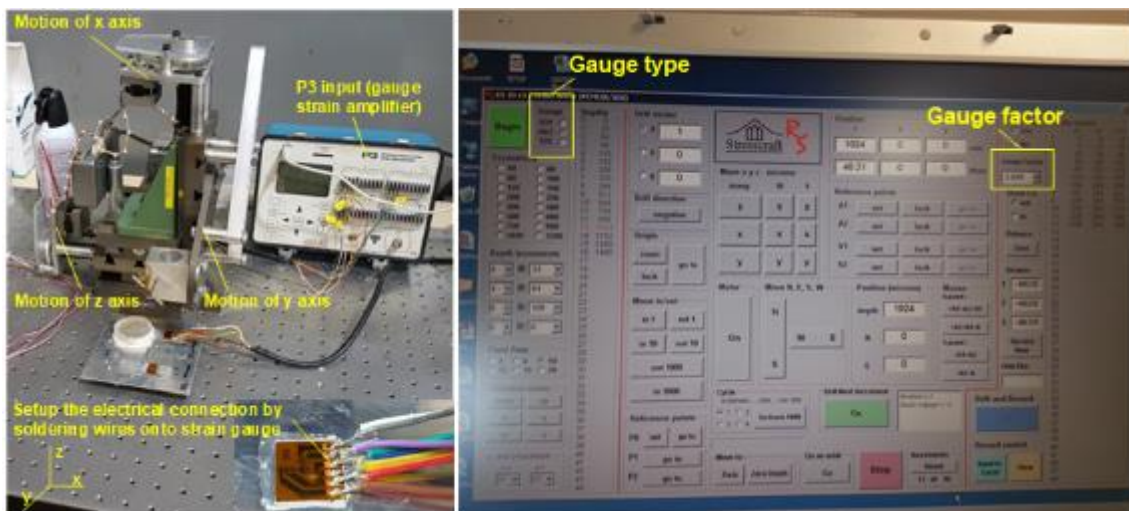
Figure 3.15 Equipment of ICHD (left) and the setting panel (right) of RS 3D

The ICHD technique was presented in chapter 2. However, it's important to remember that residual stress is measured in two perpendicular directions depending on the alignment of the strain gauge and that residual stress is measured in increments through the depth. The strain gauges are aligned to

measure residual stress parallel and perpendicular to the centre-slit (notch) (crack propagation direction) as illustrated in figure 3.15.

Adequate preparation work is also essential in order to obtain accurate measurements. For thin and distorted specimens, before conducting any measurements, solidified resin was applied to the opposite surface of measured spots, supporting thin samples. Then measured surfaces were carefully polished before placing the strain gauge. The electrical connection was set up between the strain gauge and input channels. For distorted samples, the flatness level of the measured area was ensured by adjusting the clamping tools. Gauge type and gauge factor were reported on the gauge box and inserted into the setting panel.

The gauge type of aluminium alloys in this research was CEA-XX-062UL-120 and gauge factor was 2.04 ±1%. It is compatible with all methods of introducing the hole, and the strain gauge grid geometry is identical to the 062RE pattern. The UL configuration is supplied in 1/16 in (1.6 mm) gauge length.

The original stress state in the component was evaluated from the measured strain. Both the magnitude and directions of principal stresses were calculated. To map the residual stress distribution along the entire depth (the maximum depth by ICHD can be up to 1.4mm), two drilled holes located on the symmetrical surfaces were measured, and their positions are shown in figure 3.16. In CS1, in order to build a quantitative relationship between residual stresses and distortion, the measured holes need to be drilled close to the maximum distortion if possible.
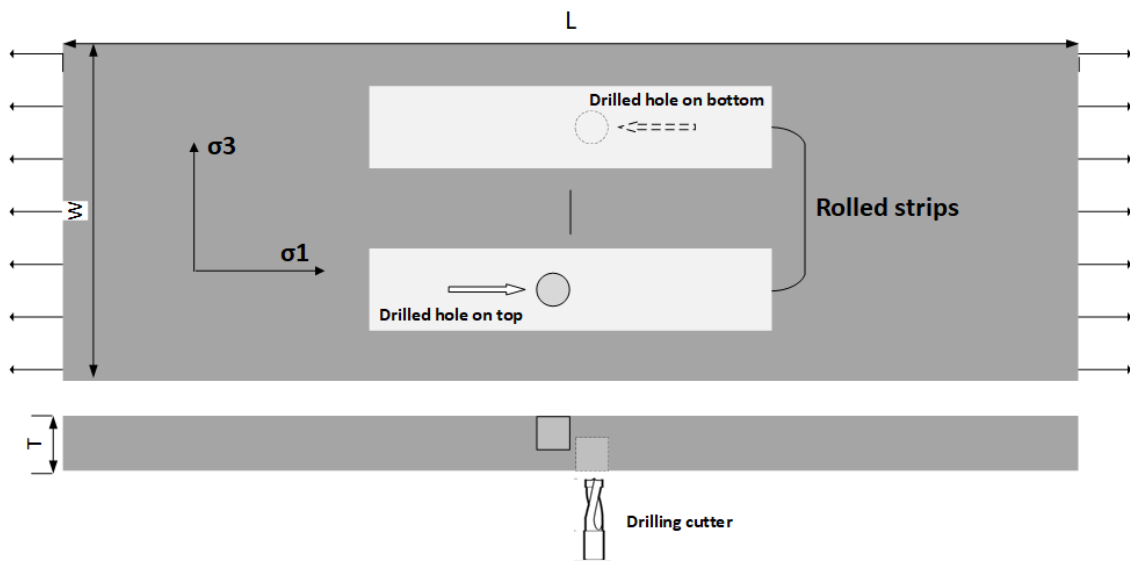
Figure 3.16 Illustration of residual stress measurements, performed on two surfaces (CS3), using ICHD

By averaging the values of residual stresses distributed along the depth, the relationship between residual stresses and distortion can be used to evaluate the DSR parameters and hence optimise this treatment. Also, through comparing the distribution of induced residual stress in-depth, optimised parameters of DSR can be used in influencing fatigue performance and fatigue crack growth rates.

3.6.2 Residual Stress Measurement by Neutron Diffraction

Two samples of different load parameters were measured by SALSA at Institut Laue-Langevin (ILL), Grenoble, France. SALSA used a hexapod as a sample manipulator which can freely move and is controlled by six independent hydraulic pistons. The load capacity of the SALSA hexapod can be over 500 kilograms, and it allowed tilts up to 30° with a translation range of 600 mm. Arrangements of the equipment and the clamping of samples are shown in figure 3.17.
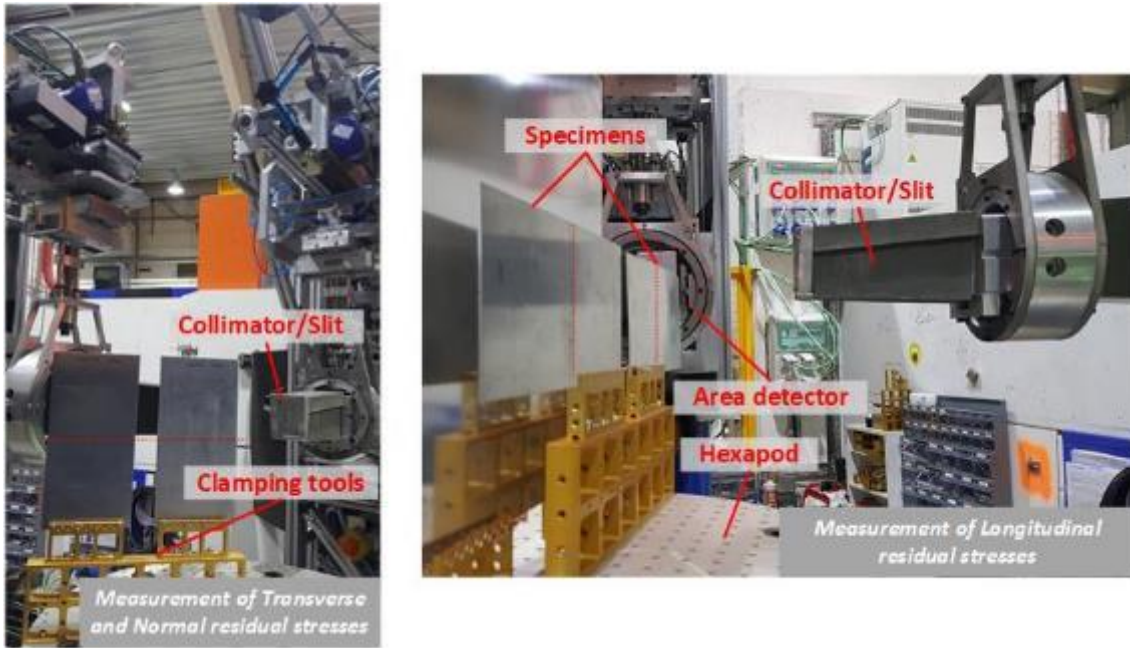
Figure 3.17 SALSA instrument for *the strain analyser applications* includes Delta table (support Hexapod), Hexapod, Monochromator, Collimator, Monitor, Area detector

The positioning accuracy is application dependent and should be to within one-tenth of the minimum gauge volume dimension. For large specimens/sampling volumes, less accuracy may be sufficient. The initial positioning of the sample can be achieved using optical instruments such as theodolites or mechanical means. The sample table should be able to move in three orthogonal directions and to rotate around the vertical axis of the instrument.

The neutron wavelength selected to probe specimens was set to 1.61 Å (=16.1 nm, where Al (3 1 1) = 1.221 Å =12.21 nm). The collimating and receiving slits were set to get a volume gauge of $0.6 \times 0.6 \times 2 \ mm^3$. The arrangements for the data acquisition can be seen with samples in place among the detector system forming an angle of 82° with the incoming beam.

Along the cross-section of the width (figure 3.18), ten positions were marked and measured by using neutron diffraction, as shown in table 3.7. 34 points of each

sample were measured and the gauge was inserted into specimens within the thickness. Each point was measured in three-dimensional directions. Each measurement was taken for a period of 15 minutes.

Table 3-7 Details of measurements by Neutron diffraction

Location	25mm	35mm	40mm	45mm	55mm	65mm	75mm	80mm	85mm	95mm
measurements	3	3	5	3	3	3	3	5	3	3
In/out patch	out	in	in	in	out	out	in	in	in	out
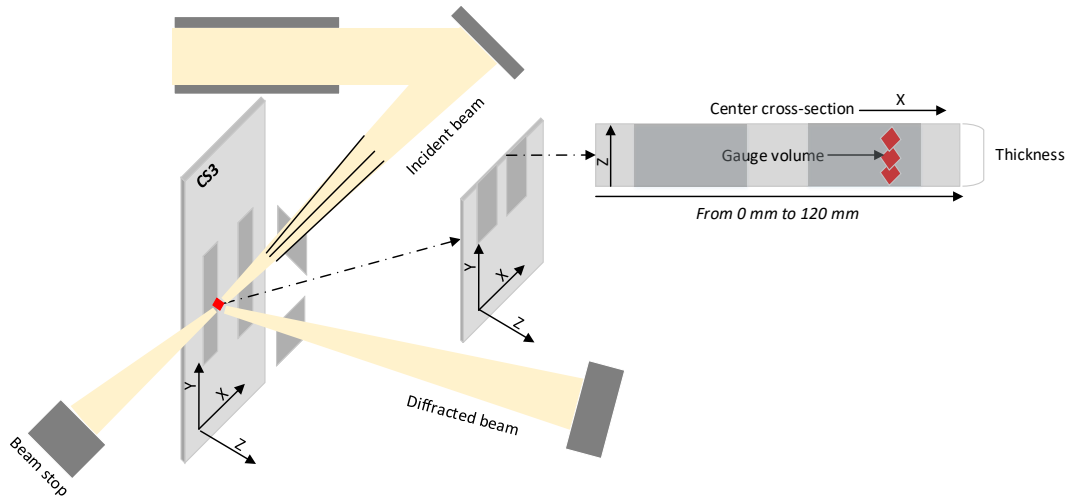
Figure 3.18 The measuring process of residual stresses by Neutron diffraction

Measurements extracted from the centre of the DSR patch were taken in-depth in order to identify the residual stress gradient and to enable to a comparison with the results of ICHD. Residual stresses were determined by three measurements in-depth (from 0.6 mm to 1.0 mm), and all measurements should be entirely confirmed as within the thickness.

Residual stress characterisation by neutron diffraction involves measuring the change in the lattice parameters or interplanar spacing by measuring peak shift

and comparing it to the unaffected metal. The peak angular position is usually obtained by fitting the experimental peak profile with an appropriate function, e.g. a Gaussian or a pseudo-Voigt function. The fitting algorithm also provides an estimate of the statistical error of the peak position, which determines the statistical error of the strain measurement ($\Delta d/d$).

The strains are then calculated using equation 3.1.

$$\varepsilon = \frac{d - d_0}{d_0} = \frac{a - a_0}{a_0} \qquad 3.1$$

Where d and a are the d-spacing and the lattice parameter, respectively, with the subscript '0' indicating the strain-free values. Following the measurement and calculation of the strain in all three directions (hoop, axial and radial), a stress component can be calculated using equation 3.2.

$$\sigma_{hoop} = \frac{E}{(1+v)(1-2v)}\big[(1 - v)\varepsilon_{hoop} + v(\varepsilon_{axial} + \varepsilon_{radial})\big], \text{ etc.} \qquad 3.2$$

Where E is the bulk Young's modulus, and v is the Poisson's ratio. For plane stress conditions ($\sigma_{zz} = 0$, because of thickness $= 1.6$ mm of thin aluminium alloys sheets), the unstressed lattice spacing d_0 is simplified to equation 3.3.

$$d_0 = \frac{v}{1+v}\big(d_{hoop} + d_{axial}\big) + \frac{1-v}{1+v}d_{radial} \qquad 3.3$$

Once the data was integrated and then corrected with the help of the LAMP (Large Array Manipulation Program), the peak height is defined to be background subtracted. Residual stresses were calculated in both the rolling direction (hoop) and perpendicular to the rolling direction (axial). Results of measured residual stresses are given in section 4.3.3.

3.6.3 Averaging Measured Residual Stresses

Induced residual stresses in treated samples are not uniformly distributed along the thickness. In order to obtain the average value of residual stresses more accurately, equation 3.4 is used in this research. Averaged residual stress is used to the calculation of K_{res}. The variable of K_{res} is very sensitive to the residual stress field.

This section introduces a mathematical method to average residual stresses in depth. The Riemann Sum formula [187] provides a precise definition of the definite integral as the limit of an infinite series. The Riemann Sum formula is as follows:

$$\int_{a}^{b} f(x)dx = \lim_{n \to \infty} \sum_{i=1}^{n} f(x_i)\left(\frac{b-a}{n}\right) \qquad 3.4$$

The sum is calculated by dividing the area below the graph up into shapes (rectangles, trapezoids, parabolas, or cubes), which together form a region that is similar to the region being measured. The area is then calculating the area for each of these shapes, and finally by adding all of these small areas together, the whole area below the graph line is estimated. This approach can be used to find a numerical approximation for a definite integral even if the fundamental theorem of calculus does not make it easy to find a closed-form solution. Figure 3.19 shows the three methods of Riemann sum commonly used.

(a) Left	(b) Right	(c) Midpoint
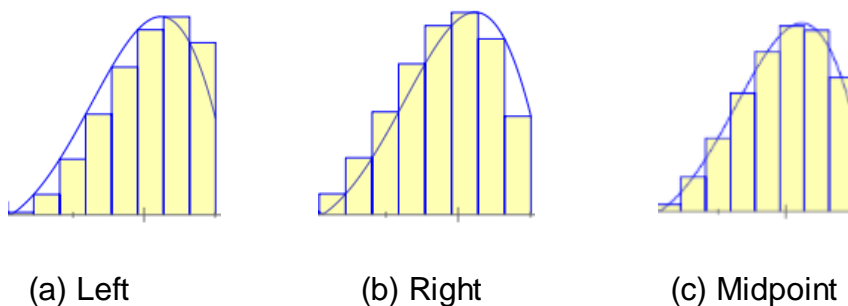
Figure 3.19 Three methods of Riemann summation: Left Riemann sum (a), Right Riemann sum (b), Midpoint rule (c)

For the left Riemann sum, approximating the function by its value at the left endpoint gives multiple rectangles with base Δx and height $f(a + i\Delta x)$. The left Riemann sum amounts to an overestimation if f is monotonically decreasing on this interval, and an underestimation if it is monotonically increasing. The parameter f is approximated here by the value at the right endpoint. This gives multiple rectangles with base Δx and height $f(a + i\Delta x)$. The right Riemann sum amounts to an underestimation if f is monotonically decreasing, and an overestimation if it is monotonically increasing. Approximating f at the midpoint of intervals gives $f(a + \Delta x/2)$ for the first interval, for the next one $f(a + 3\Delta x/2)$, and so on until $f(b - \Delta x/2)$. Summing up the areas gives:

$$A = \Delta x \left[f\left(a + \frac{\Delta x}{2}\right) + f\left(a + \frac{3\Delta x}{2}\right) + \cdots + f\left(b - \frac{\Delta x}{2}\right) \right] \qquad 3.5$$

In this study, the midpoint rule was used to estimate the residual stress data measured by ICHD and ND.

3.7 Tension-Tension Fatigue Tests

Tension-tension fatigue tests were conducted using servo-hydraulic machines with maximum load capacities of 20 kN (shown in figure 3.20) and 50 kN. Each test is detailed with the results in section 4. Fatigue crack growth tests were performed on middle tension M(T) specimens of which dimensions were shown in CS3.
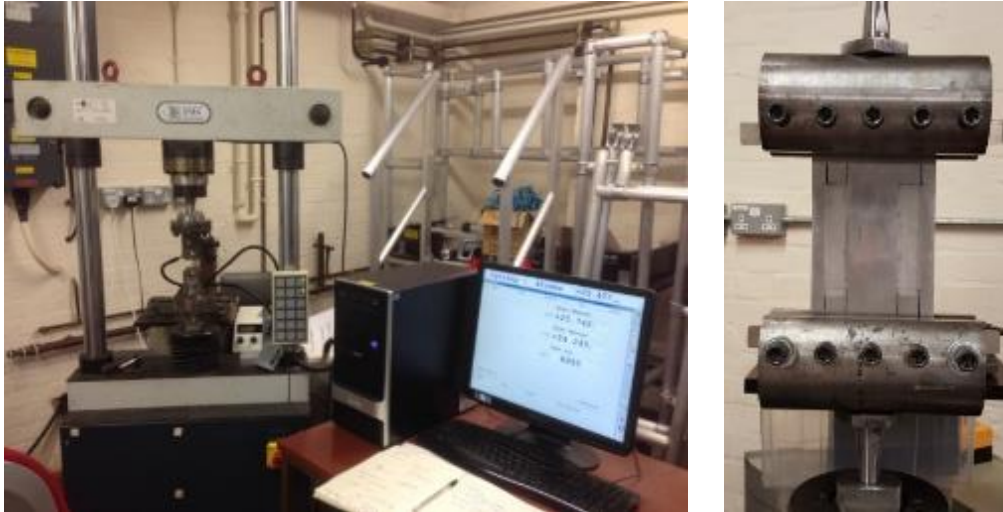
Figure 3.20 Tension-tension fatigue test using 20kN servo-hydraulic machine and the clamped M(T) sample

Tests were conducted in the tension-tension mode under constant amplitude loading with an R ratio of 0.1. Maximum stress of 100 MPa at the section of the specimen width was desired. The fatigue tests were conducted at room temperature and 8Hz. The tests were run until sample fracture. Fatigue tests of middle-tension (MT) samples were done to investigate fatigue crack growth rates induced by varying load parameters and the position of the treated locations, as summarised in table 4.5 (section 4.4).

3.8 Measurement of Fatigue Crack Growth

Fatigue crack length was measured with the help of a travelling microscope, at a magnification of 10x and the data was recorded against the number of cycles. Distortion was generated after surface treatments. Crack lengths of four typical samples were measured periodically on both sides with the help of the travelling microscope, as shown in figure 3.21. In general, all the tests and data analysis procedures were followed according to ASTM E647.
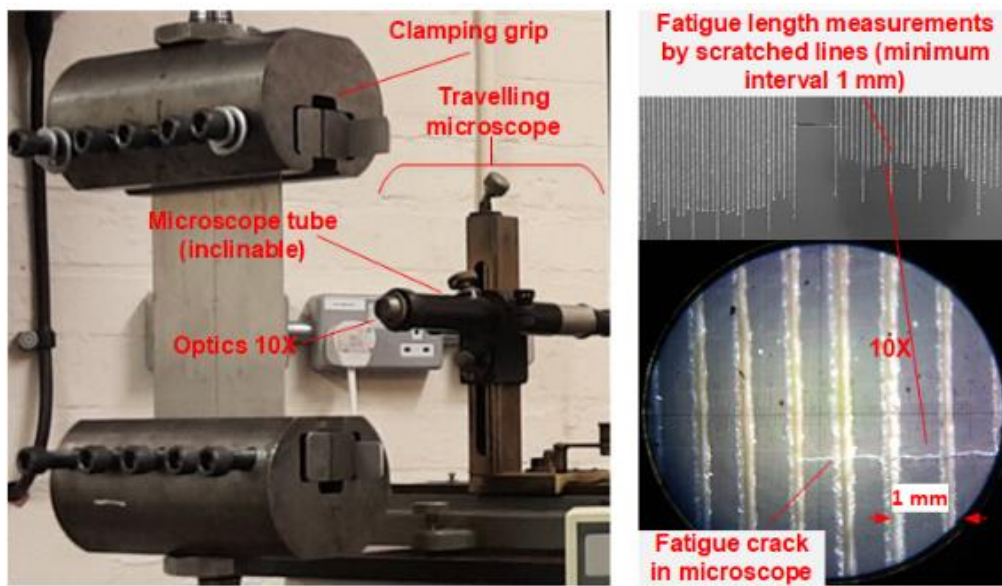
Figure 3.21 Fatigue crack length measured by travelling microscope and minimum interval 1 mm (accuracy 1 mm)

3.9 Measurement of Striation Spacings

After completion of tension-tension fatigue tests, the distance between fatigue striation marks on the fracture faces were also measured using a Phillips XL30 SFEG scanning electron microscope (SEM). The fractured samples were first cut to enable them to fit within the SEM chamber.

Dependent on the initial location of fracture faces, the spacings of striations were measured in bands of five to eight along the direction of crack propagation. In

addition bands of three at each position along the thickness were measured. The relationship between fatigue striation marks and load cycles is an ongoing debate. However, measurements made in this work mainly inspect whether there are any differences in fatigue crack growth rate (FCGR) along the thickness direction, as caused by the influences of mechanical surface treatments. Measurements of striation spacing were taken on both deep rolled samples and baselines to allow comparison of the effect on FCGR of the various loading treatments. The results of this study are given in section 4.5.

This method was used to estimate FCGR because conventional methods were not practical. It was not possible to use direct observation and measurement of crack length, in order to obtain the internal crack growth behaviour. Distributions of residual stresses were not uniform along the thickness, if the material surface was treated by DSR or peening. Influences from these non-uniform residual stresses, were found to accelerate or reduce the FCGR on the same plane.

Figure 3.22 showed the typical area in the fracture surface of one of the aluminium specimens. The fractograph pf crack propagation area was shown in figure 3.22(a). The final fracture area consisted primarily of equiaxial dimples, as shown in figure 3.22(b).
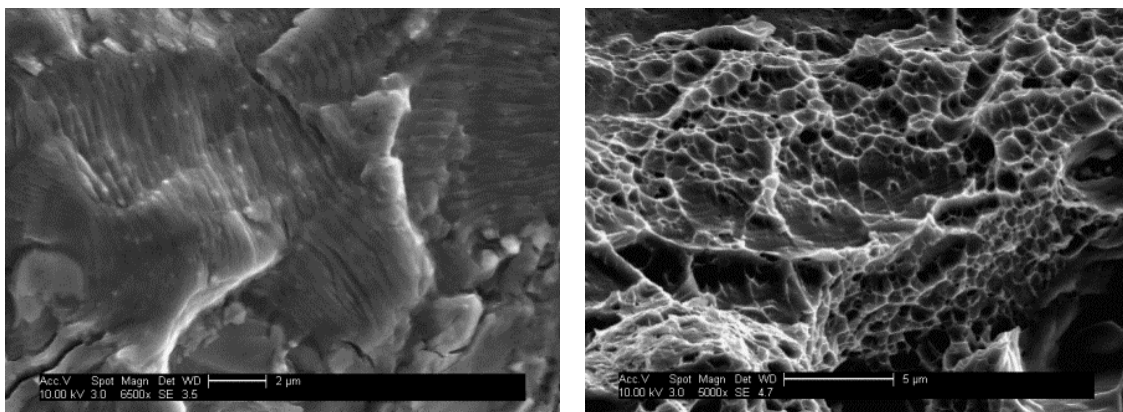
Figure 3.22 SEM micrograph of fatigue fracture surface of AA2024-T351 deep rolled. (a) Crack propagation area; and (b) final fracture area

4 Experimental Results

Material properties and experimental methods are detailed in chapter 3. Results of tensile tests showed that there are few differences between AA2024-T351 and AA2524-T351 with regard to mechanical properties. Due to a shortage of AA2524-T351 supply, distortion and residual stress were measured using AA2024-T351 sheets. Fatigue tests however were performed using both aluminium alloy sheets. In this chapter, experimental results are presented, including the results of distortion and hardness testing on samples treated by DSR and HP. Then, the results of measured residual stress induced by ICHD and ND are presented in section 4.3. All samples including baseline and surface treated specimens are listed in section 4.4, where the specific treatments and fatigue testing conditions are detailed. Experimental data obtained on the critical fatigue length and life improvement factor of each treated sample were calculated statistically. In section 4.5, fatigue databases of baseline samples have been generated using the results of the crack growth curve (crack length as a function of the number of fatigue cycles). For untreated samples, fatigue crack growth rates (FCGR) as a linear function (log-log) of the stress intensity factors (SIF) are presented in section 4.5. For treated samples, the calculated SIFs are influenced by crack closure. More specific analyses are illustrated in chapter 6. In section 4.6, fatigue crack trajectories of baselines and treated samples are reported. Finally, a summary of the experimental results is briefly presented in section 4.7.

4.1 Distortion Presentations

Case study 1 (CS1) mainly investigates the distortion behaviour induced by different loads applied to one side of the aluminium alloy sheets and both sides of sheets of the same material.

Stress-free samples were clamped during the DSR process and allowed to distort after unclamping. It was observed that the DSR treatment deforms the untreated

sheet upwards, towards the rolling surface. Whilst in experiments that involved two-side rolling methods, distortion was observed as the sheet bending upwards (towards the second rolled surface) or downwards (towards the first rolled surface). Distortion of each sample was measured by scanning the surface so that it was bending downwards, as this was more stable and reproducible for measurement.

In CS1, the effect of the maximum distortion (details in section 3.4) by applied rolling loads is demonstrated in figure 4.1.
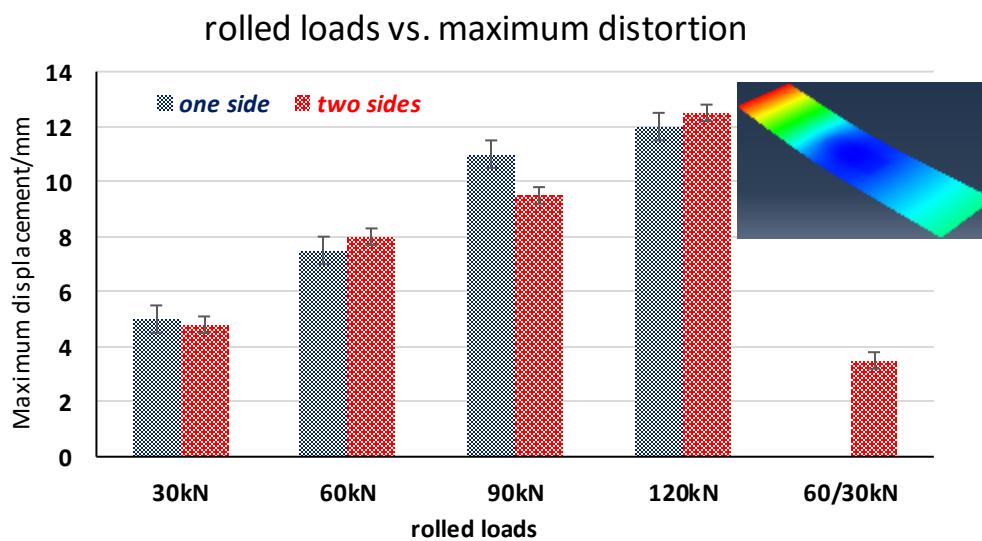
Figure 4.1 Effects on maximum distortion by applied rolling loads, results of a one-side rolling method marked in blue, ones of the two-side rolling method marked in red. Rolled samples are the AA2024-T351 sheets of CS1

In figure 4.1, the maximum distortion significantly increased with higher rolled loads. Whereas the two-side rolling method didn't significantly reduce the maximum distortion if rolled loads were the same on both surfaces. However, it is interesting to look at the result of the 60/30kN rolled sample (one surface of the sample was first rolled by the 60kN load, the opposite surface was then rolled by the 30kN load). It is observed that maximum distortion can be largely reduced if

the rolled load on the second surface is reduced by half. The applied load of 60/30kN demonstrated that this specific load application substantially lessened the maximum distortion, when compared with a single rolling load performed on one side of a specimen or the same loads applied to both sides. The results above provide notable findings to this field of research.

To further evaluate the mechanical effects of rolling loads, further results on induced residual stresses were measured using ICHD techniques. Deep surface rolling was performed on three separate samples; i) 60kN load was applied on one side, ii) 60kN load was applied on both sides, and iii) 60/30kN load was applied on both sides, respectively. Methodologies of the RS measurements are outlined in section 3.6.1. The specific measurements for CS1 and CS2 are quantified in section 4.3.1.

CS1 is initially designed to investigate the effects of applied rolling loads on distortion and magnitude of the resultant induced residual stress. Samples of CS3 were used for fatigue tests and the full scale of this residual stress study.

Distortion measurements on CS3 used the methods recorded in section 3.4. The results are demonstrated in table 4.1, where loads have been applied to both surfaces of CS3 samples, and one sample has hammer peening applied to both sides. 'Strip dimension' is defined by the rolling distance and the roller width. All deep rolled areas were rectangular; 100×20 mm (2000 mm^2). The hammer peened area was square; 20×20 mm (400 mm^2).

Table 4-1 CS3: Maximum distortion by DSR and one HP (AA2024-T351)

Rolled loads	20/10kN	30/18kN	60/15kN	HP
Max. distortion/mm	1.3	1.5~3	6~8	<1
Strip dimensions/mm^2	100×20	100×20	100×20	20×20

The maximum distortion of all measured samples was found in the CS3 samples, in those rolled with an applied load of 60/15kN. The lowest distortion of all DSR treated samples was found in those CS3 samples rolled with an applied load of 20/10kN. As the smallest treated square was generated by hammer peening, the lowest distortion of hammer peened samples was measured, to be below 1 mm.

4.2 Effects of Rolling and Hammer Peening on Microhardness

This section was motivated by an interest in the effects of strain hardening. DSR is commonly considered as a process resulting in low strain hardening [12]. However, hammer peening is categorised as a procedure causing high strain hardening treatment [110]. As far as the author is aware, no other relationship of this kind, between hardness and residual stress has been studied.

Two-directional microhardness (Vickers) was measured along the longitudinal direction and the width direction of specimens, as shown in figure 3.13 (chapter 3). All hardness was measured in the cross-section of the thickness and results of DSR and HP treated samples are shown in figure 4.2 and figure 4.3, separately. The measured hardness of the **X-Z cross-section** (perpendicular to the rolling direction, width direction) are shown in figure 4.2, and measured hardness of the **Y-Z cross-section** (parallel to rolling direction, longitudinal direction) are given in figure 4.3.
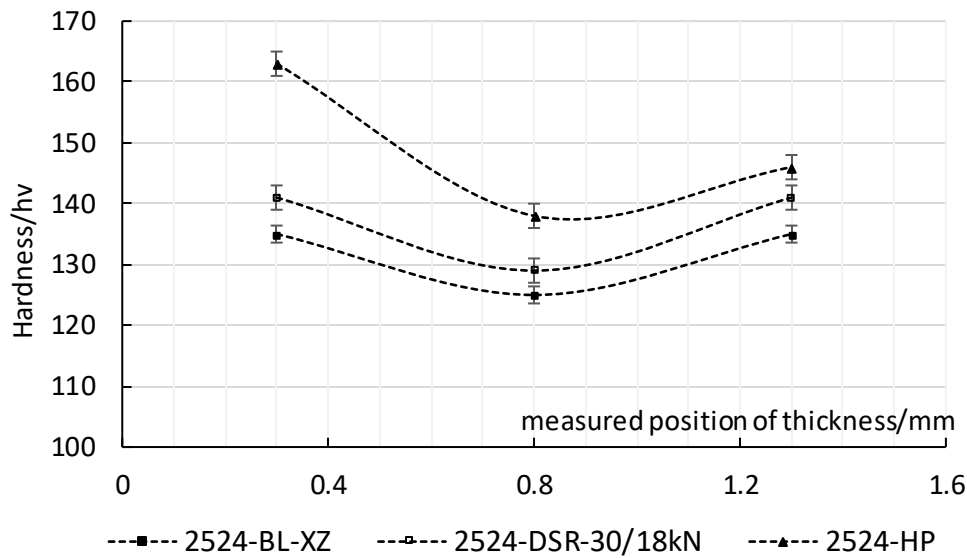
Figure 4.2 Effects of induced DSR 30/18kN and HP on microhardness of X-Z cross-section (perpendicular to rolling direction) in comparison to the baseline (BL) AA2524-T351 (see figure 3.13 of chapter 3 for measurement details)

Microhardness data showed that the hardness measurements taken at the centre of the thickness were of much lower value than the hardness measured near the surface. DSR can slightly increase the hardness in both rolling direction and perpendicular to the rolling direction. Compared with DSR specimens, the hardness values extracted from the hammer peened samples largely increased through the entire thickness, especially near the surface. Compared with measurements on untreated samples, the maximum hardness of deep rolled samples measured 141 HV near the surface, with up to 5 HV of increment. However, the maximum hardness of hammer peened samples can reach to 162 HV near the surface, with up to 26 HV of increment. More notably, there was an increase in the hardness measured in the centre of hammer peened samples, with up to 14 HV of increment.
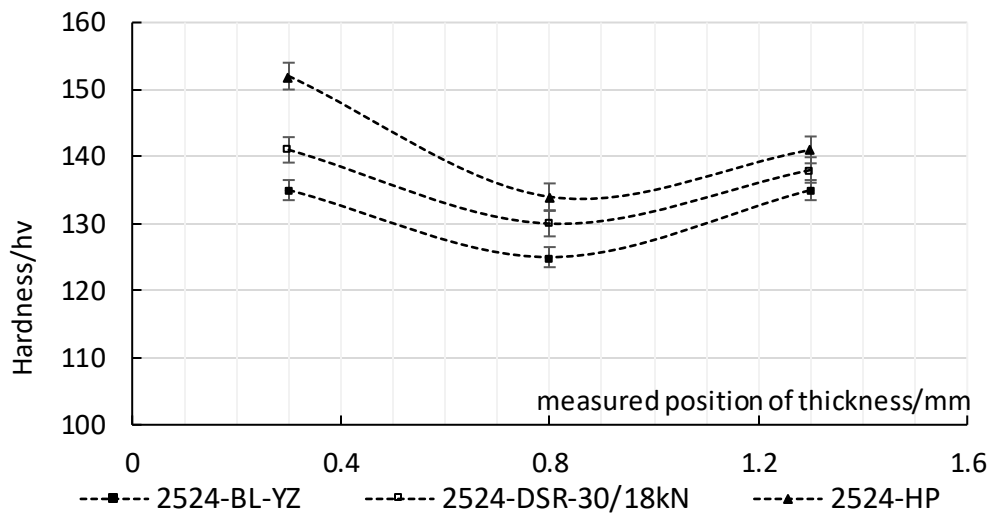
Figure 4.3 Effects of induced DSR 30/18kN and HP on microhardness of y-z cross-section (parallel to rolling direction) by comparing baseline AA2524-T351 (see figure 3.13 of chapter 3 for measurement details)

Compared with untreated samples, it was seen that the maximum hardness of deep rolled samples was 141 HV near the surface, with up to 5 HV of increment. However, the maximum hardness of hammer peened samples can reach to 152 HV near the surface, with up to 16 HV of increment. Unlike the results of figure 4.2, there was a slight increase in the hardness measured at the centre of hammer peened samples, with up to 8 HV of increment.

Therefore, it is proven that DSR treatment can slightly increase the hardness, when used as a low strain hardening method. As a novel treatment, HP can largely increase the hardness when used as a high strain hardening treatment. In most treated samples, the increment of hardness measured in near-surface locations, is greater than the increment of hardness measured at the centre of the thickness.

Matrix measurements of hardness were taken on the X-Z cross-section (perpendicular to the rolling direction, width direction) of CS3 samples. Results are given in figure 4.4.
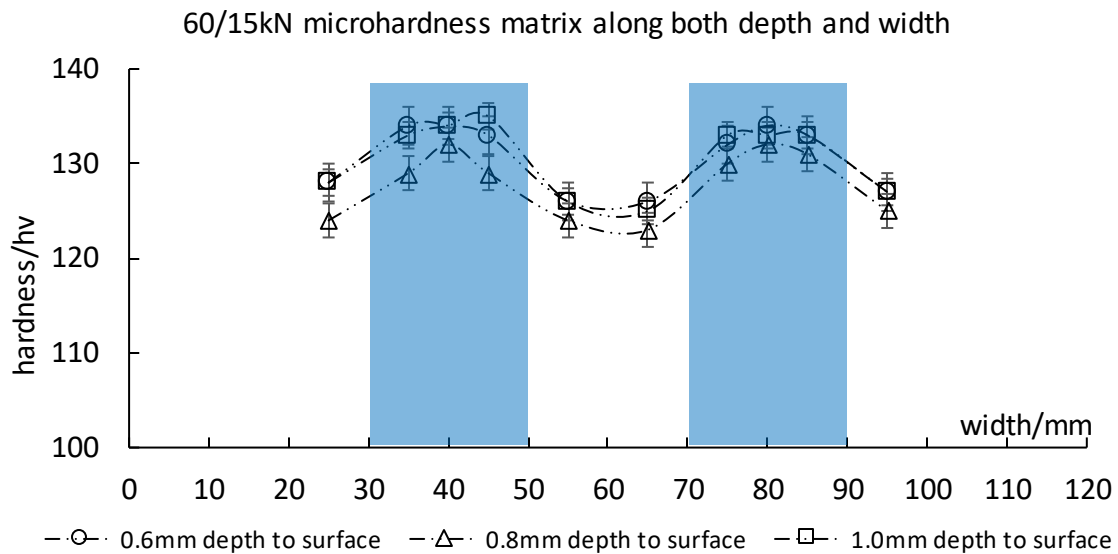
Figure 4.4 Hardness matrix bands of three measurements along thickness and bands of ten measurements along the width, CS3 of AA2524-T351

The specimen was first deep rolled using a load of 60kN on one surface, then a load of 15kN was applied to the opposite surface. The X-axis of the graph represents the full width of the deep rolled sample. The Y-axis of the graph represents the measured hardness at different depths of thickness according to increments along the width. There were ten positions marked along the width. Three measurements were taken at each position: i) at 0.6 mm depth from the top surface, ii) at the centre of the thickness, and iii) at 1.0 mm depth from the top surface.

Hardness measured in the deep rolled area increased and was greater than in the unrolled area. Similar to the results presented in figure 4.2, hardness measured in the near-surface locations were all greater than the ones measured at the centre of the thickness. The maximum hardness value extracted from the deep rolled area was measured at close to 140 HV, with up to 5 HV of increment, compared with hardness measured in the unrolled area.

4.3 Effects of DSR and HP on Residual Stresses

The distribution of residual stresses plays an important role in influencing the crack propagation behaviour. By understanding the distribution of residual stresses induced by mechanical surface treatments, optimised parameters can be determined step by step, with an aim to provide a variety of treatment options. CS1 and CS2 mainly investigated the distribution of residual stresses along the depth of a cut sample, using by the ICHD technique. In addition, experimental results of samples treated by HP were also summarised and are compared in section 4.3.2. Specimens of CS3 were exposed to modify load parameters and induced residual stresses were measured along both depth and width using *ICHD* and *Neutron Diffraction*, presented in section 4.3.1 & section 4.3.3.

4.3.1 Effects on Residual Stresses Induced by DSR

Distortion results recorded in CS1 are summarised in section 4.1. Residual stresses induced by DSR were measured along the sample thickness and are detailed below. Three samples deep rolled using three different loading parameters, were residual stress measured and the in-depth distributions are shown in figure 4.5. Notable results are presented in table 4.2. Residual stress σ_1 (parallel to the rolling direction) distribution was determined on CS1 samples rolled with a load of 60kN on a single surface, a load of 60kN on both surfaces, and two loads of 60kN and 30kN separately on both surfaces. Experimental results are shown in figure 4.5a. Residual stress σ_3 (perpendicular to the rolling direction) distribution was determined by using CS1 samples deep rolled by load parameters of 60kN on one side, 60kN on two sides and 60/30kN on two sides are shown in figure 4.5b.

CS1: σ_1 (longitudinal) residual stresses by DSR

(a)

CS1: σ_3 (transverse) residual stresses by DSR
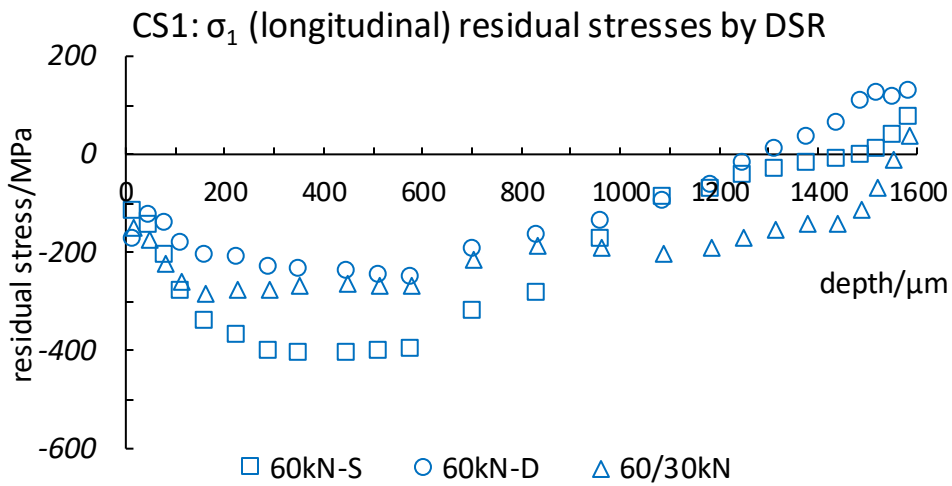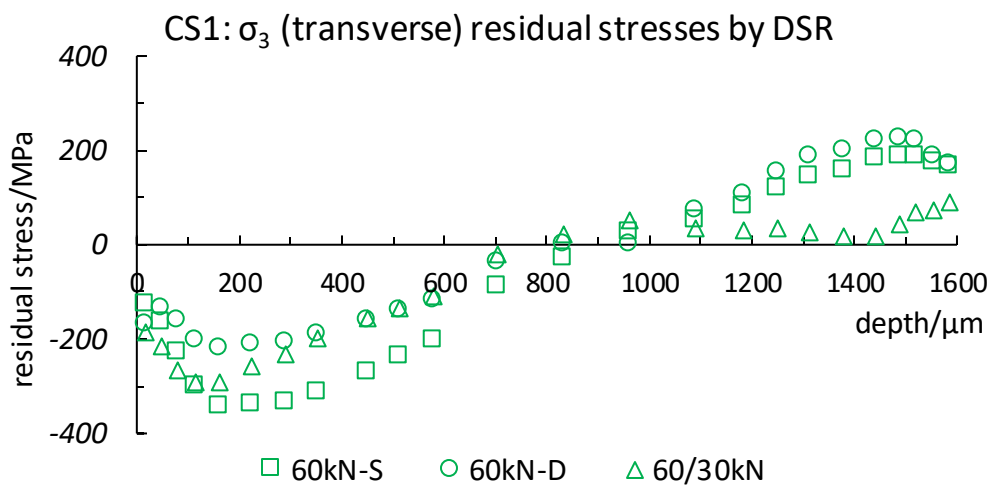
(b)

Figure 4.5 Residual stress distributions of deep rolled samples measured along the entire thickness, longitudinal distribution shown in (a); transverse distribution is shown in (b), all DSR treatment was applied on AA2024-T351 specimens of CS1

Results of CS1 sample deep rolled with a load of 60kN on a single surface showed that the highest compressive residual stresses distributed over half of the

thickness (from the initial measured surface to 800 microns of thickness). However, more tensile residual stresses were distributed along the other half of the thickness. The maximum compressive residual stress (CRS) was induced by DSR with a 60kN load applied to one side in both longitudinal and transverse directions. DSR of 60kN load on both sides caused a redistribution of residual stresses, eventually resulting in a drop in the value of the maximum of compressive residual stress over the first half of the thickness. Furthermore, the maximum value of tensile residual stress (TRS) increased in the other half of the thickness. However, if the rolling load of the other surface was reduced to half (DSR of 60/30kN load on both sides), more positive effects were observed. Firstly, although the maximum CRS resulting from rolling loads of 60/30kN was reduced in comparison with maximum CRS rolled by 60kN, either one-side rolled sample or two-side rolled sample, but the compressive range was much larger in depth. Another important finding was that the decrease of TRS in both longitudinal and transverse directions, significantly resulted in lowering the distortion, to balance the maximum CRS.

Table 4-2 Notable results from measured residual stresses

Load parameters	60kN-S	60kN-D	60/30kN-D
σ_1-Peak CRS/MPa	*406*	251	281
σ_1-Peak TRS/MPa	78	129	*40*
σ_3-Peak CRS/MPa	*340*	219	290
σ_3-Peak TRS/MPa	190	227	*89*
Averaged σ_1-RS/MPa	-212.7	-122.7	-200.0
Averaged σ_3-RS/MPa	-68.2	-14.3	-61.2

The peak value of CRS is −406 MPa (parallel to rolling direction) and −340 MPa (perpendicular to rolling direction) measured in the one-side rolled sample loaded at 60kN. The minimum value of TRS was +40 MPa (parallel to rolling direction) and +89 MPa (perpendicular to rolling direction) measured in the two-side rolled sample loaded at 60/30kN. More importantly, the averaged residual stresses of two-side rolling at 60/30kN loads, were slightly reduced when compared to those with one-side rolled at a 60kN load.

In CS1, the advantage of using 60/30kN loads was evidenced in the reduction of the maximum distortion and the averaged residual stresses tended to be compressive. CS2 further investigated the influence of load parameters on the residual stress field, where two rolled-strips were generated on one side, and another two strips were rolled on the other side using reduced loads. Three load parameters were verified, and residual stress profiles are demonstrated in figure 4.6. Due to the increase of rolled strips, the distribution of residual stresses tended to be more complex in comparison to CS1. Different to CS1, in figure 4.6a, residual stresses were not highly compressive at the very start of measurements.

Moreover, residual stresses were also not highly tensile at the very end of measurements. Induced longitudinal residual stresses of all samples presented mostly a compressive distribution. In comparison, over the three load parameters, two-side rolling 60/15kN demonstrated the advantages whether in the distribution range of compressive residual stresses or peak magnitude of compressive residual stresses. This is shown in figure 4.6a.
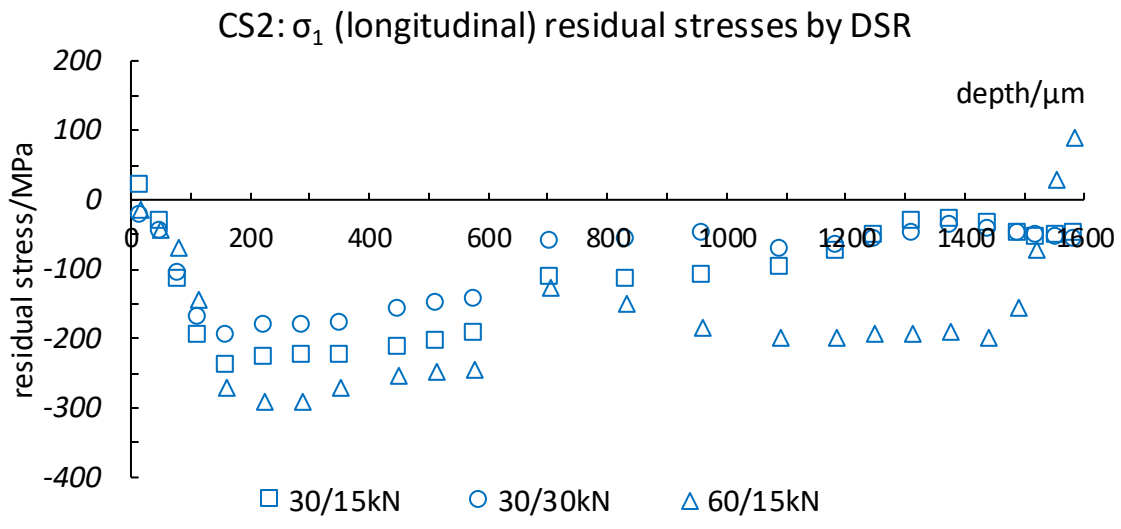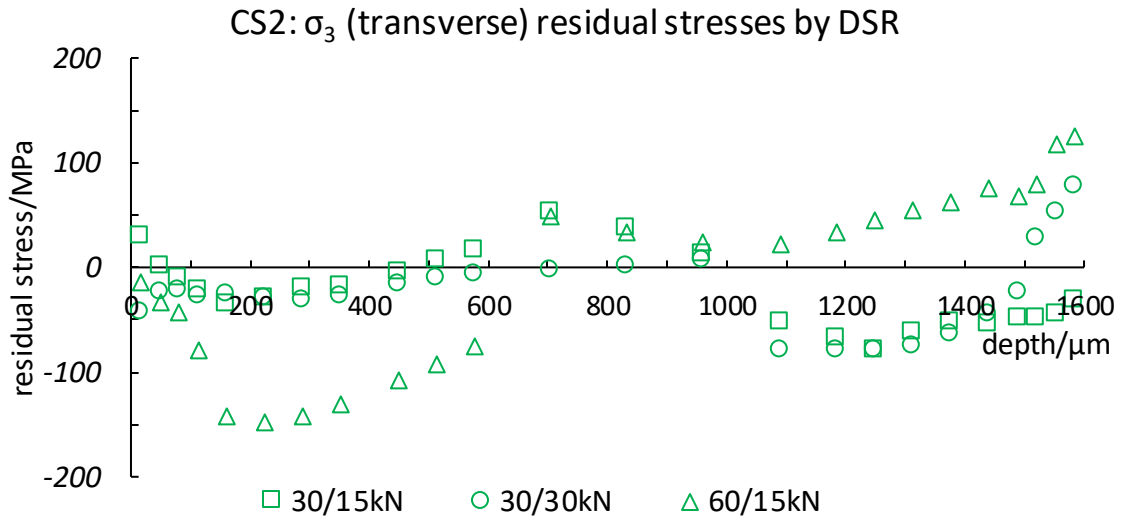
Figure 4.6 Residual stress distribution of deep rolled samples measured along the entire thickness, longitudinal distribution shown in (a); transverse distribution is shown in (b), all DSR treatment was applied on AA2024-T351 specimens of CS2

When comparing load parameters of 30/15kN and 30/30kN, the lower maximum CRS value was extracted from the rolled sample of loads 30/30kN. In addition, more tensile residual stresses (along transverse direction) were determined from the sample treated by 30/30kN loading. DSR samples at loading 30/15kN provided relatively smaller compression along the rolling direction and higher tension than in DSR samples of loads 60/15kN. As a result, DSR loads of 30/15kN applied on two sides can provide a better solution if compromising on the distortion. DSR loads of 60/15kN applied on two sides may give the best stress state for fatigue resistance.

4.3.2 Effects on Residual Stresses Induced by HP

Apart from deep surface rolling treatments, another novel treatment of hammer peening was also applied in this research. Two different parameters of the hammer peening treatment (low density and high density as presented in table 4.3) were applied, and residual stresses of HP-treated CS2 samples were measured by ICHD, as shown in figure 4.7.

Table 4-3 Parameters of hammer peening applied on CS2 samples

	Ball diameter (**D**)	Frequency (**f**)	Travel speed (**TS**)	Interval step (**S**)
Low density of HP	8 mm	220 Hz	100 mm/s	0.4 mm
High density of HP	8 mm	220 Hz	50 mm/s	0.2 mm

As an alternative treatment in this research, this prototype has not been used to treat aluminium alloys. In this stage, only two peening parameters were applied, and limited results are presented. Residual stresses were measured by the same method as presented in the previous section. These two peening parameters were used to treat those CS3 samples employed for fatigue tests as well.

CS2: σ_1 (longitudinal) residual stresses by HP

(a)

CS2: σ_3 (transverse) residual stresses by HP
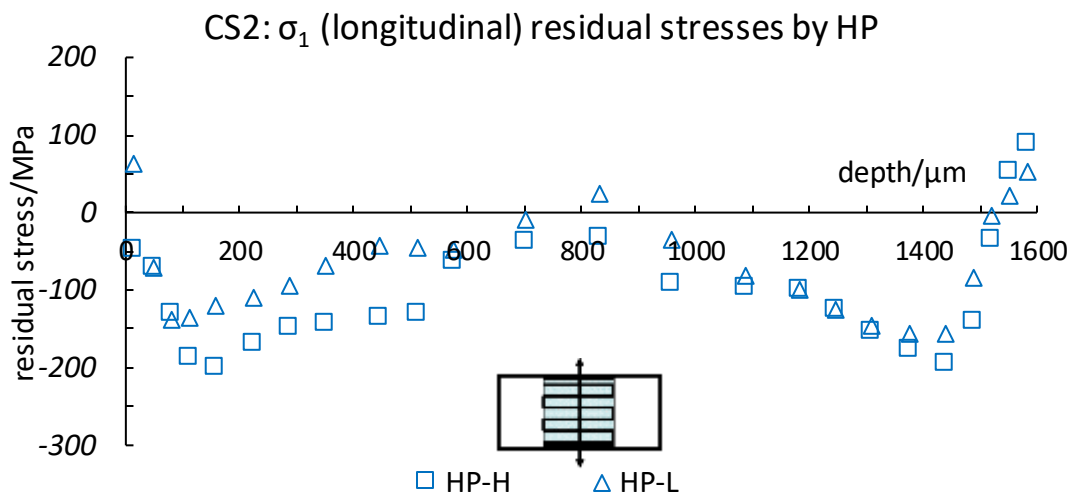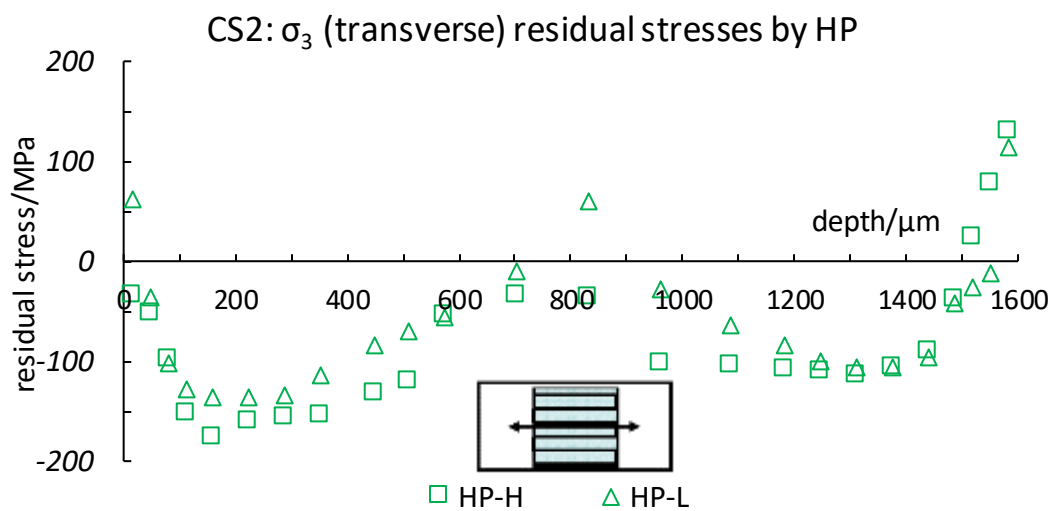
(b)

Figure 4.7 Residual stress distribution of hammer peened samples measured along the entire thickness, longitudinal distribution shown in (a); transverse distribution shown in (b)

Comparing residual stress profiles induced by DSR, the results of hammer peened samples have a more symmetric distribution along the centreline of

thickness. The maximum compressive residual stresses were located 150-microns depth from the surface. Residual stress values decreased to nearly 0 MPa in the middle of the thickness. Both surfaces of the samples were hammer peened, and measurements taken from the opposite surface showed the same tendency. The biggest differences between hammer peened, and DSR samples were observed in the induced RS distribution of σ_3 (transverse). In DSR samples, the σ_3 field demonstrated that compressive residual stress and tensile residual stress were mostly equally distributed along the thickness. Compressive residual stresses were induced in the first half of the cross-sectioned thickness, whereas tensile residual stresses were generated in the rest of the thickness. However, residual stresses induced in peened samples demonstrated that there was a clear tensile RS field very close to the sample surfaces (up to 100 microns). This phenomenon can be clearly identified on one surface. The rest of the region was full of compressive residual stresses. The average magnitude of compressive RS value was around 200MPa, as similar as σ_1 (figure 4.7b).

4.3.3 Neutron Diffraction (ND)

The method of residual stress measurements evaluated by using neutron diffraction is schematically shown in figure 4.8. The measured section is marked in red along the width direction. The three-dimensional residual strain was measured, ε_{hoop}, ε_{axial}, ε_{radial}. Strain components were determined from the full range of neutron diffraction data. For plane stress conditions, a triaxial situation of stress and strain can be calculated using a simplified method (presented in section 3.6.2). As a result, σ_{hoop} (σ_1 along Y-axis, parallel to the rolling direction) and σ_{axial} (σ_3 along X-axis, perpendicular to the rolling direction) were calculated in order to demonstrate the residual stress distributions.
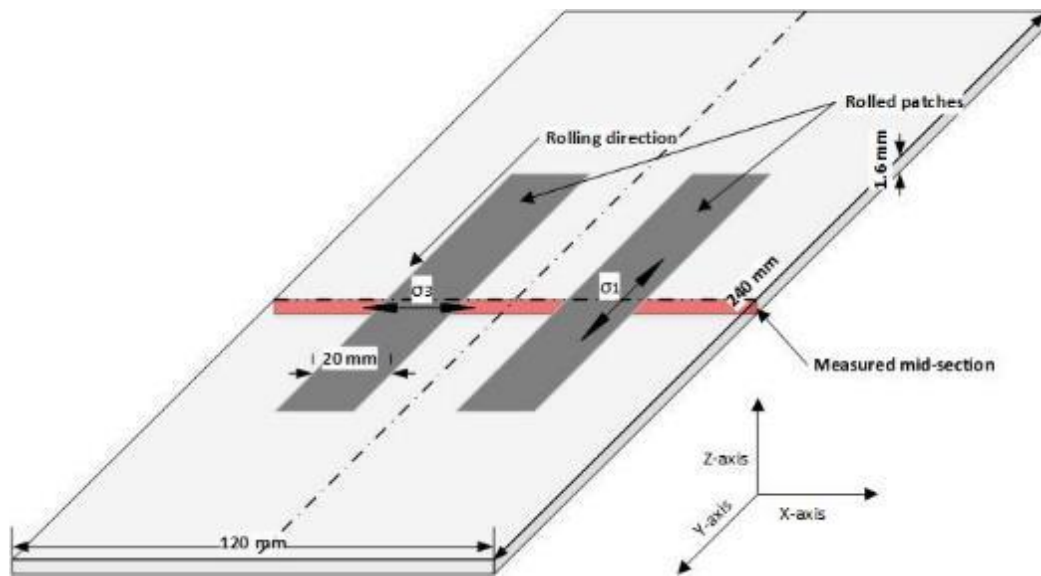
Figure 4.8 Schematic illustration of residual stress measurements by Neutron Diffraction, non-centre-slit sample of CS3

Measurements of induced residual stress by DSR were taken from the middle cross-section (marked by a red rectangular shape). The rolled patches are marked in dark grey and are symmetrically positioned across the width centreline.

Two different load parameters were applied to un-slited specimens (geometry of CS3), which were 60/15kN and 20/10kN. Then, residual stress profiles of deep rolled samples were calculated by the use of modified functions (simplified by plane stress conditions).

Surface diagrams are shown in figure 4.9 and 4.10 using three-dimensional data (position in thickness, location in width, residual stress). Figure 4.9 presents the surface diagram of the deep rolled sample using loads 60/15kN. Figure 4.9a gives a three-dimensional surface depicting residual stress distributions parallel to the rolling direction. Figure 4.9b gives a three-dimensional surface depending on residual stress distributions perpendicular to the rolling direction. The same surface diagram is given in figure 4.10, which describes the effects on residual stress fields of using a lower load parameter 20/10kN.

60/15kN σ1-residual stress distribution of centre cross-section

(a)

60/15kN σ3-residual stress distribution of centre cross-section
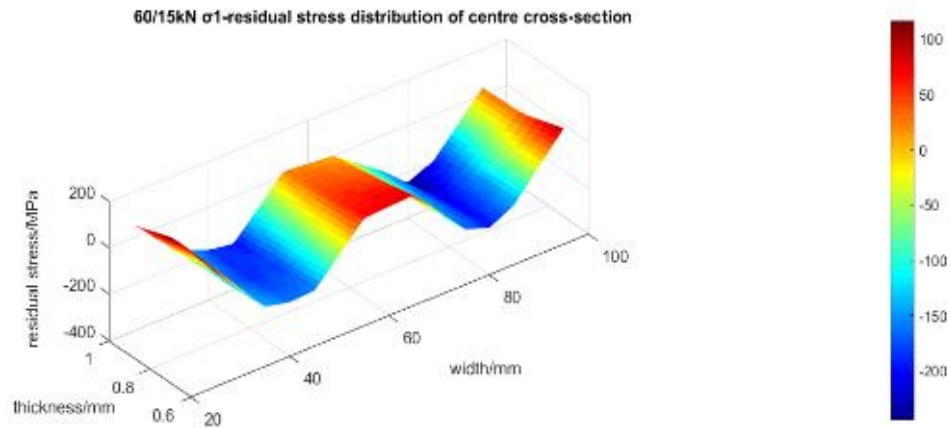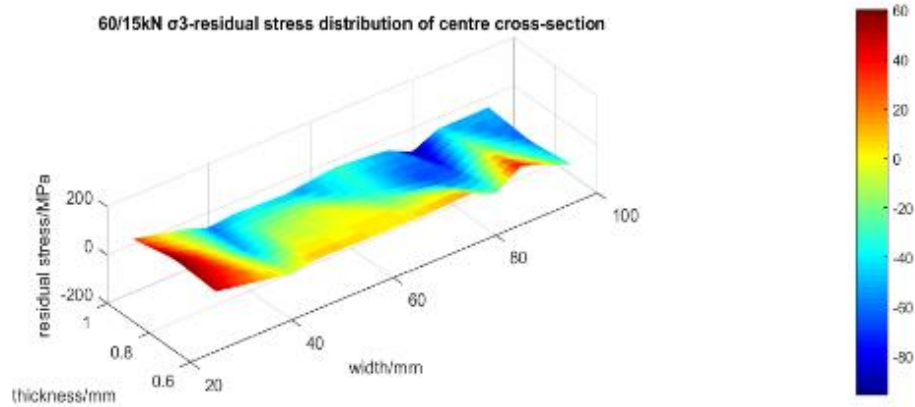
(b)

Figure 4.9 A three-dimensional surface plot of DSR of the load parameter 60/15kN AA2524-T351 sheets. *a.* **Residual stress σ_1 distribution of mid cross-section.** *b.* **Residual stress σ_3 distribution of mid cross-section**

Along the width of the cross-section (y-axis), the deep rolled area was occupied by high compressive residual stresses uniformly distributed along the thickness. Tensile residual stresses were distributed outside of the rolled area. The

maximum value of compressive residual stress could be over 200 MPa. The largest value of tensile residual stress was around 100 MPa found at the centre of the cross-section and outside of the rolled patches 40 mm away from the centre.

The residual stress field of σ_3 (transverse direction) in figure 4.9b shows a significant difference to the σ_1 distribution (longitudinal direction). The deep rolled area showed that the existence of compressive residual stresses there, was not uniformly distributed along the thickness. Residual stress presented as being more compressive nearer one side than the other side. High tensile residual stress was found at around the 20 mm mark of the width. The maximum value of compressive residual stress was around 80 MPa, whilst the maximum value of tensile residual stress was about 60 MPa. Compared to the σ_1 field shown in figure 4.9a, the residual stress field of σ_3 demonstrated that compressive residual stress and tensile residual stress were at slightly below or above 0 MPa.

Figure 4.10 demonstrates the residual stress fields of σ_1 and σ_3 induced by DSR of a load parameter 20/10kN. In figure 4.10a, along with the width of the cross-section (y-axis), similar results were summarised. High compressive residual stress was generated within the rolled area. High tensile residual stress was found near the centre and 10 mm away from the rolled area. The maximum value of compressive residual stress was over 150 MPa. The highest tensile residual stress was only up to 50 MPa.

The residual stress field of σ_3 (transverse direction) in figure 4.10b again shows a significant difference to the σ_1 distribution (longitudinal direction). The largest area that presented compressive stress was on one side of the width, and the maximum value of compressive stress was around 60 MPa. On the other side of the width, a tensile residual stress field was revealed, and the maximum tensile residual stress measured was up to 40 MPa.

In figure 4.10a, there indicates a higher compressive residual stress field generated at around 80 mm. The residual stress field of σ_3 demonstrated similar

behaviour at 80 mm across the width, where higher compressive residual stress was induced.
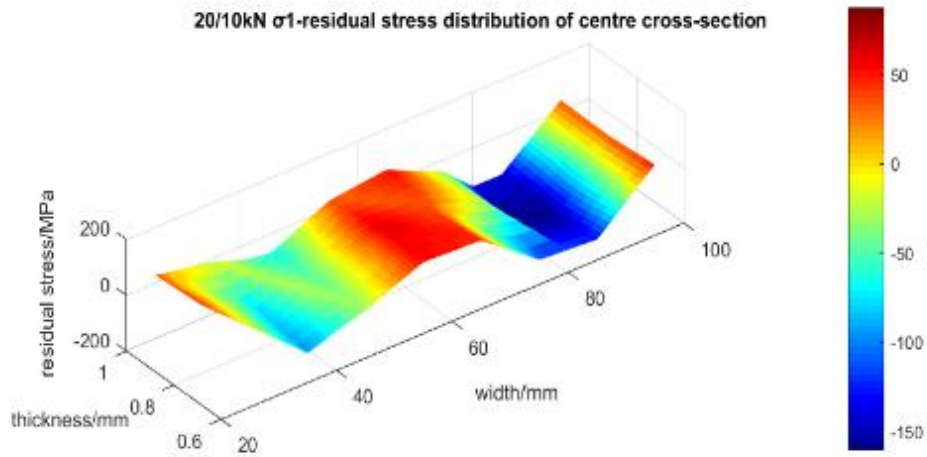
(a)
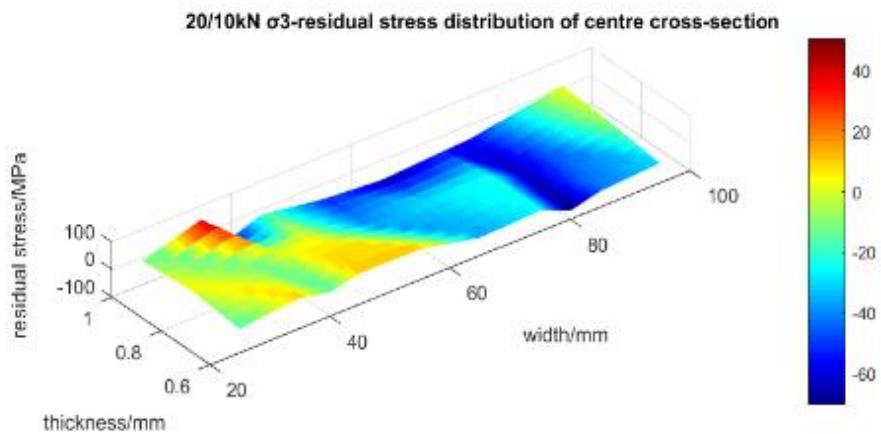
(b)

Figure 4.10 A three-dimensional surface plot of DSR of the load parameter 20/10kN AA2524-T351 sheets. *a.* Residual stress σ_1 distribution of mid cross-section. *b.* Residual stress σ_3 distribution of mid cross-section

4.4 Tension-Tension Fatigue Tests

The tension-tension fatigue test procedures were described in section 3.7. Treated parameters and descriptions are detailed in table 4.4 with the results shown in table 4.5. CS3 showed the geometry of testing samples and an 8 mm centre-slit was inserted in the middle of the sample using EDM (electrical discharge machining). Baselines without any treatments were tested three times. A summary of fatigue lives and critical fatigue crack lengths of all tested samples are presented in table 4.5.

Table 4-4 Description of tension-tension fatigue tests

Treated parameters	Test Description	
T01: Baseline	2024-T351, L/LT	
T02: Baseline	2524-T351, L/LT	
T03: DSR (20/10kN)	2024-T351, 10 mm to slit centre (LT); 100 mm × 20 mm (rolled strip)	
T04: DSR (30/18kN)	2024-T351, 10 mm to slit centre (L); 100 mm × 20 mm (rolled strip)	
T05: DSR (30/18kN)	2024-T351, 10 mm to slit centre (LT); 100 mm × 20 mm (rolled strip)	
T06: DSR (30/18kN)	2024−T351, 10mm to slit centre (45°) (LT); 100 mm × 20 mm (rolled strip)	
T07: DSR (30/18kN)	2024−T351, 10mm to slit centre (45°) (LT); 100 mm × 20 mm (rolled strip)	
T08: DSR (30/18kN)	2024-T351, 10 mm to slit centre, half rolled width (LT); 70 mm × 10 mm (rolled strip)	
T09: DSR (60/15kN)	2024-T351, 10 mm to slit centre (LT); 100 mm × 20 mm (rolled strip)	
T10: DSR (30/18kN)	2524-T351, 10 mm to slit centre; 100 mm × 20 mm (rolled strip)	
T11: DSR (30/18kN)	2524-T351, covered the slit; 100 mm × 20 mm (rolled strip)	
T12: DSR (60/15kN)	2524-T351, 10 mm to slit centre; 100 mm × 20 mm (rolled strip)	
T13: DSR (60/15kN)	2524-T351, 10 mm to slit centre; 50 mm × 20 mm (rolled strip)	
T14: DSR (60/15kN)	2524-T351, 20 mm to slit centre; 100 mm × 20 mm (rolled strip)	
T15: DSR (60/15kN)	2524-T351, 25 mm to slit centre; 100 mm × 20 mm (rolled strip)	
T16: DSR (60/15kN)	2524-T351, 20 mm to slit centre, $R=-0.1$; 100 mm × 20 mm (rolled strip)	
T17: HP (lower)	2524-T351, 10 mm to slit centre; 20 mm × 20 mm (peened patch)	
T18: HP (higher)	2524-T351, 10 mm to slit centre; 20 mm × 20 mm (peened patch)	

Table 4-5 Tension-tension fatigue test results

Test No.	Fatigue cycles	Critical fatigue crack length/mm	% Change in CFCL	Life improvement factor (LIF)
T01	47,492; 53,110; 50,368 (L) 48,916; 47,652 (LT)	39~41	n/a	n/a
T02	61,556; 63,786; 63,770 (L) 54,820; 56,996 (LT)	40~42	n/a	n/a
T03	63,410	40	n/a	1.3
T04	123,232; 303,520	~28	-30	2.4; 6.0
T05	97,696; 315,856	~28	-30	2.0; 6.5
T06	72,640	35	-12.5	1.5
T07	66,464	32	-20	1.4
T08	436,800	16	-60	9.0
T09	416,128; 947,904	22	-45	8.6; 20.0
T10	123,572; 129,509	38	5	2.0
T11	>1,409,502 (runout)	n/a	n/a	>24 runout
T12	429,274; 507,449	38	5	6.8; 8.0
T13	231,520; 281,216	22	45	3.7; 4.5
T14	42,574; 44,568	40	No change	0.7
T15	34,362; 34,514	40	No change	0.55
T16	74,720; 74,824	40	No change	1.2
T17	91,010; 108,964	35	-12.5	1.4; 1.7

4.5 Results of Fatigue Tests

In this section, fatigue growths of cracks on baseline untreated samples are demonstrated in figure 4.11 graph exhibiting the crack length against the number of cycles.
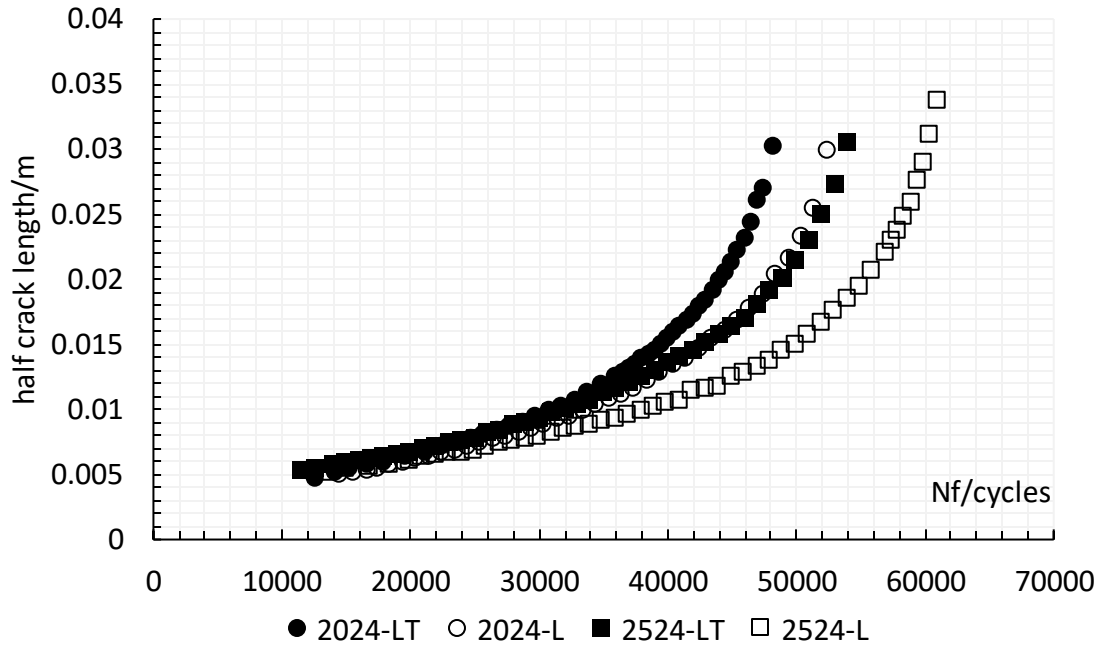
Figure 4.11 Measured crack length against the number of cycles of baselines (AA2024-T351 L/LT and AA2524-T351 L/LT)

Fatigue results of untreated samples AA2024-T351 and AA2524-T351 are shown in figure 4.11, which show the original fatigue crack data measured by an optical microscope against the number of cycles. Fatigue crack growth rates of untreated samples were calculated using the secant method detailed in ASTM E647 [188]. Stress-intensity factor ranges (ΔK) of untreated samples were further calculated by the geometry factor method shown in ASTM E647 [188]. The FCGRs of untreated samples against ΔK are presented in figure 4.12.
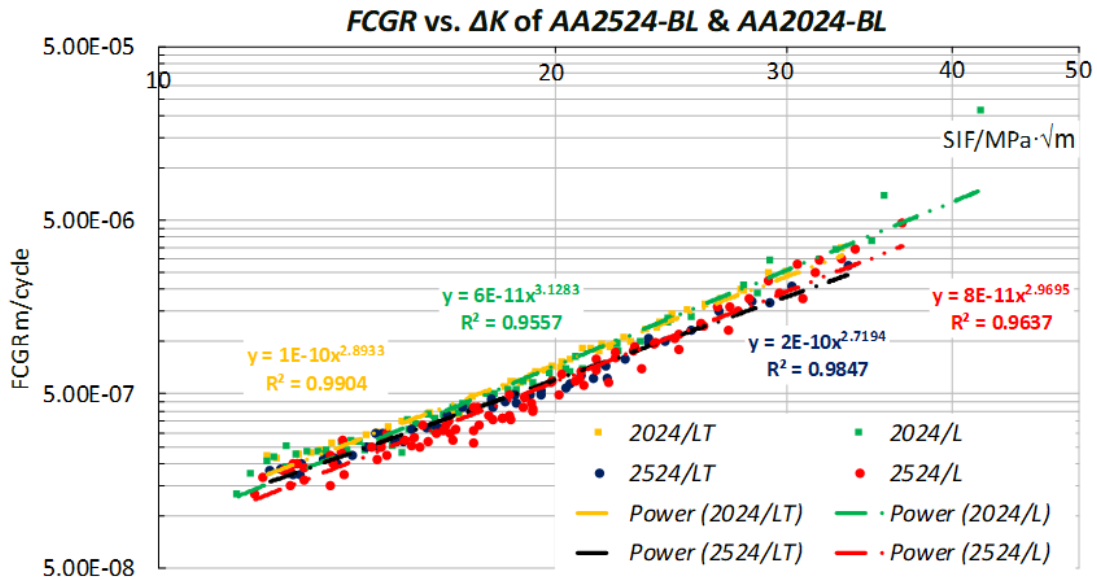
Figure 4.12 Fatigue crack growth rates of baselines (AA2524-T351 of L/LT & AA2024-T351 of L/LT) against ΔK [188]

Results in figure 4.12 show that there is no significant difference between untreated samples of AA2024 and AA2524 on FCGR. Power law was applied to the results of FCGR against SIF, which was used to determine the material constants of Paris law (equation 2.4). The material constants for the 2024-T351 plate and sheet from NASMAT material database [189] were used where C = 4.8 $\times 10^{-11}$, m = 3.2. Compared to NASMAT, obtained constants of AA2024-T351 in figure 4.12 are valid and able to be used for further mathematic models in chapter 6. Baptista [190] reported the Paris constants of AA2524-T351 (LT) by using the crack closure theory, resulting in C = 9.16×10^{-10}, n = 2.33. The linear fitting coefficient of correlation R^2 was 0.959. The Paris constants of AA2524-T351 (LT) in figure 4.12 by using the crack closure theory were calculated, C = 9.0×10^{-10}, n = 2.72, and the linear fitting coefficient of correlation R^2 = 0.9847.

Fatigue tests of deep rolled samples by 30/18kN and 60/15kN were conducted, and raw results are shown in figure 4.13a, the crack length of the half-width measured by optical microscope against the number of cycles. Figure 4.13b plotted the calculated FCGRs against the crack length of the half-width.
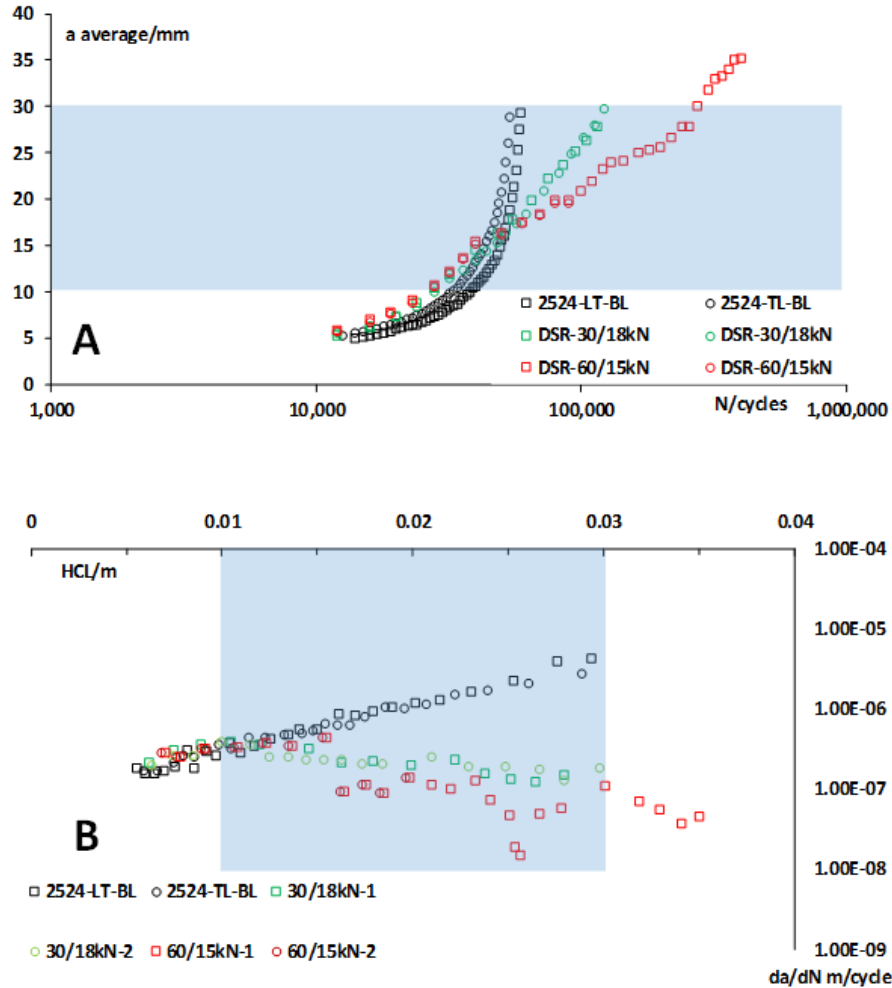
Figure 4.13 (A) Measured crack length against the number of cycles of deep rolled samples by 30/18kN and 60/15kN, (B) FCGRs of DSR samples in comparison to untreated samples, deep rolled area shaded in blue

FCGRs of deep rolled samples were lower than untreated samples. Moreover, treated samples using 60/15kN loads showed that the lowest value of FCGR found at 25mm away to the centreline of the sample, as well as 30/18kN shown.

Fatigue tests of deep rolled samples by 30/18kN and 60/15kN were conducted, and raw results are shown in figure 4.13a, the crack length of the half-width measured by optical microscope against the number of cycles. Figure 4.13b plotted the calculated FCGRs against the crack length of the half-width.
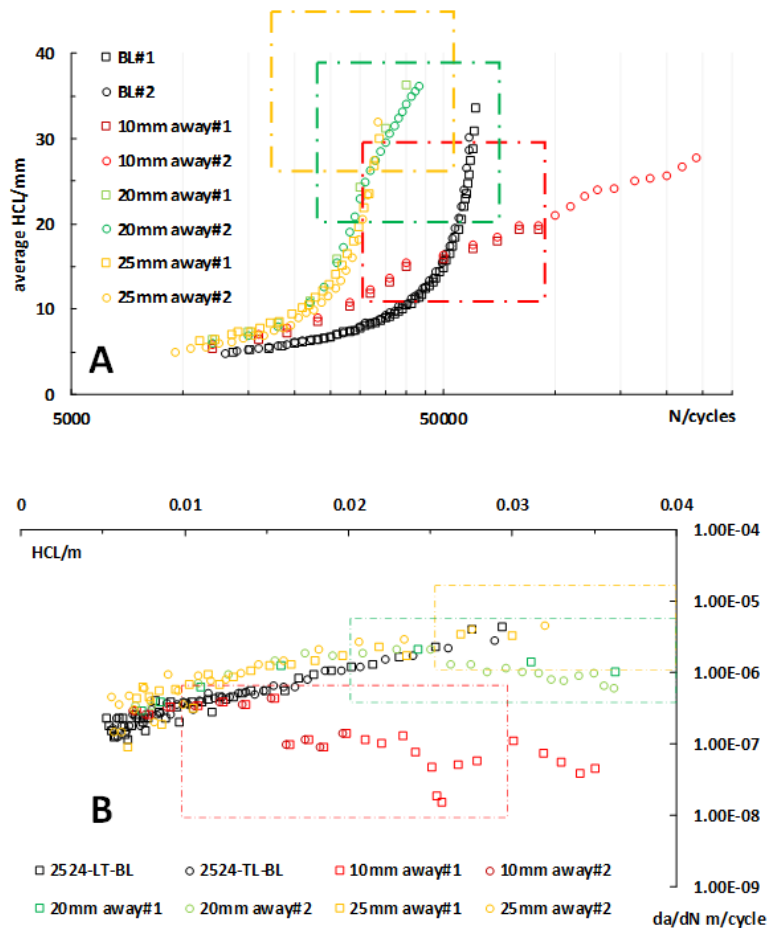
Figure 4.14 (A) Measured crack length against the number of cycles of deep rolled samples using the same loads 60/15kN, different rolled locations (10mm, 20mm, 25mm away from the centreline), (B) FCGRs of DSR samples in comparison to untreated samples, dashed squares in red, green and yellow present different rolled strips

In figure 4.14b, FCGRs of deep rolled samples increased as the deep rolled areas were moving away from the centreline.

FCGR results of other DSR samples and HP samples are given in Appendix A.

4.6 Fatigue Crack Trajectories Reports

Besides the results above, fatigue crack trajectories are reported in this section. To account for the effects of loads changing, angles changing between rolling direction and width direction (centre-slit), and roller position changing the behaviours of crack propagation trajectories are captured in figure 4.15.
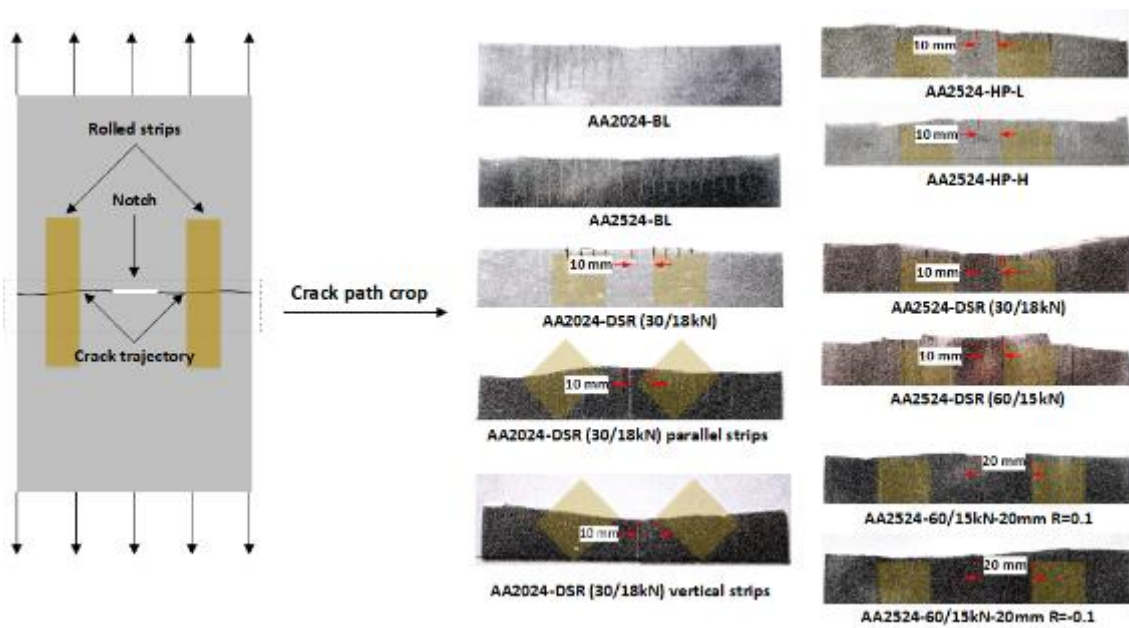
Figure 4.15 The demonstration of fatigue crack trajectories include BL, DSR-treated and Hammer peened samples

Results of figure 4.15 demonstrated that different DSR influenced the crack paths. Fatigue cracks of untreated samples propagated straightly from the start of the slit-end. Crack paths of other treated samples were slightly or largely influenced.

Crack paths of two deep rolled samples, *AA2024-DSR (30/18kN)* **parallel** *strips* and *AA2024-DSR (30/18kN)* **vertical** *strips*, showed the opposite propagation behaviours.

Because of the limited samples, statistical analysis on crack trajectories and their relationship with induced residual stress fields are not addressed in this research. Other discussions of crack paths are given in chapter 7.

The fatigue crack growth was measured and read from scratch lines under the travelling-microscope. The striations of the fracture surface were further observed by SEM. The fatigue crack growth rate was calculated by both methods and compared in figure 4.16.
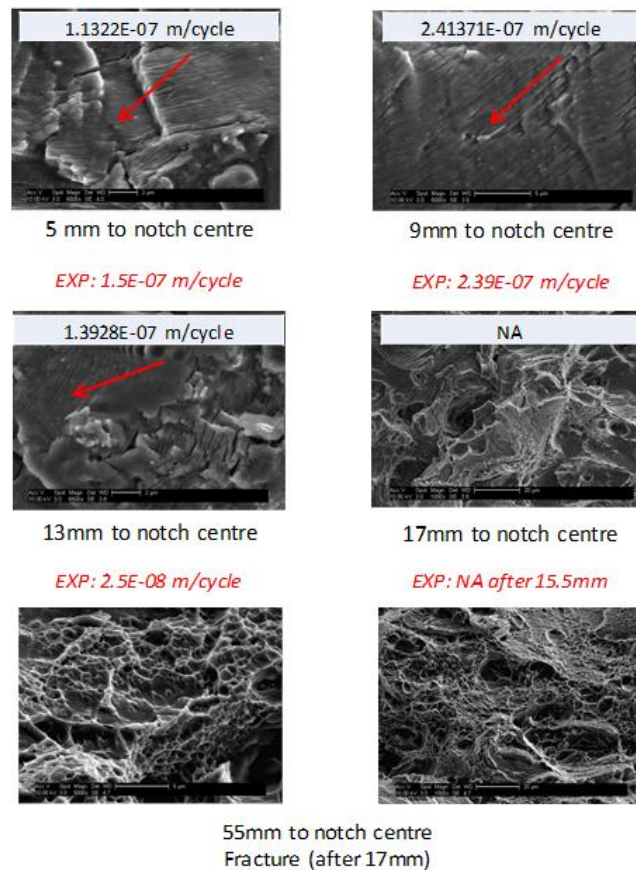
Figure 4.16 Striations measured by SEM, six measured positions (5mm, 9mm, 13mm, 17mm and 55mm) along the width (crack growth direction)

During fatigue tests, fatigue cracks were observed along the surface rolled by the 30kN load, and measured by the travelling microscope. In figure 4.16, measurements of striation spacing were taken close to the surface rolled by the 30kN load as well. The fatigue crack growth rates calculated by both methods show a good agreement in general.

5 Finite Element Simulation of Deep Surface Rolling Process

Finite element analysis (FEA), in this research, enables the prediction of the residual stress fields and the distortion under specific rolling loads. The deep rolling process, conforming to the experimental operation, was modelled in Abaqus. Section 5.1 introduces a description of, and the development of, modelling deep rolling of a material surface. Definitions of material properties and common characteristics are determined in section 5.2. DSR procedures and boundary conditions are illustrated step by step in section 5.3. Results of DSR FE models are summarised in section 5.4. Finally, a general conclusion is given in section 5.5.

5.1 Introduction of FE-DSR Model

There have been numerous studies of DSR and other similar processes in the literature, and these studies can be broadly classified into experimental, analytical, and numerical studies. Previous studies have tended to use surface roughness, surface hardness, or residual stress as response parameters. These investigations examined the global effect of the process instead of its mechanics.

The only hard contact interaction in the process is between the hydrostatically suspended ball and the component surface, leading to three-dimensional Hertzian stress patterns around the contact [149]. This concept was applied in early FE modelling (FEM) of the DCR process where it was demonstrated that the relationship between the force applied on the tool and the penetration depth was more dependent on the tool geometry rather than on material properties [149]. This finding was achieved by focusing on the contact mechanics between the ball and the workpiece.

Earlier models focused more on the use of two-dimensional modelling, due to its reduced cost and its ability to capture the effects of the key parameters of the

DSR process. These two-dimensional models however, were unable to accurately predict residual stresses in the axial (perpendicular to rolling) direction and the near-surface regions [118]. Another tested method utilised microscale FE models, which through the use of mathematical algorithms and assumptions, were able to map macroscale FE models [118].

With advancing technology and computational power becoming increasingly accessible, there are new studies looking into the mechanics of the DSR process through implementing experiments and three-dimensional FEM. It was observed that the formation and flow of a material ridge around the burnishing element, caused deformation on the component surface along a single burnished track [191]. It was reported that the FE model of DSR showed good correlation to the experimental residual stress data. As a result, FE analysis is capable of capturing the effect of the DSR process [118,149,176].

Previous studies have mainly focused on the mechanics of the DSR process. Due to the insufficient study of residual stress distributions, there was a need to investigate an FE model that would simulate this process and map the residual stress distributions in either microscale or macroscale. Understanding the residual stress distribution is especially important in the case of components in service, whilst the balancing of tensile residual stresses plays a critical role in leading the components to fail prematurely.

5.2 Methodology

The models here are based on the experimental process as referred to by Coules et al. [118]. The deep surface rolling models were built with Abaqus Standard version 6.14. The models consist of four main successive steps, loading, rolling, roller lift-up and unclamping. Samples were continuously clamped during the first three steps.

There were three types of models. In the first, the rolling simulation model of CS1 was built, and then the results of distortion and residual stress were compared to experimental measurements. The effects of distortion and residual stress profiles were simulated by the second model, of the un-slited samples of CS3. The third model investigated the distortion and three-dimensional residual stress distribution of centre-slit samples of CS3.

Figure 5.1a describes the setup of the CS1 DSR model including sample geometry and roller dimensions.
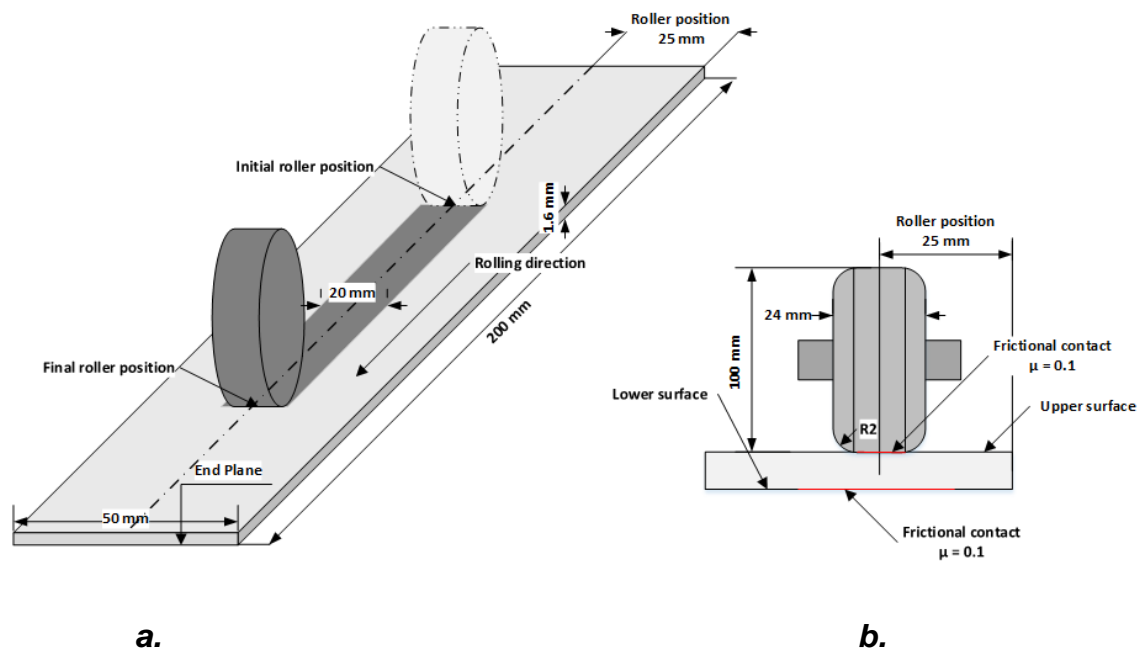
Figure 5.1 *a*. The schematic representation of CS1 rolling. *b*. Roller dimensions and position when rolling the upper surface

The roller was modelled as a rigid body, so it did not undergo any deformation. Only one roller was used in all the analyses. The dimensions are shown in figure 5.1*b*. In CS3, the diameter of the roller was 200 mm, and the width of contact was 20 mm. The rolling speed was 400 mm·min⁻¹, and no torque was applied on the

roller to drive it. Instead, a uniform translation was imposed on the roller axis, and the roller rotation only occurred when there was friction interaction with the sheet.

5.2.1 Material Characteristics

AA2024-T351 is used in the non-linear kinematic hardening simulation. Tension tests of 2024-T351 aluminium alloy specimens were reported in section 3.1. Through the developed method reported in [192], the initial kinematic hardening modulus C and the coefficient γ were accounted for, in order to define the non-linear kinematic hardening of 2024-T351 aluminium alloys.

Mechanical properties of 2024-T351 aluminium alloys were given In table 5.1 [180,192].

Table 5-1 Mechanical properties of AA2024-T351 presented in this research

Density, kg/m^3	Young's Modulus, GPa	Poisson's ratio	$\sigma|_{0,true}$, MPa	C, MPa	γ
2780	73	0.33	369.47	2447.66	10

Isotropic hardening was used and compared with the kinematic hardening. The equivalent plastic strain and stress were obtained from the tensile tests of AA2024-T351, as reported in section 3.1.

5.2.2 Common Characteristics

Hexahedral elements were used principally for the rolling models. The aluminium alloy sheets were represented by the eight-node linear brick element, hybrid formulated with reduced integration points. The number of elements, nodes and Abaqus element types, are reported in table 5.2. The element size L×W×T (mm) of low density mesh was 2×1×0.16 (mm). The element size L×W×T (mm) of high density mesh was 1×1×0.1 (mm).

Table 5-2 Element and node distribution

Model Type	Hex elements	Nodes	Element Type
CS1	50000	56661	Hex.Linear (C3D8R)
CS3 without slit	72000	81191	Hex.Linear (C3D8R)
CS3 with centre-slit	404920	451836	Hex.Linear (C3D8R)

A typical mesh used is shown in figure 5.2. It shows the variation of the mesh density across the longitudinal direction. In general, the denser mesh was implemented near the centre width, and on areas where rolling was applied.
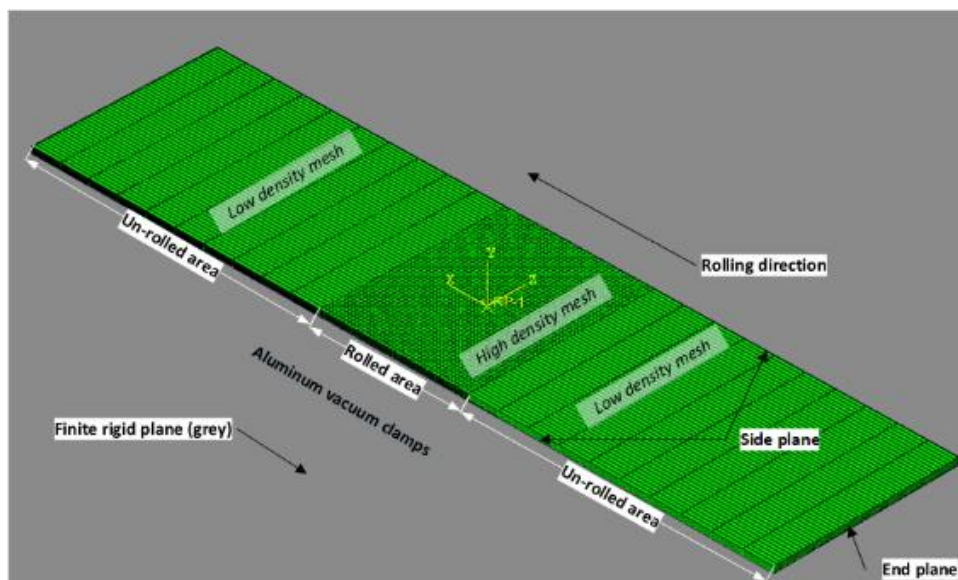
Figure 5.2 Example of different mesh density through the sheet of CS1 (element types: C3D8R)

The high-density mesh was used to capture the characteristic stress concentration of this region.

5.3 Descriptions of DSR Models

In this section, stages of the DSR processes, along with boundary conditions, are detailed. In section 5.3.1, DSR processes performed on one side are described. Boundary conditions and interaction properties follow in section 5.3.2. The strategy of two-sided DSR is illustrated in section 5.3.3. The final section explains the models of CS3 accounting for the effects of the centre-slit.

5.3.1 Steps of One-Side DSR Processes

DSR processes were assumed to be quasi-static, and hence, an implicit Newtonian solver was used (*ABAQUS/STANDARD*). The large rotations and displacements are enabled by allowing the software to account for geometric nonlinearity, which takes higher order terms into account when determining strains and stresses [118].

The first step, loading (indentation), represents the roller gaining the first contact and reaching a steady state until fully loaded, as shown in figure 5.3a. In this step, the concentrated force through the centre ref-point of the roller tool is ramped up to the constant value. This force causes a contact interaction between the flat roller and the upper surface of the aluminium alloy sheet. The depth of indentation is eventually reached when the roller and the plastically deformed workpiece reach the equilibrium state.

This is followed by a series of simulation steps, consisting of the rolling process step shown in figure 5.3b, whereby the roller is rotated when there is friction interaction between the roller and the upper surface of workpieces, the lift-up roller step in figure 5.3c, where the roller moves up, followed by the final unclamping step in figure 5.3d. It is noticed that the clamping system is applied to the first three steps.

The steps are illustrated in figure 5.3, where U1, U2 and U3 represent the displacement in the x, y, and z directions and UR1, UR2, and UR3 represent the

rotations about the x, y, and z-axes. The x, y, and z directions correspond to the longitudinal direction – parallel to the rolling direction, the depth direction – normal to the sheet surface, and the transverse direction – perpendicular to the rolling direction, respectively.

a. Loading step (indentation)

b. Rolling process

c. Lift up roller

d. Unclamping step
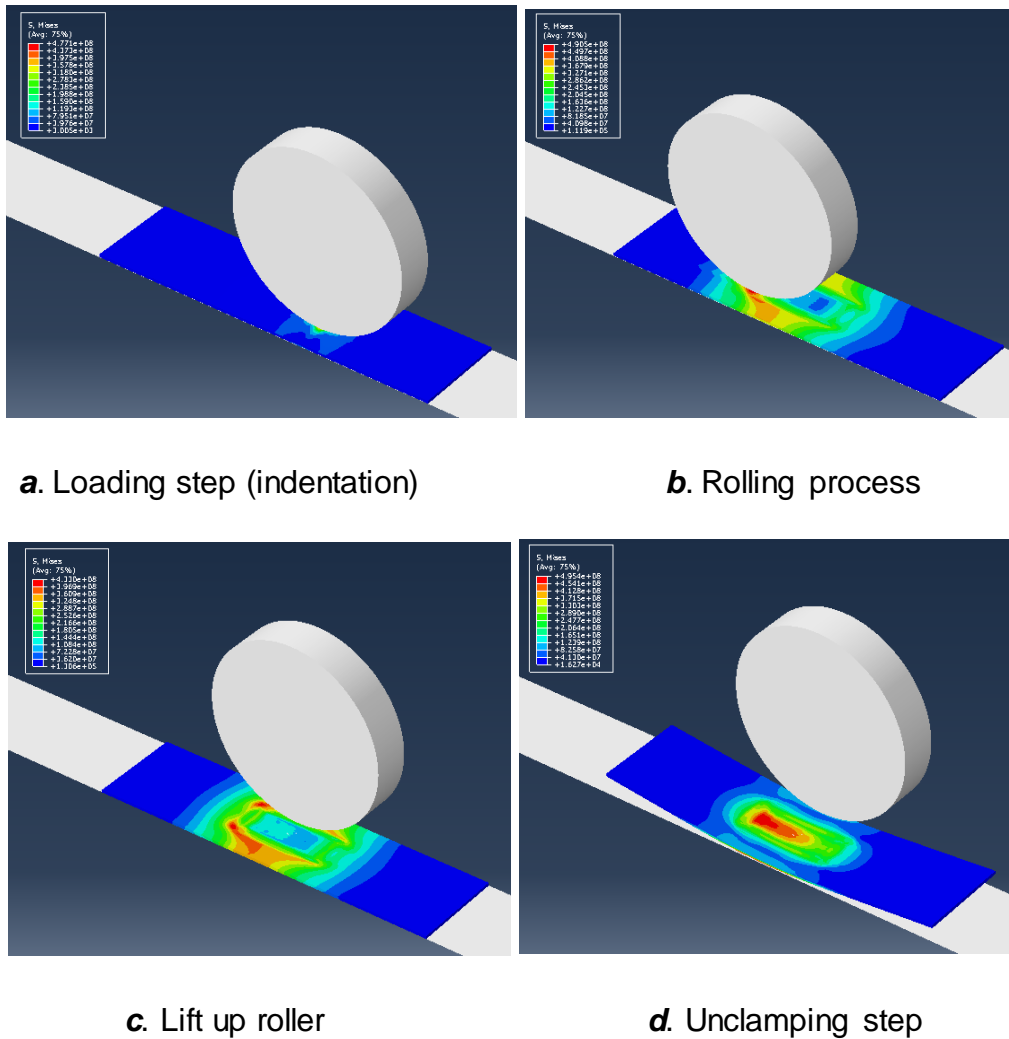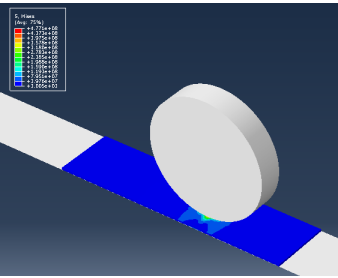
Figure 5.3 Steps of the deep rolling process: *a*. The loading step, roller (rigid) contact specimen (deformable), only rolling load is applied on the roller; *b*. The deep rolling step, both rolling load and roller speed are applied; *c*. The roller lifts step, roller leave sample, and sample are still fully constrained; *d*. The unclamping step, remove all boundary conditions (BCs), and only one node is constrained

5.3.2 Boundary Conditions and Interaction Properties

In this set of CS1 models, different rolling loads and two-sided rolling processes are investigated. The modelling parameters are shown in table 5.2. A rigid plane was included to simulate the interaction with the vacuum clamps, and the lower surface of aluminium alloy sheets, during the rolling process. The vacuum clamps were modelled by applying one-atmosphere pressure (101325 Pa) on the contact surfaces of the sheet towards the rigid plane (as shown in figure 5.2).

The influence of friction between the backing-bar, aluminium sheet, and roller was investigated. Figure 5.1b demonstrated the friction between the contact surfaces. Models of CS1 focused on the effect of different coefficients between the backing-bar and the aluminium sheet, and between the roller and the aluminium sheet, μ_1 and μ_2 were represented respectively. The influence on the residual stress distributions and distortion was compared with experiments. The best fitting combination was applied to other models. The parameters explored are reported in table 5.3.

Table 5-3 Parameters of friction coefficient investigated in CS1

Model description	μ_1 (backing-bar and sheet)	μ_2 (roller and sheet)
120mm×50mm×1.6mm CS1: 60kN load applied to one surface	0.1	0.1, 0.3, 05
	0.3	0.1, 0.3, 0.5
	0.5	0.1, 0.3, 0.5

The results were primarily compared by distortion; then the better fitting parameters were further compared by residual stress profiles. Then, the best match between models and experimental results were further applied to further FE models.

By simulating the boundary conditions of the clamped sheets, all the nodes in the opposite surface to rolling were restrained against the out-of-plane displacement. To avoid the sheet moving along the longitudinal direction during rolling, the end plane was restrained against displacement in the longitudinal direction (x-direction). To prevent the sheet moving in the transverse direction during the rolling process, four nodes on the corners of the lower surface restrained the sheet against the displacement in that direction (z-direction). Two side planes annotated in figure 5.2 were also restrained to allow rotation in the longitudinal and the normal directions. During the unclamping steps, only one node on the centre of the lower surface was fully constrained (ENCASTRE), and the boundary conditions of side planes were kept, while the rest of the mechanical constraints were removed.

5.3.3 Implemental Two-Sided DSR

By simulating the two-side rolling process, aluminium alloy sheets were rotated along the central axis of x-direction by 180°. Then, all boundary conditions had to be reset following the procedures are given in section 5.3.2. An additional procedure is necessary for this section. A predefined stress field at the initial step is defined by importing the residual stress states of the one-sided DSR.

In figure 5.4, the residual stress state was imported before the loading step, and the residual stress distribution was further modified by following the steps illustrated in figure 5.3.
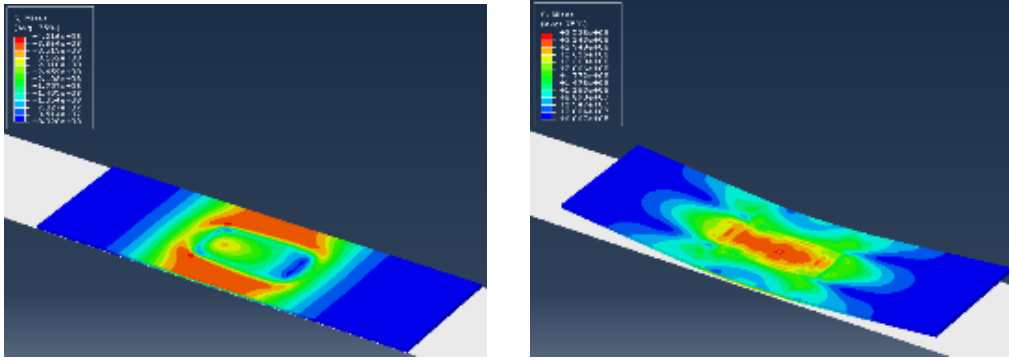
a. Predefined stress field at the initial step   *b*. Stress states after unclamping

Figure 5.4 *a*. The illustration of predefined stress field of the two-side DSR; *b*. Final stress state after unclamping. 3D FE models of CS1

By further modifying the boundary conditions, two rollers were applied at the same time to simulate two rolled strips of the one-side surface. Details of DSR processes on sheets are given in section 5.3.4.

5.3.4 Models of DSR Processes on CS3 Sheets

Differing from the DSR models of CS1, two rollers were applied in FE models (CS3), in order to simulate double rolling processes on one surface. By calibrating the roller positions to be the same as in experimental conditions, all the other boundary conditions followed the details given in section 5.3.2. The one-sided DSR process is shown in figure 5.5. In section 5.3.3, the two-sided rolling processes were simulated by changing the boundary conditions of the final unclamping step. Clamping was applied in the first three steps. To prevent the sheet moving in the transverse direction during rolling, all nodes 10 mm away from both the width edges restrained the sheet against displacement in that direction.
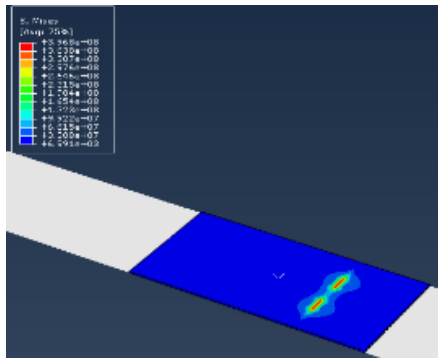
a. Loading step of one-side DSR   *b*. Rolling step
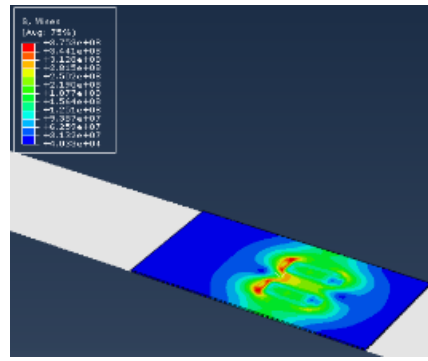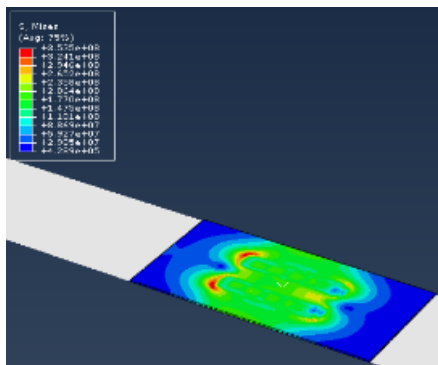
c. Roller lift-up step   *d*. Unclamping step
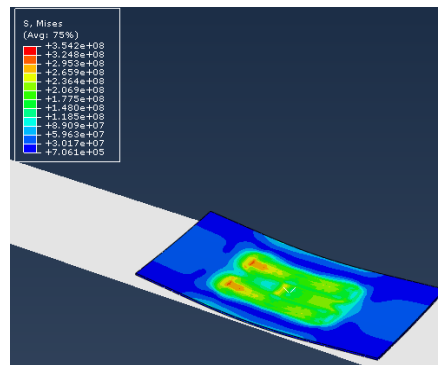
Figure 5.5 Simulation of DSR processes on one surface by two rollers *a*. The loading step, only movement of the roller along the thickness direction by a given load. *b*. Rolling process step, movement of rotation by contact interaction – friction. *c*. The step of lifting up the rollers, stable distributions of residual stresses after rolling processes. *d*. Unclamping step, redistribution of residual stresses and generation of distortion after unclamping

To simplify the DSR processes of CS3, rolling was applied by double rollers, to simulate this process instead of rolling twice on one side by a single roller. The same as the two-side rolling of CS1 in section 5.3.3, where FE models of two-side DSR processes were achieved by using a given predefined stress field. In figure 5.6, the predefined stress field and the final stress state are shown. Unlike in figure 5.4b, the behaviour of bending was captured, which was influenced by

the different load parameters. However, the same bending behaviour was obtained in the experimental findings.
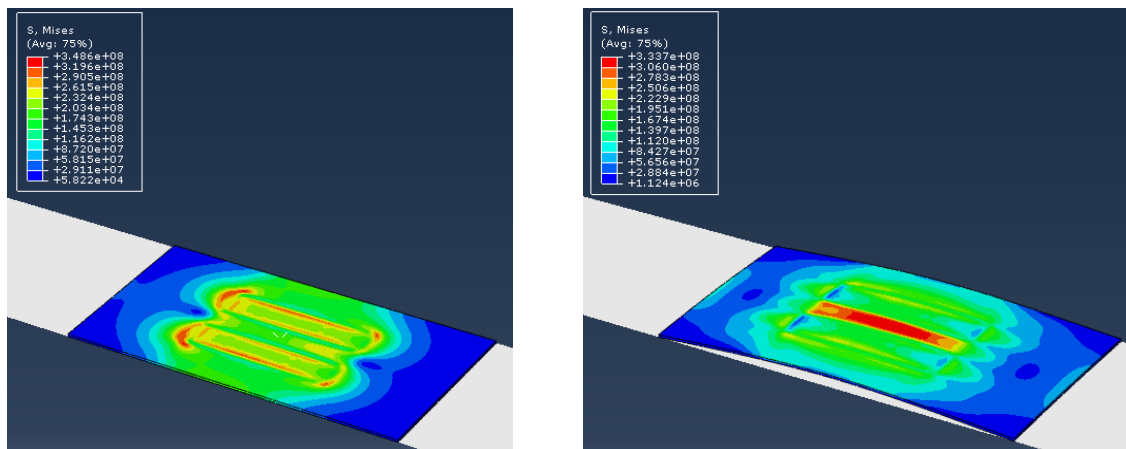
a. Predefined stress field at the initial step   *b*. Stress states after unclamping

Figure 5.6 *a*. The illustration of predefined stress field of the two-side DSR; *b*. Final stress state after unclamping. 3D FE models of CS3

In fatigue tests, all the centre-slit specimens were accomplished by EMD (Electrical Discharge Machining). Experimental measurements of residual stresses didn't account for the effects of the centre-slit. With regard to the flexibility and accuracy of FEA, a complementary model of CS3 was designed, and a centre-slit was inserted with the same geometry as ones used in MT samples. Details are shown in figure 5.7.
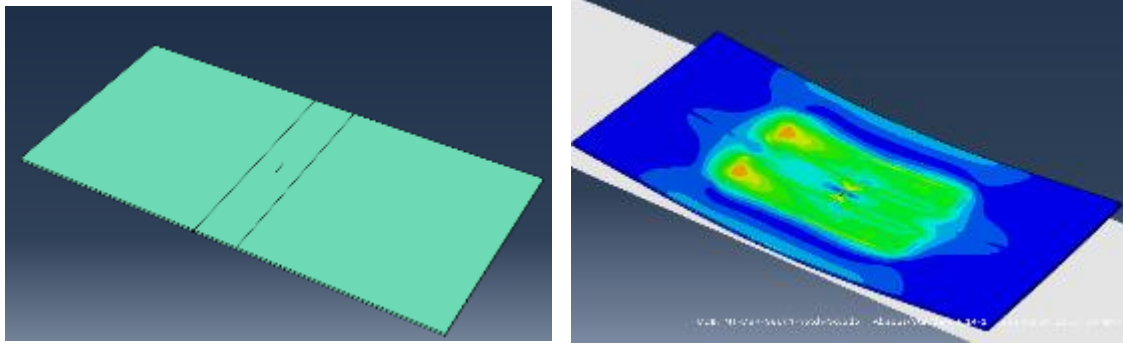
a. Redistrict regions of the centre-slit sample   *b*. RS field after unclamping

Figure 5.7 Modified CS3 including the effects of a centre-slit *a*. Partition of aluminium sheet accounts for the centre-slit geometry. *b*. Stress states of one-side DSR process after unclamping

The added centre-slit had a great effect on the meshing methodology. Figure 5.7a presents the relocation of the regions of a centre-slit (notch) sample. After meshing of the centre-slit (notch) sample, all the other settings and boundary conditions were retained in order to simulate this model. Figure 5.7b demonstrates the residual stress distributed on the centre-slit (notch) sample after unclamping.

5.4 FE Modelling Results

In this FE analysis, displacements and residual stresses were mainly predicted and exported. In this research, deep surface rolling processes involved multiple rollings on most samples. Two hardening types were investigated and compared to experimental measurements of deep rolled samples (CS1) shown in section 5.4.1 and 5.4.2. Regarding FE models of CS3, the induced residual stresses were compared to results of neutron diffraction measurements and are demonstrated in section 5.4.3. Also, a study of residual stress redistribution was carried out, and the results are presented in section 5.4.3.

5.4.1 Comparison of Hardening Models (CS1)

Two hardening types were used in this work, isotropic hardening and kinematic hardening. Residual stress results of FE models and ICHD were compared later. To measure residual stress distribution through the entire thickness, section 3.6.1 already introduced the methodologies of ICHD in CS1. Figure 5.8 shows the contour plot of the longitudinal RS of the full sheet. Moreover, the measurements are chosen in models corresponded to those holes measured by ICHD. The DSR process was applied on one surface under a load of 60 kN. The friction coefficient between the two contact surfaces was assumed to μ = 0.1.
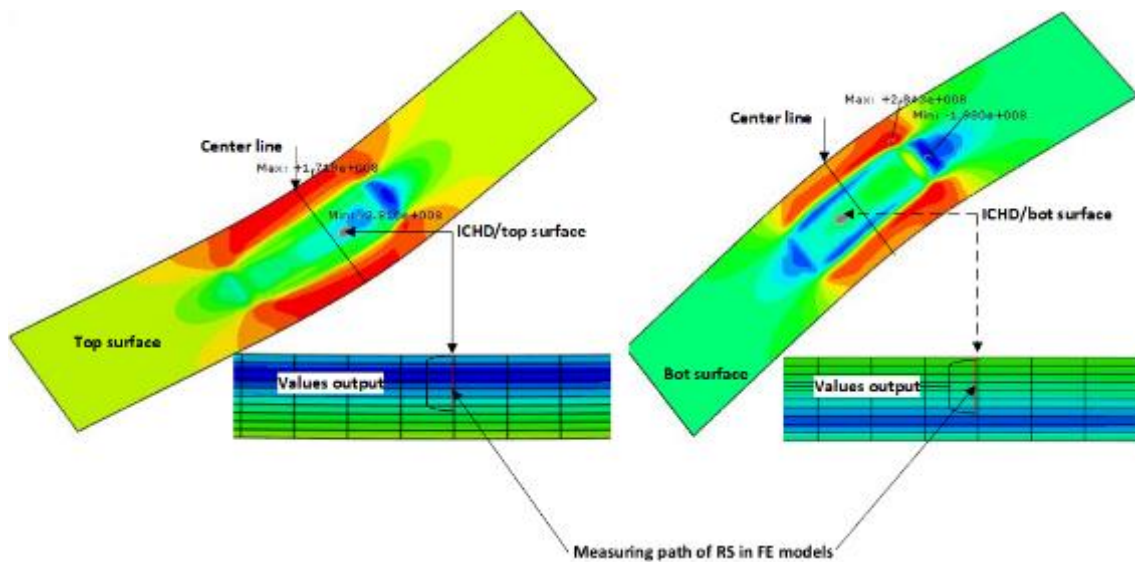
Figure 5.8 Contour plots of the longitudinal RS of the CS1 sheet after unclamping, and measuring path marked in red (Unit: Stress/Pa)

Two-dimensional residual stresses obtained from FE models were compared to experimental results measured by ICHD, The RS in the longitudinal direction is shown in figure 5.9, and the RS in the transverse direction is shown in figure 5.10. A load of 60kN was applied to one surface of the CS1 sample (AA2024-T351). Residual stress through thickness was obtained by FE modelling, as well as by ICHD. Results of longitudinal RS are shown in figure 5.9.
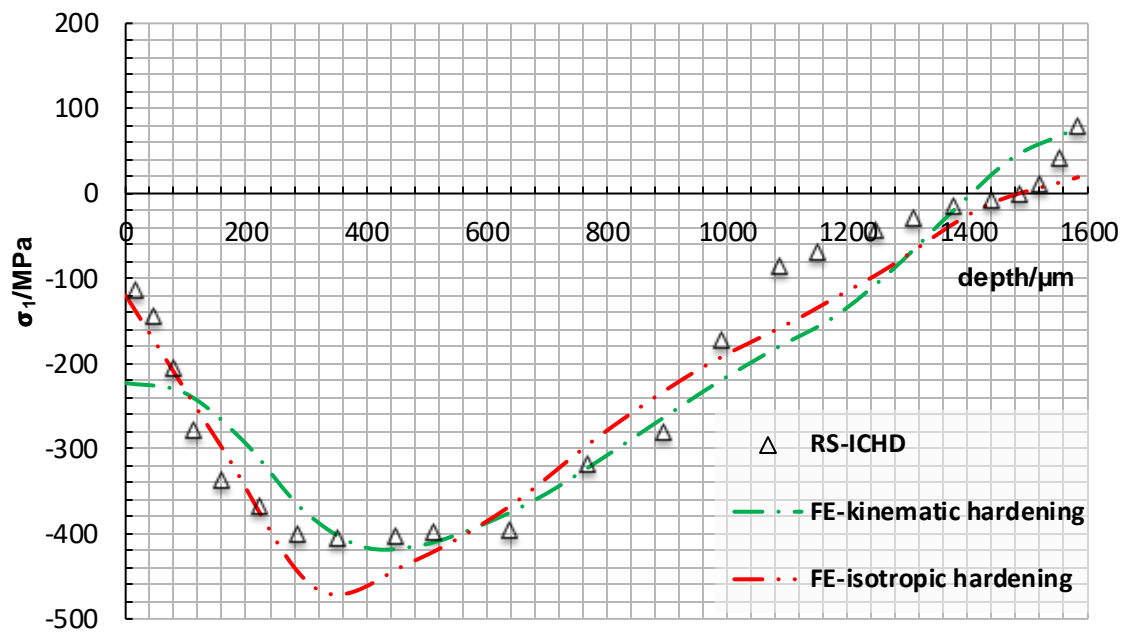
Figure 5.9 Effects of two hardening types on *longitudinal* residual stresses, compared with ICHD

Both hardening types showed a good agreement with experimental results. Being careful to notice the differences, the isotropic hardening curve showed a better agreement with ICHD within 200 microns depth. However, kinematic hardening had a better fit at around the maximum value of compressive residual stresses (CRS). Moreover, when balanced tensile residual stresses (TRS), near the other side (at about 1600 microns), residual stresses of kinematic hardening coincided with ICHD results.

Apart from the comparison of longitudinal residual stresses, results of transverse residual stresses (along with the width direction) are summarised in figure 5.10.
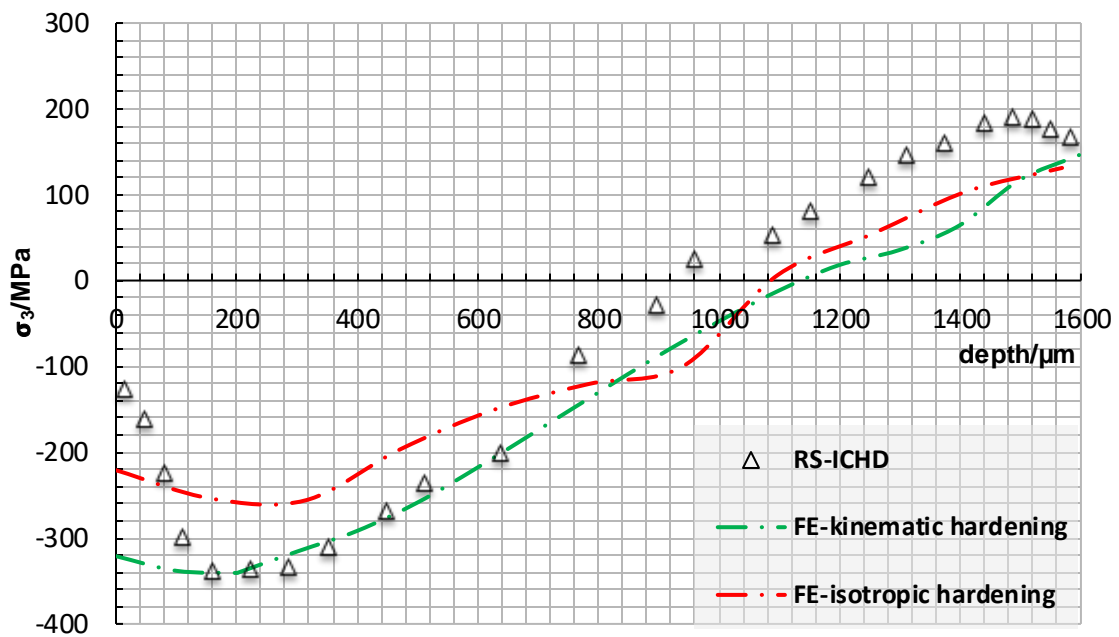
Figure 5.10 Effects of two hardening types on *transverse* residual stresses, compared with ICHD

When comparing these two hardening types with those shown in figure 5.9, results of kinematic hardening showed a better agreement at between depths of 200 microns and 800 microns. Similar findings to figure 5.9, where the maximum values of compressive residual stresses between the kinematic hardening model and ICHD data coincided, not only with the values but also with the corresponding location in depth.

Apart from the results of residual stresses, displacements of two nodes on both surfaces are measured and compared to experimental values. Measured nodes are shown in figure 5.11. Moreover, out-of-plane displacements compared to experimental values are also shown in figure 5.11.
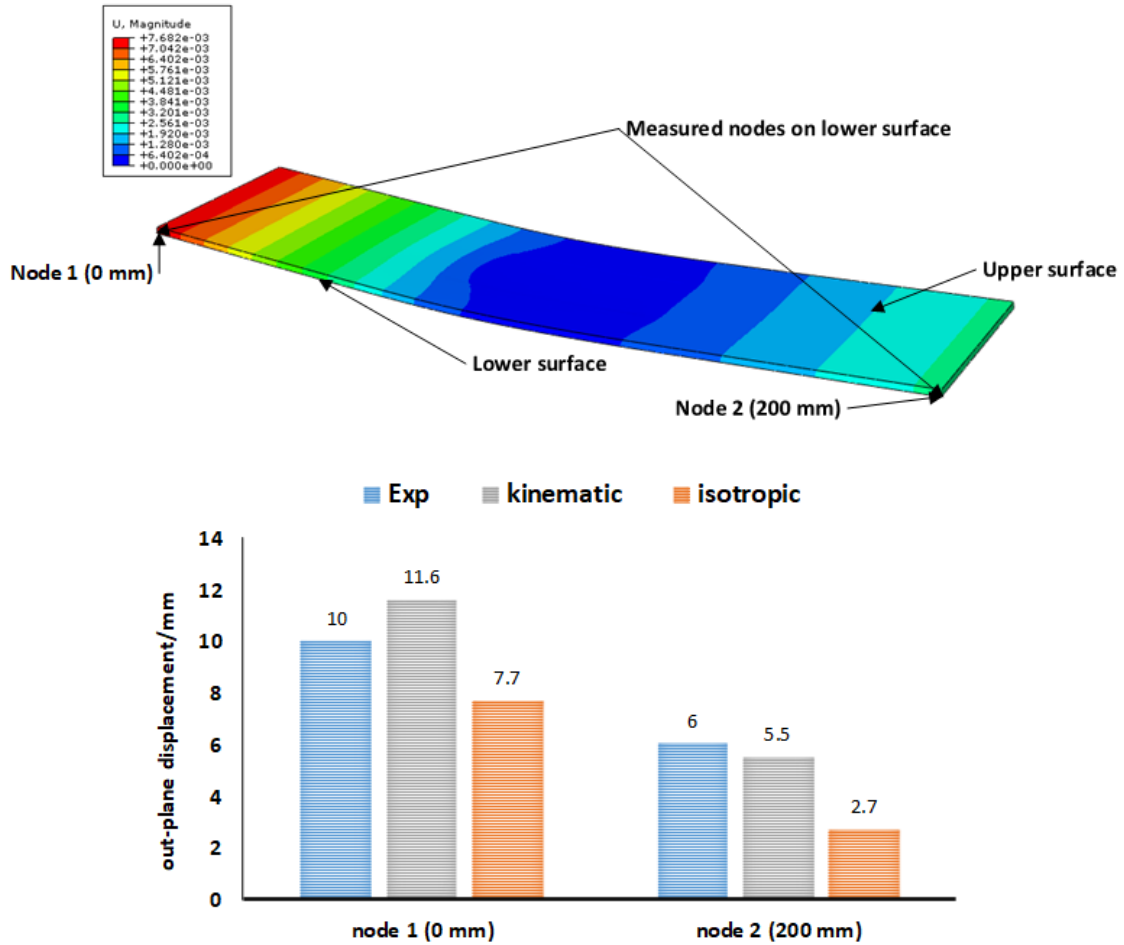
Figure 5.11 Out-of-plane displacements (distortion) at selected locations, and comparison between experimental measurements and FE models. (Unit: U/m)

If only the comparison of RS results was taken into account, both isotropic and kinematic hardening could work well using FE analysis. However, out-of-plane displacements of kinematic hardening models showed a better fit to experimental RS values extracted from rolled sheets.

Based on the above comparison results between isotropic hardening and kinematic hardening, parameters of kinematic hardening were used for the further DSR models.

5.4.2 Meshing Sensitivity Study

Low meshing density ($2\times1\times0.16$ mm^3) and high meshing density ($1\times1\times0.1$ mm^3) were applied to 3D models of CS1, simulating one surface rolled by 60kN. The friction coefficient between two contact surfaces (details in section 5.3.2) was 0.1.

The distortion and residual stress profiles were compared to experiments, as shown in figure 5.12 and figure 5.13.
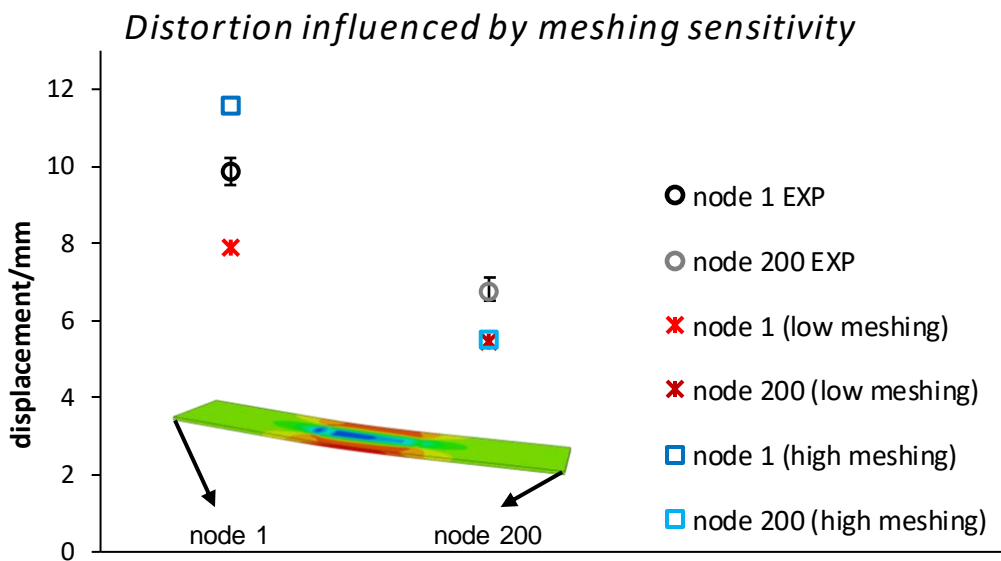
Figure 5.12 Meshing sensitivity study: two different meshing density models of CS1 compared to experiments by displacements (after unclamping)

In figure 5.12, both two models show that the displacement of the two nodes is different, not balanced. This is consistent with the distortion behaviour measured by the experiments (dark hollow dots). The model with a high meshing density fits better to the experimental displacement measured at node 200 as shown in figure 5.12.

Figure 5.13 further compared the differences in residual stress profiles between two different mesh density models and experimental values measured by ICHD.
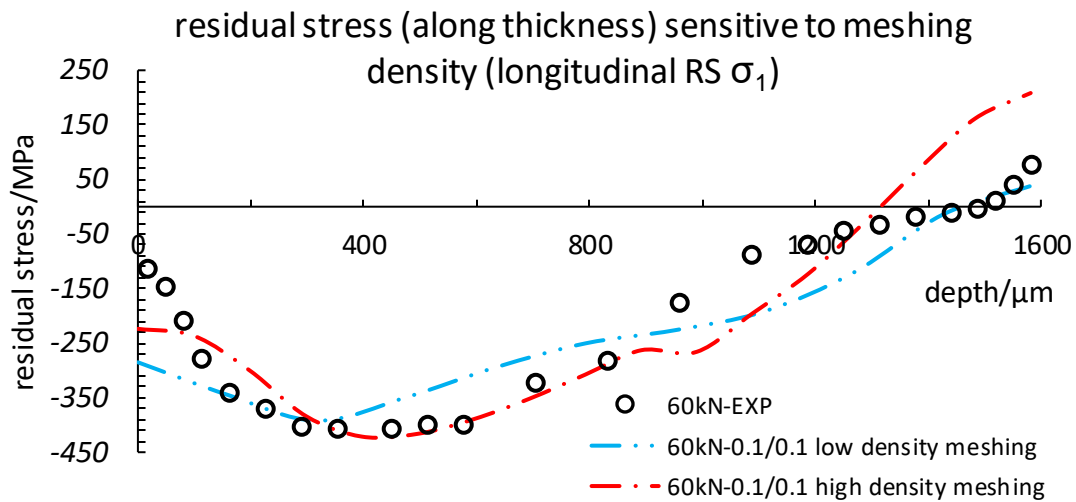
Figure 5.13 Meshing sensitivity study: two different meshing density models of CS1 compared to experiments by residual stress profiles (after unclamping)

In figure 5.13, the high density meshing model demonstrates a better fitting to the experiment, between 100 micros and 1200 micros in depth. The residual stress values within this depth range were averaged and compared with experimental data. The average residual stress of the high density meshing model was 1% different from the experimental result. However, the average of the low density model had 10% differences. Further refinement of the meshing could be possible to improve the accuracy of FE models. However, the computing time would be greatly increased. Close to both surfaces, residual stress values of FE models is not consistent with the experimental results, which may be errors in the experimental measurements of residual stress fields. The high meshing density ($1\times1\times0.1$ mm^3) is possible to meet requirements in this research.

5.4.3 Sensitivity Study of the Friction Coefficient

Kinematic hardening was applied to CS1 models, further for exploring the sensitive influence of the friction coefficient on the model accuracy. Figure 5.11 demonstrated that the method of distortion measurement by determining the out-

plane displacement (perpendicular to rolling direction) of two nodes from the lower surface.

Different friction coefficients were applied to CS1 models (low meshing density applied), for exploring the sensitive effect on the accuracy, by determining the displacements and residual stress profiles (after unclamping), results shown in figure 5.14.

a

b
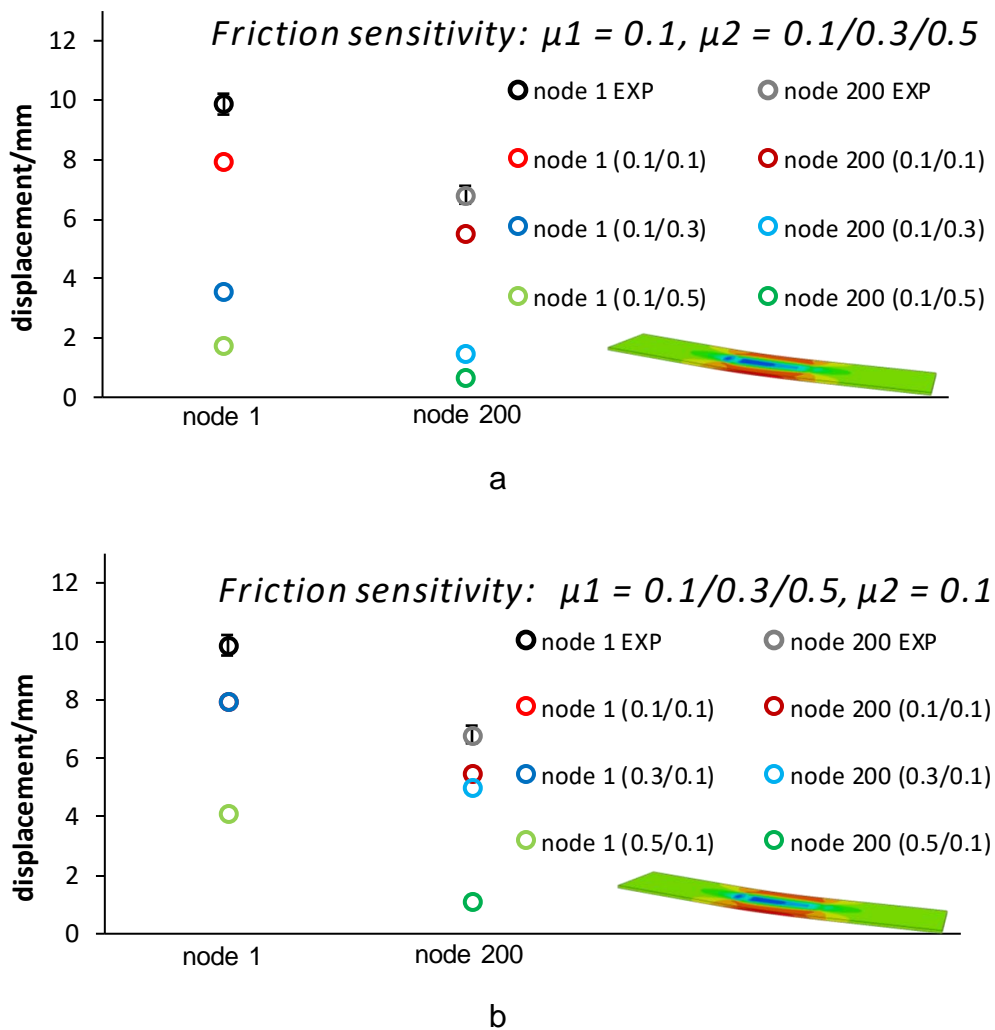
Figure 5.14 Friction sensitivity study: a. fix μ_1 = 0.1 (friction coefficient between roller and sheet), changing μ_2 = 0.1/0.3/0.5 (friction coefficient between sheet and backing-up bar); b. fix μ_2 =0.1, changing μ_1 = 0.1/0.3/0.5. Displacements measured and compared to experiments (after unclamping)

In figure 5.14a, the greatest displacements of two end nodes are reduced when increasing the friction coefficient between the sheet and back-up bar, whilst the friction coefficient at the interface between the roller and the specimen remains 0.1.

In figure 5.14b, the friction coefficient at the interface between the specimen and the backing-up bar was fixed to 0.1, the reduction of displacement was only captured in the model with two friction coefficients 0.5/0.1. The friction coefficients 0.1 and 0.3 applied to the interface between the roller and the specimen have no significant effect on the distortion behaviour of FE models.

Other combinations of friction coefficients 0.3/0.3, 0.3/0.5, 0.5/0.3 and 0.5/0.5 were compared by the largest displacements, and plotted in appendix C.

By comparing the residual stress distribution (after unclamping) calculated by the FE models with experimental results, two combinations of the friction coefficient 0.1/0.1 and 0.3/0.1 were further studied and evaluated.

Residual stress profiles of two models with different friction coefficients were compared to the ICHD experiments. The longitudinal RS (σ_1) and transverse RS (σ_3) distributed along the thickness were obtained from low density meshing applied models.

In figure 5.15, there is no significant difference in residual stress distribution between two models and the experimental RS. Residual stress result of the model with the friction coefficient 0.1/0.1 fit better to the experiments, especially at the near surface.

The study on meshing and friction sensitivity above demonstrated that high density meshing and low friction coefficient could improve the simulation accuracy of the FE model. Further study of finer partitioning meshing and more combinations of friction coefficient could contribute to the higher accuracy of the simulation. However, it would take a large amount of time.
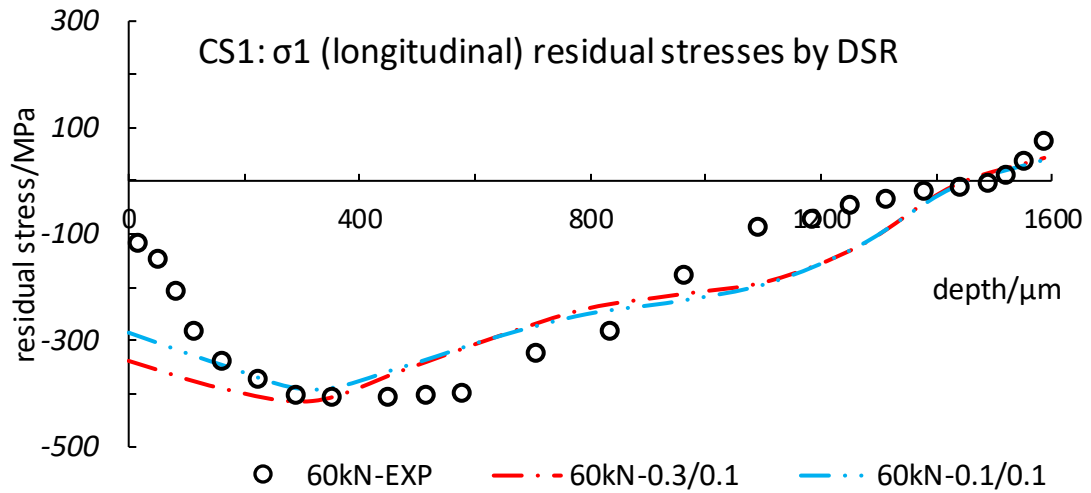
a
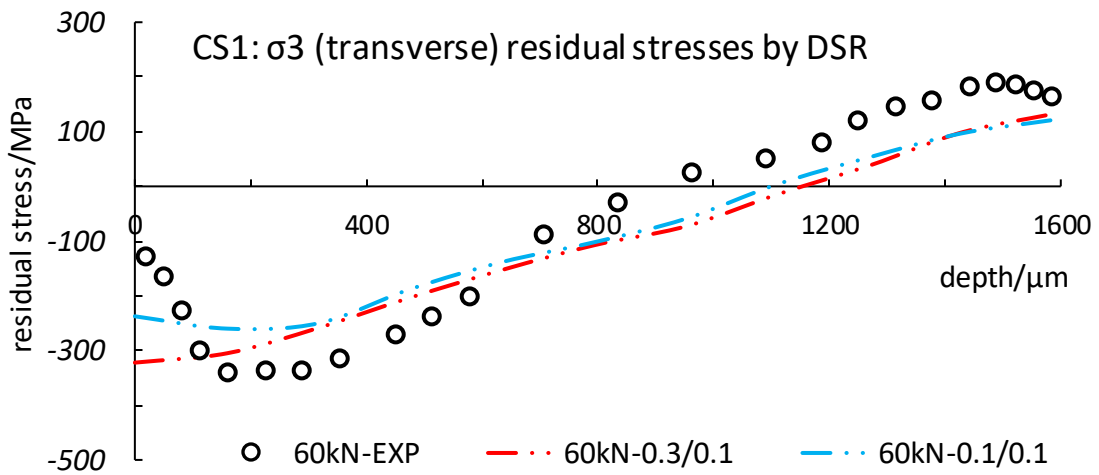
b

Figure 5.15 Friction sensitivity study: two models of CS1 with two different friction coefficient applied, compared to experiments by two directional residual stresses (after unclamping)

5.4.4 Results of One-sided DSR Simulations (CS1)

Figure 5.16 demonstrates the σ_1 field induced by the one-side DSR treatment. The rolled surface and the bottom surface, opposite to the rolled surface, are displayed in figure 5.16, the cross-section at the middle of the sample as also shown.
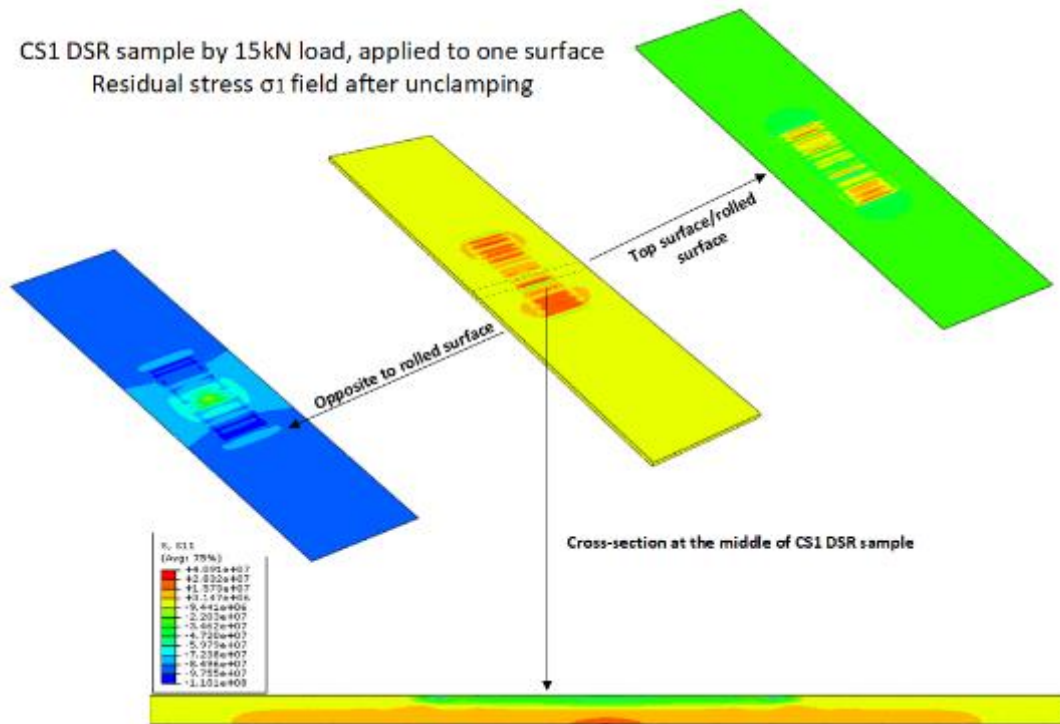
Figure 5.16 Residual stress σ_1 generated by deep rolling on one surface (top surface) The maximum value of CRS and TRS are -110.1 MPa, 40.91 MPa at the middle cross-section of CS1 sample (Unit: Stress/Pa)

Kinematic hardening was used to simulate the deep rolling process, performed on a single surface, with a load of 15kN. One advantage of FEM is to predict the accurate residual stress field in the central width (path of fatigue crack propagation). Figure 5.17 shows the residual stress induced by different loads, at the cross-section of the width. Deep rolling was applied to only one single surface of CS1 samples.
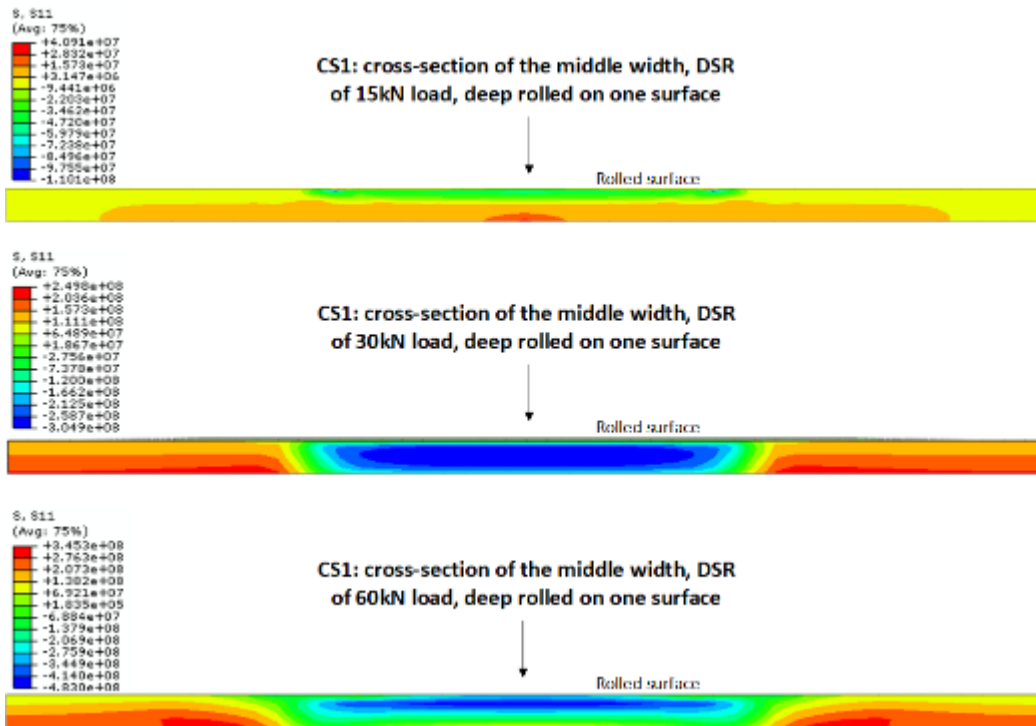
Figure 5.17 Residual stress fields of the cross-section induced by different rolling loads, DSR applied on one surface. Kinematic hardening is applied to material properties (Unit: Stress/Pa)

The maximum values of CRS and TRS induced by DSR were obtained from FE results, as shown in table 5.4.

Table 5-4 Maximum compressive residual stress and tensile residual stress from FE 3D models

	CS1: 15kN	CS1: 30kN	CS1: 60kN
Max. CRS	110.1 MPa	304.9 MPa	483 MPa
Max. TRS	40.91 MPa	249.8 MPa	345.3 MPa

For the lowest applied load sample (CS1, 15kN), it was seen that compressive residual stress was distributed near the rolled surface, whilst the balanced tensile residual stress was obtained near the opposite surface, as shown in the middle of the cross-section. When the applied load was increased to 30kN, the rolled cross-section was full of compressive residual stress, whilst the balanced tensile residual stress was found outside of the rolled area. The maximum CRS was increased by three times, where the load was only doubled. However, the maximum TRS was increased by more than six times. When comparing the 30kN rolled sample with the one rolled by 60kN, the maximum CRS was increased by 180 MPa, whilst the maximum TRS was increased by below 100 MPa.

5.4.5 Results of Two-sided DSR Simulations (CS1)

Section 5.3.3 has described the methodologies of two-sided DSR processes using FE models. One surface of the CS1 sample was firstly deep rolled using a load of 60 kN. Then, the opposite surface was deep rolled with a load of 30 kN. Experimental results of two-dimensional RS were compared to the FE results, as shown in figure 5.18. The residual stress was measured in the thickness. The X-axis represents the distance from the first rolled surface, along with the thickness of 1.6 mm. The Y-axis represents the residual stress values, measured by ICHD and averaged by FE, respectively.
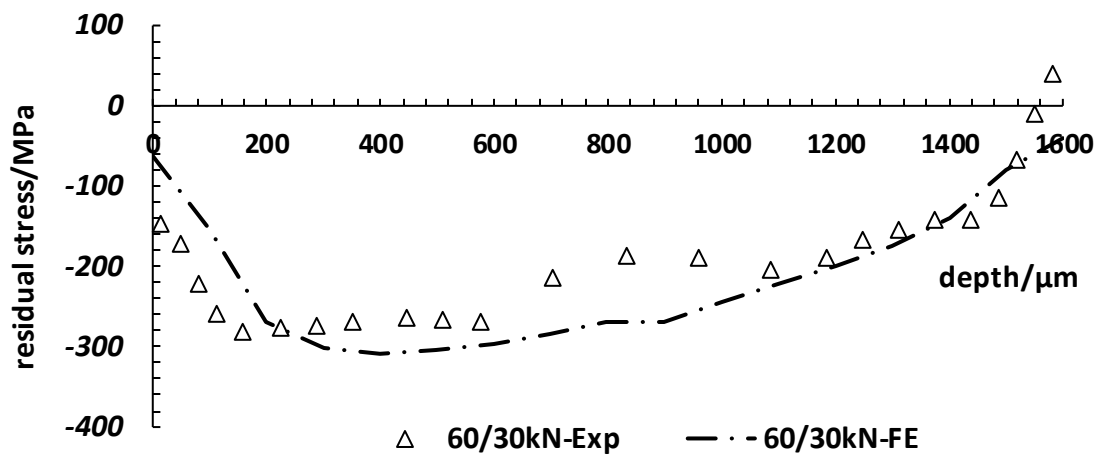
a. CS1: RS of σ₁ (longitudinal) comparison between ICHD and FE
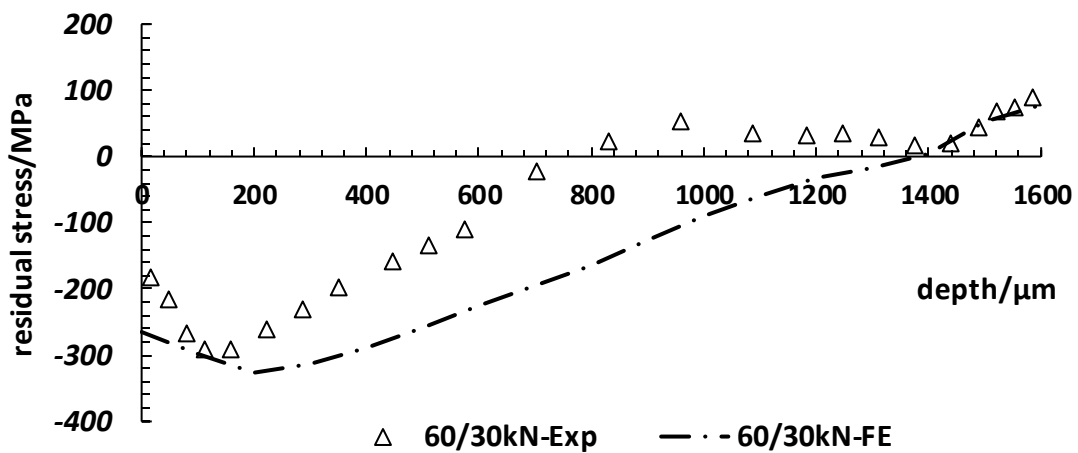
b. CS1: RS of σ₃ (transverse) comparison between ICHD and FE

Figure 5.18 Two-sided DSR by the first load 60 kN on one surface and the second load of 30 kN on the opposite surface, residual stress of σ_1 and σ_3 compared by ICHD and FE data

Results in figure 5.18 showed that RS of the FE model in σ₁ direction had a better fit when compared to date measured by ICHD. Additionally, the maximum CRS of ICHD results in both measured directions coincided with the data of the two-side DSR model.

By taking a comparison between residual stresses in the longitudinal and transverse direction, DSR induced higher compressive stress in the rolling path (σ_1). Moreover, σ_1 residual stresses show compressive along nearly the entire thickness.

Analysis of the residual stresses along the transverse direction showed that high compressive residual stresses were induced beneath one surface, whilst low tensile stresses were obtained along the opposite thickness.

The compressive residual stresses obtained along the first half of thickness were not counterbalanced by the residual stress distributed along the other half of the thickness.

Figure 5.19 shows the effect of residual stress and distortion, induced by different loads, at the cross-section of the width. Deep rolling was applied to both surfaces of CS1 samples.

Figure 5.19 Effects of induced residual stress and distortion by different DSR load parameters, 60/15kN, 60/30kN and 60/60kN (Unit: Stress/Pa)

In the three rolling load parameters, loads of 60/15kN induced the lowest distortion. The other two loading parameters caused the highest distortion, of which the maximum value of distortion at the sample edge was around 10 mm.

All samples demonstrated that σ_1 residual stress was nearly compressive along the thickness direction, within the rolled area. There was no tensile residual stress balancing the compressive residual stress within the rolled area. Higher tensile residual stress was distributed at the outside of the rolled area. It was seen that the average of compressive residual stress induced by 30/15kN loads was 300 MPa, no significant difference to the induced residual stress fields of other two samples (DSR-60/60kN: light blue corresponding 345.9 MPa). However, the distortion generated by the former loads was dramatically lower than the load parameters of the others.

The maximum values of CRS and TRS induced by DSR were obtained from FE results, as shown in table 5.5.

Table 5-5 Maximum compressive residual stress and tensile residual stress from FE 3D models

	CS1: 60/15kN	CS1: 60/30kN	CS1: 60/60kN
Max. CRS	331.4 MPa	385.9 MPa	485.3 MPa
Max. TRS	240.9 MPa	279.3 MPa	329.5 MPa

5.4.6 Results of FE Models (CS3)

In this section, results of distortion and residual stress were obtained from FE models. Firstly, distortion after deep rolling processes was compared to FE models. Then, residual stress results obtained from FE models were compared to experimental data measured by Neutron Diffraction (ND).

Results of distortion

In this section, results of out-of-plane displacements (distortion) and residual stresses after unclamping are compared between FE models and experimental measurements. An aluminium sheet of CS3 was deep rolled on both surfaces, one surface under a load of 60kN, with the opposite surface under a load of 15kN. Out-of-plane displacements were measured by using a laser scanner, and the measured path is displayed in figure 5.20, along with the centre line of the width. Both distorted surfaces were scanned along the measured path.
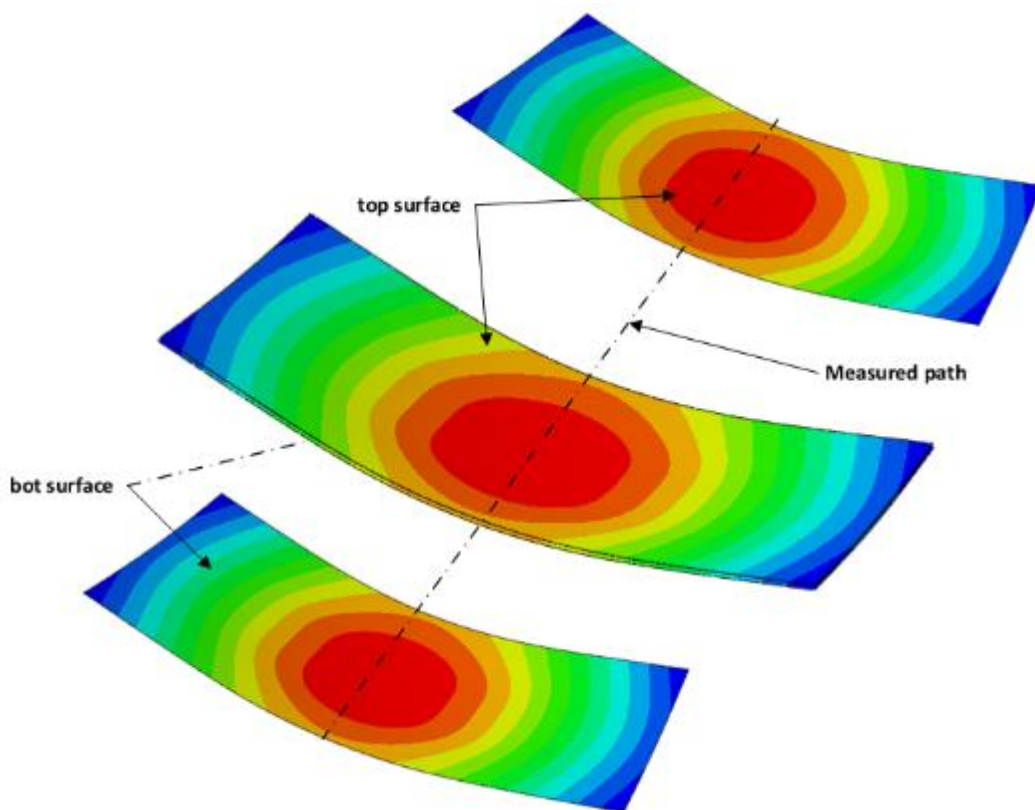
Figure 5.20 Contour plot of the out-of-plane displacements (3X magnification) and the measured path of both surfaces (CS3 samples of AA2024-T351)

Due to the position of the clamping tools used for setting up the out-of-displacement measurement, the straight dash-dot line in black on figure 5.21

represents the lowest point by assuming a zero distance between contact surfaces of the bottom surface and a fixed horizontal plane. Distorted surfaces were scanned and plotted in figure 5.21, and are represented by full coloured lines. Moreover, those distorted surfaces measured by FE models are plotted by dashed colour lines. The secondary axis denotes the reduction or increase of, the cross-section in thickness after DSR. There were little thinner of the thickness in the non-DSR region. However, within the rolled areas, there was no more than a 20% change of thickness close to the edge of the rolled strips (50 mm and 70 mm in figure 5.21).
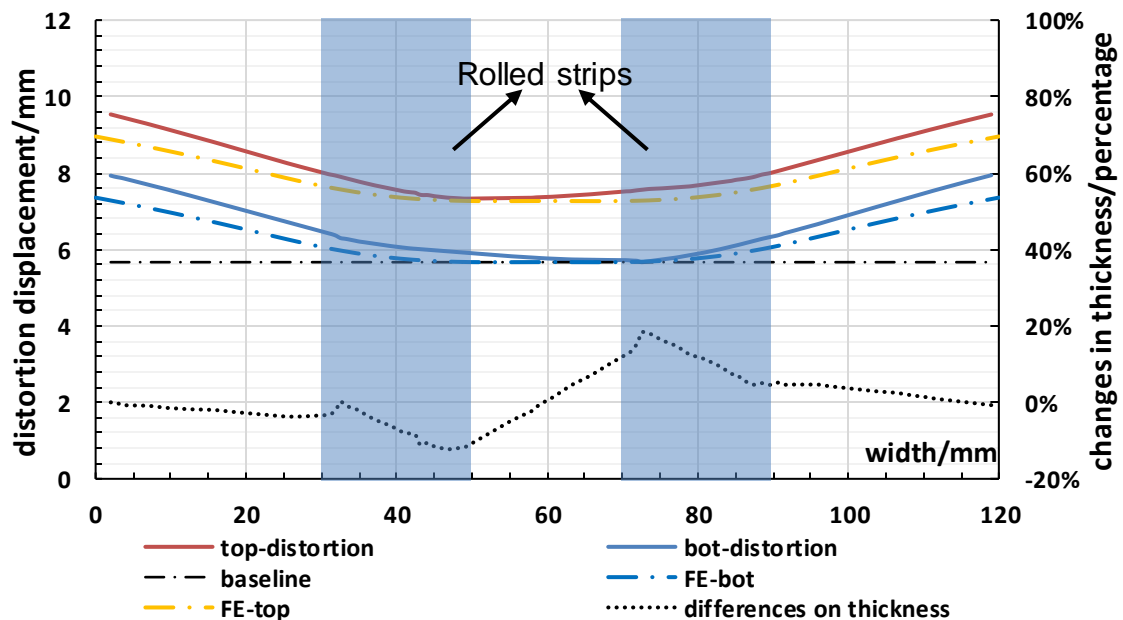
Figure 5.21 Comparison of measured distortion by the laser scanner and FE models, the changes in thickness after DSR of 60/15kN

Results of residual stress

In this part, RS results from FE models were compared to experimental data of ND measurements. Then, different loading parameters were used for comparison between distortion behaviours and residual stress fields at the cross-section of the middle width.

1. RS comparison of FE and ND

By averaging the residual stresses through the thickness (the method of data averaging is shown in section 3.6.3), a comparison could be implemented between results measured by neutron diffraction and the data exported from the CS3 model. The gauge volume of ND was 0.6×0.6 mm^2 (plane stress condition). Therefore, residual stresses were measured at three different positions along the thickness direction, as shown in figure 5.22.
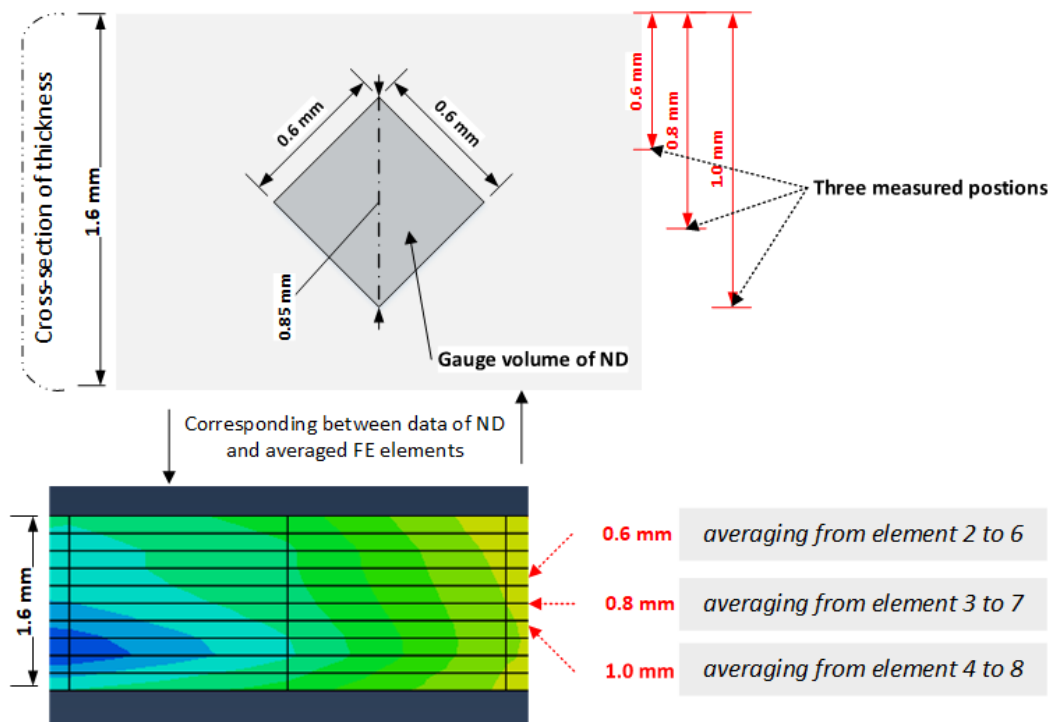
Figure 5.22 Schematic diagram of selecting FE elements to average residual stresses by the comparison with the results of Neutron diffraction

Comparison of residual stresses between measured data from neutron diffraction and averaged values of the DSR model is shown in figures 5.20 and 5.21. Longitudinal residual stresses were parallel to the rolling direction, while the transverse residual stresses were parallel to the width direction. A sample of CS3 was deep rolled using 60/15kN loads. One surface was first rolled by a 60kN load, whilst the opposite surface was then rolled by the lower load of 15kN. As a result, two rolled strips on each surface were accomplished.
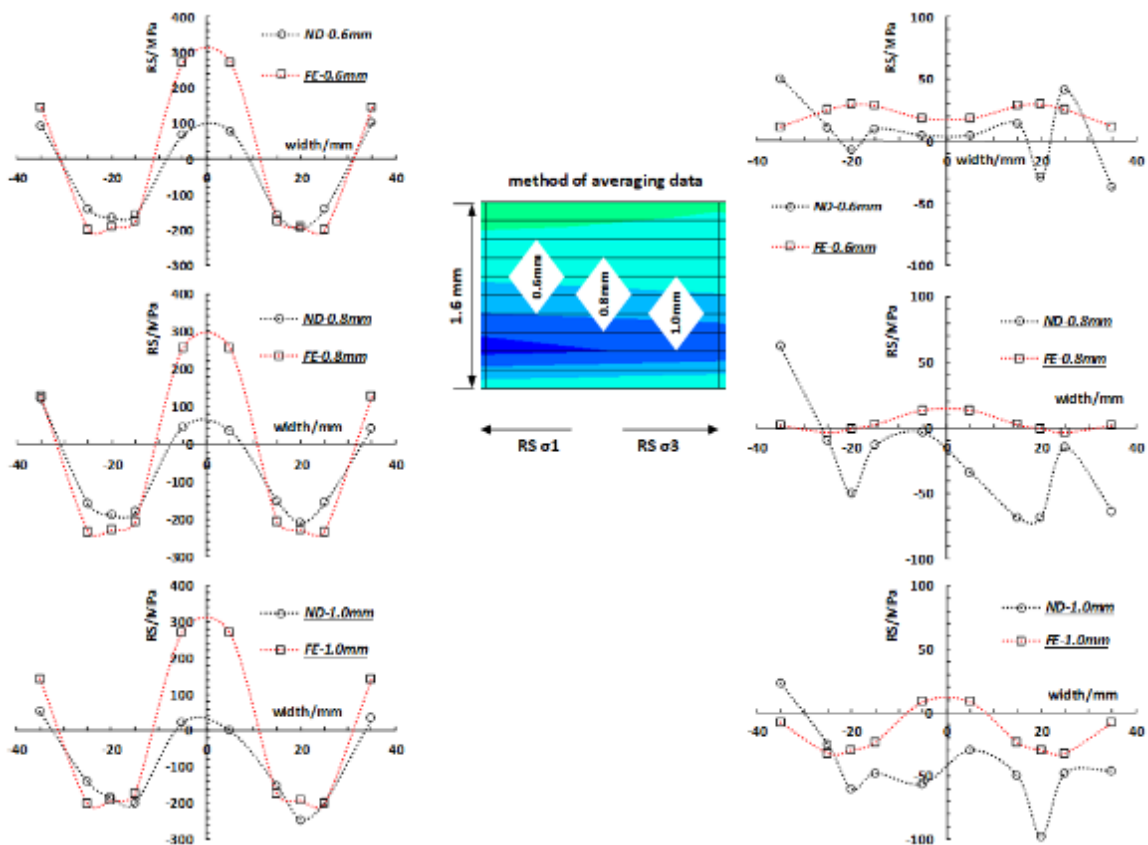
Figure 5.23 Comparison of residual stress in-depth between the FE model and experimental results of neutron diffraction, 60/15kN loads applied to a slit-free sample of CS3.

In figure 5.23, RS σ_1 of the FE model, within the rolled areas, showed good agreement with experimental values taken from neutron diffraction measurements. However, measured points of the FE model taken near the

centreline, showed higher tensile residual stress compared with those measured by ND. The same results were found in non-DS rolled areas, measured at points between 25 mm and 95 mm.

2. Comparison of distortion and RS by different loads (two-sided rolling)

Three loading parameters were applied to FE models, 20/10kN, 30/18kN and 60/15kN, respectively. FE models simulated two deep rolled areas of each surface, corresponding to four times deep rolling processes in total. The first surface was always rolled by the higher load, whilst the opposite surface was rolled by the lower load. The results of the induced distortion of the top surface (lower load applied) and residual stress at the cross-section of the middle width are reported in figure 5.24.
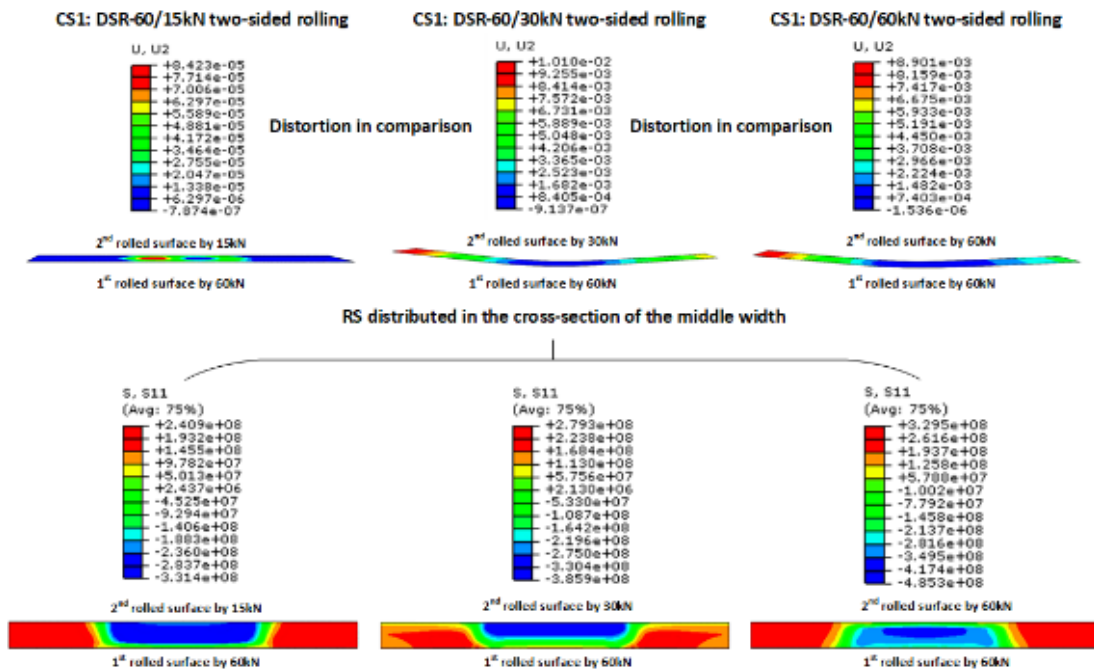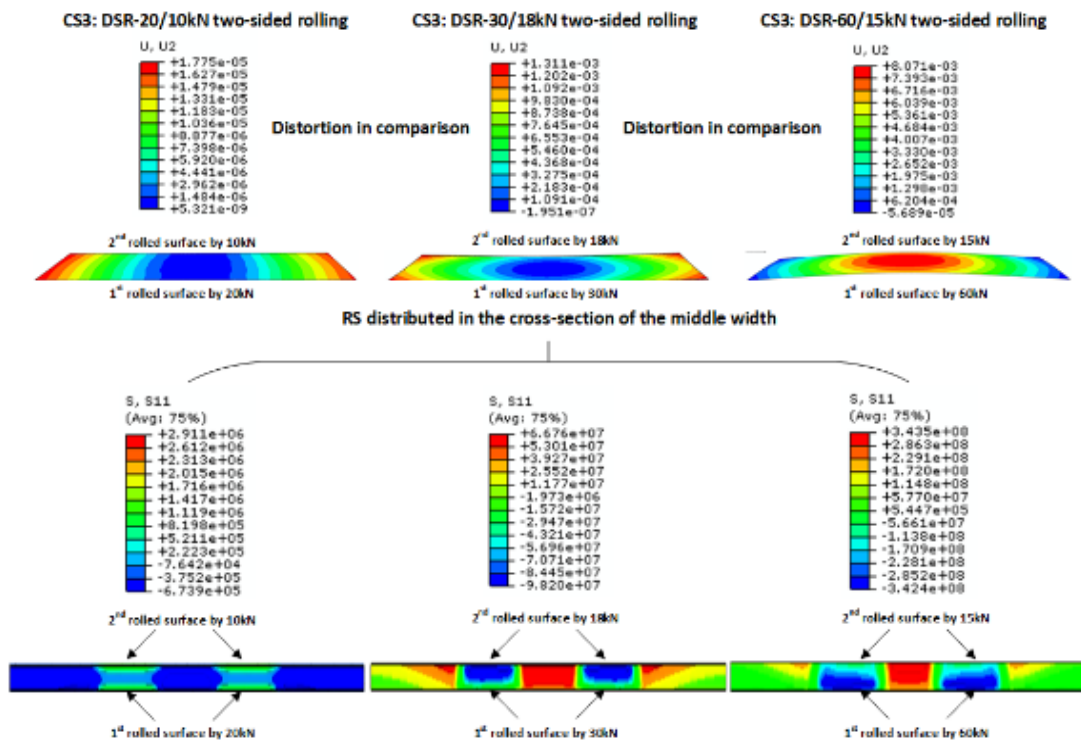

Figure 5.24 Effects of induced residual stress and distortion by different DSR load parameters, 20/10kN, 30/18kN and 60/15kN. Slit-free samples of CS3 (Unit: Stress/Pa)

Distortion results of the sample rolled by 20/10kN could be considered negligible. This FE result was consistent with the experimental result of samples treated by the same loading parameters. Differing from distorted surfaces of samples treated under loads of 20/10kN and 30/18kN, the distorted surface of the sample rolled by 60/15kN presented a convex profile, unlike the concave surface of the sample rolled by 30/18kN and others in figure 5.24. Residual stress within the rolled areas generated by 20/10kN loads demonstrated that compressive residual stresses were close to the most recently deep-rolled surface. This was more clearly seen in the result of the sample rolled under 30/18kN loading. Residual stresses within the treated area of the sample rolled by 60/15kN showed that more compressive residual stresses were close to the first deep-rolled surface (rolled by 60kN). Therefore, the sample was bending toward the first rolled surface.

3. Results of RS redistribution (compare one-sided with two-sided DSR)

Another study of residual stress redistribution was carried out using FEM. Rolling loads of 20kN, 30kN, 60kN were only applied to one single surface of the slit-free samples of CS3 (those with two rolled strips). Rolling loads of 20/10kN, 30/18kN, 60/15kN were applied to both surfaces of the slit-free samples of CS3 (those with four rolled strips). The results of residual stress fields at the cross-section of the middle width, as induced by the above loading parameters, is shown in figure 5.25.
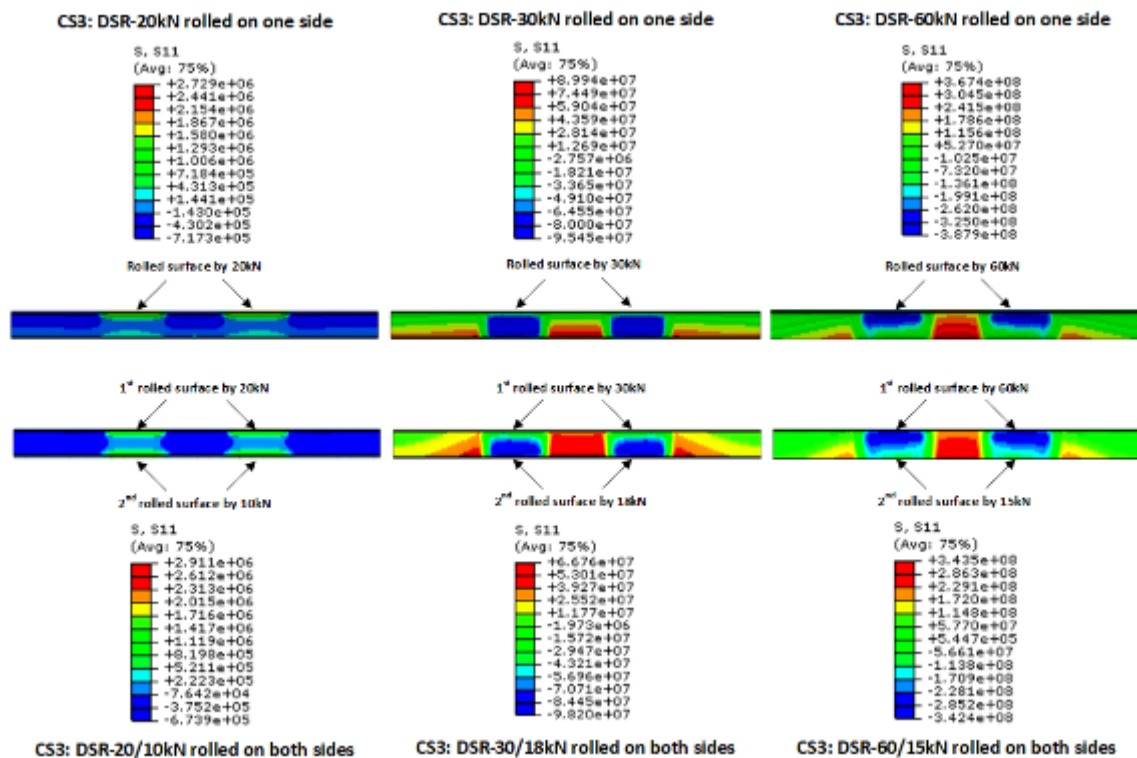
Figure 5.25 FEA on residual stress redistribution of deep-rolled samples, three different loads (20kN, 30kN, 60kN) applied to the single surface; three different loads (20/10kN, 30/18kN, 60/15kN) applied to both surfaces, σ_1 (longitudinal residual stress) used to present the FE results (Unit: Stress/Pa)

In comparing a 20kN load rolled on one surface, with 20/10kN loads rolled on both surfaces, there were no significant differences to the redistribution of residual stresses. Both CRS and TRS regions remained almost the same after the second surface was deep rolled. However, the other two FE models demonstrated a quite distinct redistribution of residual stress after deep rolling was performed to the second surface of samples. Results of the 30/18kN FE model showed, in figure 5.25, that the higher compressive region moved to the second rolled surface (rolled by the 18kN load). However, as also shown in figure 5.25, results of the 60/15kN FE models demonstrated that the higher compressive region remained close to the first rolled surface (rolled by the 60kN load). RS induced by a 60kN load rolled on one surface, compared with the RS field generated by the 60/15kN loads rolled on both surfaces, exposed that the range of CRS was significantly enlarged in the thickness, although the maximum CRS was slightly reduced.

4. Effects of RS by different roller positions

By enlarging the width of the untreated areas, between the two rolled strips, to 40 mm, the induced RS fields differed from the results above. 60/15kN loads were applied to two different FE models. Only the initial positioning of the roller was changed. The results of these residual stress fields are shown in figure 5.26.
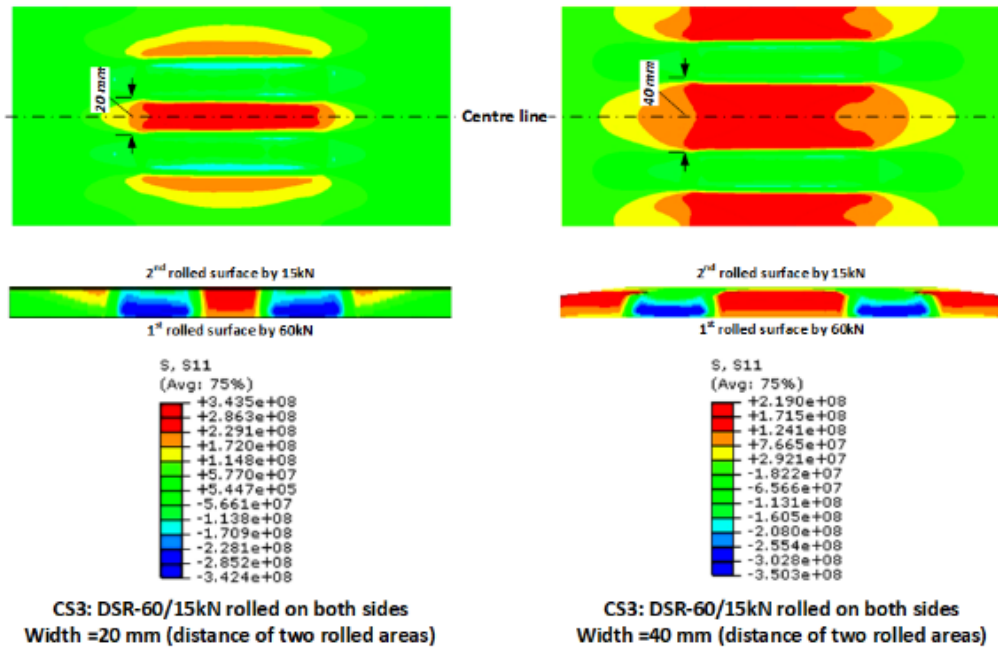
Figure 5.26 The effects on residual stress fields of FE models by positioning roller, same load parameters of 60/15kN applied on both surfaces (Unit: Stress/Pa)

It was seen from the residual stress distribution along the thickness that the area of high CRS was reduced, when the roller was positioned away from the centre. The area between two rolled strips was entirely occupied by the high tensile residual stress.

Values of residual stress σ_1 field of the middle cross-section, shown in the figure above, were averaged in the thickness and plotted against the width of the sample, as presented in figure 5.27.
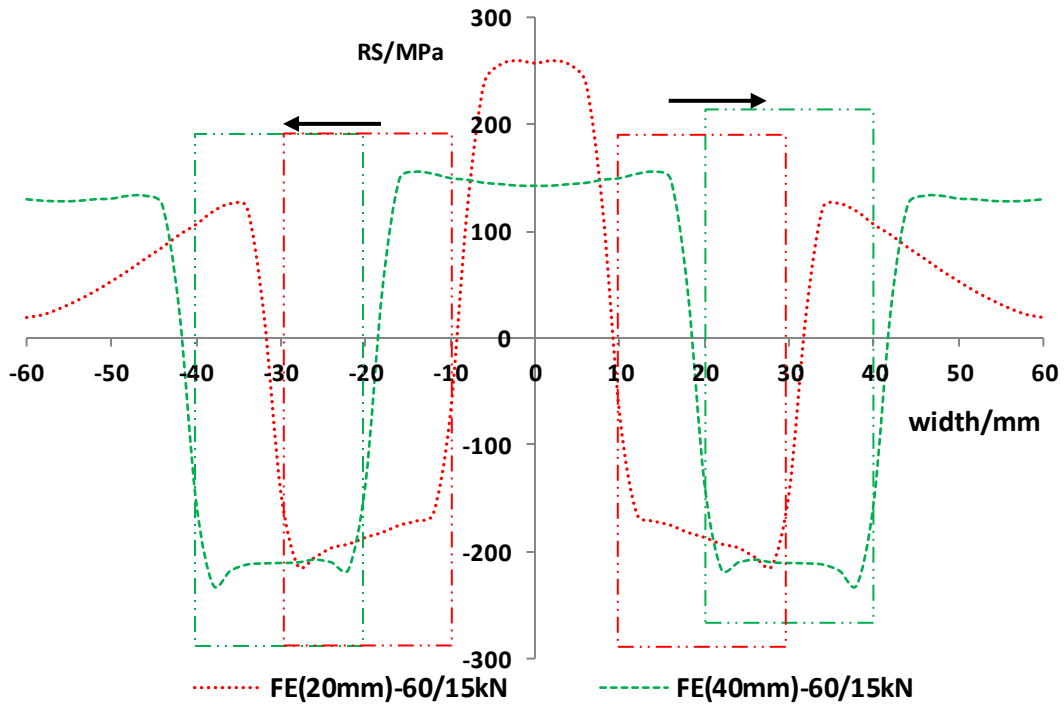
Figure 5.27 Residual stress distribution in the middle width, red dot curve represents RS and corresponding the rolled area of the red rectangular shape; green dot curve represents RS and corresponding the rolled area of the green rectangular shape

In figure 5.27, 20 mm of FE (20mm)-60/15kN represents the untreated width between two rolled regions is 20 mm. 40 mm of FE (40 mm)-60/15kN represents the untreated width between two deep rolled is 40 mm.

Residual stress results of FE (40mm)-60/15kN in figure 5.27 were used in the analytical method, for the calculation of K_{res}, illustrated in chapter 6.

The slit effects were discussed in chapter 7.

5.5 Conclusions

In this chapter, finite element simulations of deep surface rolling were presented. Isotropic hardening and kinematic hardening were applied to deep rolled samples of CS1. The meshing and friction sensitivity were studied and validated with experiments. Distortion and residual stresses of certain FE models were compared to experimental results. The effects of deep rolling loads were analysed by the comparison of distortion behaviours and residual stress distribution at the cross-section of the middle width. Rollers in different locations had a great influence on the distribution of residual stress. Through the analysis of FE results, main conclusions could be summarised below.

- Kinematic hardening was applied and contributed to more accurate results in this research.
- The high density meshing size (1×1×0.16 mm^3) significantly improved the accuracy of simulation in this FE analysis.
- The friction coefficient (0.1/0.1) was verified to offer the acceptable accuracy of FE models in this work.
- Samples were deep rolled on both upper and lower surfaces could be well realised, and the FE results of distortion and residual stress were consistent with experimental results in most aspects.
- The result of FE(40mm)-60/15kN in figure 5.23 was applied to Chapter 6.

6 Effects of Residual Stress on Stress Intensity Factor

In this chapter, the effects of residual stress on SIFs are illustrated in detail. Methods of calculating an effective stress intensity factor range for untreated samples and the DSR samples, are shown in section 6.1. Without considering the effects of residual stress fields, the stress intensity factor range (ΔK) of untreated samples were calculated by applying geometry factors and Newman approaches, and the results are plotted against FCGR and shown in section 6.2. In the next section 6.3, the process of computing residual stress intensity factors (K_{res}) is illustrated in considerable detail Effects on FCGR, using superposition and crack closure theory, are given in section 6.4. By applying the residual stress summarised from chapter 5, FCGRs are predicted and compared to experimental results, and they are presented in section 6.5. Finally, a conclusion is drawn in section 6.6.

6.1 Method of Calculating Stress Intensity Factor

For centre-slit samples, the fundamental relationship of SIF and FCGR is derived from Paris Law. In this research, fatigue testing samples had a centre-slit of 8 mm (2a) and the geometry of CS3. The stress-intensity range, corresponding to a given crack growth rate, is calculated from the following equation 6.1.

$$\Delta K = \frac{\Delta P}{B} \sqrt{\frac{\pi \alpha}{2W} \sec \frac{\pi \alpha}{2}} \qquad 6.1$$

$$\Delta P = P_{max} - P_{min} \ for \ R > 0; \ \Delta P = P_{max} \ for \ R \leq 0$$

Where α = 2a/W, a is for the crack size (half the crack length in the centre-slit specimen), ΔP is force range in fatigue experiments, W is the sample width, B is the sample thickness, R is the external load ratio. Only $R = 0.1$ is applied to all fatigue tests of untreated samples. The type of loads and the geometry of specimens influence the computed ΔK value. For DSR or HP treated samples,

equation 6.1 is not valid. Equation 6.1 doesn't consider the effects of residual stress fields or crack closure.

The effect on the applied SIF range on DSR or HP treated samples was calculated by using the modified superposition method. The maximum total stress intensity factor ($K_{tot,max}$) is calculated using equation 6.2 below.

$$K_{tot,max} = K_{app,max} + K_{res} \quad 6.2$$

The minimum total stress intensity factor ($K_{tot,min}$) is calculated using equation 6.3 below. This method accounts for crack face contact effect by setting values of $K_{tot,min}$ that are less than zero as equal to zero.

$$K_{tot,min} = \textbf{if}(K_{app,min} + K_{res}) \begin{cases} \leq 0, & 0 \\ > 0, & K_{app,min} + K_{res} \end{cases} \quad 6.3$$

For the stress intensity factor range (ΔK), K_{res} does not influence ΔK_{app}, as shown in equations 6.4 to 6.6 below.

$$\Delta K_{tot} = K_{tot,max} - K_{tot,min} \quad 6.4$$

$$\Delta K_{tot} = (K_{tot,max} + K_{res}) - (K_{tot,min} + K_{res}) \quad 6.5$$

$$\Delta K_{tot} = K_{tot,max} - K_{tot,min} = \Delta K_{app} \quad 6.6$$

At values of $K_{tot,min}$ greater than zero, ΔK_{tot} and ΔK_{app} are equivalent to values calculated in equation 6.1. However at values of $K_{tot,min}$ less than zero, ΔK_{tot} is equal to $\Delta K_{tot,max}$.

Another method using the Newman crack closure theory to calculate the stress intensity factor range, was also considered, and is detailed in section 2.2. In this research, all samples are 1.6 mm thickness (much smaller than the width of the samples), plane stress conditions were applied by using the Newman equation.

An effective SIF range (ΔK_{eff}) was calculated using equation 6.7.

$$\Delta K_{eff} = \left[\frac{1 - \sigma_{op}/\sigma_{max}}{1 - R} \right] \Delta K_{app} \quad 6.7$$

For residual stress bearing materials, the stress ratio R was replaced with the effective stress ratio R_{eff}. The effective stress ratio (R_{eff}) was calculated using equation 6.8.

$$R_{eff} = \frac{K_{tot,min}}{K_{tot,max}} \qquad 6.8$$

In the modified superposition approach, when $K_{tot,min} \leq 0$, the $R_{eff} = 0$. For the Newman method, a R_{eff} of less than zero is considered and applied to the calculation of crack opening stress ratios, prior to using the $K_{tot,max}$, when $K_{tot,min}$ approaches to negative values.

In the Newman equation, there is no clear solution for the $K_{tot,max}$ approach to negative values. Very high compressive residual stresses were obtained after DSR treatments, as shown in section 4.3. $K_{tot,max}$ could feasibly show negative values in cases where the crack had propagated into the compressive region. This research investigates the possible solutions for the situation of $K_{tot,max} \leq 0$.

6.2 Computing ΔK_{app} and ΔK_{eff} of Untreated Samples

In this section, both ΔK_{app} and ΔK_{eff} are calculated, and plotted against FCGR in untreated samples. ΔK_{app} is based on the equation of 6.1, while ΔK_{eff} is calculated by using the Newman equation (accounting for the crack opening stress ratio). Results are shown in figure 6.1. SIFs were calculated according to ASTM E647, and plotted against FCGRs in untreated samples as shown in section 4.5. Paris constants were obtained from the power fitting of ΔK_{app} and ΔK_{eff} against FCGR. A power trendline was fitted to the linear of the data in figure 6.1, and the constants C and n equal to 2.8×10^{-10} (AA2524) and 2.85 (AA2524), 2×10^{-10} (AA2024) and 3 (2024).
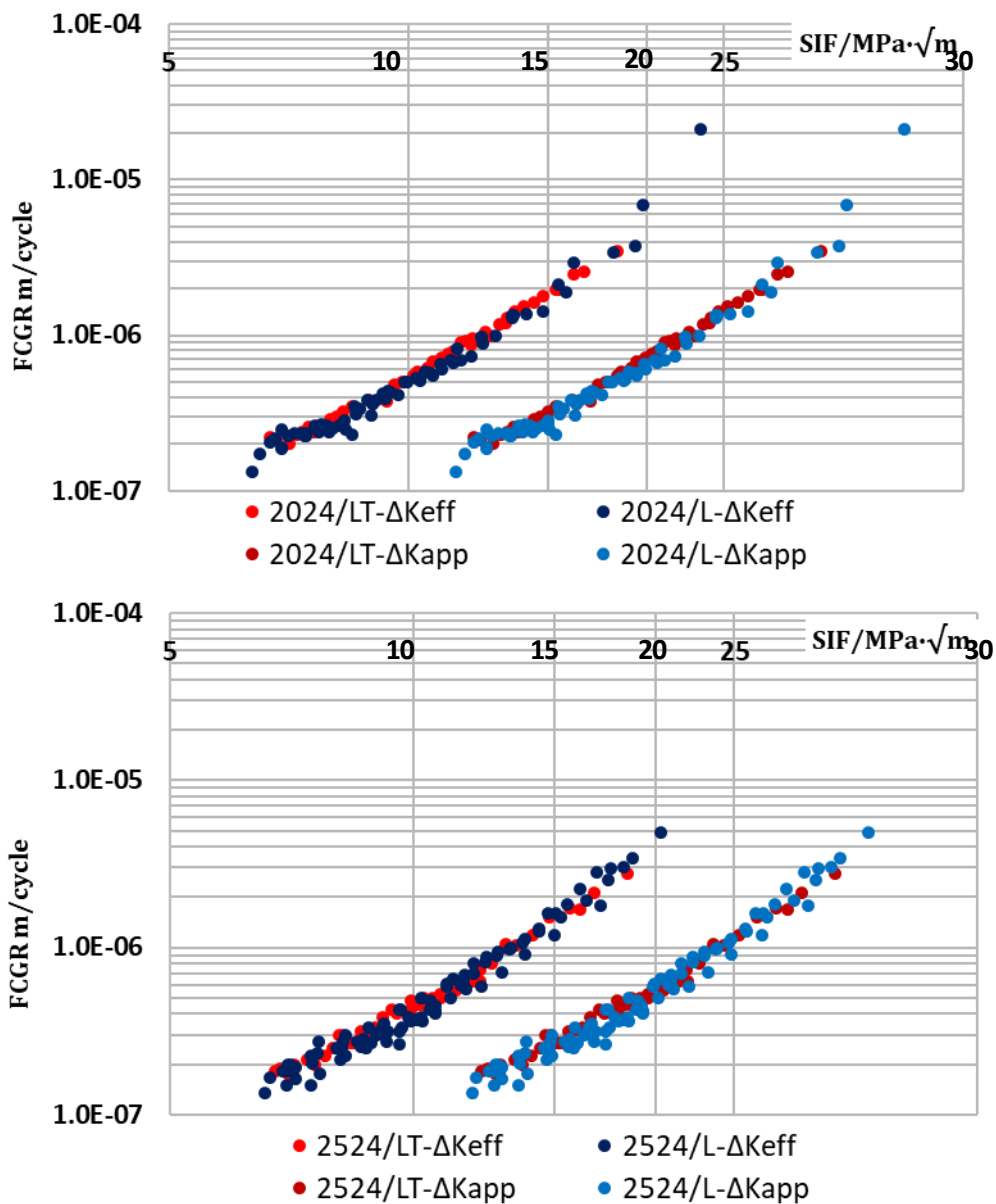
Figure 6.1 The stress intensity factor range ∆K against FCGR of baseline AA2024 and AA2524, respectively, calculated by equation 6.1 (ASTM standard) and Newman equation regarding the crack opening stress ratio

In section 4.6, the Paris constants of untreated samples (AA2024-T351) were compared to already published work, and the values found in this experimental study showed a good agreement with those in the literature. Without the consideration of any residual stress in components, ΔK_{app} can only be determined by the external load pattern, while ΔK_{eff} is computed differently by using the Newman equation.

Further sections investigate the methods of calculating residual stress intensity factors.

6.3 Calculated Residual Stress Intensity Factors

Although the distributions of induced residual stress always show diverse characteristics and profiles, due to the different surface treatment processes, from the numerical integration method point of view, the load acting on the crack length Δa can be treated as a point load when Δa is infinitesimal. Therefore, all the weight functions, including the approximate forms, developed for the point load can be applied for calculating SIFs resulting from the distributed residual stress.

As mentioned in section 2.1, the universal function of the SIF for the crack-free stress distribution by integration, was shown in equation 2.11. 60/15kN and 20/10kN loads were applied to two specimens of CS3. Measured residual stresses, using Neutron Diffraction, were averaged through the entire thickness by using the Riemann sum formula (shown in section 3.6.3). Accordingly, results were analysed and matched against the cosine function, shown in figure 6.2 and 6.3. In both figures, the grey rectangular strips are the areas where DSR was applied.

The different functions of residual stress distribution are given in table 6.1. All functions, along with measured RS results from the DSR (60/15kN) sample, are plotted and compared in figure 6.2.

By importing two experimental values of measured residual stresses (from ND results) to the different weight functions, the coefficients can be determined, and the functions are plotted in figure 6.2. After the matching process, the cos6πx function demonstrates a better agreement with experimental results, if results between 40 mm and 60 mm widths are not taken into account. Moreover, by observing numerous fatigue testing samples during the practical testing, it was noted that the fatigue crack started at the slit and ended before the 40 mm width point.

Table 6-1 Lists of equations to match the residual stress distribution in the absence of external loads

Welding RS by WFM	$\sigma(x) = \sigma_0 \cdot e^{-\frac{1}{2}\left(\frac{x}{c}\right)^2} \left[1 - \left(\frac{x}{c}\right)^2\right] + C$
cos4πx function	$\sigma(x) = \sigma_0 \cos\frac{4\pi x}{W} + C$
cos6πx function	$\sigma(x) = \sigma_0 \cos\frac{6\pi x}{W} + C$
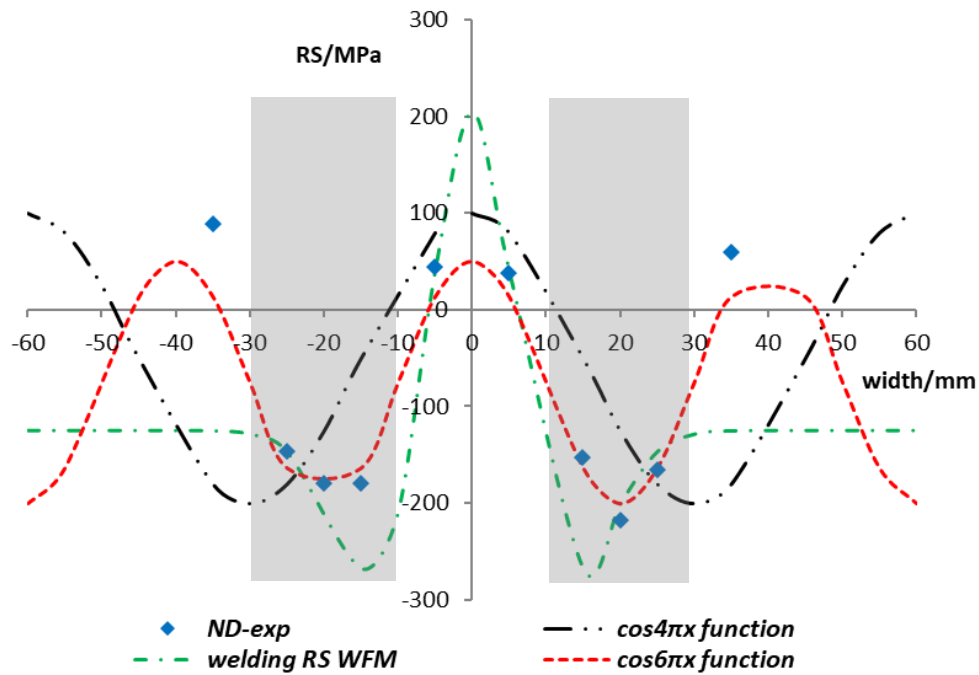
Figure 6.2 Configuration of investigating the matched functions of residual stress distribution in the absence of external loads, where blue marks are the averaged residual stresses measured by neutron diffraction, other dash curves are the equations of residual stress distribution based on the superposition principle

Cosine functions were compared with the experimental RS values found on two samples rolled under different loads and measured by using ND. Results of residual stress induced by two DSR parameters were shown in section 4.3.3. By averaging the three values of each measured position, results are summarised in figure 6.2.
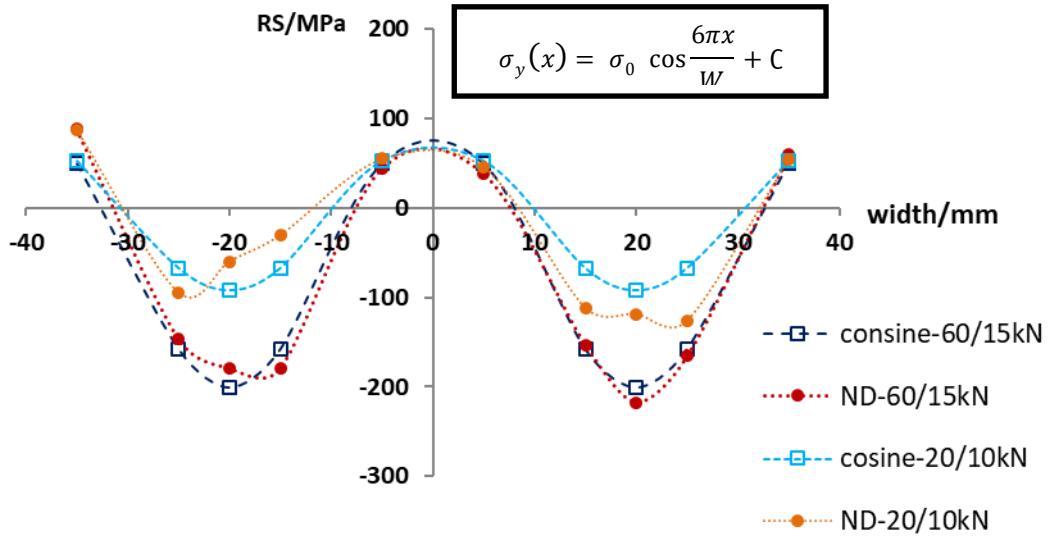
Figure 6.3 Cosine functions applied to compare the experimental RS data of 60/15kN and 20/10kN DSR samples. Material is AA2524-T351

In figure 6.3, the cosine function of 60/15kN has a better agreement with experimental values than the function of 20/10kN. The accuracy of measured residual stress data can influence the constants of cosine functions (σ_0 and C) by calculating the cosine function from the Neutron diffraction data.

After the function of residual stress distribution is determined, the SIFs for the crack-free stress distribution can be calculated by using integration equation 6.9 [58].

$$K_{res} = \frac{2}{\sqrt{\pi a}} \int_0^a \frac{\sigma(x)}{\sqrt{1 - \left(\frac{x}{a}\right)^2}} \, dx \qquad 6.9$$

By importing the $\sigma(x)$ listed in table 6.1, K_{res} can be calculated by integration as shown in equation 6.10.

$$K_{res} = \sigma_0\sqrt{\pi a}J_0\left(\frac{6\pi a}{W}\right) + C\sqrt{\pi a} \qquad 6.10$$

Where J_0 is the Bessel functions for integer order is 0. Matlab can help to calculate the part of $J_0(\frac{6\pi a}{W})$.

In figure 6.4, the residual stress distribution $\sigma(x)$ (red curve) and the calculated K_{res} (blue curve) of deep rolled samples (60/15kN and 20/10kN) are plotted together.
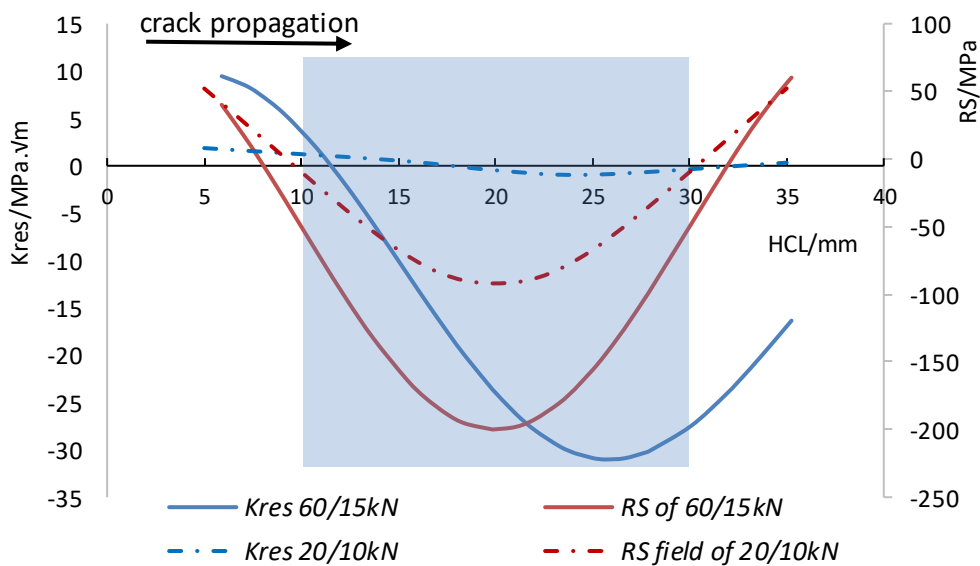
Figure 6.4 Residual stress distribution of 60/15kN DSR sample and 20/10kN DSR sample and integrated K_{res} by Green's function, where the rolled area is shaded in blue

In figure 6.4, the X-axis represents the half crack length of M(T) specimens. The first Y-axis represents the K_{res} values. The second Y-axis represents the residual stress distribution in the absence of external loads. In the treated sample rolled under 60/15kN loads, the maximum value of compressive residual stress is 200

MPa at 20 mm away from the centreline of the sample (also at the centreline of the rolled area). Whilst the maximum value of negative K_{res} is 30 MPa·√m at 25 mm away from the centreline of the sample (0 mm in figure 6.4). The treated sample rolled under 20/10kN loads, shows the maximum value of compressive residual stress is 100 MPa at 20 mm away from the centreline of the sample (also at the centreline of the rolled area). Whilst the maximum value of negative K_{res} is less than 5 MPa·√m at 25 mm away from the centreline of the sample (0 mm in figure 6.4).

The sensitivity of calculating K_{res} is associated with practical residual stress fields, resulting from various aspects. Thus, it is necessary to discuss the sensitivity that K_{res} has on the effect of residual stress fields (using cosine function or FE results). The calculation process of all DSR treated samples followed the same procedure. Modified superposition and the Newman approach of used on the DSR treated sample (60/15kN) were compared using factors $K_{tot,max}$, $K_{tot,min}$, $K_{app,max}$, $K_{app,min}$, ΔK_{tot}, ΔK_{eff}, in relation to K_{res}.

In section 6.1, the superposition method was used to calculate $K_{tot,max}$, $K_{tot,min}$ when accounting for the K_{res}. However, this method only considers when $K_{tot,min}$ is greater than zero. On the other hand, the Newman method considers the effect of negative $K_{tot,min}$. In fact, the calculation is only invalid when $K_{tot,max}$ approaches zero and negative values. The effect on the SIF range and effective stress ratios of residual stress fields is considered in figure 6.5, where K_{tot} is calculated by the superposition method.
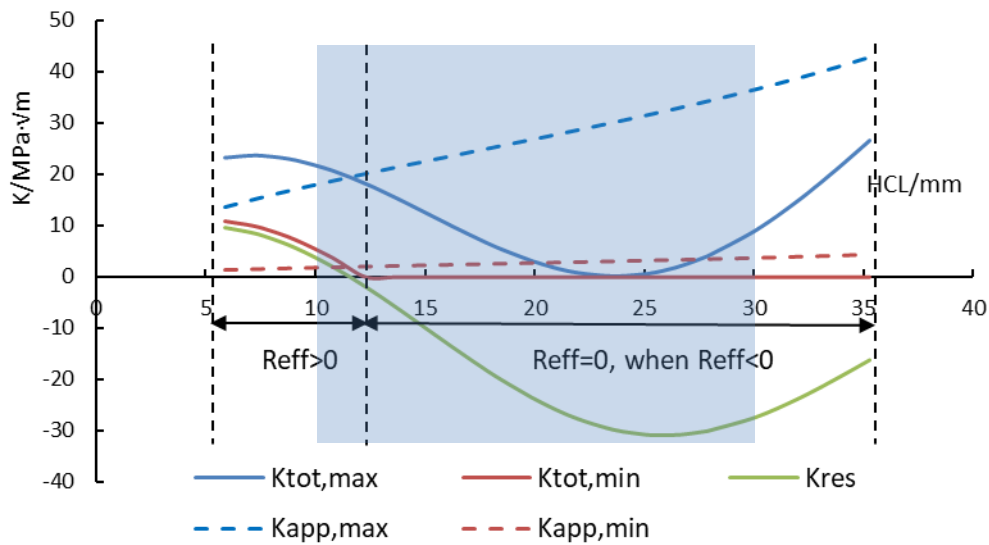
Figure 6.5 The effect on SIF range and stress ratio by using the superposition method, applied load ratio $R = 0.1$, 60/15kN applied to an AA2524-T351 sheet of CS3

By using the modified superposition method, R_{eff} is determined from $K_{tot,max}$ and $K_{tot,min}$. For the modified superposition approach when $K_{tot,min} \leq 0$ the $R_{eff} = 0$. In figure 6.6, the stress intensity factor range and stress ratio were calculated using superposition and the Newman crack closure approach. Results are presented and compared between two different DSR samples (20/10kN and 60/15kN loads) and against untreated samples. ΔK_{eff} of untreated samples were calculated by using Newman equations. The superposition method is was applied in order to calculate ΔK_{tot} of DSR samples. K_{max} was used in place of ΔK_{tot} when $R_{eff} < 0$. ΔK_{eff} of deep rolled samples were derived by using the Newman crack closure approach.
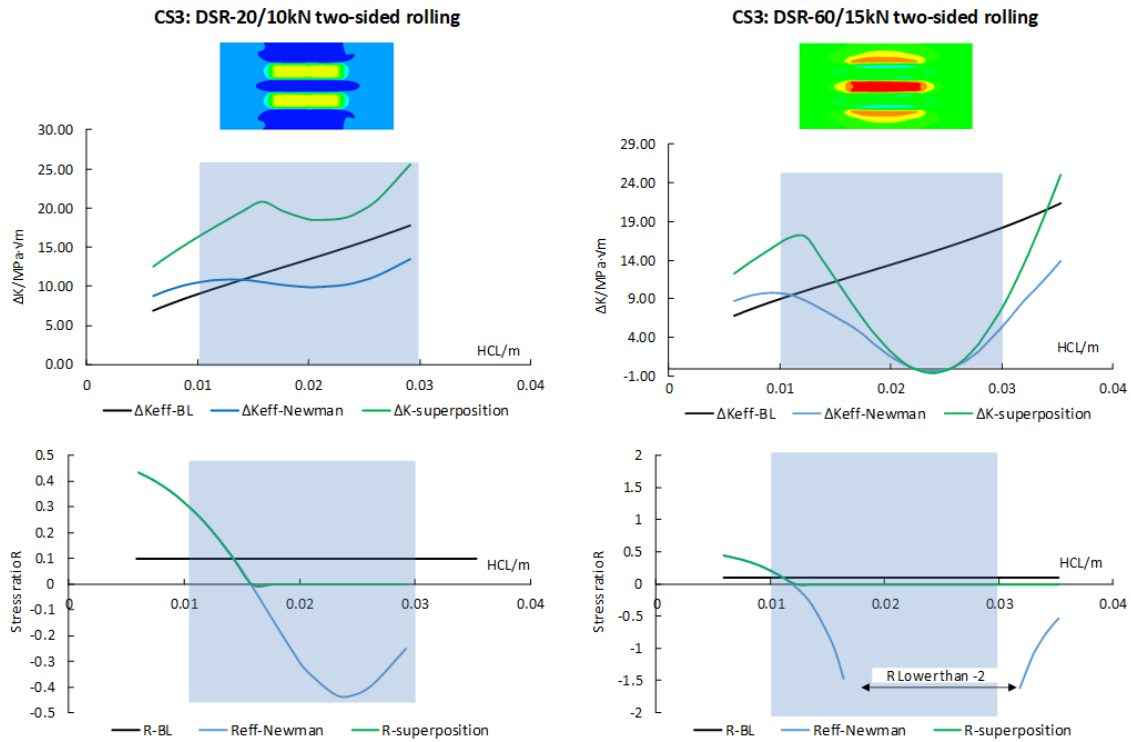
Figure 6.6 Stress intensity factor range and stress ratio calculated using superposition and Newman crack closure approach, the blue rectangular shape represents the rolled area. DSR 20/10kN and DSR 60/15kN, CS3, *R =0.1*

The modified superposition method accounts for crack face contact, by setting values of $K_{tot,min}$ that read less than zero, as equal to zero. Because the compressive residual stress field is distributed over a wide range and the extent of negative values of K_{res} is significant, the modified superposition method might not provide an accurate result if negative $K_{tot,min}$ was equal to zero. The stress ratio calculated using the Newman approach in the deep rolled sample (60/15kN), demonstrated that over 10 mm length was below −2 within the rolled area.

Slit samples of CS3 were deep rolled by a load of 60/15kN. However, the untreated area, between two rolled strips, was 40 mm wide, as shown in section 5.3. Residual stresses were obtained from the FE models, along with the direction

of the crack propagation. The cosine function was used to calculate K_{res}. The predicted RS field of the middle cross-section and integrated K_{res} are shown in figure 6.7.
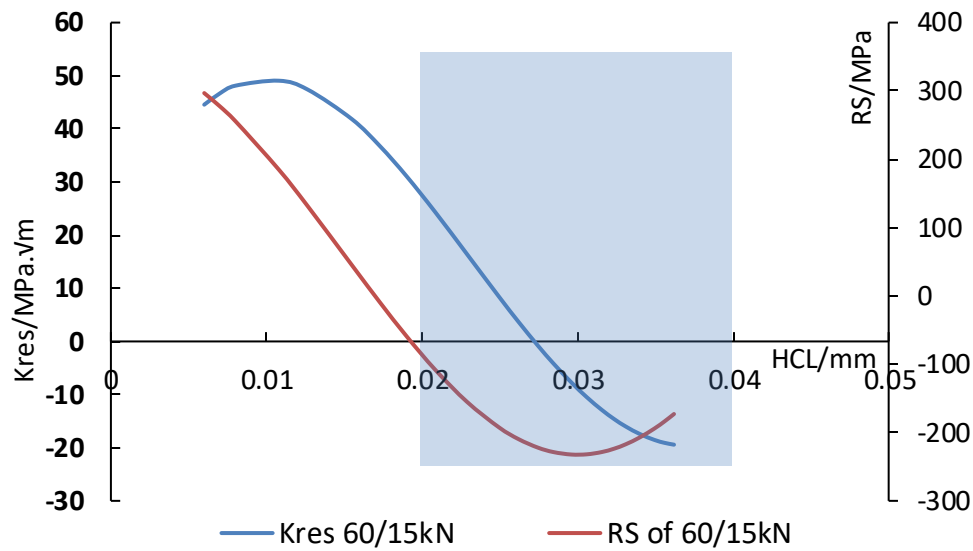
Figure 6.7 Residual stress distribution of the DSR sample (60/15kN) and integrated K_{res} by Green function, where the rolled area is shaded in blue

The stress intensity factor range and stress ratio were calculated by using superposition and the Newman crack closure approach. Two external load ratios 0.1 and −0.1 were applied in fatigue tests. Results are presented in figure 6.8.
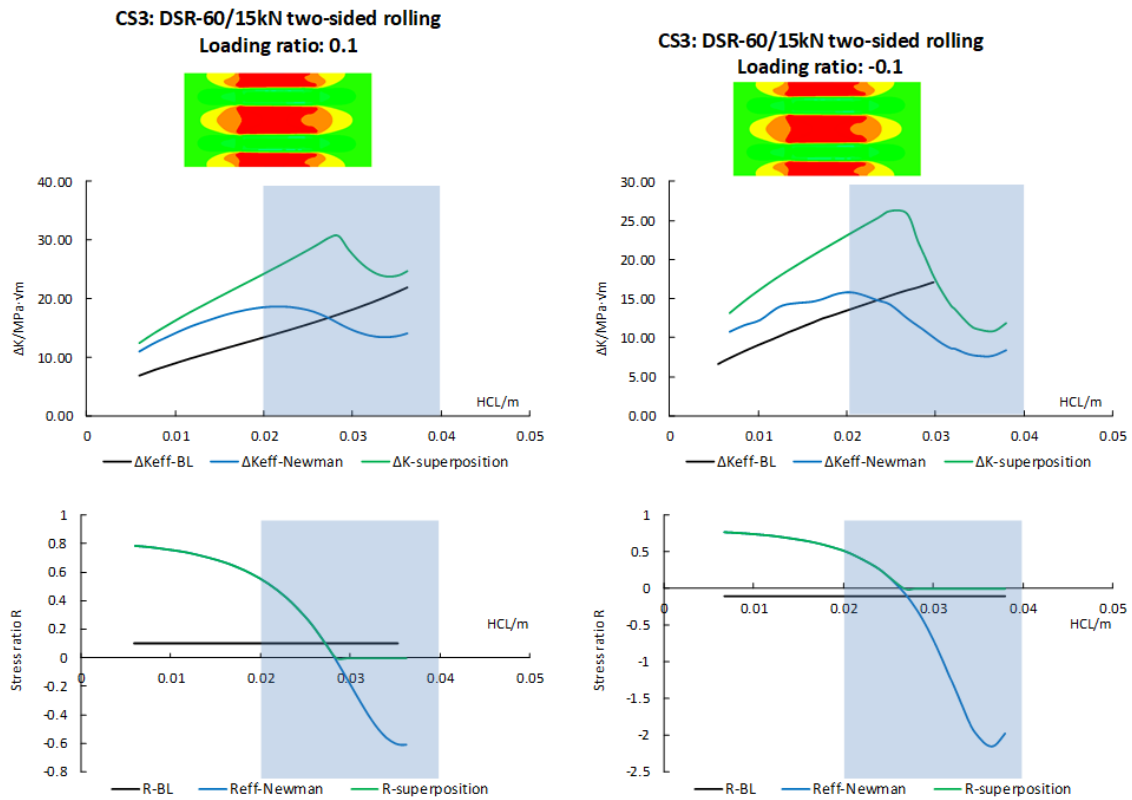
Figure 6.8 Stress intensity factor range and stress ratio calculated using superposition and Newman crack closure approach, the blue rectangular shape represents the rolled area. 60/15kN applied to both centre-slit samples of CS3, different external stress ratios 0.1 and −0.1, respectively

6.4 Effects on FCGR by Superposition and the Newman Approach

In order to validate the effects of stress ratios, a comprehensive comparison of all methods used in this research, and the experimental results could be of vital significance. Fatigue tension-tension tests were conducted, and FCGRs were calculated in section 4.5. Based on the FCGR of baseline data, the Paris law (equation 6.11) is applied in this further step of the evaluation.

$$\frac{da}{dN} = C\Delta K^n \qquad 6.11$$

In Paris law, C and n are the material constants determined, as shown in section 6.2. ΔK is calculated by the superposition and Newman crack closure methods. In section 6.3, R or R_{eff} and ΔK_{eff} were calculated by superposition and the Newman crack closure method.

In figure 6.9, calculated FCGRs of two models are compared to the results of the untreated sample and the DSR treated sample under 20/10kN loads. The hollow circle in black represents the FCGR of the untreated sample (BL) resulting from experimental data. The solid circle in red represents the FCGR of the DSR sample with 20/10kN loadings, calculated from experimental results extracted using ND. The hollow square in green represents the calculated FCGR of DSR samples, by using the superposition method (SP). The hollow square in blue represents the calculated FCGR of DSR samples by using the Newman crack closure approach (Nm). The blue shaded rectangles represent the deep rolled areas, along with the width from 10 mm to 30 mm of each side.

Figure 6.9 Effects of the superposition and Newman crack closure approach on FCGR, compared using untreated (BL) and DSR specimens, applied load ratio *R* = 0.1, applied loads 20/10kN

In figure 6.9, both superposition and Newman methods show a good fitting to experimental FCGR results from the deep rolled sample, within deep rolled areas. Close to the slit, the Newman approach demonstrated a better correlation with experimental values. At 35 mm away from the centre of the sample, both models were disappointing and yielded mismatching results, in comparison to results taken from the DSR specimen (red).

The cosine function, applied in figure 6.9, continued to calculate K_{res} in the comparison to FCGR results measured over the full crack length. The results are demonstrated in figure 6.10. Variables in figure 6.10 are the same as described above. The secondary value represents the R_{eff} by using equation 6.8.

Figure 6.10 Effects of the superposition and Newman crack closure approach on FCGR, compared using untreated (BL) and DSR specimens (full scale of measured data along half width of the sample), applied load ratio *R = 0.1*, applied loads 20/10kN

In figure 6.10, the prediction of the Newman crack closure approach (in blue) showed a better prediction compared to experimental results (in red), before R_{eff} became negative. However, the prediction of Newman crack closure approach overlapped with the superposition result, when R_{eff} was negative. The maximum compressive residual stress (CRS) induced by 20/10kN loads was only 100 MPa, as shown in figure 6.3. The calculated K_{res} was only -3 MPa√m, corresponding to the maximum CRS, resulting in no significant effect on the predicted FCGR by using two methods. Another sample treated by 60/15kN loads investigated the effect of a significant RS field on FCGR.

Figure 6.11 Effects of the superposition and Newman crack closure approach on FCGR, compared using untreated (BL) and DSR specimens, applied load ratio _R_ = _0.1,_ applied loads 60/15kN

In figure 6.11, application of the Newman model resulted in problems solving the stress ratio R < 0, as values at 20 mm and 25 mm from the centre show. Superposition cannot be accurate in predicting the FCGR resulting from the ΔK_{max}, as results tended to be negative. Figure 6.12 gives the predicted results of Newman and superposition in comparison to FCGR results measured along the full crack length. The secondary value of R_{eff} was calculated by using the equation 6.8.
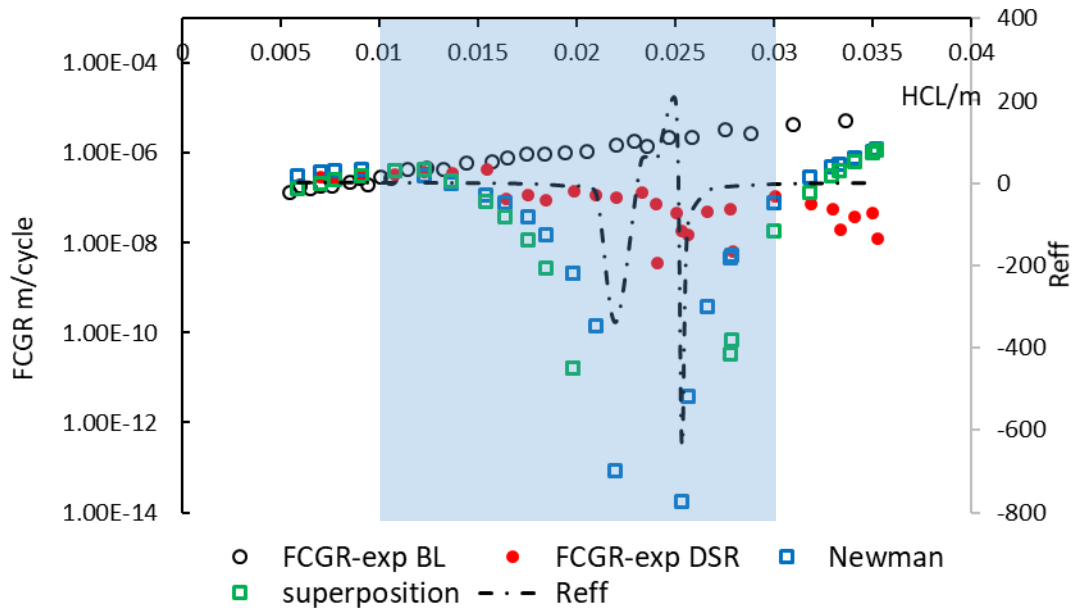
Figure 6.12 Effects of the superposition and Newman crack closure approach on FCGR, compared using untreated (BL) and DSR specimens (full scale of measured data along half width of the sample), applied load ratio *R = 0.1*, applied loads 60/15kN

In figure 6.12, the FCGR was increasing, even when the crack tip extended into the deep rolled area. However, the FCGR slowed down at 15 mm away from the centreline of the sample (0 mm). Two turning points of R_{eff} are found at 17.5 mm and 27 mm. Between 17.5 mm and 27 mm, all calculated R_{eff} values were less than −2 and the Newman equation was unable to predict the FCGR accurately. When the crack propagated through the rolled area (the compressive region), predicted FCGRs by both methods were lack of accuracy. However, in this deep rolled sample, a crack branch propagated along with an angle to the previous crack path (after 30 mm away from the centreline), shown in figure 6.13a. A deviation of crack propagation was observed and shown in figure 6.13b.
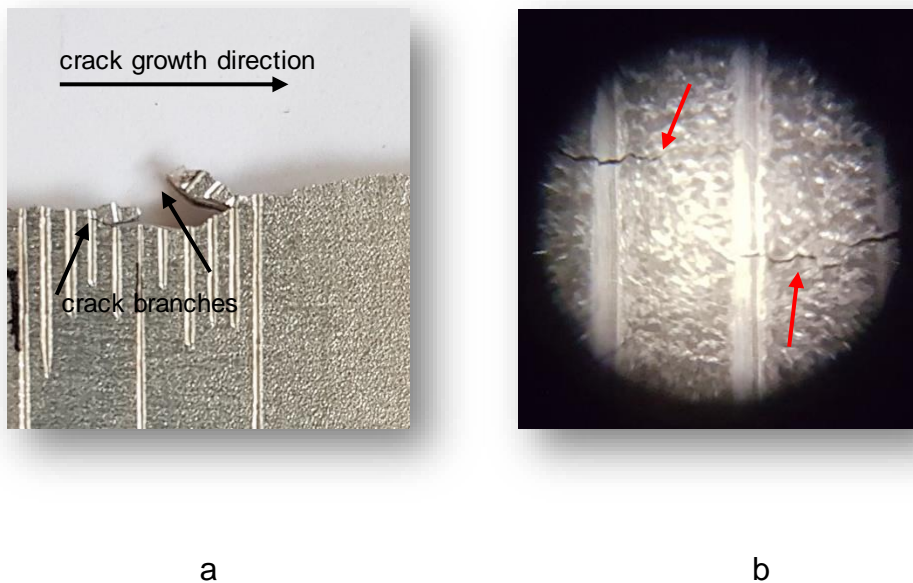
Figure 6.13 The observation of crack trajectory changes a) crack branch; b) crack deviation

Branched fatigue crack and deviations were observed at the interface between the rolled region and outside of the rolled strips. It could be caused by the uneven surface of the specimens, which resulted in the non-uniform stress field at the interface, after deep rolling. Another possible reason could be the dramatic changes of the residual stress field. Within the rolled region, ΔK was mainly affected by the localised residual stress being highly compressive. The residual stress out of the rolled region remained tensile, perpendicular to the crack propagation direction. Therefore, the crack propagation presented an unpredictable behaviour in this region. There are few published models for crack trajectory predictions and no adequate results for illustrating this effect. Further research is necessary to understand these effects using finite element analysis.

6.5 Prediction of FCGR using FE results

Centre-slit samples (CS3) were deep rolled under loads of 60/15kN. Residual stresses were obtained by using FE models, as shown in section 5.4.3. Deep rolled samples were fatigue tested using two different external stress ratios, 0.1 and −0.1.

In this section, residual stress results obtained from FEA were used to determine the K_{res}. Following the same procedures as in the SIFs and stress ratios used above, FCGR could be predicted and compared to the experimental results from analysis of FCGR.

Figure 6.14 gives the predicted FCGR of the Newman and superposition approaches in comparison to experimental results measured along the full crack length. The secondary value of R_{eff} was calculated by using the equation 6.8.
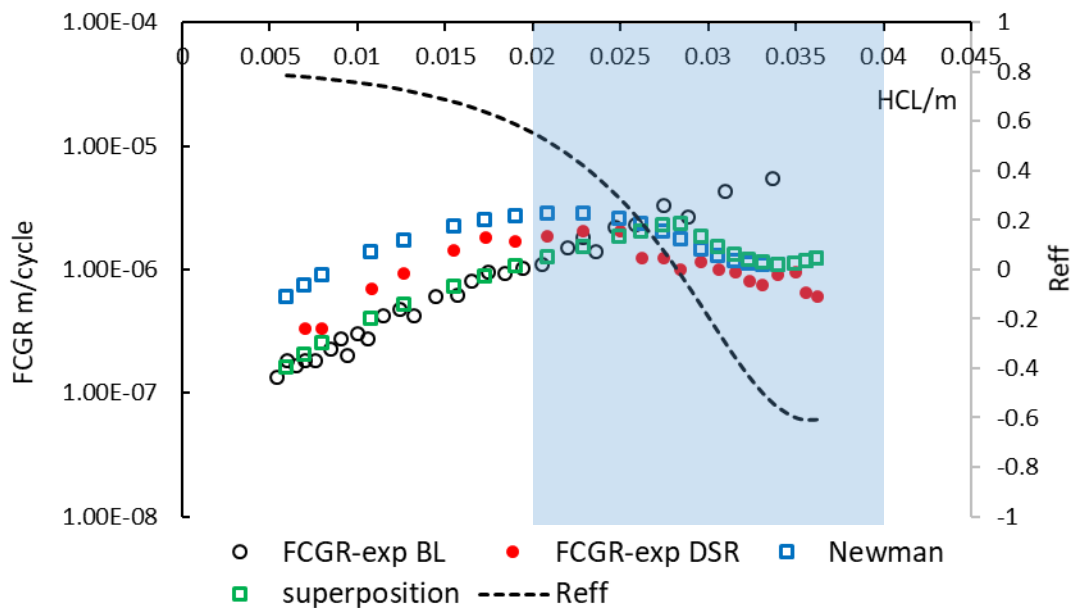
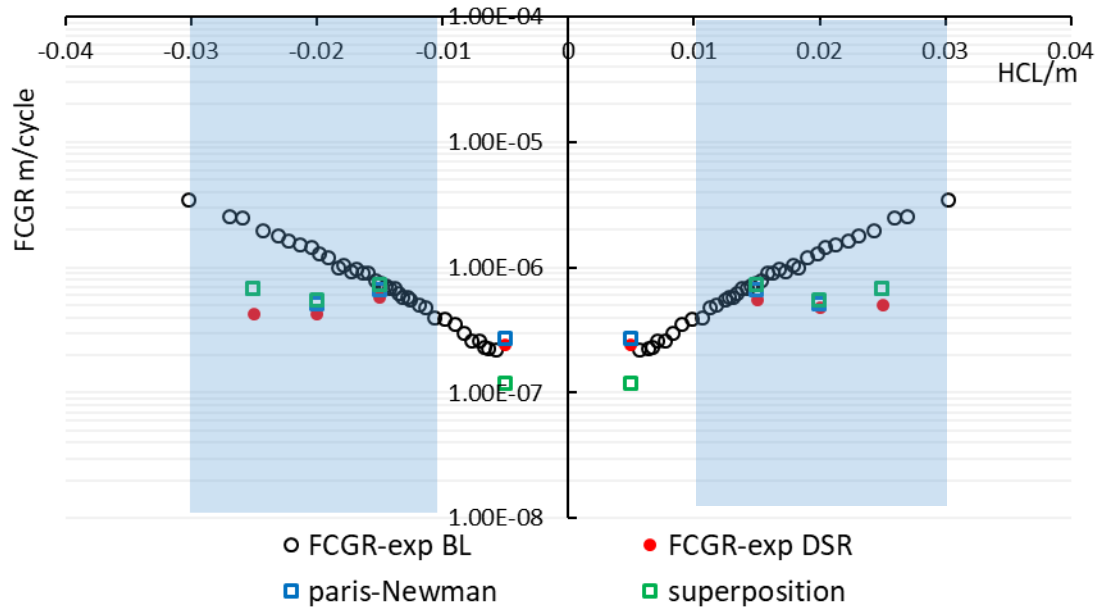**Figure 6.14 Effects of the superposition and Newman crack closure approach on FCGR, compared using untreated (BL) and DSR specimens (full scale of measured data along half width of the sample), applied load ratio R = 0.1, applied loads 60/15kN**

When the fatigue crack started from the slit, the calculated FCGR of the sample analysed using the Newman method was higher than the rate determined in the experimental FCGR specimen. This is resulting from the higher tensile residual stress obtained by using FE models. However, predicted FCGRs by both the superposition and Newman method, showed a good agreement with the experimental results within the rolled area. Within the rolled area, FE models can predict better results of residual stress fields, in comparison to compromised tensile stress area at the out of rolled strips. According to the comparison, the computed residual stress fields were shown to be more tensile than those revealed in the results of the practical experiments using deep surface rolled specimens.

Another fatigue test was carried out under $R = -0.1$ (external stress ratio). Centre-slit samples of CS3 were deep rolled using the same loads 60/15kN. The rolled regions were the same as in figure 6.14. Results of FCGRs predicted by the Newman method and by superposition are compared to those FCGRs found in experimental results, as shown in figure 6.15. R_{eff} was obtained by using Newman equations.
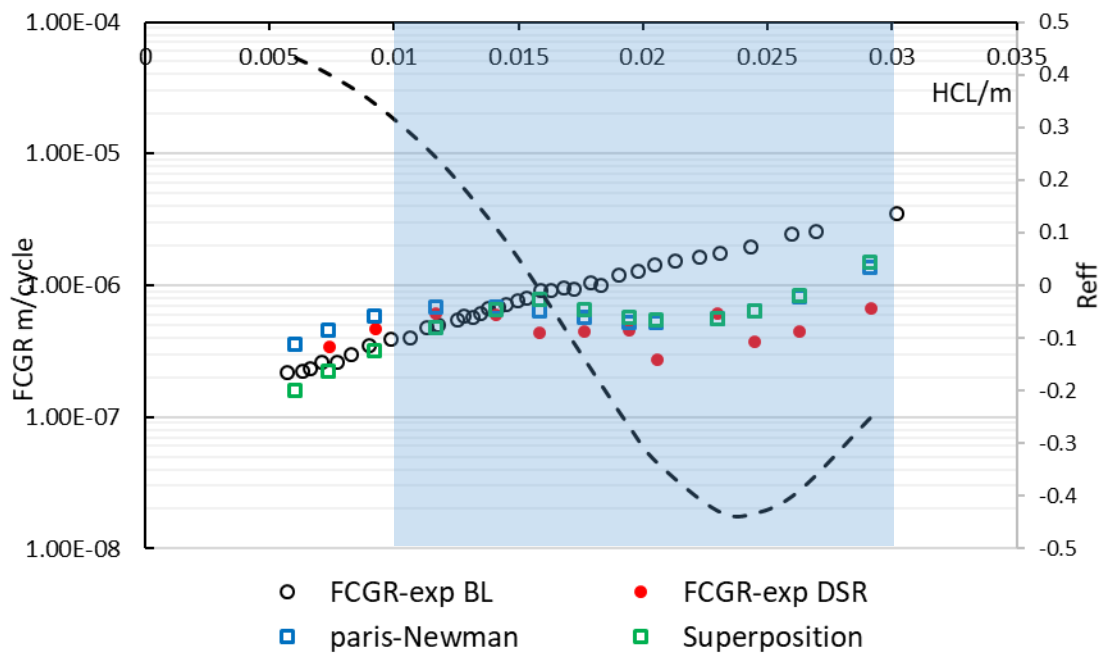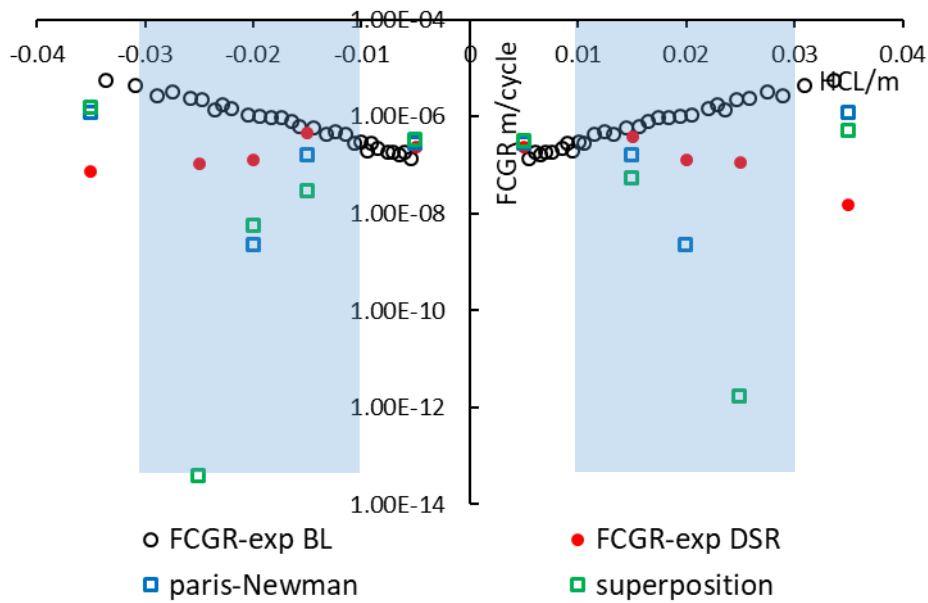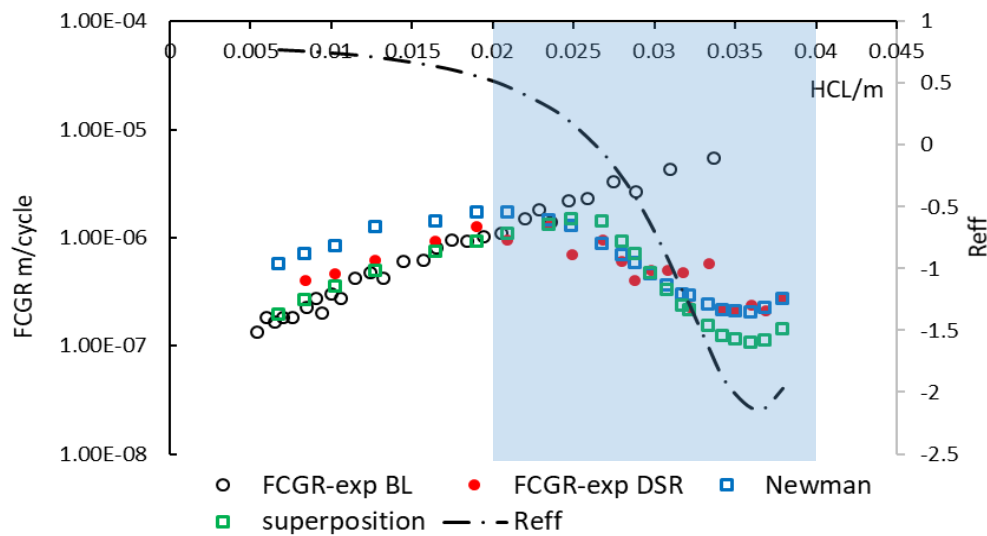
Figure 6.15 Effects of the superposition and Newman crack closure approach on FCGR, compared using untreated (BL) and DSR specimens (full scale of measured data along half width of the sample), applied load ratio *R* = −0.1, applied loads 60/15kN

FCGR of the untreated sample shown in figure 6.15 was obtained under external stress ratio *R* = 0.1.

Similar to the earlier results, the predicted FCGR by Newman method was higher than in the experimental results, in the length before the crack propagated into the rolled area. In the rolled area, both methods predicted a reduction in FCGR. Results of figure 6.15 clearly reveal that Newman prediction shows better fit when R_{eff} is between −1 and −2. Compared with the superposition, Newman crack closure can more accurately predict the FCGR within high compressive residual stress field, or when the negative load ratio is applied.

FCGRs predicted by the Newman crack closure approach demonstrated quite a good agreement with results from experimental FCGRs.

7 Discussion

One of the main objectives of the current investigation was to predict fatigue crack growth rates, within the induced residual stress fields, in deep surface rolled samples with a centre-slit. Residual stress fields within treated samples were evaluated by experimental measurements (ICHD or ND) and finite element models. In comparison to the use of a scattergram to display the measured residual stress field, the cosine function was considered to be an appropriate fitting approach. K_{res} was integrated by applying the Green's function. The superposition principle and the Newman crack closure theory were used to determine the ΔK. FCGR was predicted by using the Paris law, and validated by comparing to experimental results.

The first section mainly discusses the shortcomings of DSR treatments in this research. The second section discusses the differences between the FE models of the DSR process alongside the experimental DSR process. The third section discusses in more detail the K_{res} integration by applying the cosine function of residual stress fields. The fourth section discusses the slit effects on residual stress fields. Finally, a summary of this chapter is given at the end.

7.1 Discussion of DSR Treatments

Deep surface rolling (DSR) has been used to reduce the distortion and tensile residual stress of welded components for years. However, DSR is rarely applied to stress-free samples, with an aim to reduce the FCGR and improve fatigue performance. The main reason for this inapplicability is the significant distortion DSR can cause to a material.

In this research, the DSR process was optimised in order to try and reduce this massive distortion. Moreover, the compressive residual stress field was not significantly compromised and still demonstrated a dramatic effect on fatigue performance. Two DSR parameters were applied to the centre-slit sheets of CS3.

Maximum values of distortion and compressive residual stress were measured and then compared to the results of untreated samples (BL). The fatigue life improvement factor (LIF) of different treatments was calculated and compared to BL samples, as shown in figure 7.1.

Another study of the pre-crack located within the compressive residual stress field was also investigated. The results of maximum distortion and the LIF of this treatment are included in figure 7.1; the annotation 'DSR-30/18kN cover notch' represents this treatment.
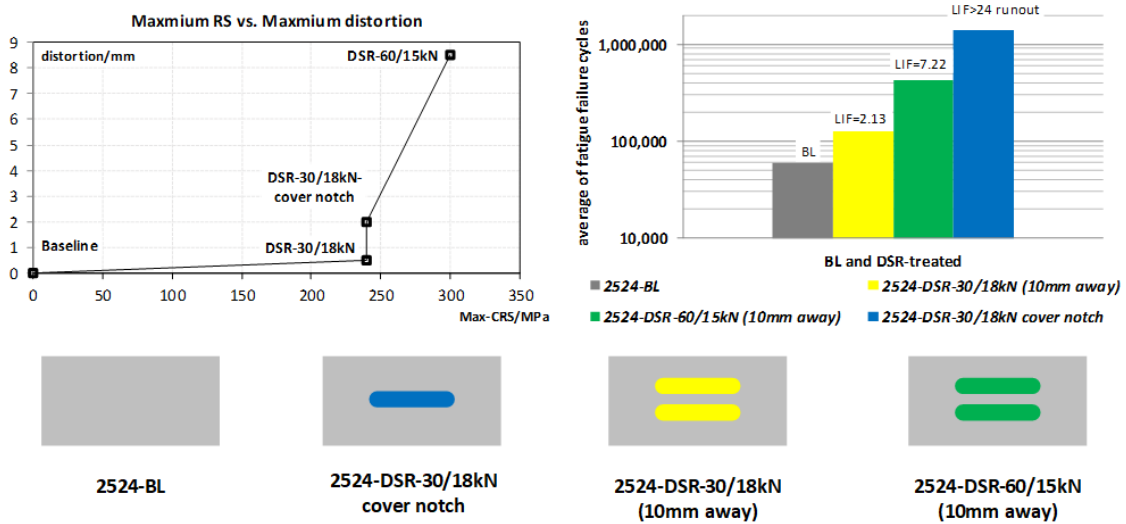
Figure 7.1 Results of fatigue life, maximum values of distortion and compressive residual stress, induced by different DSR treatments, in comparison to the untreated sample (BL)

Samples treated by DSR-60/15kN loads (LIF=7.22) and DSR-30/18kN loads (LIF=2.13) provided an effective improvement on fatigue performance, while DSR was shown to significantly improve fatigue performance if the DSR-strip thoroughly covers the slit. Although the load parameter of 60/15kN, as shown in figure 7.1, gave large distortion, the fatigue performance showed significant improvement. The load parameter of 30/18kN gave lower distortion, and the

fatigue performance showed good improvement, even though the compressive residual stress was compromised by reducing the rolling loads.

Figure 7.2 demonstrated the effect on hardness and residual stress by using the load parameter of 60/15kN, applied to AA2524-T351.
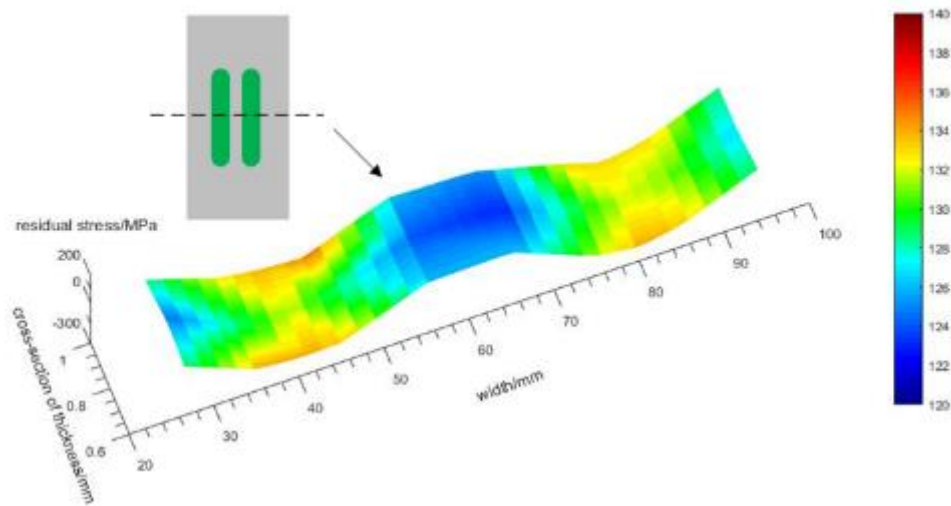
Figure 7.2 Effects on hardness and residual stress distribution by DSR treatment (load parameter, 60/15kN), AA2524-T351 sheet

In section 4.2, along with the thickness and within the deep rolled area, the increase in hardness is up to 5 HV, in comparison to the hardness ~~of~~ evaluated in untreated samples. The increase in hardness measured within the deep rolled area, as shown in figure 7.2, was about 8 HV. The closer to the rolled surface, the higher the value of hardness was obtained. The sample was deep rolled by applying a higher load parameter (60/15kN) as seen in figure 7.2, whilst the result after using the load parameter of 30/18kN was given in section 4.2. The area within the higher compressive residual stress field, resulted in higher values of hardness, as shown in figure 7.2.

7.2 Differences of FE Modelling Compared to DSR

Finite element models successfully simulated the deep surface rolling process, more particularly, in samples rolled on both surfaces, good fitting predictions were achieved. This research contained the meshing sensitivity and friction sensitivity study. The prediction of FE models could fit better with experiments if more consideration about the meshing and friction refinement were taken into.

In practical terms, when applying DSR to CS3 samples, four times deep rollings were accomplished on two surfaces. Pre-rolled areas were marked in lines by hand on both surfaces of the sample. Even though the laser marker can assist to keep an equal travel distance of each rolling, it was still challenging to keep four rolled strips perfectly symmetrical, due to the use of manual controls. As a result, the residual stress fields could not be symmetrically distributed through the thickness and the width.

For the FE study of CS3 (un-slited samples), in order to save computing time of the FE models, two rollers were used to deep roll once on one surface, instead of rolling twice on one surface by a single roller. This simplification gave an error when averaging the residual stress field in the thickness and the width.

The rolled sheet was distorted and bent towards the rolled surface after one-sided rolling. For two-sided DSR processes, an external force was applied to keep the distorted sheet flat before rolling on the opposite surface. At the same time, the sheet was constrained by the clamping system. In FE models, two-sided DSR was implemented by using a pre-defined stress field. This stress field was derived from the FE results of one-sided DSR, i.e. when the DSR was over, and there was no longer any contact between the sheet and the roller (the sheet remained flat due to the applied clamping).

In FE models used for this research, the frictional interaction between the roller and the workpiece was assumed as 0.1. However, it is known that this could influence the residual stress distribution. Coules [118] reported that both the frictionless and friction models produced virtually the same residual stress

distribution when low loads were applied. The frictional interaction displayed strong effects on the residual stress distribution when large rolling loads were used (higher loads than 100kN in the Coules study). The highest load used in this research was 60kN.

In section 6.5, FCGRs of two samples were predicted within the residual stress field induced by using FE results. All FE predicted FCGRs were higher than the experimental FCGRs, as was evidenced outside of the deep rolled area. Residual stress predicted by using FEA showed a higher tensile residual stress field in the out of the rolled area, compared to experimental results from using ND. FE simulation demonstrated a more balanced residual stress field, with a balance of tensile RS and compressive RS along the width.

7.3 Effects of Residual Stress Fields on K_{res}

In this research, the cosine function was the method used to describe the residual stress field induced by DSR treatments. The cosine function was derived from the scatter diagram of measured RS. Residual stress fields of rolled sheets were initially measured by using the Neutron diffraction technique. There were no other functions used to determine K_{res} and further prediction of FCGR.

For averaging residual stress under plane stress conditions, this research used the Riemann Sum formula, as shown in section 3.6.3.

Mathematical calculation of K_{res} was obtained by using Green's function. The FGCRs of the known residual stress fields were predicted and compared to experimental FCGRs resulting from fatigue tests.

Taddia [193] evaluated the effectiveness of the laser shock peening (LSP) in reducing the fatigue in thin aluminium specimens (2mm thickness).
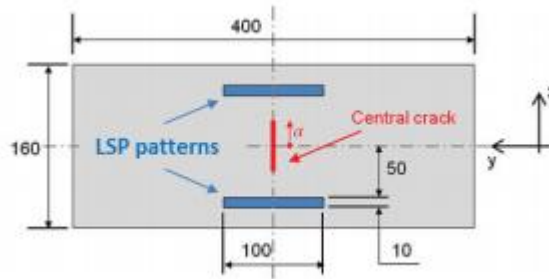
Figure 7.3 Configuration of the M(T) specimen and LSP treated pattern [193]

The function $\sigma_y(x)$ described the residual stress field perpendicular to the crack propagation. This analytical formulation of the residual stress profile was proposed by Tada [194]:

$$\sigma_y(x) = \sigma_0 \frac{\left[1-\left(\frac{x-L}{c}\right)^2\right]}{\left[1+\left(\frac{x-L}{c}\right)^4\right]} \qquad 7.1$$

Where L is the distance between the crack centre and the LSP pattern centreline, c is the representative of the point in which the residual stress field changes from tensile to compressive and σ_0 is the maximum value of the compressive residual stress. The residual stress field by analytical evaluation showed that tensile residual stresses were distributed in both the sides of the LSP pattern in order to restore the global stress equilibrium of the panel.

The tensile stresses predicted at the inlet to the shot pattern were lower than those at the exit, explaining the moderate acceleration in crack propagation, in respect to the baseline. Fatigue crack propagation slowed down in the central area subsequently, until the crack reached the pinned line (the edge of the laser peened area). A final sharp increase of FCGR could be predicted when the crack reaches the tensile stress field.

The qualitative conclusion of Taddia somewhat matched the experimental and predicted FCGR results in this research. However, in his work, there was a lack of residual stress measurements outside of the peened region.

Kashaev [11] measured LSP induced residual stress field by employing the synchrotron technique. In the laser peened area, the maximum value of compressive stress was about 100 MPa. One of the laser peened samples indicated slightly higher FCGR from the initial crack tip to a/W = 0.36 (CT specimen, a_0 = 10mm, W = 50mm). This result can be explained as being due to the presence of tensile residual stress, through the thickness, at the front of the crack tip. Compared to the untreated samples, the FCGR demonstrated significant retardation in the growth rate, when the crack propagated through the LSP treated area that contained high compressive residual stresses through the thickness. Similar results of FCGRs were found in sections 6.4 and 6.5. The most significant retardation in the FCGR was observed when the fatigue crack propagated through the DSR area containing high compressive residual stresses, through the thickness.

7.4 Investigation of Centre-slit (notch) Effects

The centre-slit in stress-free samples was made by using EDM. Results of induced residual stress fields were obtained by measuring deep rolled samples without a slit in the centre. The effects of a centre-slit on residual stress fields were investigated by using FE analysis.
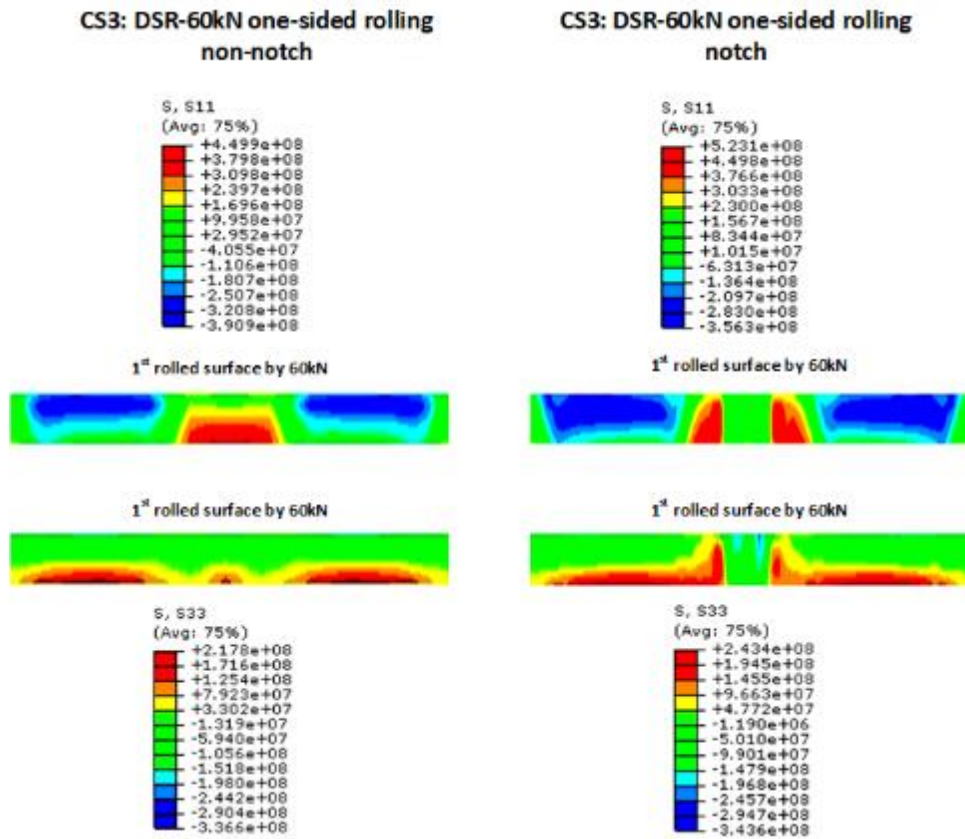
Figure 7.4 Centre-slit effects on residual stress fields compared to deep rolling of one surface by the load parameter of 60kN (Unit: Stress/Pa)

The effect of centre-slits on residual stress fields was simulated by applying the same slit geometry in the FE model as in the physically experimental sample. The mesh of the FE modelled slit sample was irregular around the centre-slit. The computing time proved costly to simulate all treatments with centre-slit samples; as a result, only one load parameter was investigated and analysed in this section, as shown in figure 7.4. In general, there was little effect from the centre-slit, on the residual stress field.

Summary of the discussions

Hypotheses in this research have been demonstrated step by step, as shown in the above chapters. The following conclusions are made based on this research presented.

i. Deep surface rolling (DSR) applied to both surfaces (upper and lower) when the rolling load applied to the lower surface reduced, the distortion could be significantly reduced. The maximum distortion could be reduced to about 2 mm (load parameters 30/18kN, M(T) sheet, 1.6 mm in thickness).

ii. Compressive residual stresses were generated and fully distributed through the thickness when using specific load parameters, 30/18kN and 60/15kN.

iii. Samples treated by DSR at 60/15kN loads (LIF=7.22) and DSR at 30/18kN loads (LIF=2.13) provided effective improvement on fatigue performance, whilst DSR was shown to significantly improve fatigue performance if the DSR-strip can fully cover the centre-slit (notch).

iv. A finite element model (FEM) was developed based on the kinematic hardening of material properties, to simulate the DSR process. Distortion and residual stresses were mainly used to validate the accuracy of models. The result of meshing density study showed that the high density model (element size $1 \times 1 \times 0.1$ mm^3) was more consistent with the experimental data, both in the distortion behaviour and the residual stress field. The model with the friction coefficient 0.1/0.1 being applied showed a better agreement with the experiments by examining the effect of friction sensitivity.

v. Distortion resulting from deep rolling process was predicted by using three dimensional FE models and showed a good agreement with experimental measurements.

vi. Residual stress (RS) values, predicted by using FE models demonstrated a good agreement with experimental results at the thickness, especially within the deep rolled area.

vii. An analytical method was used to describe the residual stress field, based on the results measured by using Neutron Diffraction. The RS derived by the analytical method was contributed to calculating residual stress intensity factor (K_{res}) by Green's function.

viii. The superposition and Newman crack closure methodologies as a basis for fatigue crack growth rate (FCGR) were compared. The Newman crack closure approach resulted in a quite good agreement with the experimental measurements of crack growth behaviour.

ix. A meritorious work has been successfully concluded to link the predicted RS of FE models with the prediction in FCGR, under plane stress conditions. Calculations using the Newman crack closure approach showed a good agreement with the experimental results within the deep rolled areas.

x. The crack propagation trajectories were influenced by the different DSR strips, as reported in section 4.6. In addition, the crack branches and crack deviations were observed at the interface between the rolled region and outside of the rolled strips, as shown in figure 6.13. Unfortunately, no reliable models which can predict fatigue crack path deflection with respect to 3D residual stress field.

xi. Specimens were distorted due to the DSR processes, but were forced to an almost flat sheet during clamping on the testing machine. This meant that initial strains were built up within the specimens, before the external loads were applied. These initial strains might be significant to fatigue crack growth rates if the initial distortion was significantly induced.

8 General Conclusions and Future works

Deep surface rolling (DSR) can easily induce compressive residual stress when compared to laser shock peening, and substantial distortion could be intentionally reduced by optimising the process. A finite element model was developed to simulate the DSR process and was validated by experimental results. DSR-FE models were flexibly used to compare distortion and residual stress by adjusting loads, the geometry of roller and workpieces. An analytical method was explored to calculate the process of K_{res}. The prediction of fatigue crack growth rate (FCGR), based on superposition and Newman crack closure approaches, can match well with experimental results. There is a significant effect on fatigue performance by repositioning the DSR treated locations away from the crack. For aerospace structures designed in accordance with the damage tolerance principles, DSR could be optimised to improve the fatigue performance. In practical structural design, deep surface rolling process could be performed at where defects may occur, or applied to the potential defects as close as possible if the structural components are irregular and difficult to treat.

Recommendations below are proposed for future work.

i. FE models can be further optimised by more involved studies of slit effects and friction interaction.

ii. Along the thickness, different regions could be divided up according to the differences of residual stress field. The FCGR can be predicted in different regions by using the analytical method.

iii. The mathematical process of K_{res} could possibly be compared with another analytical method (based on 'a crack perpendicular to the weld bead').

iv. The crack trajectories were reported in this research. Future work aims to identify the residual stress field by applying various DSR process, related to the fatigue crack trajectories.

v. The effect of different distortion on fatigue crack growth rate will be further studied through calibration measurements on initial strains.

9 REFERENCES

1. Kaufmann, M. (2009). *Cost Optimization of Aircraft Structures*. KTH Stockholm, PhD Thesis.

2. Transport Canada (2004). *Paint and sealant removal process*, Airworthiness Notice No. B071.

3. Chang, K.-H. (2013). *Chapter 4 - Fatigue and Fracture Analysis*. In K.-H. Chang (Ed.), Product Performance Evaluation with CAD/CAE (pp. 205–273). Boston: Academic Press.

4. Andersson, F., Hagqvist, A., Sundin, E., & Björkman, M. (2014). Design for manufacturing of composite structures for commercial aircraft-The development of a DFM strategy at SAAB aerostructures. *Procedia CIRP*, *17*, 362–367.

5. Salah, K. (2014). Environmental impact reduction of commercial aircraft around airports. Less noise and less fuel consumption. *European Transport Research Review*, *6*(1), 71–84.

6. Toor, P. M. (1973). A review of some damage tolerance design approaches for aircraft structures. *Engineering Fracture Mechanics*, *5*(4), 837–880.

7. Wanhill, R. J. H. (2018). Fatigue Requirements for Aircraft Structures. In *Aircraft Sustainment and Repair* (pp. 17–40). Elsevier.

8. I. altenberger, in: shot peening (ed. l. walker), will-VCH, weight, 2003, p. 421.

9. P. Strigens, Dr.-lng. Thesis, University of Darmstadt, 1971.

10. H. Wiegand, P. Strigens, Draht 20 (1969) 189.

11. G. Berstein, B. Fuchsbauer, Z. Werkstofftech. 13 (1982) 103.

12. Altenberger, I. (2005). Deep Rolling -The Past, The Present and The Future. *In: Proc. 9th Int. Conf. Shot Peening*, 144–155.

13. Altenberger, I. (2005). Alternative Mechanical Surface Treatments for Fatigue Strength Enhancement. *Materials Science Forum*, *490–491*, 328–333.

14. Kashaev, N., Ventzke, V., Horstmann, M., Chupakhin, S., Riekehr, S., Falck, R., Huber, N. (2017). Effects of laser shock peening on the microstructure and fatigue crack propagation behaviour of thin AA2024 specimens. *International Journal of Fatigue*, *98*, 223–233.

15. Nalla, R. K., Altenberger, I., Noster, U., Liu, G. Y., Scholtes, B., & Ritchie, R. O. (2003). On the influence of mechanical surface treatments-deep rolling and laser shock peening-on the fatigue behavior of Ti-6Al-4V at ambient and elevated temperatures. *Materials Science and Engineering A*, *355*(1–2), 216–230.

16. Hatamleh, O. (2006). Effects of Laser and Shot Peening on Friction Stir Welding, PhD. Thesis, University of South Carolina.

17. Cuellar, S. D., Hill, M. R., Dewald, A. T., & Rankin, J. E. (2012). Residual stress and fatigue life in laser shock peened open hole samples. *International Journal of Fatigue*, *44*, 8–13.

18. Altenberger, I., Nalla, R. K., Noster, U., Scholtes, B., & Ritchie, R. O. (1760). On the Fatigue Behavior and Associated Effect of Residual Stresses in Deep-Rolled and Laser Shock Peened Ti-6Al-4V Alloys at Ambient and Elevated Temperatures. *University of California, Berkeley*, *94720* (510).

19. Polmear, I. J. (2005). 7 - Novel materials and processing methods. In I. J. Polmear (Ed.), *Light Alloys (Fourth Edition)* (pp. 367–412). Oxford: Butterworth-Heinemann.

20. Benachour, M., Dahaoui, M., Benachour, N., Cheikh, A., & Benguediab, M. (2013). Effect of levels of residual stress at notch on fatigue crack growth. In *13th International Conference on Fracture 2013, ICF 2013* (Vol. 3, pp. 2059–2068).

21. Liljedahl, C. D. M., Zanellato, O., Fitzpatrick, M. E., Lin, J., & Edwards, L. (2010). The effect of weld residual stresses and their re-distribution with crack growth during fatigue under constant amplitude loading. *International Journal of Fatigue*, *32*(4), 735–743.

22. Anderson, T.L. (2005) Fracture Mechanics Fundamentals and Applications, 3rd ed., CRC Press.

23. Hertzberg, R.W., Vinci, R.P. and Hertzberg, J.L. (2012). Deformation and Fracture Mechanics of Engineering Materials, 5th ed., John Wiley & Sons.

24. Nagar, A. (1988). Fatigue Crack Growth in Aircraft Main Landing Gear Wheels. *Fracture Mechanics: Nineteenth Symposium, STP969-EB, Cruse, T., Ed., ASTM International, West Conshohocken, PA*, pp. 868-882.

25. Newman, J. C. (1999). Analysis of fatigue and crack-growth under constant and variable amplitude loading. Ann Fract Mech, 16, 24-35.

26. Schijve, J. (2009) Fatigue of Structure and Materials, 2nd ed., Springer.

27. Newman, J. C. (1988). Short-crack growth behaviour in an aluminium alloy—an AGARD cooperative test programme. AGARD R-732, Neuilly-sur-Seine, France.

28. Edwards, P. R. and Newman, J. C., Jr., eds., "Short-Crack Growth Behaviour in Various Aircraft Materials," AGARD R-767, 1990.

29. Newman, J. C., Jr., Wu, X. R., Venneri, S. and Li, C. (1994). Small-Crack Effects in HighStrength Aluminum Alloys. NASA RP-1309.

30. Pearson, S. (1975). Initiation of Fatigue Cracks in Commercial Aluminum Alloys and the Subsequent Propagation of Very Short Cracks. Engineering Fracture Mechanics, Vol. 7, No. 2, pp. 235-247.

31. Ohji, K. (1983). Introduction to Fracture Mechanics. *Journal of the Society of Materials Science, Japan*, *32*(359), 935–941.

32. Schijve, J. (1988). Fatigue crack closure observations and technical significance. J. C. Newman, Jr. & W. Elber (eds), Mechanics of Fatigue Crack Closure. ASTM STP 982: 5-34.

33. Irwin, G. (1957). Analysis of Stresses and Strains near the End of a Crack Traversing a Plate. Journal of Applied Mechanics, 24, 361-364.

34. Paris, P. C., & Erdogan, F. (1973). A Critical Analysis of Crack Propagation Laws. *J. Basic Engng*, *85*, 528–534.

35. Wolf, E. (1970). Fatigue crack closure under cyclic tension. *Engineering Fracture Mechanics*, *2*(1), 37–45.

36. Key to Metals AG. (2001). Fatigue crack growth. *Total Materia*.

37. Cleveringa, H. H. M., Van der Giessen, E., & Needleman, A. (2000). A discrete dislocation analysis of mode I crack growth. *Journal of the Mechanics and Physics of Solids*, *48*(6–7), 1133–1157.

38. Kenny, P., & Campbell, J. D. (1968). Fracture toughness an examination of the concept in predicting the failure of materials. *Progress in Materials Science*, *13*, 135–181.

39. Maierhofer, J., Pippan, R., & Gänser, H.-P. (2014). Modified NASGRO equation for physically short cracks. *International Journal of Fatigue*, *59*, 200–207.

40. Walker, K. (1970). The effect of stress ratio during crack propagation and fatigue for 2024-T3 and 7075-T6 aluminum. ASTM STP 462.

41. Forman, R.G., Hearney, V.E., & Engle, R.M. (1967). Numerical analysis of crack propagation in cyclic-loaded structures. Journal of Basic Engineering, vol. 89, pp. 459-464.

42. Klesnil, M. & Lukas, P. (1972). Influence of strength and stress history on growth and stabilistaion of fatigue cracks. Engineering Fracture Mechanics, vol. 4, pp. 77- 92.

43. Forman, R.G. & Mettu, S.R. (1992). Behavior of surface and corner cracks subjected to tensile and bending loads in Ti-6A1-4V alloy. ASTM STP 1131.

44. Schnubel, D. & Huber, N. (2012). The influence of crack face contact on the prediction of fatigue crack propagation in residual stress fields. Engineering Fracture Mechanics, vol. 84, pp. 15-24.

45. LaRue, J.E. & Daniewicz, S.R. (2007). Predicting the effect of residual stress on fatigue crack growth. International Journal of Fatigue, vol. 29, no. 3, pp. 508-515.

46. Kang, K.J., Song, J.H. & Earmme, Y.Y. (1989). Fatigue crack growth and closure through a tensile residual stress field under compressive applied loading. Fatigue and Fracture of Engineering Materials and Structures, vol. 12, no. 5, pp. 363-376.

47. Elber, W. (1971). The significance of crack closure. ASTM STP 486, pp. 230-242.

48. Beghini, M. & Bertini, L. (1990). Fatigue crack propagation through residual stress fields with closure phenomena. Engineering Fracture Mechanics, vol. 36, no. 3, pp. 379-387.

49. Parker, A.P. (1982) Stress intensity factors, crack profiles, and fatigue crack growth rates in residual stress fields. Residual Stress Effects in Fatigue, 776, pp. 13-31.

50. Pouget, G., & Reynolds, A. P. (2008). Residual stress and microstructure effects on fatigue crack growth in AA2050 friction stir welds. *International Journal of Fatigue*, *30*(3), 463–472.

51. AD Krawitz and TM Holden. (1990). The measurement of residual stresses using neutron diffraction. MRS Bull., XV57-64.

52. Pl Webster (1990). The neutron strain scanner: a new analytical tool for engineers' Steel Times. 218 (6), 321-323.

53. A Allen, MT Hutchings and CG Windsor. (1985). Neutron diffraction methods for the study of residual stress fields. Adv Phys., 34, 445-473.

54. S Gungor and C Ruiz. (1997). Measurement of thermal residual stresses in continuous fibre composites. Key Eng. Mat., Vol. 127, 851-859.

55. P J Webster, X D Wang, W P Kang and G Mills. (1995). Experimental verification of residual stress models using neutron strain scanning. Proc. Conf. Modelling of Casting & Welding and Advanced Solidification Processes VII, Edited by M Cross and J Campbell, The Minerals, Metals & Materials Society, 311-318.

56. T. Gnäupel-Herold, R. Schneider, P. Mikula, et al. (2003). Measurement of residual stress in materials using neutrons. Proceedings of a Technical Meeting held in Vienna, IAEA TECDOC No. 1457.

57. X.R. Wu, A.J. Carlsson. (1991). Weight Functions and Stress Intensity Factor Solutions. Pergamon Press, Oxford.

58. Tada HP, Paris C, Irwin GR. (1999). The stress analysis of cracks handbook. ASME Press, New York.

59. McEvily, A.J. (1988). On Crack Closure in Fatigue Crack Growth. ASTM STP 982.

60. Elber, W. (1970). Fatigue crack closure under cyclic tension. Engineering Fracture Mechanics, vol.2, pp. 37-45.

61. McClung, R.C. & Sehitoglu, H. (1989). On the finite element analysis of fatigue crack closure-1. Basic modeling issues. Engineering Fracture Mechanics, vol. 33, no. 2, pp. 237-252.

62. Schijve, J. (1981). Some formulas for the crack opening stress level. Engineering Fracture Mechanics, vol. 14, no. 3, pp. 461-465.

63. De Koning, A.U. (1980). A simple crack closure model for prediction of fatigue crack growth rates under variable amplitude loading. NLR MP 80006.

64. Kujawski, D. (2003). ΔKeff parameter under re-examination. International Journal of Fatigue, vol. 25, no. 9-11, pp. 793-800.

65. Kujawski, D. (2005). On assumptions associated with Δkeff and their implications on FCG predictions. International Journal of Fatigue, vol. 27, no. 10-12, pp. 1267- 1276.

66. Newman Jr., J.C. (1984). A crack opening stress equation for fatigue crack growth. International Journal of Fracture, vol. 24, no. 4, pp. R131-R135.

67. McClung, R.C., Thacker, B.H. & Roy, S. (1991). Finite element visualization of fatigue crack closure in plane-stress and plane-strain. International Journal of Fracture, vol. 50, no. 1, pp.27–49.

68. Pippan, R., & Hohenwarter, A. (2017). Fatigue crack closure: a review of the physical phenomena. *Fatigue and Fracture of Engineering Materials and Structures*, *40*(4), 471–495.

69. Dugdale, D. S. (1960). Yielding of steel sheets containing notchs. Journal of the Mechanics and Physics of Solids, 8, 100–104.

70. Budiansky, B. and Hutchinson, J. W. (1978). Analysis of closure in fatigue crack growth. Journal of Applied Mechanics, 45, 267–276.

71. Newman, J. C. (1981). A crack-closure model for predicting fatigue crack growth under aircraft spectrum loading. in STP 748 Methods and models for predicting fatigue crack growth under random loading.

72. De Koning, A. U. and Liefting, G. (1988). Analysis of crack opening behavior by application of a discretized strip yield model. in STP 982 Mechanics of fatigue crack closure 437–458.

73. Sehitoglu, H. (1985). Crack opening and closure in fatigue. Engineering Fracture Mechanics, 21, 329–339.

74. Vormwald, M. and Seeger, T. (1991). The consequences of short crack closure on fatigue crack growth under variable amplitude loading. Fatigue and Fracture of Engineering Materials and Structures, 14, 205–225.

75. Newman, J. C. (1999). An evaluation of plasticity-induced crack closure concept and measurement methods. in STP 1343 Advances in Fatigue Crack Closure Measurement and Analysis: Second Volume (eds. McClung, R. C. & Newman, J. C.) 128–144.

76. Ewalds, H.L. & Furnee, R.T. (1978). Crack closure measurements along the crack front in center cracked specimens. International Journal of Fracture, vol. 14, pp. R53-R55.

77. Pippan, R. and Riemelmoser, F. O. (1998). Visualization of the plasticity-induced crack closure under plane strain conditions. Engineering Fracture Mechanics, 60, 315–322.

78. Riemelmoser, F. O. and Pippan, R. (1998). Mechanical reasons for plasticity-induced crack closure under plane strain conditions. Fatigue and Fracture of Engineering Materials and Structures, 21, 1425–1433.

79. Riemelmoser, F. O. and Pippan, R. (1997). Crack closure: a concept of fatigue crack growth under examination. Fatigue and Fracture of Engineering Materials and Structures, 20, 1529–1540.

80. Alizadeh, H., Hills, D.A., de Matos, P.F.P., Nowell, D., Pavier, M.J., Paynter, R.J., Smith D.J. & Simandjuntak, S. (2007). A comparison of two and three-dimensional analyses of fatigue crack closure. International Journal of Fatigue, vol. 29, no. 2 pp. 222-231.

81. Beghini, M. & Bertini, L. (1990). Fatigue crack propagation through residual stress fields with closure phenomena. Engineering Fracture Mechanics, vol. 36, no. 3, pp. 379-387.

82. Kang, K.J., Song, J.H. & Earmme, Y.Y. (1990). Fatigue crack growth and closure behaviour through a compressive residual stress field. Fatigue and Fracture of Engineering Materials and Structures, vol. 13, no. 1, pp. 1-13.

83. Choi, H.-. & Song, J.-. (1995). Finite element analysis of closure behaviour of fatigue cracks in residual stress fields. Fatigue and Fracture of Engineering Materials and Structures. vol. 18, no. 1, pp. 105-117.

84. Kang, K.J., Song, J.H. & Earmme, Y.Y. (1989). Fatigue crack growth and closure through a tensile residual stress field under compressive applied loading. Fatigue and Fracture of Engineering Materials and Structures, vol. 12, no. 5, pp. 363-376.

85. Schnubel, D. & Huber, N. (2012). The influence of crack face contact on the prediction of fatigue crack propagation in residual stress fields. Engineering Fracture Mechanics, vol. 84, pp. 15-24.

86. Moshier, M.A. & Hillberry, B.M. (1999). Inclusion of compressive residual stress effects in crack growth modelling. Fatigue and Fracture of Engineering Materials and Structures, vol. 22, no. 6, pp. 519-526.

87. Gozin, M.H. & Aghaie-Khafri, M. (2012). 2D and 3D finite element analysis of crack growth under compressive residual stress field. International Journal of Solids and Structures, vol. 49, no. 23-24, pp. 3316-3322.

88. Liljedahl, C.D.M., Brouard, J., Zanellato, O., Lin, J., Tan, M.L., Ganguly, S., Irving, P.E., Fitzpatrick, M.E., Zhang, X. & Edwards, L. (2009). Weld residual stress effects on fatigue crack growth behaviour of aluminium alloy 2024-T351. International Journal of Fatigue, vol. 31, no. 6, pp. 1081-1088.

89. Wang, C.H., Barter, S.A. & Liu, Q. (2003). A closure model to crack growth under large-scale yielding and through residual stress fields. Journal of Engineering Materials and Technology, Transactions of the ASME, vol. 125, no. 2, pp. 183-190.

90. Ma, Y.E., Staron, P., Fischer, T. & Irving, P.E. (2011). Size effects on residual stress and fatigue crack growth in friction stir welded 2195-T8 aluminium - Part II: Modelling. International Journal of Fatigue, vol. 33, no. 11, pp. 1426-1434.

91. Zhu, X.Y. & Shaw, W.J.D. (1995). Correlation of fatigue crack growth behaviour with crack closure in peened specimens. Fatigue and Fracture of Engineering Materials and Structures, vol. 18, no. 7-8, pp. 811-820.

92. Ruschau, J.J., John, R., Thompson, S.R. & Nicholas, T. (1999). Fatigue crack growth rate characteristics of laser shock peened Ti-6Al-4V. Journal of Engineering Materials and Technology, vol. 121, no. 3, pp. 321-329.

93. Ruschau, J.J., John, R., Thompson, S.R. & Nicholas, T. (1999). Fatigue crack nucleation and growth rate behavior of laser shock peened titanium. International Journal of Fatigue, vol. 21, no. Suppl. 1, pp. S199-S209.

94. Hill, M.R. & Kim, J. (2012). Fatigue crack closure in residual stress bearing materials. Journal of ASTM International, vol. 9, no. 1, pp. 1-16.

95. Pouget, G., & Reynolds, A. P. (2008). Residual stress and microstructure effects on fatigue crack growth in AA2050 friction stir welds. *International Journal of Fatigue*, *30*(3), 463–472.

96. Shokrieh, M. M., & Ghanei Mohammadi, A. R. (2014). The importance of measuring residual stresses in composite materials. In *Residual Stresses in Composite Materials* (pp. 3–14). Elsevier.

97. Prater, T. (2014). Friction stir welding of metal matrix composites for use in aerospace structures. Acta Astronautica, vol. 93, pp. 366-373.

98. Imuta, M. & Kamimuki, K. (2005). Development and application of friction stir welding for aerospace industry. Welding Research Abroad, vol. 51, no. 1, pp. 35-41.

99. Freeman, R. (2008). Welding and joining developments in the aerospace industry. Welding and Cutting, vol. 7, no. 5, pp. 274-275.

100. Altenberger, I. (2005). Alternative Mechanical Surface Treatments for Fatigue Strength Enhancement, 328–333.

101. Hatamleh, O. (2006). Effects of Laser and Shot Peening on Friction Stir Welding, (281), 1–10.

102. Walker, D. (2001). Residual Stress Measurement Techniques. *Advanced Materials & Processes*, *159*(8), 30–33.

103. Withers, P. J., & Bhadeshia, H. K. D. H. (2001). Residual stress. Part 1– measurement techniques. *Materials Science and Technology*, *17*(April), 355–365.

104. Rokkam, S., Rebak, R. B., Cui, B., & Dryepondt, S. (2017). Environmentally Assisted Stress Corrosion Cracking. *JOM*, *69*(12), 2851–2852.

105. Richard a lane. (2005). Editorial: Failure is an Integral Part of Success. *Amptiac*.

106. Metal Improvement Company. (2012). Shot Peening [online]. available: http://www.metalimprovement.com/shot_peening.php

107. Brockman, R.A., Braisted, W.R., Olson, S.E., Tenaglia, R.D., Clauer, A.H., Langer, K. & Shepard, M.J. (2012). Prediction and characterization of residual stresses from laser shock peening. International Journal of Fatigue, vol. 36, no. 1, pp. 96-108.

108. Evan Aldrine, M., Mahendra Babu, N. C., & Anil Kumar, S. (2017). Evaluation of Induced Residual Stresses due to Low Plasticity Burnishing through Finite Element Simulation. *Materials Today: Proceedings*, *4*(10), 10850–10857.

109. Klopfen, P., & Kaltschmiedewerkzeug, F. (2014). Vorstellung Werkzeug bzw. System FORGEfix.

110. Lienert, F., Hoffmeister, J., & Schulze, V. (2013). Residual Stress Depth Distribution after Piezo Peening of Quenched and Tempered AISI 4140. *Materials Science Forum*, *768–769*, 526–533.

111. Institute for Production Engineering and Laser Technology. (2015). Functionalising of surfaces via machine hammer peening.

112. Prevéy, P., Jayaraman, N., & Ravindranath, R. (2004). Introduction of Residual Stresses to Enhance Fatigue Performance in the Initial Design.

113. McClung, R. C. (2007). A literature survey on the stability and significance of residual stresses during fatigue. *Fatigue and Fracture of Engineering Materials and Structures*, *30*(3), 173–205.

114. Gourdin, S., Cormier, J., Henaff, G., Nadot, Y., Hamon, F., & Pierret, S. (2017). Assessment of specific contribution of residual stress generated near surface

anomalies in the high temperature fatigue life of a René 65 superalloy. *Fatigue and Fracture of Engineering Materials and Structures*, *40*(1), 69–80.

115.   Schulze, V. (2006). Procedures of Mechanical Surface Treatments. In Modern Mechanical Surface Treatment, V. Schulze (Ed.).

116.   Broszeit, E. , Preussler, T. , Wagner, M. and Zwirlein, O. (1986), Stress Hypotheses and material stresses in Hertzian contacts. Mat.-wiss. u. Werkstofftech., 17: 238-246.

117.   O. Vo˙hringer. (1986). Relaxation of residual stresses. In: Residual Stresses (Edited by E. Macherauch and V. Hauk), DGM, pp. 47–80.

118.   Coules, H. E., Horne, G. C. M., Kabra, S., Colegrove, P., & Smith, D. J. (2017). Three-dimensional mapping of the residual stress field in a locally rolled aluminium alloy specimen. *Journal of Manufacturing Processes*, *26*, 240–251.

119.   Kandil, F. A., Lord, J. D., Fry, A. T., & Grant, P. V. (2001). A Review of Residual Stress Measurement Methods -A Guide to Technique Selection. *NPL Materials Centre*.

120.   ASTM. (2008). Determining Residual Stresses by the Hole-Drilling Strain-Gage Method. *Standard Test Method E837-13a*, *i*, 1–16.

121.   Gnäupel-Herold, T., Schneider, R., Mikula, P., Paranjpe, S. K., Teixeira, J., Torok, G. Youtsos, A. G. (2005). Measurement of residual stress in materials using neutrons Proceedings of a technical meeting held in Vienna 13-17 October, 2003. *International Atomic Energy Agency*, 1–99.

122.   Masubuchi K. (1980). Analysis of welded structures, *Pergamon Press*.

123.   Leggatt, R. H., Smith, D. J., Smith, S. D., & Faure, F. (1996). Development and experimental validation of the deep hole method for residual stress measurement. *The Journal of Strain Analysis for Engineering Design*, *31*(3), 177–186.

124.   Schajer, G. S. (2018). Non-uniform residual stress measurements by the hole drilling method. *Strain*, *28*(1), 19–22.

125.   Cullity B. D. (1956). Elements of X-ray Diffraction, ADDISON-WESLEY.

126.   Webster, P. J., Oosterkamp, L. D., Browne, P. A., Hughes, D. J., Kang, W. P., Withers, P. J., & Vaughan, G. B. M. (2001). Synchrotron X-ray residual strain scanning of a friction stir weld. *The Journal of Strain Analysis for Engineering Design*, *36*(1), 61–70.

127.   Rustichelli, G. A. and G. B. and A. C. and F. F. and M. R. and F. (1999). Determination of residual stresses in materials and industrial components by neutron diffraction. *Measurement Science and Technology*, *10*(3), R56.

128.   Rossini, N. S., Dassisti, M., Benyounis, K. Y., & Olabi, A. G. (2012). Methods of measuring residual stresses in components. *Materials and Design*.

129.   ZHOU, J., & TSAI, H. L. (2005). Welding heat transfer. In *Processes and Mechanisms of Welding Residual Stress and Distortion* (pp. 32–98). Elsevier.

130.   Dong P., Hong J.K. & Leis B.N. (2006). "Computational simulation of line-pipe fabrication processes" Proceedings of the 6th International Pipeline Conference, September 25-29, Calgary, Canada.

131.   Otsuka, Y., Nagaoka, S., & Mutoh, Y. (2011). Effects of dissolved oxygen on fatigue characteristics of austenitic stainless steel in 0.9wt% sodium chloride solutions. *Procedia Engineering*, *10*, 1333–1338.

132.   Beghini, M., Bertini, L. & Vitale, E. (1994). Fatigue crack growth in residual stress fields: experimental results and modelling. *Fatigue & Fracture of Engineering Materials & Structures*. Vol. 17, no. 12, pp. 1433-1444.

133.   Bussu, G. & Irving, P.E. (2003). The role of residual stress and heat affected zone properties on fatigue crack propagation in friction stir welded 2024-T351 aluminium joints. *International Journal of Fatigue*. Vol. 25, no. 1, pp. 77-88.

134. Liljedahl, C.D.M., Tan, M.L., Zanellato, O., Ganguly, S., Fitzpatrick, M.E. & Edwards, L. (2008). Evolution of residual stresses with fatigue loading and subsequent crack growth in a welded aluminium alloy middle tension specimen. *Engineering Fracture Mechanics*. Vol. 75, no. 13, pp. 3881-3894.

135. Reed, E.C. & Viens, J.A. (1960). The Influence of Surface Residual Stress on Fatigue Limit of Titanium. *Journal of Engineering for Industry*. Vol. 82, pp. 76-78.

136. Mutoh, Y., Fair, G.H., Noble, B. & Waterhouse, R.B. (1987). The effect of residual stresses induced by shot-peening on fatigue crack propagation in two high strength aluminium alloys. *Fatigue and Fracture of Engineering Materials and Structures*. Vol. 10, no. 4, pp. 261-272.

137. Pradesh, U., & Pradesh, U. (2015). A study on methods to measure residual stress 1 1 2, *1*(2), 112–114.

138. O.J. Horger, Journal Appl. Mech. 58 (1936) 91.

139. O. Foppl, Stahl und Eisen 49 (1929) 575.

140. A. Thum., W. Bautz, Forsch. Ing. Wesen 6 (1935) 121.

141. P. Strigens, Dr.-lng. Thesis, University of Darmstadt, 1971. 5.

142. H. Wiegand, P. Strigens, Draht 20 (1969) 189.

143. G. Berstein, B. Fuchsbauer, Z. Werkstofftech. 13 (1982) 103.

144. S. Gruber, G. Holzheimer, H. Naundorf, Z. Werkstofftech. 14 (1984) 41.

145. E. Broszeit, Z. Werkstofftech. 15 (1984) 416.

146. Zhuang, W., Liu, Q., Djugum, R., Sharp, P. K., & Paradowska, A. (2014). Deep surface rolling for fatigue life enhancement of laser clad aircraft aluminium alloy. *Applied Surface Science*, *320*, 558–562.

147. Prevéy, P. S., & Lane, F. (2004). The influence of surface enhancement by low plasticity on the corrosion fatigue performance of AA7075: I. *J. Fatigue*, *26*(9), 975.

148.   Maawad, E. K. S. (2013). Residual Stress Analysis and Fatigue Behavior of Mechanically Surface Treated Titanium Alloys.

149.   Lim, A., Castagne, S., & Cher Wong, C. (2016). Effect of Deep Cold Rolling on Residual Stress Distributions Between the Treated and Untreated Regions on Ti–6Al–4V Alloy. *Journal of Manufacturing Science and Engineering*, *138*(11), 111005.

150.   Oberwinkler, B., Leitner, H., & Stoschka, M. (2008). Influence of Shot Peening on the Fatigue Behaviour of Ti-6Al-4V in Respect of Multiaxial Loading. *on Shot Peening (ICSP10)*

151.   Colosimo, B. M., & Monno, M. (1999). Surface Strengthening by Water Jet Peening BT - AMST '99. In E. Kuljanic (Ed.) (pp. 627–634). Vienna: Springer Vienna.

152.   Cary, P.E. (1982). History of shot peening. Shot Peener, pp. 23-28.

153.   Soady, K.A. (2013). Life assessment methodologies incoroporating shot peening process effects: Mechanistic consideration of residual stresses and strain hardening: Part 1 - Effect of shot peening on fatigue resistance. Materials Science and Technology, vol. 29, no. 6, pp. 637-651.

154.   White, R.M. (1963). Elastic wave generation by electron bombardment or electromagnetic wave absorption. Journal of Applied Physics, vol. 34, no. 7, pp. 2123-2124.

155.   Mallozi, P.J. & Fairand, B.P. (1974). Industrial Materials Limited Altering material properties, U.S. Pat. 3,850,698.

156.   Mannava, S., McDaniel, A.E., Cowie, W.D., Halila, H., Rhoda, J.E., Gutknecht, J.E., General Electric Company. (1997). Laser shock peened gas turbine engine fan blade edges, U.S. Pat. 5,591,009.

157.   Shidid, D.P., Gollo, M.H., Brandt, M. & Mahdavian, M. (2013). Study of effect of process parameters on titanium sheet metal bending using Nd: YAG laser. Optics and Laser Technology, vol. 47, pp. 242-247.

158.   Hu, Y., Xu, X., Yao, Z. & Hu, J. (2010). Laser peen forming induced two way bending of thin sheet metals and its mechanisms. Journal of Applied Physics, vol. 108, no. 7.

159.   Ganesh, P., Sundar, R., Kumar, H., Kaul, R., Ranganathan, K., Hedaoo, P., Tiwari, P., Kukreja, L.M., Oak, S.M., Dasari, S. & Raghavendra, G. (2012). Studies on laser peening of spring steel for automotive applications. Optics and Lasers in Engineering, vol. 50, no. 5, pp. 678-686.

160.   Zhu, J., Jiao, X., Zhou, C. & Gao, H. (2012). Applications of Underwater Laser Peening in Nuclear Power Plant Maintenance. Energy Procedia, vol. 16, pp. 153-158.

161.   Hu, Y. & Yao, Z. (2008). Overlapping rate effect on laser shock processing of 1045 steel by small spots with Nd:YAG pulsed laser. Surface and Coatings Technology, vol. 202, no. 8, pp. 1517-1525.

162.   Kalainathan, S., Sathyajith, S. & Swaroop, S. (2012). Effect of laser shot peening without coating on the surface properties and corrosion behavior of 316L steel. Optics and Lasers in Engineering, vol. 50, pp. 1740-1745.

163.   Ling, X., Peng, W. & Ma, G. (2008). Influence of laser peening parameters on residual stress field of 304 stainless steel. Journal of Pressure Vessel Technology, Transactions of the ASME, vol. 130, no. 2, pp. 0212011-0212018.

164.   Fang, Y.W., Li, Y.H., He, W.F. & Li, P.Y. (2013). Effects of laser shock processing with different parameters and ways on residual stresses fields of a TC4 alloy blade. Materials Science and Engineering A, vol. 559, pp. 683-692.

165.   Smith, P.R., Shepard, M.J., Prevéy III, P.S. & Clauer, A.H. (2000). Effect of power density and pulse repetition on laser shock peening of Ti-6Al-4V. Journal of Materials Engineering and Performance, vol. 9, no. 1, pp. 33-37.

166.   Cao, Y., Shin, Y.C. & Wu, B. (2010). Parametric study on single shot and overlapping laser shock peening on various metals via modeling and experiments.

Journal of Manufacturing Science and Engineering, Transactions of the ASME, vol. 132, no. 6, pp. 0610101-06101010.

167.   Gomez-Rosas, G., Rubio-Gonzalez, C., Ocaña, J.L., Molpeceres, C., Porro, J.A., Morales, M. & Casillas, F.J. (2010). Laser Shock Processing of 6061-T6 Al alloy with 1064 nm and 532 nm wavelengths. *Applied Surface Science*. Vol. 256, no. 20, pp. 5828-5831.

168.   Sathyajith, S., Kalainathan, S. & Swaroop, S. (2013). Laser peening without coating on aluminum alloy Al-6061-T6 using low energy Nd:YAG laser. *Optics & Laser Technology*. Vol. 45, no. 0, pp. 389-394.

169.   Rankin, J.E., Hill, M.R. & Hackel, L.A. (2003). The effects of process variations on residual stress in laser peened 7049 T73 aluminum alloy. Materials Science and Engineering A, vol. 349, no. 1-2, pp. 279-291.

170.   RadajD., (1992). Heat effects of welding: temperature field, residual stress, distortion, Springer-Verlag, Berlin.

171.   DydoR.J., CastnerH.R., and Koppenhoefer K., (1999). Guidelines for The Control of Distortion in Thin Ship Structures, Columbus, Ohio.

172.   SunY.-J., ZangY., and ShiQ.-Y. (2010). Numerical Simulations of Friction Stir Welding Process and Subsequent Post Weld Cold Rolling Process. Key Eng. Mater., 419, pp. 433–436.

173.   WenS.W., ColegroveP., WilliamsS.W., MorganS.A., WescottA., and PoadM. (2010). Rolling to control residual stress and distortion in friction stir welds. Sci. Technol. Weld. Join., 15(6), pp. 440–447.

174.   AltenkirchJ., Steuwera., WithersP.J., WilliamsS.W., PoadM., and WenS.W., (2009). Residual stress engineering in friction stir welds by roller tensioning. Sci. Technol. Weld. Join., 14(2), pp.185–192.

175. KondakovG.F., and MartynovA.N., (1986). Effect of methods of local deformation on residual stresses and properties of welded joints. Weld. Prod. (English Transl. Svarochnoe Proizv., 33(5), pp. 28–30.

176. Bäcker, V., Klocke, F., Wegner, H., Timmer, A., Grzhibovskis, R., & Rjasanow, S. (2010). Analysis of the deep rolling process on turbine blades using the FEM/BEM-coupling. *IOP Conference Series: Materials Science and Engineering*, *10*(1), 012134.

177. Manouchehrifar, A., & Alasvand, K. (2012). Finite element simulation of deep rolling and evaluate the influence of parameters on residual stress. *Proceedings of the 3rd International Conference on Theoretical and Applied Mechanics*, 121–127.

178. Sartkulvanich, P., Altan, T., Jasso, F., and Rodriguez, C. (2007). Finite Element Modeling of Hard Roller Burnishing: An Analysis on the Effects of Process Parameters Upon Surface Finish and Residual Stresses. ASME J. Manuf. Sci. Eng., 129(4), pp. 705–716.

179. Afazov, S., Becker, A., and Hyde, T. (2012). Mathematical Modeling and Implementation of Residual Stress Mapping From Microscale to Macroscale Finite Element Models. ASME J. Manuf. Sci. Eng., 134(2), p. 021001.

180. SPD-10-036: Alloy 2024 sheet and plate (2001) United States: Alcoa Mill Products.

181. Campbell, F. C. (2008). Aluminum. *Elements of Metallurgy and Engineering Alloys*, *3*, 487–508.

182. ASTM Int. (2009). Standard Test Methods for Tension Testing of Metallic Materials 1. *Astm*, *i*(C), 1–27.

183. Kim, J. H., Rhorer, R. L., Kobayashi, H., McDonough, W. G., & Holmes, G. A. (2011). Effects of fiber gripping methods on single fiber tensile test using Kolsky bar. In T. Proulx (Ed.), *Dynamic Behavior of Materials, Volume 1* (pp. 131–136). New York, NY: Springer New York.

184. Coules, H. E., Cozzolino, L. D., Colegrove, P., & Wen, S. W. (2011). The effect of pre-weld rolling on distortion and residual stress in fusion welded steel plate. *Materials Science Forum*, *681*, 486–491.

185. Method, S. T. (2010). Standard Test Method for Microindentation Hardness of MaterialsKnoop and Vickers Hardness of Materials 1. *Annual Book of ASTM Standards*, 1–42.

186. ASTM. (2008). Determining Residual Stresses by the Hole-Drilling Strain-Gage Method. *Standard Test Method E837-13a*, *i*, 1–16. https://doi.org/10.1520/E0837-13A.2

187. Nykamp DQ, "Calculating the area under a curve using Riemann sums." From Math Insight. http://mathinsight.org/calculating_area_under_curve_riemann_sums

188. ASTM E647, A. S. (2016). ASTM E647 - Standard Test Method for Measurement of Fatigue Crack Growth Rates. *ASTM Book of Standards*, *03*(July), 1–49.

189. NASGRO (2002) Fracture Mechanics and Fatigue Crack Growth Analysis Software, Version 4.02, NASA-JSC and SwRI.

190. Baptista, C. A. R. P., Adib, A. M. L., Torres, M. A. S., & Pastoukhov, V. A. (2012). Describing fatigue crack growth and load ratio effects in Al 2524 T3 alloy with an enhanced exponential model. *Mechanics of Materials*, *51*, 66–73.

191. Uddin, M. S. (2018). Finite Element Analysis of Surface Integrity in Deep Ball-Burnishing of a Biodegradable AZ31B Mg Alloy, 1–17.

192. Maximov, J. T., Duncheva, G. V., Anchev, A. P., & Ichkova, M. D. (2014). Modeling of strain hardening and creep behaviour of 2024T3 aluminium alloy at room and high temperatures. *Computational Materials Science*, *83*(November), 381–393.

193. Taddia, S., & Troiani, E. (2015). *Effect of Laser Shock Peening on the Fatigue Behavior of Thin Aluminum Panels*. *Materials Today: Proceedings* (Vol. 2). Elsevier Ltd.

194. Tada, H., & Paris, P. C. (1983). The stress intensity factor for a crack perpendicular to the weld- ing bead, *21*, 279–284.

195. Bao, R., Zhang, X., & Yahaya, N. A. (2010). Evaluating stress intensity factors due to weld residual stresses by the weight function and finite element methods. Engineering Fracture Mechanics, 77(13), 2550–2566.

196. Servetti, G. (2011). Modelling and predicting fatigue crack growth behaviour in weld induced residual stress fields (PhD), Cranfield University.

197. Chahardehi, A., Brennan, F. P., & Steuwer, A. (2010). The effect of residual stresses arising from laser shock peening on fatigue crack growth. *Engineering Fracture Mechanics*, *77*(11), 2033–2039.

10 APPENDICES

Appendix A Fatigue Performance between HP and DSR

Hammer peening samples were fatigue tested. Half crack length against number of cycles was shown in figure 9.1. Y-axis represents the half crack length, averaged by full crack length *2a*. X-axis represents the records of cycle numbers.
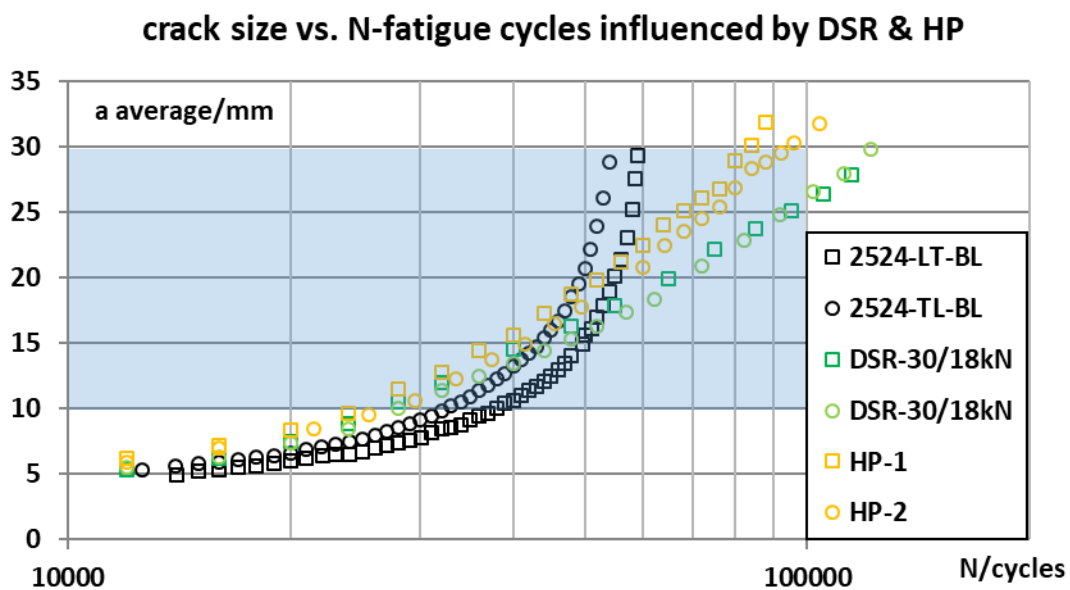

Figure 10.1 Fatigue data of HP (L) and DSR (30/18kN) treated samples

Hammer peening (HP) treatment in this research was used by a prototype kit. As a result, only two samples were used to be treated by HP. The compressive residual stress induced by HP was not as high as induced by DSR of 60/15kN. The fatigue performance of hammer peened samples was close to the fatigue data of DSR (30/18kN).

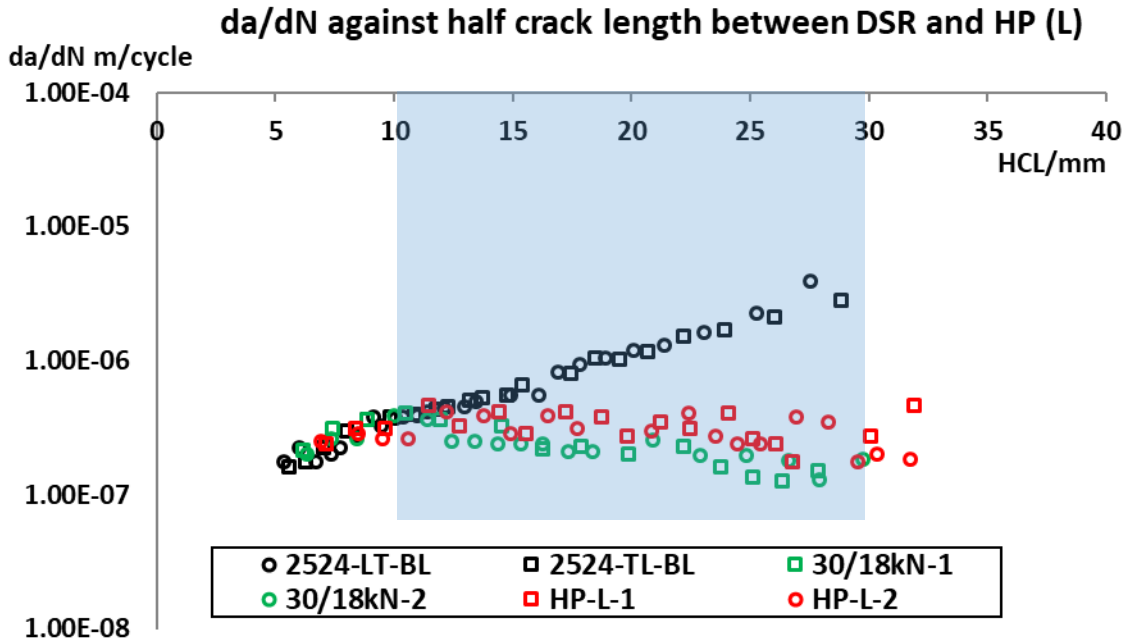The FCGR of HP (L) and DSR (30/18kN) is shown in figure 9.2.

Figure 10.2 FCGR of HP (L) and DSR (30/18kN) compared to untreated samples (BL), AA2524-T351, stress ratio *R = 0.1*

The maximum value of compressive residual stress caused by HP (L) was 150 MPa. By averaging residual stress in the thickness, value of averaged RS was −92 MPa. The value of averaged RS by DSR (30/18kN) was −175 MPa. That explained the result in figure 9.2. DSR (30/18kN) showed down the FCGR, more significantly compared to the hammer peening treatment (HP-L).
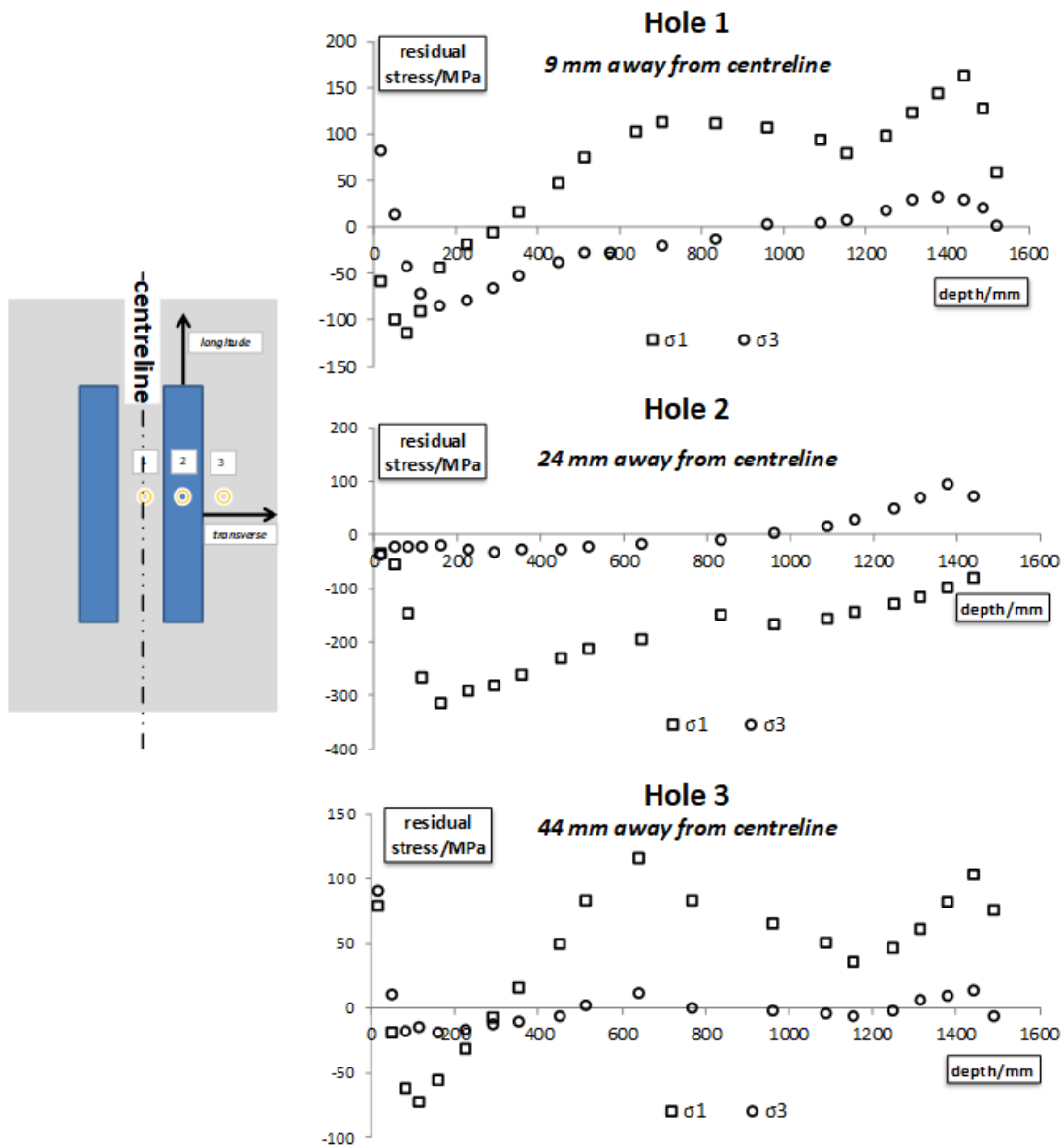
Appendix B Residual Stress by ICHD

Figure 10.3 Residual stress measured in-depth, three positions along the width. DSR (30/18kN), AA2524-T351

Residual stress of hole 1, hole 2 and hole 3 were measured, 9 mm away from the centreline, 24 mm away from the centreline and 44 mm away from the centreline, respectively.
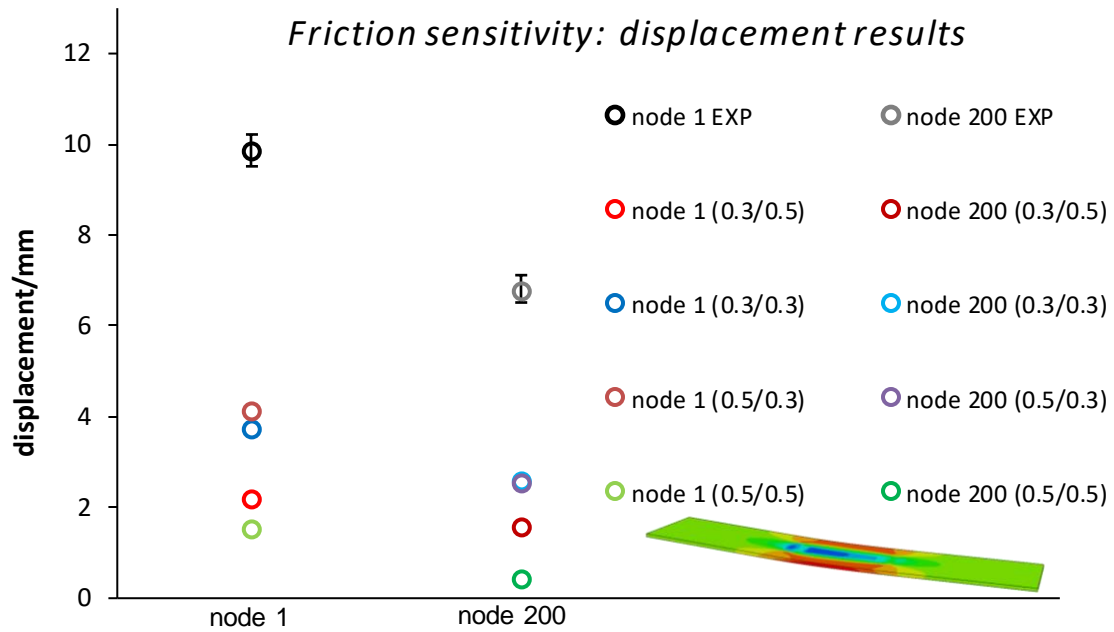
Appendix C Friction Coefficient Study

Figure 10.4 Friction coefficient study: other combinations of friction coefficients 0.3/0.3, 0.3/0.5, 0.5/0.3, 0.5/0.5, performed by the largest displacements, obtained from two end nodes